
Comprehensive study of the background for the Pixel Vertex Detector at Belle II

Andreas Moll

Dissertation
an der Fakultät für Physik
der Ludwig-Maximilians-Universität
München

vorgelegt von
Andreas Moll
aus München

München, den 24.06.2015

Erstgutachter: Prof. Dr. Christian Kiesling

Zweitgutachter: Prof. Dr. Thomas Kuhr

Tag der mündlichen Prüfung: 31.07.2015

Contents

Abstract	v
Zusammenfassung	ix
1 Introduction	1
2 Physics at Belle II	5
2.1 The Standard Model of particle physics	5
2.1.1 The electromagnetic interaction	7
2.1.2 The strong interaction	7
2.1.3 The weak interaction and electroweak unification	8
2.1.4 The Standard Model	9
2.2 CP-Violation in the Standard Model	10
2.3 CP-Violation measurement	16
2.4 Beyond the Standard Model	20
3 The SuperKEKB $e^+ e^-$ collider	25
3.1 The SuperKEKB storage ring	26
3.2 The coordinate system	28
3.3 Beam Transport System	28
3.4 Beam focusing	29
3.5 Beam dynamics	33
3.6 Luminosity and nano-beam scheme	37
3.7 Particle generation and acceleration	40
3.8 Injection scheme	41
3.9 Beam and particle loss	41
3.10 Simulation of the beam transport	42
4 The Belle II Detector	45
4.1 The coordinate system	48
4.2 The Interaction Region	48
4.3 The Pixel Vertex Detector	51
4.3.1 The DEPFET pixel sensor	51

4.3.2	Sensitive area layout	53
4.3.3	Readout cycle	54
4.3.4	Gated mode	54
4.3.5	Mechanical layout	55
4.3.6	Radiation damage	56
4.3.7	Power consumption and Cooling	57
4.3.8	Naming convention	58
4.4	The Silicon Vertex Detector	60
4.4.1	Layout	60
4.4.2	Sensors	61
4.4.3	Readout	63
4.5	The Central Drift Chamber	64
4.6	The Time of Propagation Counter	65
4.7	The Aerogel Rich Detector	67
4.8	The Electromagnetic calorimeter	69
4.9	The Solenoid	71
4.10	The KLM	71
4.10.1	Barrel KLM	72
4.10.2	Endcap KLM	74
4.11	Trigger	75
4.12	Data Acquisition	76
5	The Belle II Software Framework	79
5.1	The Framework Core	80
5.2	Event and Particle Generation	83
5.3	Geometry Handling	85
5.4	Full Detector Simulation	89
5.5	Digitisation for the PXD	91
5.6	Clustering in the PXD	95
5.7	Data Persistency and the PXD Event Model	96
5.8	Impact parameter resolution	98
6	Measurement of e^+e^- pairs from the two-photon process	103
6.1	Introduction	103
6.2	Two-photon processes	104
6.3	Generation of Monte Carlo events	109
6.3.1	The generators	110
6.3.2	The two-photon event production	111
6.3.3	4-vector comparison	114

6.4	The QED Experiment at Belle	117
6.4.1	The KEKB asymmetric electron-positron collider	117
6.4.2	The Belle detector	117
6.4.3	The dedicated background experiment	118
6.5	Analysis of low pt two-photon events	122
6.5.1	SVD hit multiplicity measurement	122
6.5.2	CDC correction	124
6.5.3	Systematics	127
6.5.4	Comparison with Monte Carlo data	129
6.6	Reconstruction and analysis of high pt two-photon events	129
6.6.1	Normalisation of the random trigger events	129
6.6.2	Monte Carlo generation	139
6.6.3	Reconstruction of the two-photon events	140
6.6.4	Results from data	142
6.7	Conclusion	148
7	Expected background for the PXD	151
7.1	Introduction	151
7.2	Detailed simulations of the PXD background	151
7.2.1	Relative normalisation of backgrounds	152
7.2.2	PXD simulation and reconstruction	153
7.3	Figures of merit	153
7.3.1	Particle flux	153
7.3.2	Origin of particles	154
7.3.3	Occupancy	154
7.3.4	Cluster analysis	154
7.3.5	Radiation dose	158
7.3.6	Neutron flux	158
7.4	Beam-induced processes	160
7.4.1	Touschek effect	160
7.4.2	Beam-Gas	173
7.4.3	Synchrotron radiation	183
7.5	Luminosity-dependent processes	206
7.5.1	Radiative Bhabha scattering	206
7.5.2	Two-photon events	218
7.6	Summary of all PXD backgrounds	225
7.6.1	Particle flux	225
7.6.2	Origin of particles	228
7.6.3	Occupancy	228
7.6.4	Cluster analysis	231

7.6.5	Radiation dose	232
7.6.6	Neutron flux	234
7.7	Background merging for physics events	235
7.8	Concluding remarks on the PXD backgrounds	237
8	Conclusion and Outlook	239
A	Tables and figures for the two-photon process measurement	245
A.1	Tables	245
A.2	Figures	255
A.2.1	Momentum distribution of the recorded data, simulated background and the simulated BDK signal after each reconstruction step	255
A.2.2	Momentum distribution of the recorded data, simulated background and the simulated KoralW signal after each reconstruction step	256
A.2.3	Opening angle distribution of the recorded data, simulated background and the simulated BDK signal after each reconstruction step	257
A.3	The Belle and Belle II boost	258
B	Theory of additional background components	261
B.1	Beam-Gas Bremsstrahlung	261

Abstract

The highly successful Belle experiment was located at the KEKB accelerator in Tsukuba, Japan. KEKB was an electron-positron ring accelerator running at the asymmetric energies of 8 GeV (e^-) and 3.5 GeV (e^+). The Belle experiment took data from 1999 to 2010, but was shut down in June 2010 in order to begin a major upgrade of the accelerator and the detector. Belle played a crucial role in the award of the 2008 Nobel Prize for Physics to M. Kobayashi and T. Maskawa. The main physics goal of Belle was the measurement of CP -violation in the B -meson system.

This mission, as well as the search for physics beyond the Standard Model, has been passed to the Belle II experiment located at the SuperKEKB accelerator, the direct successors of the Belle experiment and KEKB respectively. The precise measurement of CP -violation and the search for rare or “forbidden” decays of the B -meson and the τ -lepton as signals for New Physics relies heavily on a large number of recorded events and the precision with which B -meson and lepton decay vertices can be reconstructed. Thus, the accelerator upgrade aims for an increase of the luminosity by a factor of 40, resulting in a peak luminosity of $8 \times 10^{35} \text{ cm}^{-2} \text{ s}^{-1}$. This upgrade is scheduled to be finished by 2017 and will result in asymmetric beam energies of 7 GeV (e^-) and 4 GeV (e^+), provided by beams with a vertical size of only 48 nm (“nano-beam optics”), a size that has never been reached at any particle collider before.

The accelerator upgrade will result in the desired increase of the collision rate of particles, while it will also inevitably lead to an increase in the background for all sub-detectors. The Belle detector would not have been able to handle the new background conditions expected at SuperKEKB, hence an upgrade of the Belle detector to the Belle II detector was necessary. Additionally the upgrade aims to increase the physics performance of the detector, making it more sensitive to the effects of New Physics. The detector upgrade will see improvements and redesigns of almost all subsystems as well as the inclusion of a whole new sub-detector, the PiXel vertex Detector (PXD). The introduction of the PXD will ensure that decay vertices are reconstructed with an extremely high precision in the harsh background conditions expected at Belle II. The PXD is a semi-conductor based particle tracking detector and will be the innermost sub-detector of Belle II. It offers excellent track and vertex reconstruction capabilities, while having a thickness of only 75 μm in order to minimise multiple scattering effects.

Due to the innovative concept of a high-luminosity nano-beam accelerator, the scale of background being produced at the future SuperKEKB cannot be derived from a traditional electron-positron collider and has, therefore, to be simulated using first-principle Monte Carlo tech-

niques. This thesis focuses on a detailed study of the expected background for the pixel vertex detector at the upcoming Belle II experiment. It starts with a comprehensive summary of the key components of the SuperKEKB accelerator and the Belle II detector before delving into the details of the Belle II simulation and reconstruction framework basf2. It was decided to develop the basf2 framework from scratch, rather than adapting the software framework used at Belle. The changes made in the upgrade from the Belle to the Belle II detector, would have required major modifications of nearly all existing libraries.

This thesis continues by explaining, in detail, the measurement and analysis of an experiment conducted at Belle in 2010, shortly before the KEKB accelerator and the Belle detector were shut down. The experiment aimed at establishing the validity of a major background for the PXD, namely the two-photon process into an electron-positron pair, described by the Monte-Carlo generators KoralW and BDK, which have never been tested in the kinematical region relevant for the PXD. From a comparison based on Monte Carlo data it is found that the difference between KoralW and BDK in the high cross-section, low p_t region (smaller than 20 MeV) for the produced electron and positron is very small, and that both Monte-Carlo generators agree with the experiment in this important low momentum regime. However, the question arises as to whether the delivered cross-section of the Monte Carlo generators is correct over a wider phase space, but still below the centre-of-mass energies where these generators have been verified experimentally (e.g. at the e^+e^- colliders PETRA and LEP). In order to answer this question, a comparison between recorded detector data and Monte Carlo data is performed, an analysis that has never been done for centre-of-mass energies of the order of those of the Belle and Belle II experiments. From the results the conclusion is drawn that both Monte Carlo generators, KoralW and BDK, agree very nicely for low values of p_t but differ significantly for intermediate values where the total cross-sections are already very small. The recorded data proved that for intermediate p_t ranges the behaviour of BDK is correct, while KoralW overshoots the data. Since, however, the cross-section peaks strongly for low values of p_t both generators can be used for further background studies.

Furthermore, this thesis includes a detailed basf2 simulation study of the major beam and QED backgrounds that are expected at Belle II and their impact on the PXD. Various figures of merit are estimated, such as particle flux, radiation dose and occupancy. On average the inner layer experiences a particle flux of 6.1 MHz cm^{-2} and the outer layer of 2.5 MHz cm^{-2} . The distribution of the particle flux along the global z -axis is fairly flat meaning that the radiation damage is evenly distributed along the PXD ladders. The simulation shows that the inner layer of the PXD is exposed to a radiation dose of 19.9 kGy/smy^1 and the outer layer to a dose of 4.9 kGy/smy . Irradiation tests of DEPFET sensors with 10 MeV electrons showed that the sensors work reliably for a dose of at least 100 kGy. It is believed that they can even cope with up to 200 kGy. Using the radiation dose values obtained from the simulation, the numbers translate to a lifetime of roughly 10 years for the PXD sensors, the typical operation time of a high energy physics

¹1 smy = 1 snowmass year = 10^7 s

detector. The study shows that the expected PXD occupancy, summing over all background sources, is given by

inner layer : $1.28 \pm 0.03\%$

outer layer : $0.45 \pm 0.01\%$

The upper limit for the PXD, imposed by the data acquisition and the track reconstruction, is 3 %. The estimated values are well below this limit and, thus, the PXD will withstand the harsh background conditions that are expected at Belle II.

Zusammenfassung

Das sehr erfolgreiche Belle Experiment war am KEKB Beschleuniger in Tsukuba, Japan beheimatet. KEKB war ein Elektron-Positron Ringbeschleuniger mit den asymmetrischen Energien 8 GeV (e^-) und 3.5 GeV (e^+). Das Belle Experiment sammelte von 1999 bis 2010 Daten, wurde aber im Juni 2010 abgeschaltet, da mit einem umfassenden Upgrade des Beschleunigers und des Detektors begonnen werden sollte. Belle spielte eine wesentliche Rolle für die Arbeiten von M. Kobayashi und T. Maskawa, welchen hierfür im Jahre 2008 der Nobelpreis verliehen wurde. Das vorrangige Ziel der Physik an Belle war die Messung der CP -Verletzung im B -Mesonen System.

Diese Aufgabe, wie auch die Suche nach Physik jenseits des Standard Modells, wurde an das Belle II Experiment, das nun am SuperKEKB Beschleuniger angesiedelt ist, weitergereicht. Belle II und SuperKEKB sind die direkten Nachfolger des Belle Experimentes und des KEKB Beschleunigers. Die Genauigkeit, mit der CP -Verletzung gemessen werden kann, wie auch die Durchführung der Suche nach seltenen oder “verbotenen” Zerfällen der B -Mesonen und Tau -Leptonen als Signale von Neuer Physik, hängt stark von der Anzahl an aufgezeichneten Ereignissen und der Rekonstruktionspräzision von B -Meson und Lepton Zerfallsvertices ab. Daher ist es das Ziel des Beschleuniger Upgrades, die Luminosität um einen Faktor 40 auf die Instantane Luminosität von $8 \times 10^{35} \text{ cm}^{-2} \text{ s}^{-1}$ zu erhöhen. Das Upgrade, das bis 2017 abgeschlossen sein soll, wird Strahlen mit den asymmetrischen Energien 7 GeV (e^-) und 4 GeV (e^+) erzeugen. Die vertikale Breite wird nur 48 nm (“nano-beam optics”) betragen, eine Breite, die noch nie zuvor bei einem Teilchenbeschleuniger erreicht wurde.

Das Beschleuniger Upgrade wird nicht nur, wie erwünscht, die Teilchenkollisionsrate erhöhen, sondern zwangsläufig auch zu einer Erhöhung des Untergrunds in allen Subdetektoren führen. Da der Belle Detektor den zu erwartenden Untergrundbedingungen bei SuperKEKB nicht gewachsen wäre, wurde ein Upgrade des Belle Detektors zum Belle II Detektor notwendig. Ebenso hat das Upgrade eine Verbesserung der Physik Performance des Detektors zum Ziel, um ihn sensitiver auf Effekte Neuer Physik zu machen. Während des Upgrades werden fast alle Subsysteme verbessert und überarbeitet. Zusätzlich wird ein komplett neuer Subdetektor, der PiXel vertex Detector (PXD), eingebaut. Durch den PXD wird sichergestellt, dass Zerfallsvertices auch unter den rauen Untergrundbedingungen von Belle II mit einer extrem hohen Präzision rekonstruiert werden können. Der PXD ist ein halbleiter-basierter Spurdetektor und wird der innerste Subdetektor von Belle II sein. Er bietet exzellente Spur- und Vertex - Rekonstruk-

tionsfähigkeiten und ist dabei nur $75 \mu\text{m}$ dünn, um Mehrfachstreuungseffekte zu minimieren.

Da das neuartige Beschleunigerkonzept mit sehr hoher Luminosität und Strahlen im Nanometerbereich arbeitet, ist die Größenordnung des vom zukünftigen SuperKEKB Beschleuniger erzeugten Untergrundes unbekannt und kann nicht von einem traditionellen Elektron-Positron Beschleunigers abgeleitet werden. Daher kann der Untergrund nur mit Hilfe von Monte Carlo Techniken simuliert werden. Diese Arbeit befasst sich mit der detaillierten Studie des zu erwartenden Untergrundes des Pixel Vertex Detektors an dem zukünftigen Belle II Experiment. Sie beginnt mit einer umfassenden Zusammenfassung der Kernkomponenten des SuperKEKB Beschleunigers und des Belle II Detektors, bevor sie mit den Details zum Belle II Simulations und Rekonstruktions Framework basf2 fortfährt. Anstatt das bestehende Belle Software Framework anzupassen, wurde die Entscheidung getroffen, das basf2 Software Framework von Grund auf neu zu entwickeln, denn das Upgrade des Belle Detektors zum Belle II Detektor hätte umfangreiche Anpassungen in fast allen bestehenden Software Bibliotheken notwendig gemacht.

Die vorliegende Arbeit fährt mit einer detaillierten Beschreibung der Messung und Analyse eines Experimentes fort, welches im Jahr 2010 bei Belle durchgeführt wurde, kurz bevor der KEKB Beschleuniger und das Belle Experiment abgeschaltet wurden. Das Experiment hatte zum Ziel, die Korrektheit des Hauptuntergrundes des PXDs festzustellen, den zwei-Photon Prozess in ein Elektron-Positron Paar, beschrieben durch die Monte Carlo Generatoren KoralW und BDK, welche noch nie zuvor in der kinematischen Region getestet wurden die für den PXD relevant ist. Durch einen Vergleich der Monte Carlo Daten ist bekannt, dass der Unterschied zwischen KoralW und BDK für die Region mit hohem Wirkungsquerschnitt und kleinem p_t (kleiner als 20 MeV) für das erzeugte Elektron und Positron sehr klein ist. In dieser Region stimmen die beiden Monte-Carlo Generatoren mit dem Experiment überein. Allerdings stellt sich die Frage, ob der erzeugte Wirkungsquerschnitt der Monte Carlo Generatoren für einen erweiterten Phasenraum korrekt ist. Um diese Frage zu beantworten wurden die aufgezeichneten Detektordaten mit Monte Carlo Daten verglichen. Diese Analyse wurde noch nie zuvor bei Schwerpunktsenergien wie derer von Belle und Belle II durchgeführt. Aus den Ergebnissen wird die Schlussfolgerung gezogen, dass beide Monte Carlo Generatoren sehr gut für kleine Werte von p_t übereinstimmen, aber für grössere Werte bei denen der totale Wirkungsquerschnitt bereits sehr klein ist erheblich voneinander abweichen. Die aufgezeichneten Daten beweisen dass, das Verhalten von BDK für grössere Werte von p_t korrekt ist, während KoralW weit oberhalb der Daten liegt. Da der Wirkungsquerschnitt sein Extremum bei kleinen Werten von p_t hat, können beide Generatoren für weitere Untergrundstudien benutzt werden.

Darüber hinaus enthält die Doktorarbeit eine detaillierte basf2 Simulationsstudie des bei Belle II zu erwartenden Beschleuniger und QED Untergrundes und dessen Einfluss auf den PXD. Verschiedene Bewertungskriterien werden herangezogen, unter anderem der Teilchenfluss, Strahlungsdosis und Okkupanz. Im Mittel ist die innere Lage einem Teilchenfluss von 6.1 MHz cm^{-2} und die äussere Lage einer Teilchenfluss von 2.5 MHz cm^{-2} ausgesetzt. Die Verteilung entlang der globalen z -Achse ist relativ flach, was bedeutet, dass Strahlungsschäden gleichmässig über

den PXD ladder verteilt sind. Die Simulation zeigt, dass die innere Lage des PXDs eine Strahlungsdosis von 19.9 kGy/smy^2 und die äussere Lage eine Dosis von 4.9 kGy/smy erhält. Bestrahlungstests eines DEPFET Sensors mit 10 MeV Elektronen haben gezeigt, dass die Sensoren bis zu einer Dosis von mindestens 100 kGy zuverlässig funktionieren. Es wird angenommen, dass sie sogar einer Dosis von bis zu 200 kGy standhalten können. Nimmt man den vorhergesagten Wert der Strahlungsdosis aus der Simulation, bedeutet dies, dass die PXD Sensoren eine Lebensdauer von etwa 10 Jahren besitzen, was der typischen Laufzeit eines Detektors in der Hochenergiephysik entspricht. Die Studie zeigt folgende Werte für die zu erwartende Okkupanz, summiert über alle Untergrundquellen

innere Lage : $1.28 \pm 0.03\%$

äussere Lage : $0.45 \pm 0.01\%$

Die obere Grenze der Okkupanz des PXDs, die von der Datennahme und der Spurrekonstruktion festgelegt wird, beträgt 3 %. Der vorhergesagte Wert liegt unterhalb dieser Grenze. Es ist daher davon auszugehen, dass der PXD den rauen Untergrundbedingungen bei Belle II standhalten wird.

²1 smy = 1 snowmass year = 10^7 s

1 Introduction

It started with the Big Bang 13.8 billion years ago [1, 2]. The Universe was born from an incredibly high temperature and high energy density where all elementary particles (quarks and leptons) and their anti-particles were created at equal rates. After about 10^{-37} seconds an era of exponential growth, known as **cosmic inflation**, began which increased the volume of the Universe by a factor of at least 10^{78} . What followed is still a mystery today and the motivation for the construction of the Belle II experiment. A process called **baryogenesis** violated the conservation of the baryon number and created an imbalance between baryons and anti-baryons. In the following time, the Universe continued to cool down and the fundamental forces of physics came into action. After 10^{-6} seconds the quarks formed baryons such as protons and neutrons. Eventually, the temperature became too low to create new particle/antiparticle pairs. The existing pairs annihilated and left the Universe with matter but no antimatter. Finally, after a few minutes, neutrons combined with protons to form deuterium and helium nuclei. After about $4 \cdot 10^5$ years, electrons and nuclei combined into atoms.

While the timeline of the Big Bang starting with the formation of the baryons can be reproduced at particle colliders today, the mystery of the missing antimatter in the Universe has not been solved yet. In 1967 Andrei Sakharov¹ formulated three necessary conditions that must be fulfilled to produce matter and antimatter at different rates [3]:

- Violation of the Baryon number
- Violation of C-symmetry and CP-symmetry
- Deviation from the thermal equilibrium

Of particular interest for the Belle II experiment, and the motivation for its existence, is the violation of the CP-symmetry. This violation ensures that the number of produced left-handed baryons (left-handed anti-baryons) is not equal to the number of right-handed anti-baryons (right-handed baryons), thus creating an excess of matter during the baryogenesis. It has been found that the known sources for the violation of the CP-symmetry, as formulated in the Standard Model, are not nearly enough to account for the matter/anti-matter asymmetry observed in the Universe today [4, 5]. Additional sources have to be found. These sources could come from new, not yet discovered physics.

¹A. Sakharov, 1921-1989, father of the hydrogen bomb in the USSR and winner of the Nobel peace price 1975 (for later efforts unrelated to the bomb).

There are two approaches to search for New Physics; increasing the centre-of-mass energy of the collision (“high energy frontier”) or improving the measurement precision (“intensity frontier”). While the first approach is taken by the LHC², SuperKEKB (Belle II) aims for high luminosity and high precision experiments. The LHC with its high centre-of-mass energy is designed to produce and measure new particles directly. On the other hand, SuperKEKB will search for indirect effects of New Physics, by measuring small deviations from the Standard Model expectations. This requires a high measurement precision but allows one to test, by means of quantum loop corrections to the Standard Model, for new particle masses that are beyond the reach of the LHC.

The key to the high precision measurements at SuperKEKB lies in the capability of an e^+e^- collider to produce an extremely large number of “clean” events. While the available energy at the LHC is distributed among the various constituents taking part in the collision, the initial state at an e^+e^- collider is very well defined as the electron annihilates with the positron in order to create new particles. In addition, e^+e^- colliders do not suffer from pileup from additional collisions during the bunch crossing, providing a better control over the background and enabling the measurement of cross-section normalisations. These advantages allow very precise measurements especially of events where particles, such as neutrinos, escape undetected. For example, by setting the centre-of-mass energy of SuperKEKB to the mass of the $\Upsilon(4S)$ resonance, exactly one B -meson and one \bar{B} -meson is produced (see section 2.3). The decay products of one of the B -mesons can then be fully reconstructed and thus the remaining particles, including any undetected particles, are known to belong to the other B -meson. This allows the reconstruction of B -mesons with “invisible” decay products. Examples for applications using this technique are the measurement of the CKM element $|V_{ub}|$ via the semi-leptonic decay $b \rightarrow ul\bar{v}$ and the measurement of the processes $B \rightarrow K\nu\bar{\nu}$ and $B \rightarrow \tau\nu$. But not only do the measurements of final states containing neutrinos benefit from the clean environment at SuperKEKB, it is also essential for the precise measurement of final states that involve γ , π^0 and K_L^0 particles. It should be noted that SuperKEKB (Belle II) is not a competitor to the LHC experiments, but rather a complementary experiment. While SuperKEKB offers a very clean environment, the LHC strength lies in a very large production cross-section for b quarks in the hadron environment allowing it to perform measurements such as $B_s \rightarrow \mu\mu$ with a higher accuracy. It can, however, only reconstruct B -mesons having charged particles as the final decay products.

The high measurement precision at Belle II is achieved in two ways: a very large number of collisions is recorded in order to provide a high statistics sample for analyses and, secondly, an excellent reconstruction of the particle trajectories, especially of their decay vertices, is performed. SuperKEKB aims for an unprecedented instantaneous luminosity of $8 \times 10^{35} \text{ cm}^{-2} \text{ s}^{-1}$. The physics program and the prospects for discovering New Physics at Belle II rely on the precise reconstruction of the decay vertices of particles, in particular of B -mesons, as will be explained

²Large Hadron Collider: a proton-proton and heavy ion collider located at CERN. The largest and most powerful particle collider in the world, as at the time of writing.

in more detail in the next chapter. In order to reach a very good decay vertex measurement precision, the Belle II detector is equipped with a PiXel vertex Detector (PXD) very close to the beampipe. The PXD will be the innermost sub-detector of Belle II and record the passage of particles with a minimal amount of disturbance to their trajectory. An optimal vertex reconstruction is achieved by placing the PXD as closely as possible to the interaction point of the collider. The innermost layer of the PXD is only 14 mm away from the interaction point.

The SuperKEKB accelerator will produce particle beams with a vertical size of only 48 nm; a size that has never been reached at any collider before. Such a high particle density³ leads to a large number of intra-beam scattering (“Touschek”) events that contribute as beam-background events to the overall background in the PXD. In addition, the large luminosity at SuperKEKB will not only produce physics events but also QED background events at a very high rate. Thus, the small beam size and large luminosity will result in a high background level at Belle II, especially in the vicinity of the interaction point. This is the reason that a pixel detector and not a strip detector was chosen as the innermost sub-detector for Belle II. Since there exists no experience with the type and amount of background created by such a small beam at such a high luminosity, the background and its impact on the PXD has to be carefully simulated in detail, using state-of-the-art Monte Carlo techniques. The amount of background in the PXD has a direct impact on the particle trajectory finding and fitting precision. This, in turn, defines the precision with which a decay vertex can be reconstructed and heavily influences the performance of the physics analyses at Belle II.

The goal of this thesis is the evaluation of all possible background sources at Belle II. It was suspected from the beginning that an irreducible background from the QED reaction $\gamma\gamma \rightarrow e^+e^-$ might dominate the background for the PXD. However, the very low energy (tens of MeV) of the e^+e^- pairs made it impossible to study this background (no possibility to trigger) and to validate the Monte Carlo generators in this new phase space. Therefore a special experiment was performed at the KEKB collider in order to study this background for the first time. Two background Monte Carlo generators are compared with the recorded data and the expected background for the Belle II Pixel Vertex Detector is estimated on the basis of these studies. In the following the chapters in this thesis are summarised:

Chapter 1 introduces the field of particle physics and motivates the studies presented in this thesis.

Chapter 2 explains, in more detail, the Standard Model of particle physics including CP -violation, the primary motivation for the construction of B -factories in general and Belle II in particular. It illustrates the limitations of the Standard Model and briefly describes a few extensions that are able to fill the gaps.

³about 10^{11} particles are squeezed into a “bunch”

Chapter 3 provides an in-depth introduction to the SuperKEKB accelerator and the basics of accelerator physics. It lays the ground work for the background simulation chapters and explains the most important design parameters of SuperKEKB.

Chapter 4 focuses then on the measurement device; the Belle II detector. Each part of the detector is described in detail, with particular emphasis on the PXD. The section about the PXD covers its mechanical design, the measurement principle of a DEPFET, the readout scheme and radiation damage effects. In addition to the various sub-detectors, the data acquisition and trigger systems are explained as well.

Chapter 5 is dedicated to the Belle II software framework, a newly developed reconstruction and analysis framework for the Belle II experiment. As the software is crucial for the estimation of the background in the PXD, it is covered in great detail, including the framework core; geometry and simulation tools; digitisation and clustering algorithms in the PXD; and the event model. The chapter closes with the measurement of the expected track impact parameters, highlighting the importance of the PXD at Belle II.

Chapter 6 presents the validation of the two-photon Monte Carlo generators BDK and KoralW with a special data sample taken at the Belle experiment. It starts with the theory of two-photon events and explains why the process $e^+e^- \rightarrow e^+e^-\gamma\gamma \rightarrow e^+e^-e^+e^-$ is the main background for the PXD, followed by a discussion of the experimental setup of the special background runs taken for this validation at Belle in the year 2010, just before KEKB was shut down. The full reconstruction and analysis chain is explained in detail. The chapter finishes with studies to possible backgrounds and the final analysis results.

Chapter 7 fully covers the main backgrounds that are expected at Belle II and their impact on the PXD. Each background is theoretically motivated and the Monte Carlo generation process is explained. The impact on the PXD is quantified by different figures of merit and a simple characterisation of each background type is provided. At the end of the chapter the estimated amount of background is compared to the limits of the PXD.

Chapter 8 summarises the studies presented in this thesis and lists its most important outcomes. Both the impact of the results as well as an outlook are given.

2 Physics at Belle II

This chapter introduces the Standard Model of particle physics and presents the basic concepts of *CP*-violation, the primary motivation of the Belle and, in turn, of the Belle II experiment. It also motivates the physics case for Belle II and possible physics models beyond the Standard Model (“New Physics”, NP).

2.1 The Standard Model of particle physics

At the end of the nineteenth century many physicists thought that all the basic laws of physics were discovered, and what was left to be done is just to refine their details. It was assumed that the laws of Newton [6] and Maxwell’s equations [7] were sufficient to describe all present and future physics phenomena. However, physicists such as Planck, Lorentz, Einstein, Bohr, de Broglie, Schrödinger, Heisenberg, Dirac, and others showed that this assumption was wrong. They introduced revolutionary new concepts and theories, the most important of which being **special relativity** and **quantum mechanics**.

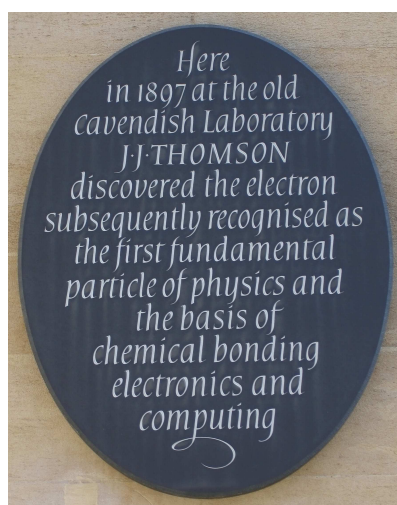


Figure 2.1: Plaque outside the Cavendish laboratory in Cambridge commemorating Sir Joseph Thomson’s discovery of the electron.

In terms of particle physics, important experimental milestones that mark the beginning of this field include the discovery of the electron in 1897 by J.J. Thomson [8] (see figure 2.1) and the discovery of the atomic nucleus from an experiment that involved the scattering of alpha-particles by a thin gold foil, investigated by Geiger, Marsden and Rutherford [9] in 1911. About 100 years and a number of experimental results later, it is believed that the constituents of matter are **elementary particles** carrying spin $\frac{1}{2}$. There are two types: **quarks** and **leptons**. Quarks can only exist combined into a composite particle, called a **hadron**. Examples of hadrons are protons and neutrons, the constituents of atomic nuclei. There are, in total, six types of quarks (and their anti-quarks): **u**(up), **d**(down), **c**(charm), **s**(strange), **t**(top) and **b**(bottom or beauty). The different types of quarks are also called the quark flavours. Leptons, on the other hand, can exist on their own. The most famous example being the electron. A more detailed overview of the elementary particles is given in section 2.1.4.

In classical mechanics, the forces, such as the electric attraction, acting between particles are mediated by fields. In quantum mechanics, however, the interactions between particles are mediated by the exchange of virtual particles having spin 1. Those force carrying particles are called **gauge bosons**. The four fundamental forces of physics, ordered in increasing value of their strength, are listed in table 2.1.

Force	Acts on	Particles experiencing	Relative strength	Range [m]	Particle mediating
Gravity	Mass	All massive particles	10^{-38}	∞	Graviton
Weak	Weak isospin	Most elementary particles	10^{-6}	10^{-18}	W^+, W^-, Z^0
Electromagnetic	Electric charge	Electrically charged	1/137	∞	Photon
Strong	Colour charge	Quarks, Gluons	1	10^{-15}	Gluon

Table 2.1: The fundamental forces [10]. They are ordered in ascending order of their strength. The strength values are normalised to the strength of the strong force.

The first force, the gravitational force, is very small in all known atomic and subatomic processes and therefore its effect is negligible in particle physics. Only the weak, electromagnetic and strong force play an important role in this field of physics.

2.1.1 The electromagnetic interaction

Classical electromagnetism defines the electric field and the magnetic field which obey Maxwell's equations [7]. With their work on the spectrum of black-body radiation, the photoelectric effect and the scattering of photons by electrons, Planck [11], Einstein [12] and Compton[13] showed that the electromagnetic field is quantised, with the quantum of the field being the photon. It was Dirac who proposed in 1928 [14] a first-order linear differential equation which describes the quantum mechanics of point-like, spin $\frac{1}{2}$ particles, completely consistent with special relativity. Applying this equation to electrons, he predicted an electrically positive version of the electron, now known as the positron, which was discovered 3 years later in cosmic radiation [15]. The combined theory, describing the interaction of the charged Dirac field with the quantised electromagnetic field, is called **Quantum ElectroDynamics** (QED). It was finished in 1950 by Feynman [16], Schwinger [17] and Tomonaga [18] who received the Nobel Prize for Physics for their work on QED in 1965. The associated mathematical symmetry group is constructed by applying a simple local gauge invariance. This leads to a field that has all the properties of the electromagnetic field, with the strength of the interaction being g_{em} determined by a constant of the gauge transformation. The strength g_{em} is identified as the charge of the particle. This symmetry group is called **U(1)** and predicts one massless gauge boson associated with the field. This gauge boson, mediating the interaction between electrically charged particles, is the well-known **photon**.

2.1.2 The strong interaction

The quarks and anti-quarks are bound by the strong force, which has a strength that is approximately 10^{38} times higher than the one of the gravitational force (determined by the values of the corresponding coupling constants). The strong force is mediated by virtual particles called **gluons**. Apart from electrical charge, quarks and gluons carry a special charge, the colour charge or, in short, **colour** [19]. There are three kinds of colours (and their anti-colours): **red**, **green** and **blue**. Every quark can possess any of the three colours. Unlike the photon in QED, the gluon carries the interaction charge (colour and a different anti-colour) and can therefore interact with other gluons. Quarks and gluons are not directly observable; they always form colourless composite particles, called **hadrons**. By separating two coloured objects, for example a quark/anti-quark pair, a flux tube of self-interacting gluons is formed; the colour field. Due to the gluon force being almost constant with increasing distance, it would take an infinite amount of energy to separate both objects. This property is called **colour confinement**. There are two ways to combine coloured quarks to form a colourless hadron. Either a red, a green and a blue quark form a three-quark hadron (a **baryon**), or a quark-antiquark pair, where the first carries any colour and the second the respective anti-colour, form a quark-antiquark hadron (a **meson**). Two well-known examples for baryons are the proton and the neutron. The proton

consists of two up and one down quark (uud) and the neutron of one up and two down quarks (udd). Examples for typical mesons are the **pions** π^+, π^- ($u\bar{d}, \bar{u}d$), the **kaons** K^+, K^- ($u\bar{s}, \bar{u}s$), the D -mesons D^+, D^-, D^0, \bar{D}^0 ($c\bar{d}, \bar{c}d, c\bar{u}, \bar{c}u$) and the B -mesons B^0, \bar{B}^0 ($\bar{d}b, d\bar{b}$). The theory of the quark-gluon interaction is described by **Quantum ChromoDynamics** (QCD) and the associated symmetry group is the **SU(3)**.

2.1.3 The weak interaction and electroweak unification

The weak interaction is very different from the electromagnetic and strong interactions discussed above. This interaction is mediated by the massive gauge bosons called W^+ , W^- and couples to all quark and lepton doublets. Additionally, the W^\pm boson can change the flavour of particles and is therefore responsible for the majority of particle decays. A well-known example for the manifestation of the weak interaction is the β^- decay

$$d \rightarrow u + e^- + \bar{\nu}_e$$

It describes the conversion of a bound neutron into a bound proton, emitting an electron and a neutrino. The weak interaction is called weak because its strength is comparatively quite small (see table 2.1). It is characterised by long lifetimes (compared to hadronic processes) and small cross-sections. From a mathematical point of view, the weak interaction is governed by the symmetry group **SU(2)**.

The electromagnetic and weak interactions can be unified in the framework of

$$SU(2) \otimes U(1)$$

gauge interaction. The unified interaction is called **electroweak interaction**. The work on formulating a single, locally gauge invariant electroweak theory was done by Glashow, Weinberg and Salam [20, 21, 22, 23] who received the Nobel Prize in 1979. The symmetry group of this theory requires four massless spin-1 bosons as carriers of the interaction: One triplet, consisting of W^+ , W^- , W^0 ($W_\mu^i, i = 1, 2, 3$) and a neutral singlet called B^0 (B_μ). From experimental observations [24], it is known that the three gauge bosons mediating the weak interaction are W^+, W^-, Z^0 where the Z^0 is predicted by the electroweak unification. The gauge boson mediating the electromagnetic interaction is the photon (γ). In the electroweak theory, Z^0 and γ are therefore created as a linear combination of the two electrically neutral components W^0 and B^0 . Written in terms of the neutral fields W_μ^3, B_μ , the photon field A_μ and the Z -boson field Z_μ become

$$\begin{aligned} A_\mu &= B_\mu \cos \theta_w + W_\mu^3 \sin \theta_w \\ Z_\mu &= -B_\mu \sin \theta_w + W_\mu^3 \cos \theta_w \end{aligned}$$

The angle θ_w is called Weinberg angle and parametrises this mixing. In experiments the bosons W^+ , W^- and Z^0 are found to have mass. But any naive way to introduce masses would

violate the underlying gauge symmetry. Thus, a mechanism is required that gives mass to the bosons W^+ , W^- and Z^0 and leaves the photon massless. By introducing a new field, the **Higgs field** [25], and one accompanying massive spin 0 boson, the **Higgs boson**, such a mechanism is created. The Higgs field has a non-zero vacuum expectation value. This property is responsible for spontaneously breaking the electroweak gauge symmetry into the electromagnetic and the weak one. This is referred to as the Higgs mechanism [25] and is named after P.W. Higgs who proposed it in 1964. The Higgs mechanism is responsible for giving mass to the gauge bosons W^+ , W^- and Z^0 and, at the same time, leaving the photon massless. The masses of fermions can also be explained by the Higgs theory. While the gauge bosons get their masses via spontaneous symmetry breaking, the fermions acquire mass by coupling to the Higgs boson.

2.1.4 The Standard Model

Grouping together QCD and the electroweak theory leads to the **Standard Model** of particle physics. It describes the currently known elementary particles and their interactions.

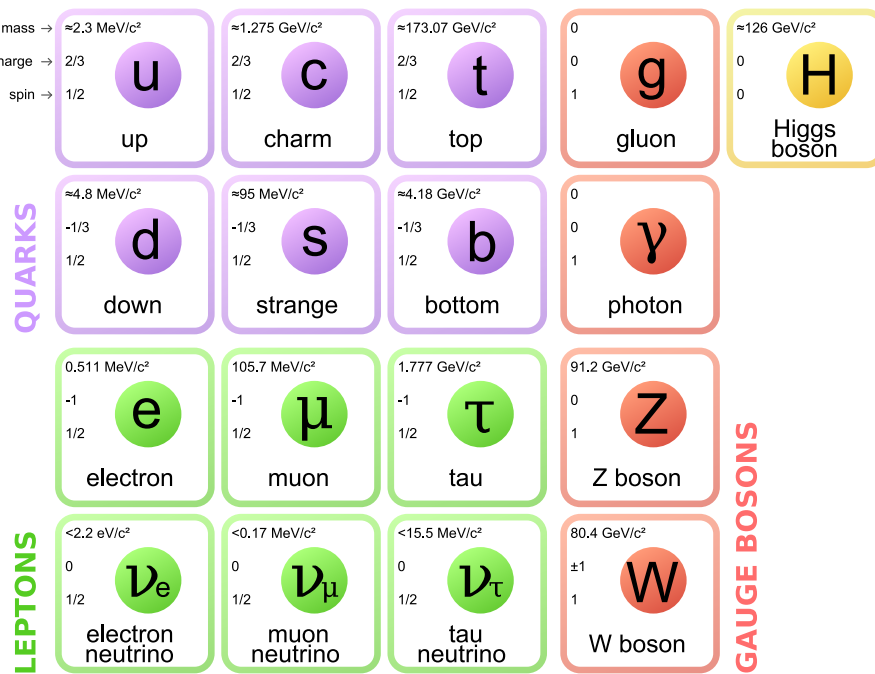


Figure 2.2: The Standard Model of particle physics consists of elementary particles divided into three generations of leptons, quarks and gauge bosons as force carriers and the Higgs boson [26].

From a mathematical point of view, the Standard Model is a gauge theory with the combined symmetry group

$$SU(3) \otimes SU(2) \otimes U(1)$$

Figure 2.2 shows a summary of the fermions, gauge bosons and the Higgs boson of the Standard Model. The elementary particles are grouped into three generations of spin $\frac{1}{2}$ fermions, the quarks (up, down), (charm, strange) and (top, bottom) and the leptons (e, ν_e), (μ, ν_μ) and (τ, ν_τ). The first generation alone suffices to build all visible matter. The heavier particles from the second and third generation are unstable and decay into the lighter particles of the first generation. The Standard Model describes three interactions, mediated by spin 1 bosons. The electromagnetic interaction, mediated by the massless photon, the weak force mediated by three massive bosons W^+, W^- and Z^0 and the strong interaction mediated by eight coloured gluons. Due to colour confinement, quarks and gluons are not directly observable. But the existence of quarks was shown in hadron spectroscopy, deep inelastic lepton scattering by nucleons [27], production of hadrons in $e^+ e^-$ annihilation and other experiments. All leptons have been observed directly, by observation of the free particle itself (e^- and μ^-) [28, 29], its decay products (τ^-) [30] and by observation of collisions caused by the particle (ν_e, ν_μ and ν_τ) [31]. The last lepton to be discovered was the τ neutrino. It was announced on 21st July 2000 that the τ neutrino was observed at the DONuT experiment [32] at Fermilab. As the existence of the anti-fermions is certain and confirmed in all cases, it is the Higgs boson that remained to be found. This missing particle was found by the ATLAS and CMS collaborations with data from the LHC in the year 2012 [33, 34]. All measured decay properties of the discovered Higgs boson are consistent with the Standard Model at present. However, more precise measurements in future running will show whether the observed “Higgs” is really the “SM Higgs”.

2.2 CP-Violation in the Standard Model

Symmetries play an important role in physics as they give rise to conservation laws[35] and help to understand the dynamics of a given system. If the laws of physics are invariant under certain transformations, a system exhibits the property of symmetry. There are two types of transformations: continuous transformations (such as rotations or translations) and discrete transformations (such as reflections or charge conjugations). Of particular interest for the physics at Belle II are the two discrete transformations that change the sign of the space coordinates and convert a particle into its anti-particle.

The first of the two transformations is called **parity-transformation** and changes the handedness of a system by flipping the sign of its axes $(x, y, z) \rightarrow (-x, -y, -z)$. Thus, a right-handed system becomes left-handed and vice-versa. If the physics is invariant under this transformation, it preserves the **parity symmetry**, referred to as **P**.

The effect of the parity transformation on the different types of fields can be summarised as follows:

scalar field	$\phi(\vec{x}, t)$	\rightarrow	$\phi(-\vec{x}, t)$
pseudoscalar field	$P(\vec{x}, t)$	\rightarrow	$-P(-\vec{x}, t)$
Dirac spinor	$\psi(\vec{x}, t)$	\rightarrow	$\gamma_0\psi(-\vec{x}, t)$
vector field	$V_\mu(\vec{x}, t)$	\rightarrow	$-V^\mu(-\vec{x}, t)$
pseudovector field	$A_\mu(\vec{x}, t)$	\rightarrow	$A^\mu(-\vec{x}, t)$

The second transformation converts a particle into its anti-particle

$$C|p\rangle = |\bar{p}\rangle$$

This transformation is called **charge-conjugation** and is responsible for the associated symmetry, referred to as **C**. It should be noted that not only does the charge flip sign under charge-conjugation but also the other additive internal quantum numbers, such as the baryon or lepton number, change sign.

For a long time it was assumed that all elementary processes are invariant under the application of each of the two operations **P** and **C** separately. In 1956, Lee and Yang realised that while there was evidence for parity invariance in strong and electromagnetic processes, there was a conundrum in particle decays (the famous “theta-tau puzzle”[36]) apparently violating the **P** symmetry. They proposed a further experiment that was carried out in the same year [37] and proved that parity symmetry is indeed violated in weak interactions. In addition, it turns out that **C** is violated in weak interactions as well. For years it seemed that the combined symmetry, the **CP** symmetry, was preserved in weak processes. In 1964 however, Cronin and Fitch discovered the violation of **CP** [38, 39, 40] in the Kaon-system.

Due to their non-zero strangeness two neutral Kaons K^0 and \bar{K}^0 exist. The decay of K^0 and \bar{K}^0 into two pions had been observed experimentally, meaning that they can mix via

$$K^0 \rightarrow \pi^+ \pi^- \rightarrow \bar{K}^0$$

From the Hamilton operator¹, governing the time evolution of the system, the mass eigenstates of the system are

$$|K_1\rangle = \frac{1}{\sqrt{2}} (|K^0\rangle + |\bar{K}^0\rangle) \quad (2.1)$$

$$|K_2\rangle = \frac{1}{\sqrt{2}} (|K^0\rangle - |\bar{K}^0\rangle) \quad (2.2)$$

Applying CP to the Kaon mass eigenstates and the two and three-pion states² results in

$$CP|K_1\rangle = +|K_1\rangle \quad (2.3)$$

$$CP|K_2\rangle = -|K_2\rangle \quad (2.4)$$

$$CP|\pi\pi\rangle = +|\pi\pi\rangle \quad (2.5)$$

$$CP|\pi\pi\pi\rangle = -|\pi\pi\pi\rangle \quad (2.6)$$

This means the $\pi\pi$ state is fed by K_1 decays only, while the leading non-leptonic channel for K_2 is the three-pion decay [41]. Due to the mass of three pions being 420 MeV and the mass of K_2 being 500 MeV the phase space for $K_2 \rightarrow \pi\pi\pi$ is very restricted, resulting in a very long lifetime of K_2 (8.9×10^{-11} s) compared to K_1 (5.1×10^{-8} s). This difference is denoted by using the subscripts L(long) and S(short) so that $K_1 \equiv K_S$ and $K_2 \equiv K_L$.

In 1964 Cronin and Fitch conducted an experiment [38] in which K^0 and \bar{K}^0 were created and sent down a long collimator. Due to the collimator's length and the short lifetime of K_S , an almost pure K_L beam left the collimator and entered a Helium bag. Detectors attached to the bag measured the three-momenta of the decay products [41]. They expected to see the decay $K_L \rightarrow \pi\pi\pi$ (branching ratio $(32.06 \pm 0.13)\%$ [42]), but to their surprise found in addition the decay $K_L \rightarrow \pi\pi$ (branching ratio $(2.83 \pm 0.01) \times 10^{-3}$ [42]). They had measured CP -violation!

This means that this process provides, for the first time, an absolute distinction between matter and anti-matter and, hence, **CP-violation** plays an important role in explaining the dominance of matter over anti-matter in the Universe. Kobayashi and Maskawa were the first to realise that three quark families are required in order to incorporate CP -violation into the Standard Model [43]. Before Kobayashi and Maskawa's work, only three quarks were assumed to exist: u , d , s . Their prediction of three quark families in the Standard Model was confirmed and they were awarded with the Nobel prize in 2008.

¹including weak interactions

²because of $J^{PC}(\pi) = 0^{-+}$

The idea is that the weak force does not couple to the physical quark pairs

$$\begin{pmatrix} u \\ d \end{pmatrix} \quad \begin{pmatrix} c \\ s \end{pmatrix} \quad \begin{pmatrix} t \\ b \end{pmatrix}$$

but instead to a new set of quark pairs (with the same u , c and t quark)

$$\begin{pmatrix} u \\ d' \end{pmatrix} \quad \begin{pmatrix} c \\ s' \end{pmatrix} \quad \begin{pmatrix} t \\ b' \end{pmatrix}$$

that contain linear combinations d' , s' and b' of the physical quarks. The physical quark states are called **mass eigenstates** and the “rotated” states **flavour eigenstates**. They are related by a 3x3 matrix called the Cabibbo-Kobayashi-Maskawa (**CKM**) matrix

$$\underbrace{\begin{pmatrix} d' \\ s' \\ b' \end{pmatrix}}_{\text{flavour eigenstates}} = \underbrace{\begin{pmatrix} V_{ud} & V_{us} & V_{ub} \\ V_{cd} & V_{cs} & V_{cb} \\ V_{td} & V_{ts} & V_{tb} \end{pmatrix}}_{V_{\text{CKM}}} \cdot \underbrace{\begin{pmatrix} d \\ s \\ b \end{pmatrix}}_{\text{mass eigenstates}} \quad (2.7)$$

The CKM matrix contains four real, independent parameters, where three represent the Euler-angles ($s_{ij} = \sin \theta_{ij}$, $c_{ij} = \cos \theta_{ij}$) needed for the three-dimensional rotation and one is a irreducible complex phase δ [42]

$$V_{\text{CKM}} = \begin{pmatrix} c_{12}c_{13} & s_{12}c_{13} & s_{13}e^{-i\delta} \\ -s_{12}c_{23} - c_{12}s_{23}s_{13}e^{i\delta} & c_{12}c_{23} - s_{12}s_{23}s_{13}e^{i\delta} & s_{23}c_{13} \\ s_{12}s_{23} - c_{12}c_{23}s_{13}e^{i\delta} & -c_{12}s_{23} - s_{12}c_{23}s_{13}e^{i\delta} & c_{23}c_{13} \end{pmatrix} \quad (2.8)$$

It is this complex phase which gives rise to CP -violation in the Standard Model. The CKM matrix V_{CKM} can be written as an approximation using the Wolfenstein parametrisation [44]

$$V_{\text{CKM}} \simeq \begin{pmatrix} 1 - \lambda^2/2 & \lambda & A\lambda^3(\rho - i\eta) \\ -\lambda & 1 - \lambda^2/2 & A\lambda^2 \\ A\lambda^3(1 - \rho - i\eta) & -A\lambda^2 & 1 \end{pmatrix} + \mathcal{O}(\lambda^4) \quad (2.9)$$

using the Cabibbo angle $\lambda = \sin \theta_c \approx 0.22$.

The matrix is unitary and thus allows to write twelve equations given by

$$\sum_k V_{ki} V_{kj}^* = \delta_{ij}$$

Six of these equations with $i \neq j$ can be geometrically represented as triangles in a complex plane, called **unitary triangles**. The size of the angles in the unitary triangle are a measure for the size of the CP -violation. For the Kaon-system the first and second column are used to generate the triangle. Of particular interest for Belle II are the relations for the B -meson system. Carter and Sanda suggested in 1981 [45] that CP -violation can also occur in the decay of neutral B -mesons. By comparing the orders of magnitude for λ in the B -meson and the Kaon-system going into the unitary relation, it is apparent that the angles of the triangle and thus the CP -violation in B -decays is much larger than in Kaon-decays and that the sides of the unitary triangle are about the same size in the B -meson system. In fact, it is three orders of magnitude larger. This was one of the main motivations leading to the construction of the two experiments Belle and BABAR, that focused on exploring the physics of B -meson decays at the so-called **B-factories** SLAC and KEK. In summer 2001, CP -violation was observed in the B -meson system by the Belle [46] and the BABAR [47] experiments with the measurement of $\sin 2\phi_1 \neq 0$ in $B^0 \rightarrow J/\psi K_s^0$ decays.

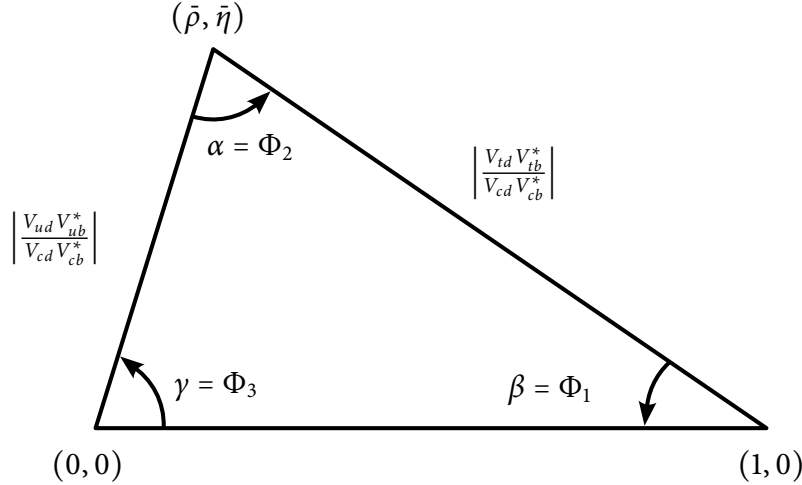


Figure 2.3: The normalised unitary triangle in the B -meson system.

Figure 2.3 shows an illustration of the unitary triangle for the B -meson system. Its angles are given by

$$\phi_1 \equiv \arg \left[-\frac{V_{cd}V_{cb}^*}{V_{td}V_{tb}^*} \right], \phi_2 \equiv \arg \left[-\frac{V_{td}V_{tb}^*}{V_{ud}V_{ub}^*} \right], \phi_3 \equiv \arg \left[-\frac{V_{ud}V_{ub}^*}{V_{cd}V_{cb}^*} \right] \quad (2.10)$$

and the length of its sides by

$$R_b \equiv \left| \frac{V_{ud} V_{ub}^*}{V_{cd} V_{cb}^*} \right| = \left(1 - \frac{\lambda^2}{2} \right) \frac{1}{\lambda} \left| \frac{V_{ub}}{V_{cb}} \right| \quad (2.11)$$

$$R_t \equiv \left| \frac{V_{td} V_{tb}^*}{V_{cd} V_{cb}^*} \right| = \frac{1}{\lambda} \left| \frac{V_{td}}{V_{cb}} \right| \quad (2.12)$$

The triangle provides five observables that can be measured. However, only two observables are required in order to check whether the triangle closes or not (“overconstrained”), as the Standard Model predicts the triangle to be closed. Any inconsistency in the measurement of angles or sides is a clear hint for deviations from the Standard Model. *CP*-violation manifests itself as a non-zero area of the triangle [48]. Figure 2.4 summarises the status of the unitary triangle measurements for the B -meson system as of 2013.

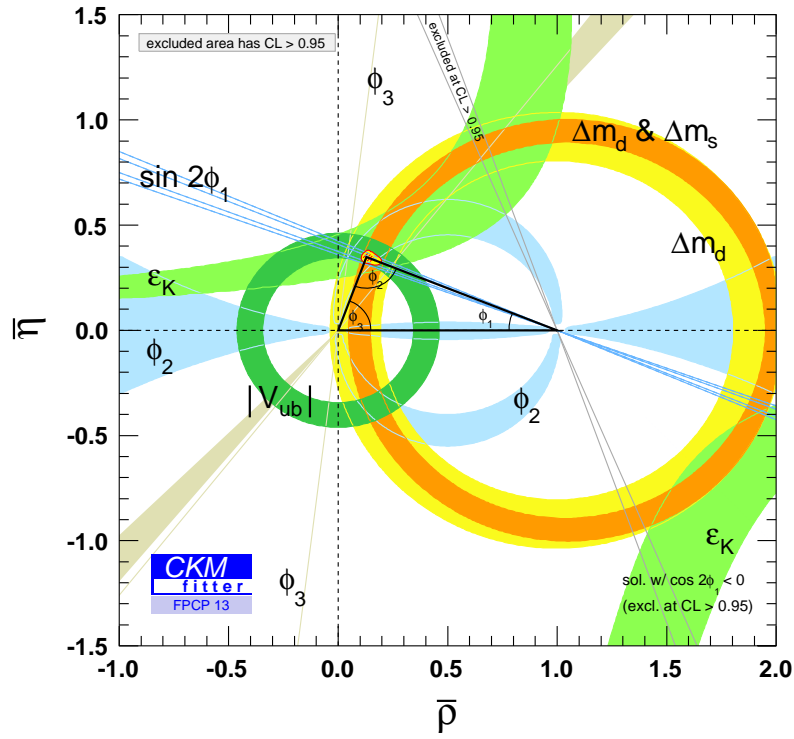


Figure 2.4: Summary of the measurements for the unitary triangle as of 2013. Compiled by the CKMfitter group [49]. The yellow area around the top tip of the triangle depicts the one sigma range of the average of all individual measurements.

2.3 CP-Violation measurement

At Belle II, B -mesons will be produced mainly via the decay of the $\Upsilon(4S)$ resonance. By colliding electrons with positrons at a centre-of-mass energy equal to the mass of the $\Upsilon(4S)$ resonance (which is 10.58 GeV and thus only 20 MeV larger than the mass of a $B\bar{B}$ pair) Belle II produces almost exclusively ($\sim 96\%$) $B\bar{B}$ pairs, where the two B -mesons are the only initial state particles that are produced in the collision. This lead to the term “ B -factory” for colliders operating at the $\Upsilon(4S)$ resonance. Their advantage lies in the fact that they produce B -mesons in a clean environment where all subsequent decay particles can be attributed to either the B or the \bar{B} -meson. Half of the $B\bar{B}$ pairs are neutral $B^0\bar{B}^0$ pairs. The $\Upsilon(4S)$ resonance is a bound state of $b\bar{b}$ quarks with the quantum numbers $J^{PC} = 1^{--}$. The decay of the $\Upsilon(4S)$ into a $B^0\bar{B}^0$ pair is a strong interaction process and thus conserves the quantum numbers. Neutral B -mesons are pseudo-scalar particles with $J^{PC} = 0^{--}$. The $B^0\bar{B}^0$ state is produced in a p-wave configuration, resulting in an orbital angular momentum of the system of $L = 1$ and parity $P = (-1)^L = -1$. A free B -meson can oscillate between its matter (B) and its anti-matter (\bar{B}) form. This means the spatial part of the $B^0\bar{B}^0$ state’s wave function is antisymmetric. However, Bose-Einstein statistics requires the overall wave function to be symmetric. Therefore, the flavour part of the wave function has to be antisymmetric too. The fact that the strong interaction produces the B -mesons as a pure flavour eigenstate means that the $B^0\bar{B}^0$ mesons are in an entangled state and evolve coherently. Consequently, the decay of one of the B -mesons determines the flavour of the other B -meson to be opposite at the time of the decay. It should be noted that this is the practical realisation of the Einstein-Podolsky-Rosen paradox [50]. Since the mass and the flavour eigenstate are different for the B^0 -meson, the meson can oscillate between a B^0 and a \bar{B}^0 . This process is called $B^0\bar{B}^0$ mixing and is mainly mediated by a second order process where the b and d quarks couple to W bosons and t quarks. The Feynman diagrams for this process are drawn in figure 2.5.

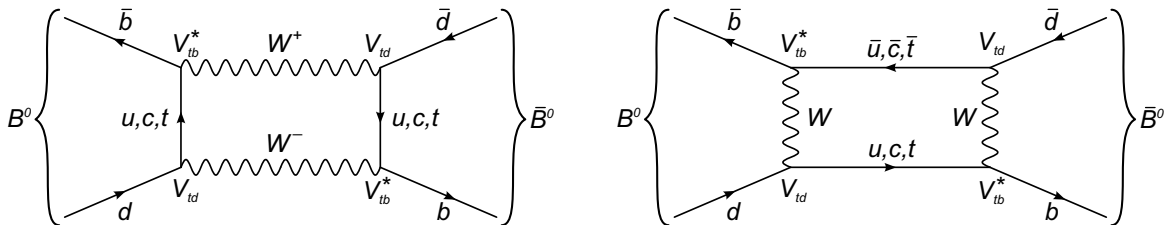


Figure 2.5: The leading order box diagrams involved in flavour mixing.

Mixing is governed by the mass eigenstates of the B -mesons. The mass eigenstates are derived from the Schrödinger equation

$$i \frac{d}{dt} \begin{pmatrix} |B(t)\rangle \\ |\bar{B}(t)\rangle \end{pmatrix} = H \begin{pmatrix} |B(t)\rangle \\ |\bar{B}(t)\rangle \end{pmatrix} \quad (2.13)$$

where

$$H = \begin{pmatrix} m & M_{12} \\ M_{12}^* & m \end{pmatrix} + \frac{i}{2} \begin{pmatrix} \Gamma & \Gamma_{12} \\ \Gamma_{12}^* & \Gamma \end{pmatrix}$$

is the Hamiltonian consisting of the mass and decay matrices. The off-diagonal elements represent the flavour changing transitions $B^0 \leftrightarrow \bar{B}^0$ and, when not zero, imply that mass and flavour eigenstates are not the same. Diagonalising the Hamiltonian yields the two mass eigenstates B_H and B_L with the associated masses m_H and m_L . The mass eigenstates are a linear combination of $|B\rangle$ and $|\bar{B}\rangle$

$$|B_L\rangle = p|B\rangle + q|\bar{B}\rangle \quad (2.14)$$

$$|B_H\rangle = p|B\rangle - q|\bar{B}\rangle \quad (2.15)$$

where

$$|p|^2 + |q|^2 = 1 \quad \text{and} \quad \frac{q}{p} = \sqrt{\frac{M_{12}^* - \frac{i}{2}\Gamma_{12}^*}{M_{12} - \frac{i}{2}\Gamma_{12}}}$$

In weak decays of charged and neutral B -mesons CP -violation can occur in three ways: CP -violation in decay, in mixing, and in the interference between mixing and decay. CP -violation in **decay**, also called **direct** CP -violation, is observed when the decay rate of a B -meson to a final state, f , differs from the decay rate of an anti- B -meson to the CP -conjugated final state, \bar{f} . Since charged mesons do not undergo mixing, this is the only type of CP -violation that can occur in charged B -meson decays. CP -violation in **mixing** on the other hand implies that the oscillation from B to \bar{B} is different from the oscillation from \bar{B} to B . Experimentally semi-leptonic decays of both the B and the \bar{B} are studied. If an event with two leptons carrying equal charge in the final state is found, it means that one of the B -mesons has oscillated (see figure 2.6 for an example).

The third way CP -violation can occur is in the interference between mixing and decay, also called **mixing-induced** CP -violation. Also this form of CP -violation only exists for neutral B -mesons and is observed in decays to a common final state for the B^0 and the \bar{B}^0 -meson, preferably a pure CP -eigenstate $f = \bar{f} = f_{CP}$. Using a pure CP -eigenstate means that there are two amplitudes that contribute to the transition amplitude from the initial state of the B^0 to

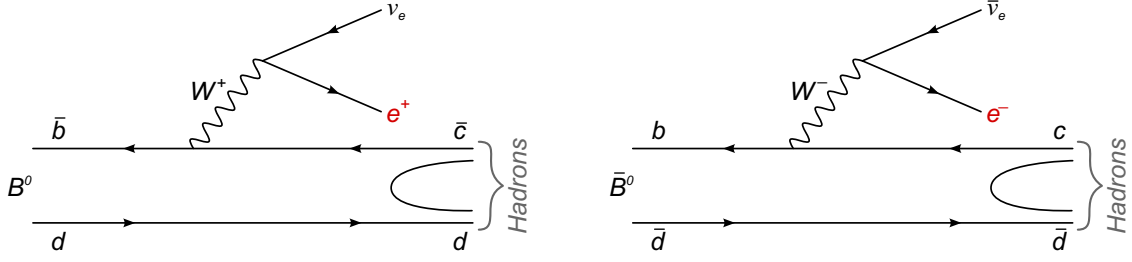


Figure 2.6: Semi-leptonic B decays, where the charge of the lepton is used in order to tag the event. If an e^+ is found it must have originated from a B^0 , if an e^- is found it must have originated from a \bar{B}^0 .

f_{CP} : $A(B^0 \rightarrow f_{CP})$ and $A(\bar{B}^0 \rightarrow \bar{B}^0 \rightarrow f_{CP})$. Since the mixing between the B^0 and \bar{B}^0 is time-dependent, as the time dependent decay rates illustrate

$$\begin{aligned} \Gamma(B^0 \rightarrow f_{CP}) &= |\langle f_{CP} | B^0(t) \rangle|^2 \\ &= \frac{e^{-\Gamma t}}{2} |A_{CP}|^2 \left[(|\lambda_{CP}|^2 + 1) - (|\lambda_{CP}|^2 - 1) \cos(\Delta m t) - 2\text{Im}(\lambda_{CP}) \sin(\Delta m t) \right] \\ \Gamma(\bar{B}^0 \rightarrow f_{CP}) &= |\langle f_{CP} | \bar{B}^0(t) \rangle|^2 \\ &= \frac{e^{-\Gamma t}}{2} |A_{CP}|^2 \left[(|\lambda_{CP}|^2 + 1) - (|\lambda_{CP}|^2 - 1) \cos(\Delta m t) + 2\text{Im}\left(\frac{1}{\lambda_{CP}}\right) \sin(\Delta m t) \right] \end{aligned} \quad (2.16)$$

a time-dependent asymmetry between the decay rates is measured [41]

$$a_{CP}(t) = \frac{\Gamma(\bar{B}^0(t) \rightarrow f_{CP}) - \Gamma(B^0(t) \rightarrow f_{CP})}{\Gamma(\bar{B}^0(t) \rightarrow f_{CP}) + \Gamma(B^0(t) \rightarrow f_{CP})} \quad (2.17)$$

this asymmetry can be written using two CP parameters as

$$a_{CP}(t) = \mathcal{A}_{CP} \sin(\Delta m t) + \mathcal{S}_{CP} \cos(\Delta m t) \quad (2.18)$$

where $\Delta m = m_H - m_L$ is the mass difference of the mass eigenstates of the B -mesons, \mathcal{A}_{CP} represents direct CP -violation and \mathcal{S}_{CP} mixing-induced CP -violation.

They are defined in the B -meson system as

$$\mathcal{A}_{CP} = \frac{|\lambda_{CP}|^2 - 1}{|\lambda_{CP}|^2 + 1} \quad S_{CP} = \frac{2\text{Im}(\lambda_{CP})}{|\lambda_{CP}|^2 + 1} \quad |\lambda_{CP}|^2 = \frac{|\bar{A}_{CP}|^2}{|A_{CP}|^2} \quad (2.19)$$

where A_{CP} and \bar{A}_{CP} are the amplitudes of the decays $B^0 \rightarrow f_{CP}$ and $\bar{B}^0 \rightarrow f_{CP}$ respectively.

The measurement of the asymmetry in equation 2.17 requires the measurement of the decay time difference between the B^0 -meson and the \bar{B}^0 -meson. However, the lifetime of the neutral B -meson is about 1.5 ps and thus too short to be measured directly. Therefore, B -factories such as PEP II, KEKB and, of course, SuperKEKB apply a boost to the $\Upsilon(4S)$ system, such that the B -mesons travel a small distance in the laboratory system before they decay, thereby translating the decay time difference measurement into a spatial distance measurement. This distance measurement can be performed very precisely. The boost is created by having asymmetric beam energies for the electron and the positron beam (see section 3.1), resulting in a boost mainly along the z -direction of the Belle II detector (see section 4.1 for the definition of the coordinate system). By measuring the distance Δz between the decay vertices, the decay time difference can then be calculated by

$$\Delta t = \frac{\Delta z}{\langle \beta \gamma \rangle c} \quad (2.20)$$

The boost at SuperKEKB is $\beta \gamma = 0.287$ (see section 3.1), resulting in a travel distance of the B -meson of about 130 μm .

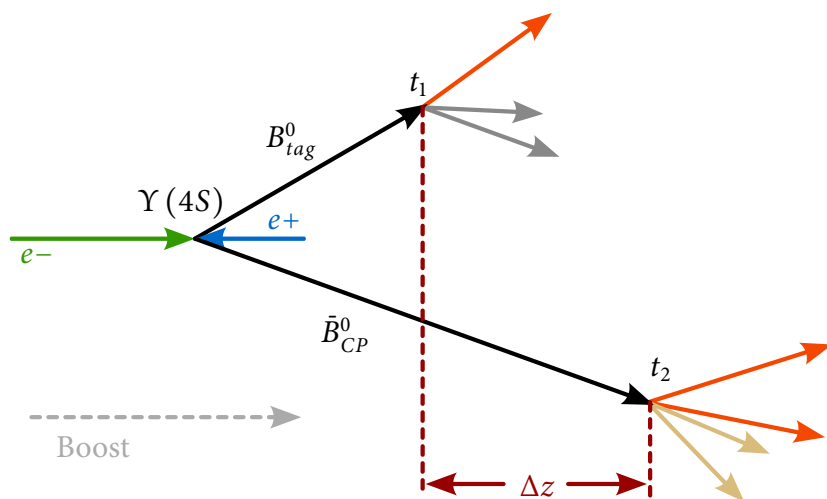


Figure 2.7: Production of two entangled B -mesons from the $\Upsilon(4S)$ resonance.

The measurement principle at Belle II is illustrated in figure 2.7. Starting with the decay of the $\Upsilon(4S)$, the B^0 -mesons are boosted and travel a certain distance before they decay. At time t_1 the first B -meson decays (a B^0 in the example illustrated in figure 2.7). Due to the entanglement of the B -mesons, the flavour of the second B -meson is known at t_1 to be the opposite of the decayed B -meson (a \bar{B}^0 in the drawing). As soon as the first B^0 has decayed, the second is free to oscillate until it decays at time t_2 . The time difference is then $\Delta t = |t_2 - t_1|$. So far, only the time difference is measured but the asymmetry in equation 2.17 also requires the flavour of the B^0 -meson at the time of its decay. In the case of a pure CP -eigenstate, however, both B^0 and \bar{B}^0 decay into the same final state. In order to differentiate between a B^0 and \bar{B}^0 , events are selected in which the flavour of one of the B -mesons is determined by a flavour-specific decay, the so-called **tag side**. The other B -meson decays into the CP -eigenstate, the **CP side**. From the exact flavour and time evolution of the second B -meson and due to the entanglement of the B -mesons the flavour of the CP side B -meson can be determined. A precise measurement of the decay time difference requires a very precise measurement of the spatial separation of the decay vertices and, in turn, an extremely precise measurement of the location of each decay vertex. But it was only after the development of semi-conductor based detectors recording the position of the passage of particles, that experiments could be conducted that measured the decay vertices of B -mesons with the required precision. At Belle II this precision is achieved using a series of tracking detectors, in particular the pixel vertex detector (PXD), a detector specifically built for this task. This makes the PXD one of the crucial sub-detectors for the precise measurement of CP -violation and the search for New Physics at Belle II, and therefore the main topic of this thesis.

2.4 Beyond the Standard Model

There is no doubt that the Standard Model has been an enormous success in the past 30 years. It predicted new particles and allowed the calculation of quantities that have been confirmed by experiments. Despite its success, however, it cannot be the end of the story. There are simply too many unanswered questions that the Standard Model does not cover. For example, the Standard Model does not provide a way to calculate many of its parameters, such as the coupling constants, the CKM matrix and the quark and lepton masses. Those numbers have to be taken from experimental results and plugged into the Standard Model. A mature theory, though, should be able to explain them. In total, there are about 20 parameters in the Standard Model, and none of their values is given by the Standard Model itself [51]. As has been explained in the previous sections, CP -violation occurs in weak interactions of quarks and is nicely integrated into the Standard Model by a complex phase in the CKM matrix. It turns out, however, that this source of CP -violation is not even nearly enough to account for the matter/anti-matter asymmetry found in the Universe [4, 5]. Additional sources are necessary. A potential source for additional CP -violation could come from neutrinos. As neutrinos have mass, in contrast to

the Standard Model where they are massless, they are subject to flavour oscillation, very much like the mixing for $B^0\bar{B}^0$.

In general, New Physics is expected to be found at much higher particle masses than the current accelerators are able to provide. This means that, as the first chapter points out, there are two approaches to search for New Physics: either by increasing the available centre-of-mass energy or by improving the measurement precision. While, at first glance, a high precision experiment seems not to be able to reach into the realm of an high energy experiment, it can through measuring processes involving internal loops. They allow one to gain access to high mass scales that accelerators, including the LHC, cannot reach. New particles, for example, could reveal themselves through their virtual effects in processes involving only the well-known particles from the Standard Model. This approach has already been successful in the past [23]. Since the masses of new particles are expected to be very large, the effects measured at a next generation B -factory, such as SuperKEKB, will be small. This explains the demand for a high precision, high luminosity machine. Of particular interest are Flavour Changing Neutral Currents, FCNC, that only exists beyond the tree level in the Standard Model. The B -meson system is the ideal place to study FCNC processes, because the b quark belongs to the third generation of fermions and thus processes with b quarks involve all existing generations of quarks. Examples are the radiative decay $b \rightarrow s\gamma$, the semileptonic decay $b \rightarrow sl^+l^-$, and the hadronic decay $b \rightarrow sq\bar{q}$. Since the loop diagrams can contain new, heavy virtual particles, these processes are sensitive to New Physics effects that can occur in extensions to the Standard Model (see figure 2.8).

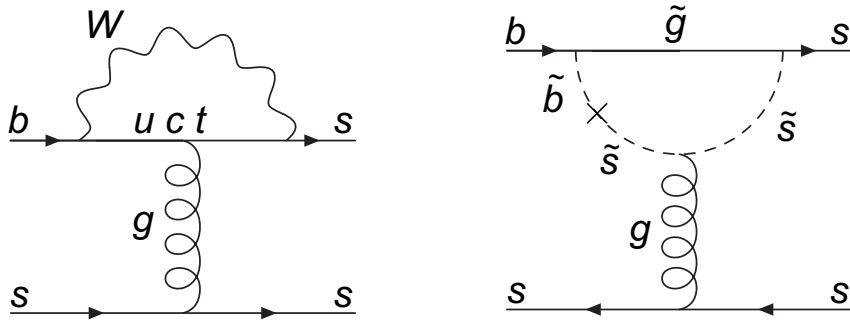


Figure 2.8: The left diagram shows the lowest order Feynman diagram for the transition $b \rightarrow s$ in the Standard Model. The right drawing shows possible physics beyond the Standard Model, which changes the prediction for observables such as the branching ratios or the angles in the unitary triangle.

Belle II will also resolve currently standing tensions between measurements. Examples can be found in the measurement of the ϕ_1 angle of the CKM triangle. The measured value in the penguin process $b \rightarrow sq\bar{q}$ differs by up to 3σ from the value measured in $B \rightarrow J/\psi K_s^0$ [52, 53] and leads to speculations about the existence of a new CP phase in the penguin process. Another example is the forward/backward asymmetry of the leptons in $B \rightarrow K^* l^+l^-$. The asymmetry

is about 2σ higher than the prediction from the Standard Model [54]. As a final example, the discrepancy of the direct CP -violation asymmetries in $B \rightarrow K^+\pi^-$ and $B \rightarrow K^+\pi^0$ should be mentioned. Both values differ significantly even if, according to [55], they should be the same. A detailed coverage of the physics program at Belle II can be found in [56].

It should be noted that there is a large variety of concepts and models trying to answer the open questions of the Standard Model. They will only be mentioned briefly here. From the four existing forces, the Standard Model only incorporates three. Gravity is not part of the Standard Model and only a couple of theories exist, most notably the superstring theory, that are able to combine quantum field theory with general relativity. A problem arises from the fact that the coupling constants (such as g_{em}, g_s) are not constant. They vary with the momentum transfer and, therefore according to the Standard Model prediction, the gauge couplings do not meet in a single point as is shown in figure 2.9(a).

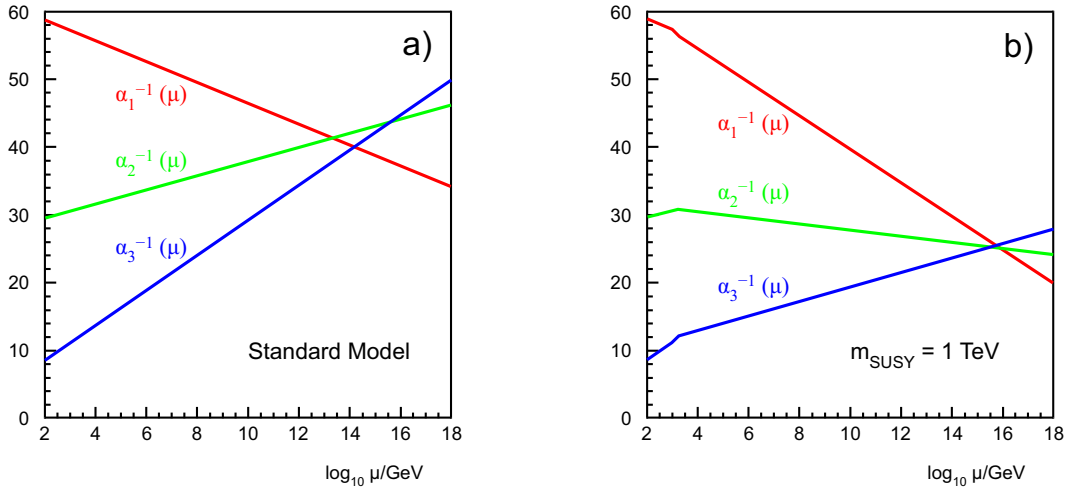


Figure 2.9: The three coupling constants within the Standard Model a) and the MSSM b).

It is found that an extension to the Standard Model called **Supersymmetry** proposes a solution to this “problem”. It introduces a bosonic partner to each fermion and a fermionic partner to each boson, thereby doubling the number of particles. Figure 2.9(b) shows the gauge couplings in the so-called Minimal Supersymmetric Model (MSSM) [57, 58]. However, recent results from the LHC restrict the possible parameter space for supersymmetry significantly, leading to doubts as to whether the supersymmetry models at hand are still feasible [59, 60].

If one goes up in energy, the four interactions start to merge, until they become one single force (see figure 2.10). A theory describing this unification of interactions is the ultimate goal of physics.

Data from astrophysical experiments [1] show that only about 4.9 % of the total energy in the Universe is of baryonic origin (mostly protons), 26.8 % accounts for the not yet discovered **dark matter** and the missing 68.3 % are assigned to the so-called **dark energy**. This means the Stand-

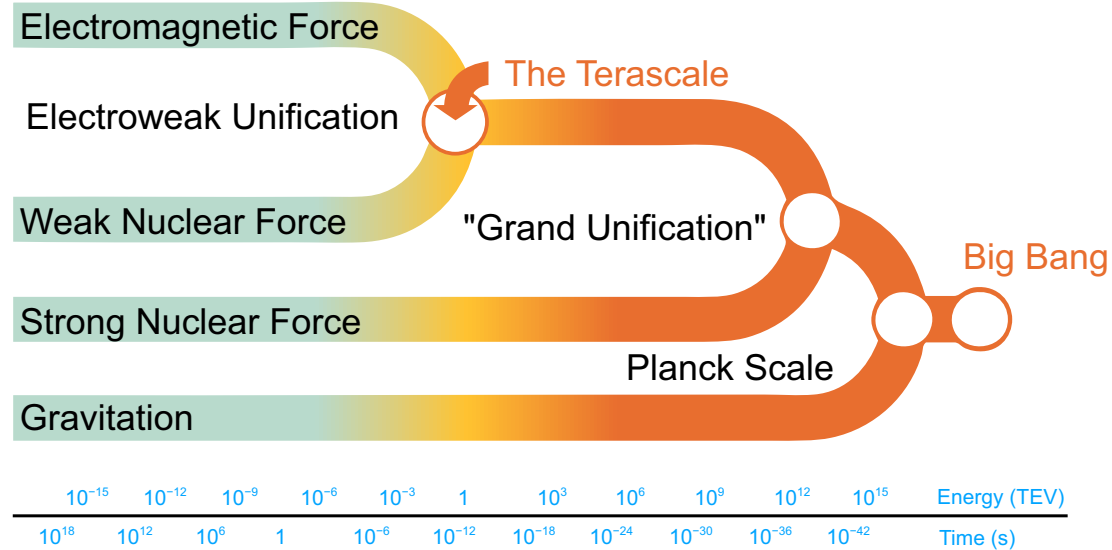


Figure 2.10: Unification of all four forces in a Grand Unification Theory [61].

ard Model is not able to account for over 95 % of the total energy in the Universe. Observational evidence for the existence of dark matter comes from galaxy rotation curves [62, 63], velocity dispersions of elliptical galaxies [64], gravitational lensing [65, 66] and angular fluctuations in the cosmic microwave background [67]. While the structure and origin of dark energy remains mostly unknown, several candidates for a dark matter particle exist. Among them are the lightest supersymmetric particle, provided by supersymmetry, the axion [68, 69] a hypothetical particle postulated in 1977 to explain *CP* conservation in the strong interaction [70] and **WIMPs** (Weakly Interacting Massive Particles). However, experimental measurement of a dark matter particle is very difficult due to its weakly interacting nature. The biggest challenge in Dark Matter experiments is the suppression of background coming from cosmic rays. Therefore dark matter experiments are performed in underground laboratories located in salt mines or next to road tunnels under mountains. As of 2013, no experiment has detected a dark matter signal [71, 72], even though some claim to have seen anomalies in the DAMA experiment [73].

The deficits in the Standard Model together with the recent findings at LHC and the prospects for Belle II will almost certainly lead to an exciting future. Particle physics may stand at the border of a fundamental revolution, as it was 40 years ago with the introduction of the quark model and over a century ago with Rutherford's atomic model and Thomson's discovery of the electron.

3 The SuperKEKB $e^+ e^-$ collider

SuperKEKB is an electron-positron accelerator and collider located in Tsukuba, Ibaraki, Japan. It is the successor of the **KEKB** collider [74], which was shut down on June, 30th, 2010 after more than 10 years of successful operation. SuperKEKB accelerates and collides **electrons** with **positrons** at different energies (“asymmetric collider”), which are counter-rotating in a double-ring structure, with a “high energy” ring (**HER**) for the electrons and a “low energy” ring (**LER**) for the positrons. The electrons and positrons are generated and accelerated in a linear accelerator and then injected into the main storage ring. Figure 3.1 shows a schematic overview of the main storage ring.

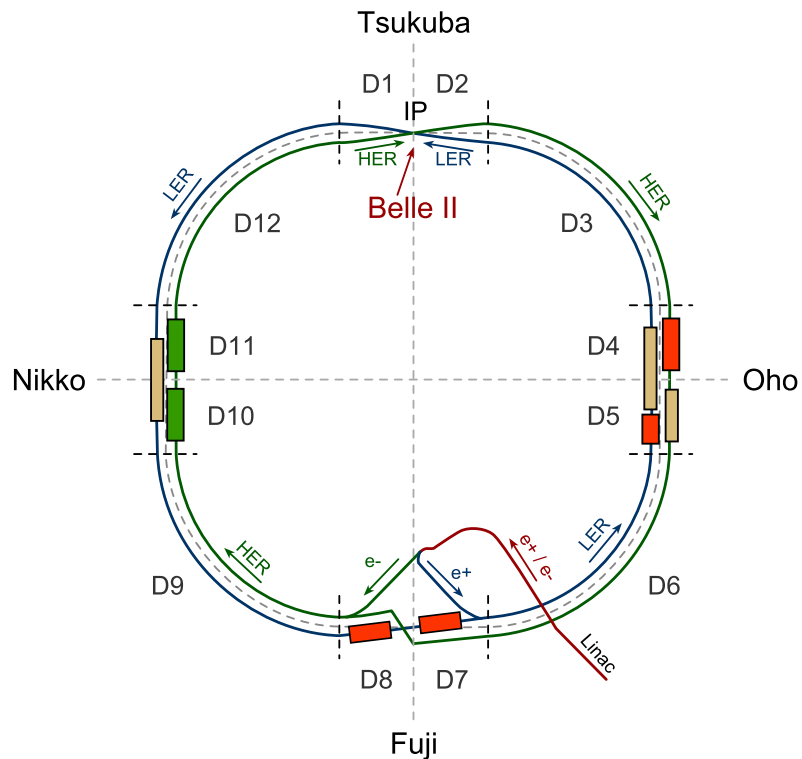


Figure 3.1: The SuperKEKB double-ring structure. Shown are the HER and LER for the electrons and positrons, respectively. The particles collide at the IP, which is surrounded by the Belle II detector. The wigglers in the straight sections are drawn as brown rectangles, the ARES cavities as red rectangles and the SCC cavities as green rectangles (see sections 3.3 and 3.8).

This chapter presents the SuperKEKB storage ring and provides an introduction to the basic principles of its operation. The theory of the transport and the focusing of a particle beam is briefly explained, followed by sections about the creation and acceleration of the electrons and positrons at SuperKEKB. The chapter closes with a discussion of the novel nano-beam scheme, an introduction to the different mechanisms of particle loss in the machine, and a table summarising the most important parameters of SuperKEKB.

3.1 The SuperKEKB storage ring

The SuperKEKB accelerator complex consists of two independent rings: the High Energy Ring (**HER**), which hosts the electron beam, and the Low Energy Ring (**LER**), which hosts the positron beam. The storage ring consists of four arc sections (*D3, D6, D9, D12*) and four straight sections (*Tsukuba, Oho, Fuji, Nikko*). Its total circumference is 3016 m, comprised of 1861 m for the four arc sections and 1155 m for the four straight sections. Like in any circular accelerator, there is exactly one trajectory, the **design** or **nominal orbit**, on which all particles should travel along the ring. In order to achieve this the arc sections are equipped with **bending magnets**, guiding the beams around the arcs. Additionally, both the arc and the straight sections contain **focusing magnets** and collimators in order to counteract the expansion of the beam. The evolution of the beam particle trajectories under the influence of bending and focusing magnets is called **beam dynamics** or **beam optics**. The collection of bending and focusing magnets is the **magnet lattice** of the ring and the complete system is called the beam transport system. As has been pointed out in chapter 1, the measurement of the B -meson flight time requires a boost in the laboratory system. This is accomplished with **asymmetric beam energies**, with the following energies chosen for SuperKEKB

$$E_{HER}(e^-) = 7 \text{ GeV} \quad E_{LER}(e^+) = 4 \text{ GeV}$$

The circulating electron and positron beams are brought to collision at the interaction point (IP), located at the centre of the Tsukuba straight section. Surrounding the IP, the **Belle II detector** records the outcome of the particle collisions. It is described in detail in chapter 4. The beams do not collide head-on, but at a rather large (compared to the KEKB case) **crossing angle** of 83 mrad. This ensures that the beams are kept separate before and after the collision. The value of the crossing angle is mainly driven by the design of the interaction region optics and magnets.

The beam energies are chosen such that the centre-of-mass (CMS)¹ is

$$E_{CM} = 2 \cdot \sqrt{E_{HER} \cdot E_{LER}} = 10.58 \text{ GeV} \quad (3.1)$$

which is exactly the mass of the $\Upsilon(4S)$ resonance (see figure 3.2), the most important “running mode” of SuperKEKB. The mass of the $\Upsilon(4S)$ resonance is about 20 MeV above the mass of two charged or neutral B -mesons, allowing it to decay exclusively into a BB meson pair (decays with more than 96 % probability [42] to B^+B^- and $B^0\bar{B}^0$ pairs). The boost with which the $\Upsilon(4S)$ is produced, is (see chapter 5)

$$\beta\gamma = 0.287 \quad (3.2)$$

In addition, SuperKEKB is designed to cover the full CMS range from the $\Upsilon(1S)$ to the $\Upsilon(6S)$ resonance and can even reach a CMS energy of 12 GeV.

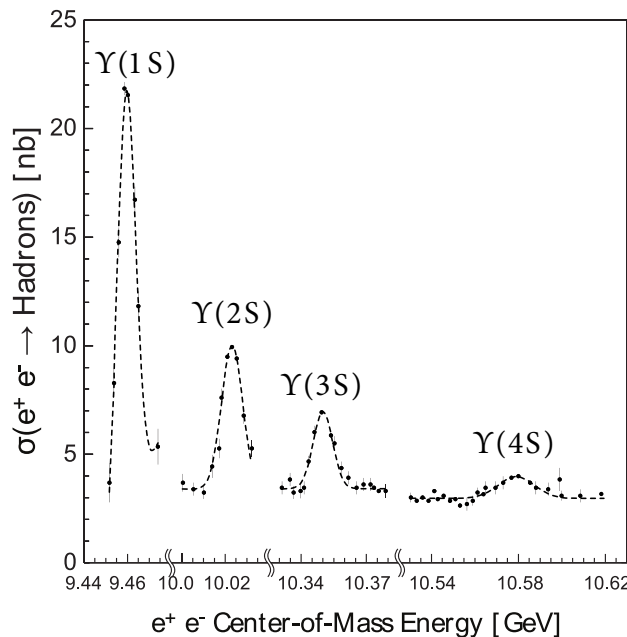


Figure 3.2: Total hadronic cross-section in nb for $e^+ e^-$ collisions as a function of the $e^+ e^-$ centre-of-mass energy [75].

¹The centre-of-mass system (CMS) is the system that moves with the centre-of-mass of the colliding particles. In the CMS the vector sum of all momenta is zero. Throughout the collision this sum is preserved, as is the total energy.

3.2 The coordinate system

The **coordinate system** used to describe the motion of the beam particles, as it is employed in the subsequent chapters, is shown in figure 3.3. The orthogonal, right-handed coordinate system moves with the beam particles along the nominal orbit of the LER and HER. The coordinate vector x is perpendicular to the direction of motion of the particle and points into the “outward” direction of the ring. The y vector represents the vertical component of the motion and points downwards to the “ground”. While the s vector is parallel to the flight direction of the positrons, it is anti-parallel to the flight direction of the electrons. The coordinate system is mainly used for the simulation of the beam transport and the description of the beam optics. It should be noted that it differs from the coordinate system used for the Belle II detector, which is described in chapter 4.

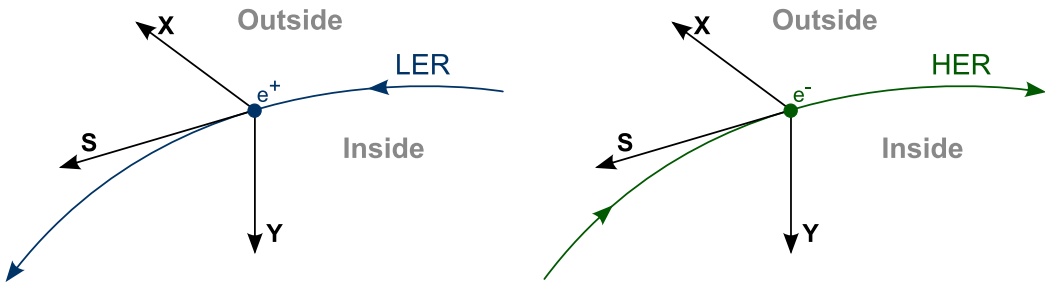


Figure 3.3: The coordinate system used to describe the motion of particles in the accelerator. The left drawing shows the definition for the LER (positrons), with the s vector being parallel to the particle’s flight direction. The right drawing shows the definition for the HER (electrons), with the s vector being anti-parallel to the particle’s flight direction.

3.3 Beam Transport System

Circular accelerators make use of electric fields to accelerate the beam particles and of magnetic fields to guide them along the design orbit. The beam particles are grouped into so-called **bunches** where each bunch contains about 10^{11} particles. At SuperKEKB, the beam particles are delivered with their nominal energy to the main storage ring (see section 3.7). During their journey through the ring, the circulating beam particles lose energy due to synchrotron radiation [76]. The storage ring recovers the energy loss with a mixture of normal conducting and superconducting RF acceleration structures. Two types of RF cavities have been successfully tried and tested at KEKB and thus will be re-used at SuperKEKB: the **ARES** (Accelerator Resonantly coupled with Energy Storage) [77] and the Single-Cell superconducting Cavities (**SCC**) [78]. The main advantage of these over other types of RF cavities is their ability to avoid uncontrollable beam instabilities [79, 80], a main concern for SuperKEKB. The HER is equipped

with 8 ARES cavities along the Oho straight section and 8 SCC cavities along the Nikko straight section, while the LER has 6 ARES cavities along the Oho straight section and 16 ARES cavities along the Fuji straight section. Figure 3.1 gives a rough idea of their location.

In order to guide the beam particles along the design orbit, magnets generating a homogeneous magnetic field, which is perpendicular to the particles' flight direction, are installed. The particles experience the Lorentz force, induced by the magnetic field, and follow a curved trajectory. SuperKEKB uses normal-conducting **dipole magnets** for bending the beam, which create a transverse magnetic field that is constant and homogeneous in the vicinity of the nominal orbit. The magnetic field is generated by an electrical current flowing through a coil which surrounds the magnetic poles. The magnetic flux is returned by a ferromagnetic yoke. Figure 3.4 shows a schematic drawing of the SuperKEKB dipole magnet.

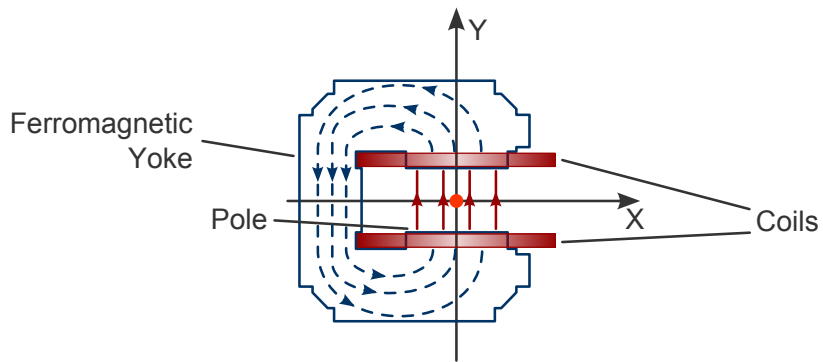


Figure 3.4: A schematic drawing of the SuperKEKB dipole magnet.

3.4 Beam focusing

In an ideal world where the beam particles weren't interacting with each other and could be injected exactly onto the design orbit, the bending magnets would be sufficient to keep them on their design orbit and guide them around the accelerator. However, during their journey most of the particles will deviate slightly from the design orbit. If they are not bent back, they might collide with the beampipe, collimators or other structures and be lost. The bending magnets themselves can provide a correction mechanism if their magnetic field is not homogeneous along the x direction. as a result the magnet exhibits a small gradient in its profile, such that $\partial B_y / \partial x \neq 0$. This is illustrated in figure 3.5.

The force restoring the particles along the x -axis, is given by [82]

$$F_x = -\frac{\gamma m v^2}{R} \frac{x}{R} (1 - n) \quad (3.3)$$

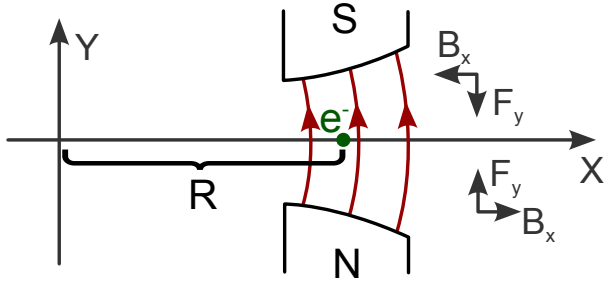


Figure 3.5: Weak focusing magnetic field of a bending magnet [81]. The beam particle enters the plane.

where x is the horizontal deviation of the particle from the design orbit, R the radius of the orbit, v the velocity of the particle and n the **field index**

$$n = -\frac{R}{B_y(R)} \frac{\partial B_y}{\partial x} \quad (3.4)$$

The equation of motion, using $F_x = \gamma m \ddot{x}$, is

$$\ddot{x} + \omega_x^2 x = 0 \quad (3.5)$$

This equation describes an harmonic oscillator, with the frequency

$$\omega_x = \omega_0 \sqrt{1 - n} \quad (3.6)$$

where ω_0 is the **revolution frequency** of the particles. Equation 3.6 describes a beam particle oscillating around the design orbit with a frequency ω_x . The oscillation is called **betatron oscillation**, as it was discovered during the development of the betatron. A stable particle beam is maintained as long as the amplitude of the betatron oscillation does not grow exponentially. The stability of the beam along the y direction is accomplished if the bending magnets are designed in such a way that their magnetic field contains a radial component B_x . This is shown in figure 3.5. The vertical betatron oscillation frequency is

$$\omega_y = \omega_0 \sqrt{n} \quad (3.7)$$

The stability of the particle beam due to betatron oscillation is summarised by Steenbeck's stability criterion [83]

$$0 < n < 1 \quad (3.8)$$

As it can be seen from equations 3.6 and 3.7, the betatron oscillation wavelength is larger than the circumference of the accelerator ring. This means that large deviations from the design orbit are possible [81] and large magnet apertures [84] are required. Hence, this type of focusing is called **weak focusing** ($n < 1$). This problem can be solved by applying the **strong focusing** powers of higher order magnets ($n \gg 1$). The design of those can be obtained by solving the Laplace equation by means of a multipole expansion [85]. This yields a solution that can be decomposed into independent multipole terms. The terms that are interesting for accelerator physics are **dipole**, **quadrupole** and **sextupole** terms. Higher order multipole terms are very rarely useful and are not used at SuperKEKB. The dipole term motivates the design of the dipole magnet whose usage as a bending magnet was introduced above. Another type of magnet arises from the quadrupole term. The magnetic quadrupole potential V_2 is given as [85]

$$\frac{e}{cp} V_2 = \underbrace{-\frac{1}{2} k^* (x^2 - y^2)}_{Im} + \underbrace{kxy}_{Re} \quad (3.9)$$

where the first part on the left side is the imaginary part and the right side the real part of the complex potential. The magnet strength is given by k , the multipole strength parameter. The imaginary part describes a quadrupole field, which is rotated by 45° with respect to the quadrupole field described by the real part. However, for the design of the **quadrupole magnets** at SuperKEKB only the real part of the potential is used. The quadrupole magnetic field of the real part is then

$$\frac{e}{cp} B_x = ky \quad \frac{e}{cp} B_y = kx \quad (3.10)$$

It should be noted that the vertical(horizontal) component of the Lorentz force depends only on the vertical(horizontal) position of the particle. The consequence is that the horizontal and vertical betatron oscillations are decoupled and the flat beam at SuperKEKB remains flat. The magnetic field pattern is drawn on the left side of figure 3.6.

In comparison to the weak focusing capabilities of dipole magnets, quadrupole magnets provide a strong focusing effect on the beam. The strong focusing scheme was independently invented by Christofilos [86] and Courant et al. [87]. The magnet pole shape for a quadrupole magnet is defined by the equipotential surface $kxy = \text{const}$. This equation describes a hyperbola, which is

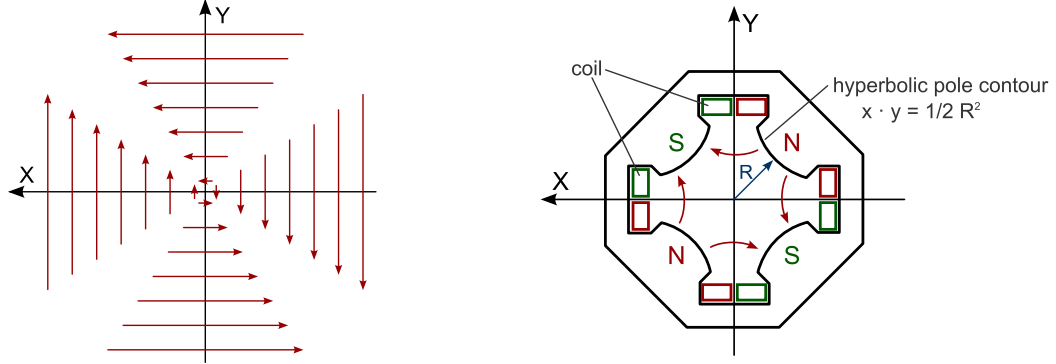


Figure 3.6: Left: Magnetic field of a quadrupole magnet [85]; Right: The technical realisation of a quadrupole magnet [81]. The strength of the magnetic field scales linearly with the deviation from the axis: $B_x \propto y$, $B_y \propto x$. The shown magnet is horizontally focusing and vertically defocusing.

the pole shoe contour for the quadrupole magnet. The drawing on the right side of figure 3.6 illustrates the technical realisation of a quadrupole magnet. At SuperKEKB quadrupole magnets are used throughout the whole ring and for the final beam focusing in the interaction region (see section 4.2). In the quadrupole configuration shown in figure 3.6, a beam particle moving at a distance $|x| > 0$ from the s -axis is deflected towards the centre. But particles moving at a distance $|y| > 0$ from the s -axis are deflected outwards. Thus, this quadrupole magnet focuses the beam in the x -plane but defocuses it in the y -plane. This effect is the realisation of Earnshaw's theorem [88], which states that simultaneous focusing in both planes is impossible. Nevertheless, it turns out that focusing of the beam in both planes can be achieved, if two quadrupole magnets are placed next to each other. They just require a gap of a certain length between them, and the second magnet to be rotated by 90° compared to the first one. This arrangement is called a **FODO** lattice, where **F** is a horizontally focusing but vertically defocusing quadrupole, **D** a vertically focusing but horizontally defocusing quadrupole and **O** the gap between the magnets. The FODO describes the most simple strong focusing lattice. It exhibits a strong similarity to an optical system of focusing and defocusing lenses, giving the system of magnets the name “beam optics”. In general, various properties of lenses can also be defined for focusing magnets, such as the focal length and point to point imaging. Assuming that the length of a quadrupole magnet is small compared to its focal length, the thin lens approximation [89] can be used to formulate the well known expression for the focal length of a system of two magnets (lenses), being separated by a distance L

$$\frac{1}{f} = \frac{1}{f_1} + \frac{1}{f_2} - \frac{L}{f_1 f_2} \quad (3.11)$$

By setting the strengths of the magnets such that, for example, $f_1 = -f_2 = f_{12}$, one gets a system of **F** and **D** quadrupole magnets focusing the beam in both planes with a total focal length

of $f^{-1} = L/f_{12}^2$. So far, it was silently assumed that all particles within a bunch have the same energy. But, in reality, the energies of the particles are distributed statistically (e.g. from energy loss due to synchrotron radiation in the bending magnets) with the effect that particles with higher energies are bent less by a quadrupole magnet than those with lower energies. This means that the focal point of higher energetic particles is further away and the bunch gets spread out or defocused in the longitudinal direction. This effect is called **chromatic aberration** and can be corrected by **sextupole magnets**, the technical realisation of the sextupole term of the multipole expansion. The sextupole design is similar to the quadrupole design, but with six magnets instead of four magnets. They are arranged in an alternating order of north and south magnetic poles. However, unlike the quadrupole, the magnetic field varies like $\propto x^2$, rather than $\propto x$ for the quadrupole case. This leads to a larger focusing effect for particles that are displaced further from the design orbit. At SuperKEKB the quadrupole magnets are always followed by sextupole magnets, in order to correct for the chromatic aberration that was introduced by the quadrupole magnets.

3.5 Beam dynamics

The previous sections described the effects of bending and focusing magnets on individual particle trajectories. However, as specified in table 3.1, about 10^{11} particles are grouped into a single particle bunch. It is impractical to describe the trajectory for each particle in a bunch separately. Instead, it is more convenient to represent the bunch by its boundaries and position (the “centre-of-mass” of the bunch). The particles within a bunch oscillate independently from each other around the origin of the bunch. In the following the mathematical description of a bunch and its properties is motivated.

Each particle is represented by a point in the six-dimensional phase space, defined by

$$(x, x', y, y', s, E)$$

where $x' = dx/dt$, s is the position along the trajectory and E the energy of the particle. Under the assumption that the coupling between the horizontal and the vertical plane can safely be ignored in first order and can be added later as a perturbation, the six-dimensional phase space can be split into three independent two-dimensional phase planes. The description of a particle bunch in a two-dimensional phase plane is derived from equation 3.5 by generalising it to an s -dependent restoring force. This yields **Hill's equation** [84]

$$\frac{d^2x}{ds^2} + K(s)x = 0 \quad (3.12)$$

Solving this equation leads to expressions for x and x'

$$x(s) = \sqrt{\epsilon\beta(s)} \cos \phi(s) \quad x' = -\alpha(s)\sqrt{\epsilon/\beta(s)} \cos \phi(s) - \sqrt{\epsilon/\beta(s)} \sin \phi(s) \quad (3.13)$$

where ϵ is a constant and depends on the initial conditions. However, the parameters α , β and the phase ϕ depend on the position s . Plotting x' versus x for ϕ going from 0 to 2π results in the so-called **phase space ellipse** shown in figure 3.7.

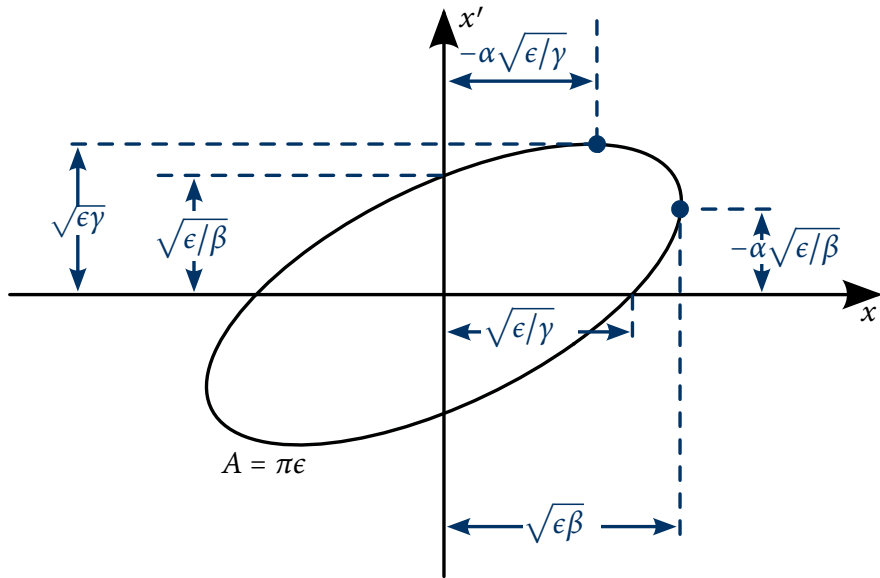


Figure 3.7: The beam phase space ellipse [85]. Shown is the (x, x') slice through the six-dimensional phase space.

The equation of the ellipse is

$$\gamma(s) x^2(s) + 2 \alpha(s) x(s) x'(s) + \beta(s) x'^2(s) = \epsilon \quad (3.14)$$

with $\gamma = (1 + \alpha^2) / \beta$. The ellipse parameters $\alpha(s)$, $\beta(s)$ and $\gamma(s)$ are called **Twiss parameters** [90] and determine the shape and the orientation of the ellipse. Since they depend on s and equation 3.12 describes an oscillatory motion of a particle along the ring, they are also called **betatron functions**. Of particular interest is β , as the other parameters depend on it. It is called the **beta function** and evaluated for the whole accelerator ring. The constant ϵ in equation 3.14 is the **beam emittance** and remains constant as long as Liouville's theorem holds. Under the

assumption that the particles in the beam follow a Gaussian distribution the **beam size** is given as

$$\sigma(s) = \sqrt{\epsilon \cdot \beta(s)} \quad (3.15)$$

As the ellipse moves along the SuperKEKB ring, its shape changes under the influence of the bending and focusing magnets, but its area $\epsilon\pi$ remains the same. Convergent beams are characterized by a rotated phase space ellipse spreading from the upper left corner to the lower right corner. Whereas divergent beams extend from the lower left corner to the upper right corner. If a drift section of the accelerator is long enough the beam transforms eventually into a divergent beam. Without any counter measures a divergent beam fills after some distance the whole beam aperture. Figure 3.8 shows what happens to the phase space ellipse after it got deflected by a quadrupole magnet focusing in the x-direction.

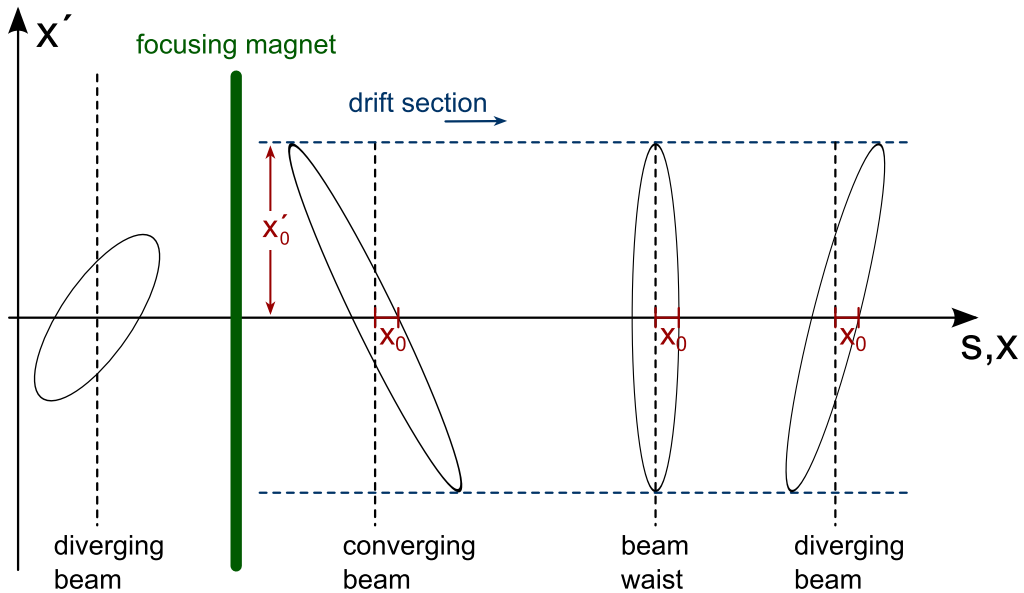


Figure 3.8: Before entering the quadrupole magnet focusing in the x-direction, the ellipse represents a diverging beam. After the magnet, the ellipse is rotated and the beam is converging. The drift section leads to a distortion of the beam such that it becomes divergent again. The **beam waist** is the location of the beam at which it reaches its minimum size in the drift section. In order to prevent the diverging beam from growing beyond the vacuum chamber aperture and being lost as a result another focusing magnet follows each drift section.

According to equation 3.13, a particle at point (x, x') moves around the ellipse as the ellipse travels along the accelerator ring. This leads to the betatron oscillations of the beam particles, which is illustrated in figure 3.9.

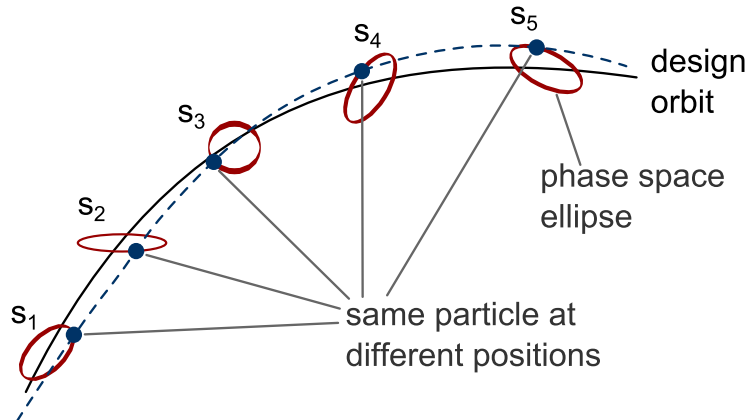


Figure 3.9: Influence of the bending and focusing magnets on the ellipse. A point on the ellipse moves around the ellipse as it travels along the accelerator ring.

The number of betatron oscillations per turn of the particle around the ring is called the **betatron tune** $v_{x,y}$. Equations 3.13 are in general not periodic and thus allow for non-integer values for the betatron tune (see figure 3.10). It should be noted that an integer number for the betatron tune should absolutely be avoided, because otherwise a small perturbation at a certain location is experienced by the particle at every passage with the same betatron phase angle. This results in a resonance-like increase in the betatron amplitude and will inevitably lead to the loss of the particle.

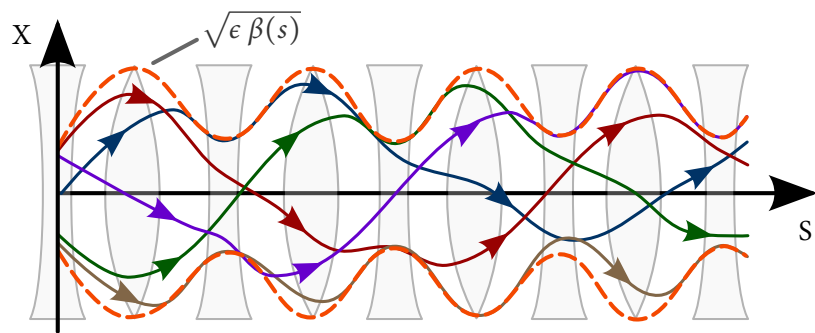


Figure 3.10: A FODO lattice of focusing and defocusing magnets where each peak originates from a F and each valley from a D. Shown is a single particle with a non-integer betatron tune making multiple turns around the ring. Each turn has a different colour. The dashed line represents the beam envelope.

3.6 Luminosity and nano-beam scheme

The instantaneous **Luminosity** is defined as the collision rate per unit area per unit time and is a measure for the performance of an accelerator. The luminosity is a proportionality factor between the number of events per second dN/dt and the cross-section σ of a particular process

$$\frac{dN}{dt} = L \cdot \sigma \quad (3.16)$$

For two charged beams colliding in a storage ring and under the assumption that both beams are Gaussian distributed, the luminosity can be written as [91]

$$L = \frac{N_+ N_- f_c}{2\pi \sqrt{\sigma_{x,+}^2 + \sigma_{x,-}^2} \sqrt{\sigma_{y,+}^2 + \sigma_{y,-}^2}} \cdot R_L \quad (3.17)$$

where N is the number of particles per bunch, f_c the bunch crossing frequency, σ_x , σ_y the horizontal, vertical beam size at the collision point and the signs depict the electron (–) or positron (+) beam. The factor R_L is a luminosity reduction factor [79], which is mainly driven by the **beam-beam effect** and the finite crossing angle. The beam-beam effect is the result of the electro-magnetic interaction between two beams. A moving bunch generates an electric field as well as a magnetic field. Those fields do not only exert a force on the field-generating bunch itself, called **space charge** force, but also affect the opposite bunch during a collision, leading to a reduction of the luminosity. If the beam sizes of the two charged beams are the same, equation 3.17 simplifies to

$$L = \frac{N_+ N_- f_c}{4\pi \sigma_x \sigma_y} \cdot R_L \quad (3.18)$$

The instantaneous luminosity is often expressed using a different set of parameters. Among those parameters is the **vertical beam-beam parameter** $\xi_{y,\pm}$, which is defined as [92]

$$\xi_{y,\pm} = \frac{r_e N_\pm \beta_{y,\pm}}{2\pi \gamma_\pm \sigma_{y,\mp} (\sigma_{x,\mp} + \sigma_{y,\mp})} R_{\xi_y} \quad (3.19)$$

where γ_\pm is the Lorentz factor, r_e the classical electron radius, R_{ξ_y} the beam-beam parameter reduction factor [79] and $\beta_{y,\pm}$ the vertical beta function from equation 3.14. All parameters are evaluated at the IP. For the sake of simplicity, the derivation of the luminosity formula is shown for the positron beam only.

Dividing the luminosity from equation 3.18 by the beam-beam parameter $\xi_{y,+}$ (equation 3.19) yields

$$\frac{L}{\xi_{y,+}} = \frac{N_+ \gamma_+ f_c (\sigma_x + \sigma_y)}{2 r_e \sigma_x \beta_{y,+}} \frac{R_L}{R_{\xi y}}$$

with $N_+ f_c = I_+ / e$ [91], the luminosity can then be written as

$$L = \frac{\gamma_+}{2 e r_e} \left(\frac{I_+ \xi_{y,+}}{\beta_{y,+}} \right) \left(1 + \frac{\sigma_y}{\sigma_x} \right) \frac{R_L}{R_{\xi y}} \quad (3.20)$$

where $R_L/R_{\xi y} \approx 1$ at SuperKEKB. The accelerator is designed to reach an instantaneous luminosity of

$$L = 8 \cdot 10^{35} \text{ cm}^{-2} \text{ s}^{-1}$$

In order to reach this value, SuperKEKB employs the so-called **nano-beam scheme**, which has been proposed by P. Raimondi for the defunct SuperB collider [93]. In this scheme, the vertical beta function $\beta_{y,\pm}$ of the beam is squeezed at the IP, leading to a very small beam size of only 48 nm and hence a high particle density. In comparison with the previous collider KEKB [74], the vertical beta function is 20 times smaller and the total beam current I_{\pm} is two times larger at SuperKEKB. This means that the luminosity at SuperKEKB is 40 times larger than that at KEKB, as it can be seen from equation 3.20. Table 3.1 summarises the SuperKEKB storage ring parameters used to achieve the design luminosity with the nano-beam scheme.

		LER	HER	unit
Beam energy	E	4.000	7.007	GeV
Beam current	I	3.6	2.6	A
Particles/bunch	n_b	9.04	6.53	10^{10}
Number of bunches	N	2500		
Bunch spacing	s_b	1.2		m
	t_b	2		ns
Bunch crossing frequency	f_b	508		MHz
Circumference	C	3016.315		m
Crossing angle	θ_x	83		mrad
Horizontal emittance	ϵ_x	3.2	4.6	nm
Vertical emittance	ϵ_y	8.64	12.9	pm
Coupling parameter	κ	0.27	0.28	
Horizontal beta function at IP	β_x^*	32	25	mm
Vertical beta function at IP	β_y^*	0.27	0.30	mm
Horizontal bunch size	σ_x	10	11	μm
Vertical bunch size	σ_y	48	62	nm
Bunch length	σ_z	6	5	mm
Radiation loss	U_0	1.87	2.43	MeV/turn
Synchrotron tune	ν_s	-0.0247	-0.0280	
Horizontal betatron tune	ν_x	44.53	45.53	
Vertical betatron tune	ν_y	44.57	43.57	
Horizontal beam-beam	ξ_x	0.0028	0.0012	
Vertical beam-beam	ξ_y	0.0881	0.0807	
Momentum compaction	α_p	3.25	4.55	10^{-4}
Momentum spread	σ_δ	8.08	6.37	10^{-4}
RF voltage	V_C	9.4	15.0	MV
Luminosity	L	$8 \cdot 10^{35}$		$\text{cm}^{-2} \text{ s}^{-1}$

Table 3.1: The SuperKEKB storage ring parameters.

3.7 Particle generation and acceleration

A “particle gun” and a linear accelerator, the **injector linac**, are responsible for producing, accelerating and delivering the electrons and positrons for the SuperKEKB storage ring. In order to reach the design luminosity of $8 \times 10^{35} \text{ cm}^{-2} \text{ s}^{-1}$ [80], the SuperKEKB accelerator requires a small emittance (see equation 3.17), high intensity electron beam. A standard thermionic electron gun, which uses thermionic emission [94] to create bunches of electrons, is not able to deliver the required electron beam properties. Thus, a photocathode **RF gun** [95] is used, delivering a low-emittance electron beam. A Nd:YAG solid state laser [96] generates 30 ps short photon pulses with a wavelength of 226 nm. The photons hit a 6 mm diameter LaB_6 photocathode [97] and create a cloud of electrons by photo emission [98]. Due to the low work function of $\sim 2.7 \text{ eV}$ [99] and a high electron emissivity (quantum efficiency $\sim 10^{-4}$) of the photocathode at room temperature, the RF gun is able to produce high density electron bunches with a bunch charge of 5 nC. The whole structure is inserted directly into an accelerating RF field that accelerates the generated electrons to 1.7 GeV. The electrons leave the RF gun in groups of two bunches and are accelerated further to 3.5 GeV before they enter the linac straight section where they are accelerated to their final energy of 7 GeV. A schematic drawing of the linac is shown in figure 3.11.

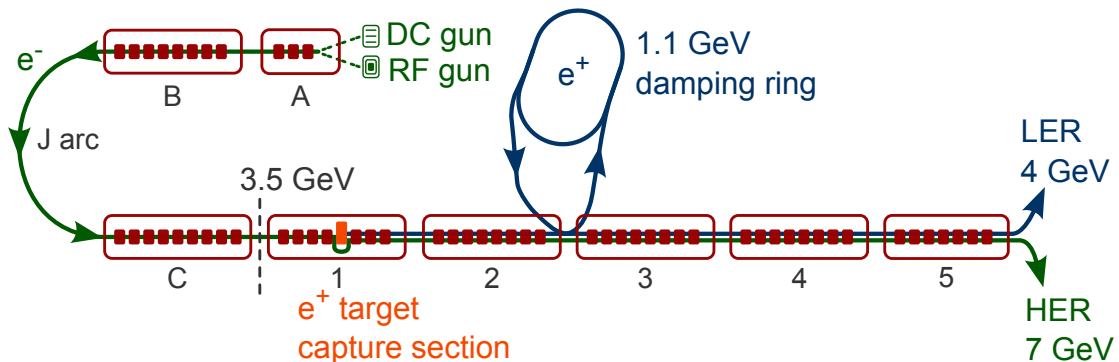


Figure 3.11: The J-shaped linear accelerator delivers the electrons and positrons for SuperKEKB. Its total length is 600 m and the circumference of the damping ring is 136 m.

The positrons, on the other hand, are created as secondary particles. For the creation of positrons an electron beam with a high current is required, which cannot be produced with the aforementioned RF gun. Therefore, a thermionic electron gun, called **DC gun**, together with an RF field is used to generate bunches of electrons. They are accelerated to 3.5 GeV, using the same acceleration structures as those used for the RF gun electrons. The electrons then hit a 14 mm thick amorphous tungsten target, where they undergo bremsstrahlung. The produced photons convert inside the target to electron-positron pairs and the positrons are separated from the electrons by means of a 6 T magnetic field. But the emittance of the positrons leaving the capture section is larger than SuperKEKB requires. Therefore, the positrons are sent to a damping ring,

where they lose their transverse momentum dispersion and large beam divergence through the emission of synchrotron radiation. This process is called radiative cooling [100] and results in a reduction of the emittance by a factor of 130. The electrons/positrons enter the linac in groups of two bunches, where each bunch carries a bunch charge of 4 nC.

The final acceleration for both electrons and positrons takes place in the last sections of the linac. Since electrons and positrons make use of the same acceleration structures, they are generated in an alternating way with a frequency of 50 Hz. The positron target contains a little hole such that the electrons can pass the target unaffected. The electrons leave the linac with an energy of 7.0 GeV, while the positrons have an energy of 4.0 GeV.

3.8 Injection scheme

SuperKEKB follows a continuous injection scheme, with the alternating injection of electron and positron bunches every 20 ms. This means that two new electron/positron bunches are injected into the SuperKEKB storage ring every 40 ms. According to **Liouville's theorem** [101, 91], which states that for a system of non-interacting particles the density in phase space along the trajectory is constant, new bunches cannot be injected directly onto the ideal orbit where the main bunches are located. Instead they are injected by a septum magnet [102] next to the main bunches such that they perform Betatron-oscillation around the ideal orbit. By using mechanisms that “violates” Liouville's theorem, such as synchrotron radiation, the transversal momentum of the newly injected bunches is reduced until they become one with the main bunches. This process is called **beam cooling** [103]. At SuperKEKB the electron and positron bunches are sent through a **wiggler** [104, 105], an arrangement of a row of alternately deflecting bending magnets which do not introduce a net deflection to the bunch. During their journey through the wiggler, the particles inside the bunch emit synchrotron radiation and thus cool down. The wigglers are placed in the Oho and Nikko straight section, as figure 3.1 illustrates. While the newly injected bunches “cool” down into their main bunches an increased background level in the Belle II detector is the result, requiring special treatment of the sub-detectors. The counter-measure of the Pixel Vertex Detector to such a **noisy bunch** is explained in chapter 4.

3.9 Beam and particle loss

The loss of the full beam or parts of it can be divided into two categories: **irregular** and **regular** losses. The first category comprises the loss due to misaligned beams, operation failure, broken magnet power supplies etc. These losses can occur at any point in the accelerator and are not bound, for example, to collimation systems. They often result in the complete loss of the beam and their effect ranges from an increased background level in the Belle II detector to the

destruction of the beam pipe or the collimators. Examples for irregular losses are discussed in [106, 107, 108]. In comparison to the irregular losses, the regular losses are localised on collimator systems or on other aperture limits and are usually not avoidable. They occur continuously during the operation of the accelerator and result in the loss of beam particles, thus limiting the beam-lifetime. Table 3.2 summarises the expected beam-lifetime at SuperKEKB due to different types of regular loss effects.

	LER	HER
Touschek	586	650
Beam-Gas	1470	2760
Radiative Bhabha	1680	1200
Total	335	366
Loss rate	10 mA/s	7.2 mA/s

Table 3.2: The expected beam-lifetime at SuperKEKB. All values are given in seconds.

Typical processes leading to a continuous loss of particles are the Touschek effect and the Coulomb scattering on residual gas nuclei (Beam-Gas). More information can be found in chapter 7 where various loss effects are discussed in more detail. Particles which undergo such a process leave their nominal beam orbit and are subject to betatron oscillations with increased amplitudes. This allows scattered particles to travel along the ring until they collide with the beampipe or a collimator and can produce showers of secondary particles. If the beam particles collide with material of the vacuum system or components of the magnet system within a few meters from the IP, they result in an increased background level in the Belle II detector. In order to shield the Belle II detector from those particles, collimators are installed along the LER and HER. They remove particles that are too far away from the nominal beam orbit. However, removing particles also means a shortened beam-lifetime. Therefore, SuperKEKB uses collimators with an adjustable aperture, called **movable masks** [109]. They allow the adaptation of the collimator aperture to the background level, while keeping the lifetime of the beam high. Figure 3.12 illustrates the design of the SuperKEKB movable mask.

3.10 Simulation of the beam transport

The design and optimisation of the SuperKEKB magnet lattice requires a detailed study and understanding of the beam dynamics in the vicinity of magnets and collimators. However, it is not possible to calculate the trajectory of the beam particles analytically. Under the assumption that the magnet strength parameters are constant within each magnet, a matrix method can be applied [110]. For each element of the beam transport system, such as bending, quadrupole and sextupole magnets, collimators and drift spaces, a **transformation matrix** is defined. The beam

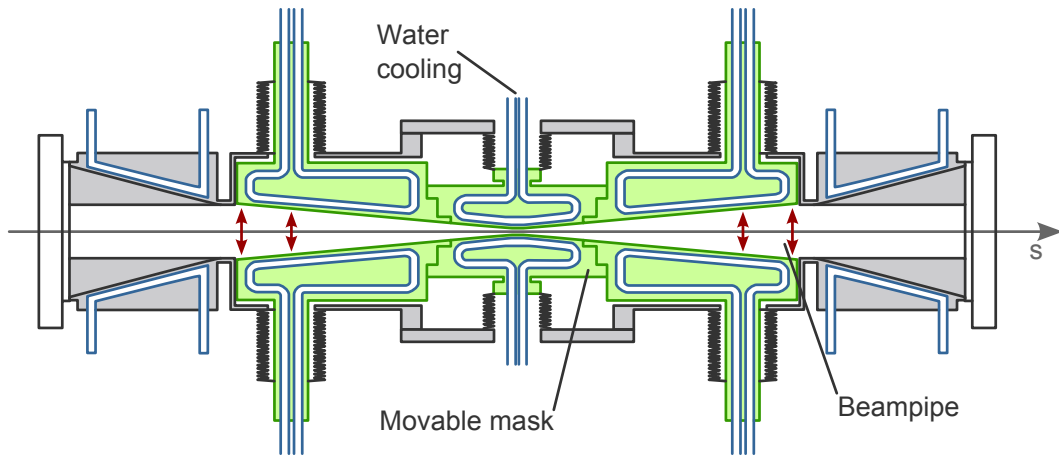


Figure 3.12: The SuperKEKB movable mask. The collimator is cooled with water and has an adjustable aperture.

transport through the ring is then accomplished by multiplying the transformation matrices for all elements the particles pass. The total matrix is then applied to the betatron functions, hence allowing to describe the beam at any point in the lattice. This scheme can be implemented quite effectively in software, such as **TURTLE** [111] and **SAD** (Strategic Accelerator Design) [112]. The latter is of particular interest, because it has been developed at KEK by the accelerator theory group and is used for the magnet lattice design and optimisation for SuperKEKB. SAD also incorporates higher order effects and corrections to the transformation matrices, such as **fringe fields**. A fringe field is the part of a magnetic field that extends beyond the edges of the magnet. In chapter 7, SAD plays an important role for the estimation of the beam background for the Belle II detector.

4 The Belle II Detector

The Belle II detector is a general-purpose particle physics detector [113] designed primarily for precision B -physics at energies around the $\Upsilon(4S)$ threshold. The detector surrounds the interaction point (IP) of SuperKEKB and is located inside Tsukuba hall at the KEK high energy research centre in Japan. An artistic rendering of the Belle II detector is shown in figure 4.1. The detector is 7.4 m long and has a diameter of approximately 7 m. It covers a large angular **acceptance** of $17^\circ < \theta < 150^\circ$ in order to provide an excellent hermeticity for the observation of particle collisions.

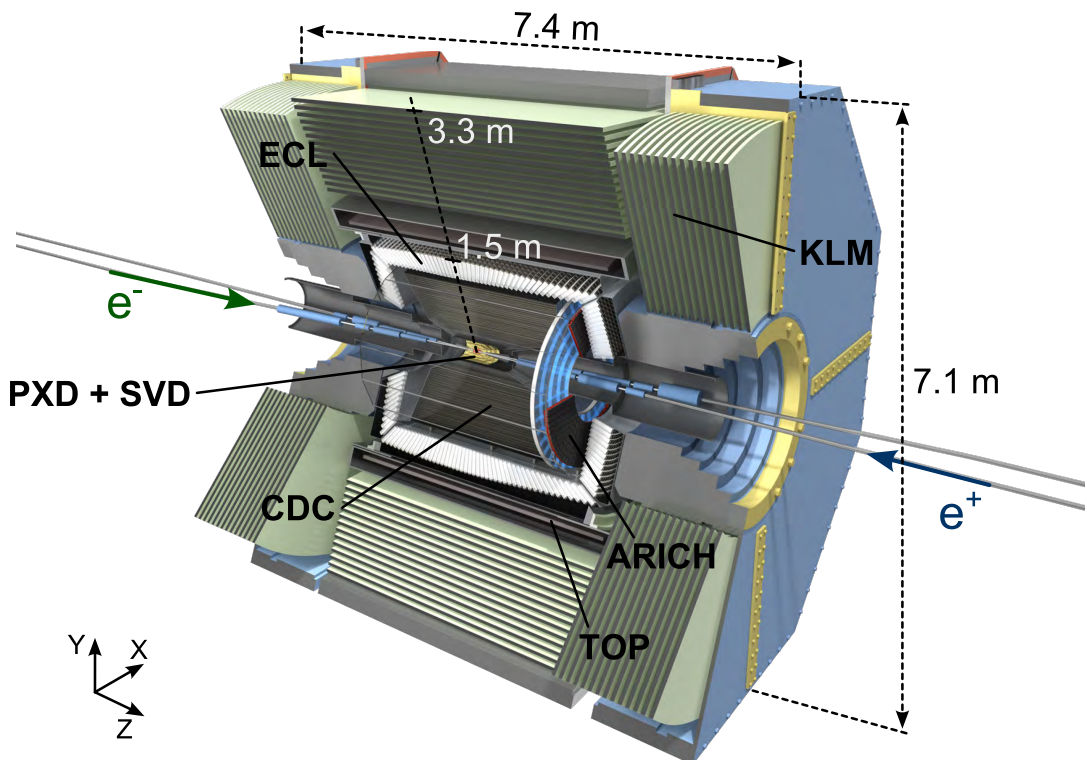


Figure 4.1: An artistic rendering of the Belle II detector [114].

The boost of the centre-of-mass frame of the collision and the flight direction of the produced B -mesons towards the forward part of Belle II requires an asymmetric detector along the z -axis. Thus, the angular acceptance of the detector can be split into three distinct polar angle ranges: a **Forward**, a **Barrel** and a **Backward** region. The Forward region covers $17^\circ < \theta < 30^\circ$, the Barrel region $30^\circ < \theta < 125^\circ$ and the Backward region $125^\circ < \theta < 150^\circ$. Apart from the outermost sub-detector, all components of Belle II are within a constant and solenoidal **magnetic field** of 1.5 T, which is parallel to the main detector axis. A single particle collision, producing on average 12 tracks for a typical $e^+e^- \rightarrow \Upsilon(4S) \rightarrow B\bar{B}$ reaction, is called an **event** once it has been recorded. In such an event the final particles that are detected are mainly electrons, positrons, photons, muons, π^\pm mesons and K^\pm mesons. Particle measurement takes place in the various **sub-detectors** of Belle II, optimised for the detection of different particle species. Among them are the tracking sub-detectors that measure the momentum of the particles and the position of their decay vertices, the particle identification sub-detectors that determine the particle type and the calorimeter that allows the reconstruction of the energy of photons and electrons. Table 4.1 shows the required transverse momentum for a charged particle to reach a specific sub-detector. A short summary of all sub-detectors, ordered in increasing distance from the interaction point, is given below.

- **The Interaction Region (IR)**

The Interaction Region surrounds the interaction point and extends to about 4 m along the HER and LER into the forward and backward direction. It consists of the beampipe and the final focusing magnets. While the IR does not actively participate in the observation of events, its design plays a significant role for the amount and distribution of the background that is expected at Belle II.

- **Pixel Vertex Detector (PXD)**

The Pixel Vertex Detector is the innermost detector of Belle II. Its two layers with about 8 million pixels measure the position of traversing charged particles.

- **Silicon Vertex Detector (SVD)**

Like the PXD, the Silicon Vertex Detector is a semi-conductor based detector, which measures the passage of particles in four layers. However, unlike the PXD, it uses strips instead of pixels for the detection of traversing particles.

- **Central Drift Chamber (CDC)**

The Central Drift Chamber consists of a volume filled with gas that contains 14336 electric wires, which provide more than 50 three-dimensional space points on a charged particle's trajectory.

- **The Time of Propagation Counter (TOP)**

The Time of Propagation Counter is part of the particle identification system in the barrel region of Belle II. Its main purpose is to provide an efficient separation of K^\pm from π^\pm by measuring the velocity of the particles.

- **The Aerogel Rich Detector (ARICH)**

The Aerogel Rich Detector provides particle identification of K^\pm and π^\pm for the forward region of Belle II by measuring the velocity of the particles.

- **The Electromagnetic calorimeter (ECL)**

The main purpose of the Electromagnetic calorimeter is the detection and measurement of the energy and angular coordinates of electrons and neutral particles, mainly photons.

- **Solenoid**

The whole detector, apart from the KLM, is surrounded by a superconducting solenoid producing a longitudinal magnetic field of 1.5 T.

- **The KLM**

The KLM is a detector which has been specifically designed to identify K_L and muons with a momentum above ~ 0.6 GeV. An iron return yoke returns the magnetic flux and serves as a an absorber for the KLM at the same time.

Detector	inner radius [mm]	minimal p_t [MeV]
PXD	14	3.15
SVD	38	8.55
CDC	168	37.8
TOP	1190	267.75
ECL	1250	281.25
KLM	2019	454.27

Table 4.1: Required minimal transverse momentum in order to reach a specific sub-detector. The values are calculated using the well-known formula for relativistic electrons: $p_t[\text{GeV}] = 0.3 \cdot B[\text{Tesla}] \cdot R[m]$

4.1 The coordinate system

The Belle II detector is described using a **Cartesian, right-handed** coordinate system. The **origin** of the coordinate system is located at the nominal interaction point, with the axes described as follows: the **z -axis** pointing along the direction of the magnetic field of the solenoid; the **y -axis** pointing upwards, in the direction of the detector hall roof; and the **x -axis** pointing along the radial direction towards the outside of the accelerator ring. This definition is shown in figure 4.2.

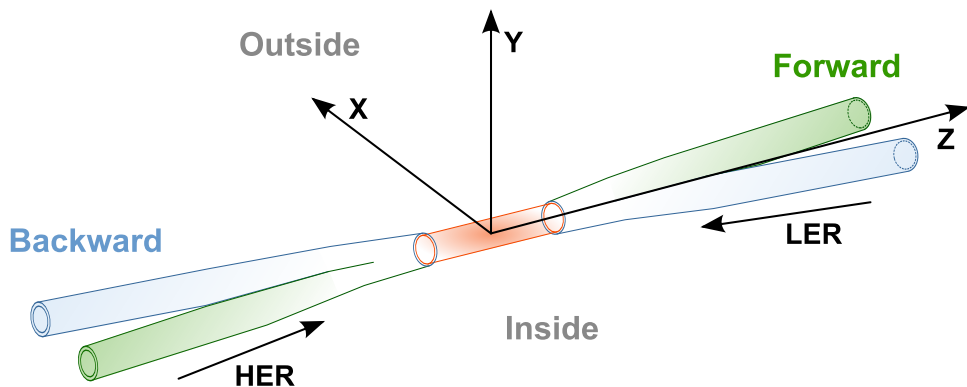


Figure 4.2: The Belle II coordinate system.

The coordinate system's positive z -axis points towards the forward direction and the negative z -axis towards the backward direction. If not otherwise specified, all xy projections showing any part of the Belle II detector are drawn such that the projected detector is seen from the forward to the backward direction. This means that the z -axis points out of the page, the x -axis to the right and the y -axis upwards.

4.2 The Interaction Region

The interaction region is responsible for guiding the beams to and from the interaction point and for maintaining the vacuum inside the beampipe. The beams meet within an area, referred to as the **beamspot**, that can be described by a three-dimensional Gaussian with the following values for its spread (standard deviations) at Belle II [115]: $\sigma_x = 6.18 \mu\text{m}$, $\sigma_y = 59 \text{ nm}$, $\sigma_z = 154 \mu\text{m}$. The interaction region extends to about 4 m into the forward and backward region, as shown in figure 4.3. Various quadrupole magnets (section 3.4) focus the beam, where QC1RP and QC1LP are responsible for the final focusing of the LER beam and QC1LE and QC1RE for

the final focusing for HER beam. As described in section 3.1, the particles collide with a crossing angle of 83 mrad. Thus, the quadrupole magnets are inclined by 41.5 mrad with respect to the Belle II detector solenoid axis. Focusing magnets are realized as super conducting magnets and contain an iron yoke, except for the two magnets closest to the IP. Table 4.2 lists all focusing magnets, together with their most important specifications. Two solenoid compensating magnets, one for the forward and one for the backward direction, protect the inner magnets from the Belle II detector solenoid field.

Name	Ring	Focusing	Field gradient	Length [m]	Current [A]	Position [mm]	Iron yoke
			[T/m]				
QC2LE	HER	horiz	20.2	0.7	724.1	-2700	Yes
QC2LP	LER	horiz	27.15	0.41	817.3	-1925	Yes
QC1LE	HER	vert	70.68	0.38	1558.5	-1410	Yes
QC1LP	LER	vert	67.94	0.34	1609.3	-935	No
QC1RP	LER	vert	66.52	0.34	1575.6	935	No
QC1RE	HER	vert	66.22	0.38	1460.3	1410	Yes
QC2RP	LER	horiz	27.17	0.41	817.9	1925	Yes
QC2RE	HER	horiz	34.9	0.37	1044.9	2925	Yes

Table 4.2: The final focusing magnets of Belle II as illustrated in figure 4.3. The position of each magnet is measured from the IP.

The beampipe surrounding the IP is illustrated in figure 4.4. It consists of a middle section made from Beryllium followed by a Titanium part. The Beryllium section is constructed from two layers, with paraffin flowing between the layers as a coolant. Beryllium is used for the beampipe as it offers a large stiffness at a low atomic number and a good thermal stability. Its diamagnetic nature does not lead to interferences with the field from the final focusing magnets. The outer parts, connecting the beampipe with the final focusing magnets are made from Tantalum and cooled with water. Tantalum is used because it provides an effective shielding against backgrounds from particle showers. The inside of the beampipe is coated with gold [116] in order to suppress photons originating from synchrotron radiation. In order to stop direct synchrotron radiation, the inner diameter of the incoming beampipe is gradually reduced from 20 mm to 8.4 mm for QC1RP and QC1LP and from 30 mm to 9.8 mm for QC1RE and QC1LE. After this reduction, the incoming beampipe widens again to 20 mm, the inner diameter of the middle beampipe section. Due to space constraints around the IP, the vacuum pumps are located outside of the IR. This leads to a pressure at the IP of $\sim 10^{-5}$ Pa which is worse than the vacuum level at Belle as the pumps could be installed closer to the IP at KEKB.

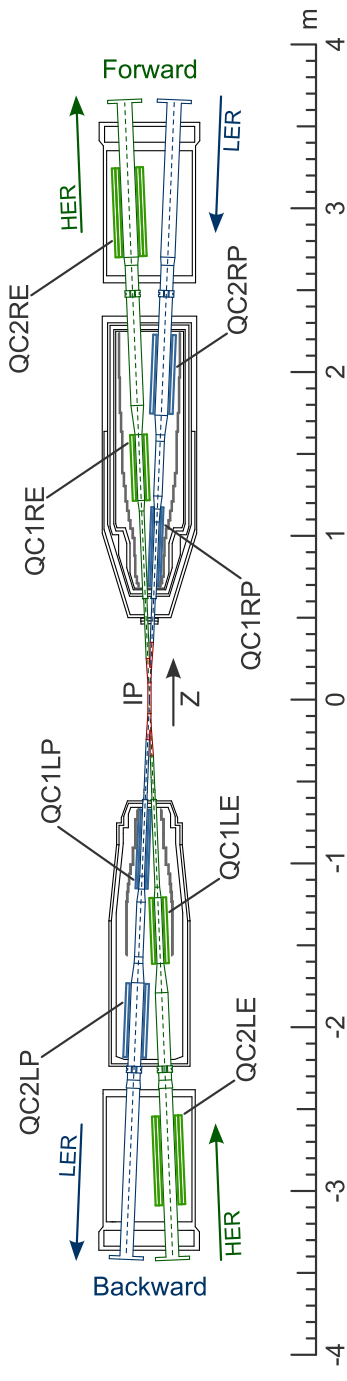


Figure 4.3: The IR of Belle II. Shown are the incoming and outgoing beampipes and the final focusing magnets [117].

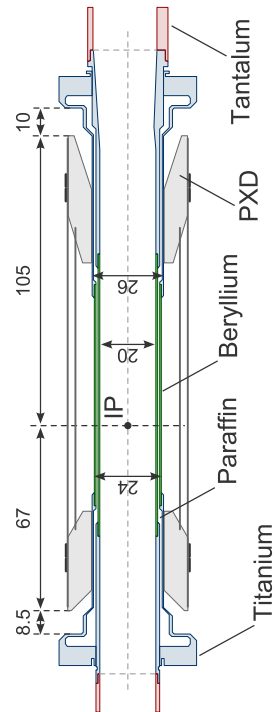


Figure 4.4: The beampipe surrounding the IP including the support structure for the PXD [118].

4.3 The Pixel Vertex Detector

The Pixel Vertex Detector (**PXD**) is the innermost sub-detector of Belle II. It is a semi-conductor device, based on the **DEPFET** (DEPleted Field Effect Transistor) technology [119, 120, 121]. The PXD measures the position of traversing particles originating from a particle collision. The main purpose of the PXD is the precise reconstruction of decay vertices. In order to achieve the required precision the PXD is placed very closely to the interaction point. The PXD covers the full polar angle range $17^\circ < \theta < 150^\circ$ of Belle II and only contributes with 0.21 % of a radiation length for each layer to the total amount of material in the detector. Figure 4.5 provides an overview of the PXD layout.

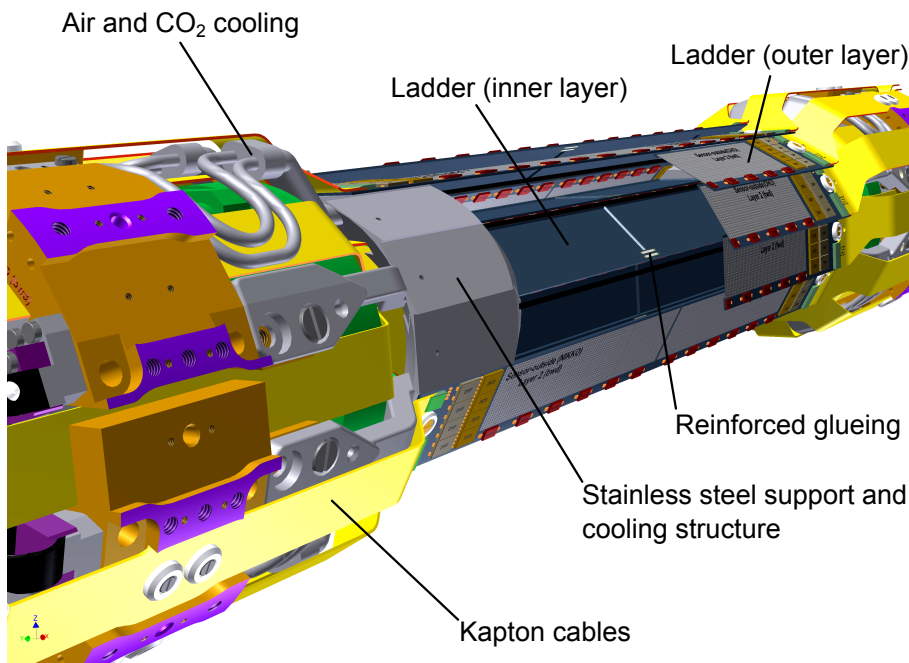


Figure 4.5: The layout of the Belle II Pixel Vertex Detector [122].

4.3.1 The DEPFET pixel sensor

The DEPFET (DEPleted Field Effect Transistor) is a semi-conductor sensor that combines the detection of the passage of charged particles and the amplification of their deposited energy within one device. The DEPFET principle has been proposed by Kemmer and Lutz in 1987 [119] and was experimentally confirmed three years later [120]. A DEPFET pixel [121] is a p-channel **MOSFET** [123, 124], integrated onto a high-resistivity silicon detector substrate, called **bulk**. The bulk is fully depleted [125] from movable charge carriers by applying a sufficiently large negative voltage to a p+ contact at its backside. For the PXD DEPFET pixel, the p+ back

contact is initially set to -30 V but might require voltages as low as -60 V to compensate for radiation damage. A potential minimum for electrons is created by an additional n-implant underneath the transistor channel at a depth of about $1\ \mu\text{m}$. Negative charges, collected in the potential minimum, create image charges in the transistor channel. Those image charges increase the channel conductance therefore acting in a similar way as the external MOSFET gate. The implanted potential minimum is called **internal gate**. The charges inside the internal gate modulate a current flowing from the source to the drain of the DEPFET, thus allowing to amplify and measure the deposited charge. Figure 4.6 shows a schematic drawing of the PXD DEPFET pixel.

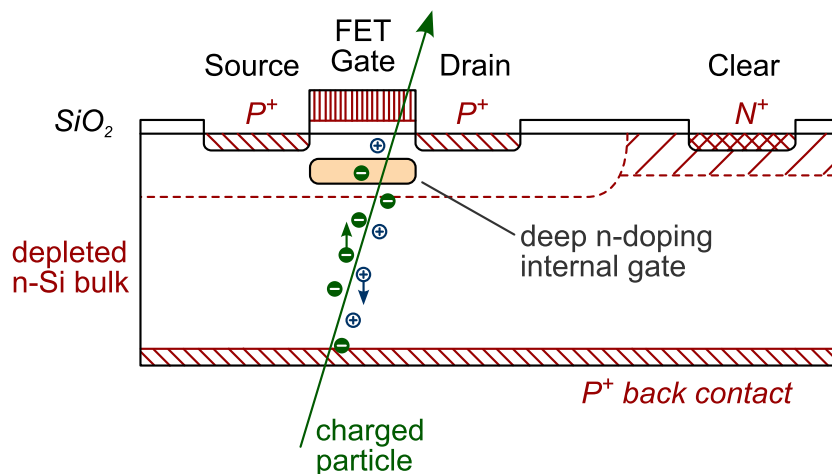


Figure 4.6: Schematic drawing of the operating mode of a DEPFET [121]. An internal gate modulates the channel current that flows from the Source to the Drain. The external gate is used to switch the DEPFET on and off. In order to remove the collected charges in the internal gate, the Clear contact is used.

A charged particle traversing the DEPFET pixel generates electron-hole pairs in the fully depleted bulk. A MIP, for example, generates ~ 6000 electron-hole pairs along its track through the $75\ \mu\text{m}$ thick silicon bulk. While the holes drift to the p+ back contact, almost all electrons drift to the potential minimum and are collected in the internal gate. The required drift field has been designed and optimised using simulation tools [126]. The internal gate is able to store ~ 40000 electrons without degrading the linear behaviour of the channel current modulation. A saturation due to charge overflow is reached at ~ 60000 electrons. The numerical value for the collected charge in the pixel is determined by measuring the channel current difference between the empty internal gate before, and the occupied internal gate after the collection of electrons. In order to prepare the sensor for a new measurement, the electrons have to be removed from the internal gate. This is accomplished with a neighbouring n+ contact, the **Clear** contact, which is pulsed at a positive voltage providing a punch-through into the internal gate.

4.3.2 Sensitive area layout

The sensitive area of the PXD is assembled from 40 **modules**, where each module consists of a 250×768 pixel matrix of DEPFET pixel **sensors**. The size of each pixel is defined by physics requirements, design and space limitations and readout speed. The final pixel size and the thickness of the sensors has been optimised through MonteCarlo studies [127]. In particular, the effect of different pixel layouts, sizes and thicknesses on the impact parameter resolution of charged tracks and on the reconstruction resolution of decay vertices was studied. In order to improve the resolution around the interaction point and to decrease the readout time, each PXD sensor is split into two **segments**. The pixels of the segment closer to the IP are arranged in a matrix of 250×256 pixels, while the outer segment hosts 250×512 pixels. Figure 4.7 illustrates the sensor layout. The sensor data is read in the so-called **rolling shutter** mode (see section 4.3.3). This mode requires a certain region of the sensitive area to be selected at a given time, which is accomplished by a row of 6 chips, the **switchers**, bump-bonded on a balcony-like area on the longer edge of the module. The 6 switcher chips are arranged such that two of them address the pixel rows of the smaller segment and the remaining four the rows of the larger segment. A list of the pixels sizes and the active area can be found in table 4.3.

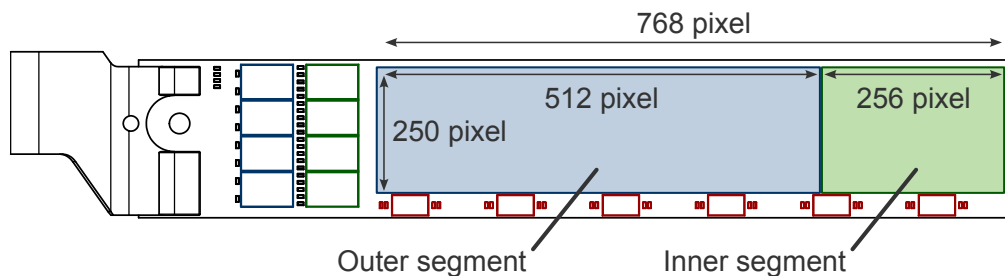


Figure 4.7: The layout and number of pixels for the two sensors. The red rectangles represent the 6 switchers.

	Inner segment	Outer segment	Active area
Layer 1	$50 \mu\text{m} \times 55 \mu\text{m}$	$50 \mu\text{m} \times 60 \mu\text{m}$	$12.5 \text{ mm} \times 44.8 \text{ mm}$
Layer 2	$50 \mu\text{m} \times 70 \mu\text{m}$	$50 \mu\text{m} \times 85 \mu\text{m}$	$12.5 \text{ mm} \times 61.44 \text{ mm}$

Table 4.3: The pixel size and the active area for the PXD sensors. The pixel size is given as width \times length.

4.3.3 Readout cycle

The rolling shutter readout mode of the PXD works by selecting pixel rows consecutively and reading out all columns of a single row. In order to speed up the readout, 4 pixel rows are selected and read out in parallel. It takes 104.17 ns to readout each row. For 768 rows and a parallel readout of four rows this results in a total readout time of 20 μ s for a single sensor, which is twice the time a bunch takes to travel through the accelerator (see section 3.8). The selection of a pixel row is performed by the switcher chip. It turns the pixels on by sending an appropriate voltage to their external gates. The current, flowing from the Source to the Drain in the DEPFET, is then received by Drain Current Digitizer (DCD)[128] chips. In order to minimise the spread between the base current (**pedestal**) of different pixels, a pre-defined current value is subtracted from each pixel using a 2 bit DAC (Digital Analog Converter) inside the DCD. An 8 bit ADC digitises the remaining current and sends an 8 bit ADC value to a Digital Handling Processor (**DHP**)[129]. The DHP extracts the signal for each pixel by subtracting each pixel's pedestal value. The pedestal values for all pixels are stored in a table inside the DHP. In order to minimize the pick-up noise created during the digitisation, the average of all pixels below a certain threshold (**common mode**) is subtracted from all ADC values. Finally, a zero suppression is applied by storing only pixels with values above a pre-defined noise level in a ring-buffer. There, the pixels wait for an external trigger to initiate the full sensor readout. After having read a pixel row, the pixels are reset by removing the charge inside their internal gates. The switcher chips generate the required voltage for the pixels' clear contacts and the punch-through into the internal gate.

4.3.4 Gated mode

In addition to its primary task, the clear contact is also used for another purpose. The PXD experiences a highly increased background level for 4 ms every 20 ms due to noisy bunches originating from the continuous injection at SuperKEKB (see section 3.8). Because a bunch takes about 10 μ s around the accelerator ring and the readout time of the PXD is 20 μ s, the PXD would accumulate the signal generated by a noisy bunch for 4 ms, leading to a dead time of 20 % for the PXD. In order to shield the PXD sensors from collecting noise signal, the DEPFET is operated in the so-called **gated mode**[130] during the passage of a noisy bunch. While being in the gated mode, the clear contact is temporarily set to a positive voltage, which offers a much more attractive target for newly generated electrons than the internal gate. This mode makes the DEPFET pixel blind for the charge deposited during the injection. By applying a small gate voltage it is made sure that the electrons inside the internal gate are not affected. Thus, the charge that has already been collected in the internal gate is preserved during the gated mode phase. This countermeasure avoids the 20 % dead time for the PXD.

4.3.5 Mechanical layout

The PXD consists of two **layers** of pixel modules positioned at the radii of 14 mm and 22 mm, respectively. The inner layer combines 16 modules into 8 planar **ladders** by glueing together two modules to form a single ladder. The join of the two modules is reinforced by very small ceramic (ZnO_2) inserts. The ladders are arranged in a windmill-like structure (see figure 4.8). A single ladder of the inner layer has a width of 15.4 mm and contains a **sensitive area** of 12.5 mm \times 90.45 mm. The outer layer is composed from 12 ladders (24 modules), where each ladder has a width of 15.4 mm and a sensitive area of 12.5 mm \times 123.73 mm. Due to mechanical constraints, the ladders of the inner layer are flipped and mounted up-side-down, compared to the ladders of the outer layer, as can be seen in figure 4.8.

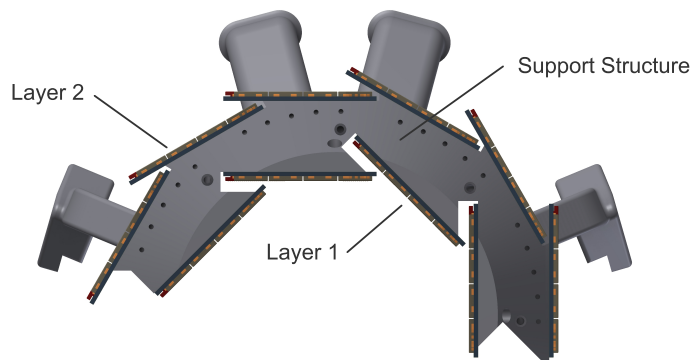


Figure 4.8: The windmill-like arrangement of the PXD ladders, with the inner layer being flipped [122].

The sensitive area for all ladders is split into two areas due to the join of the two modules. The join results in a small, non-sensitive gap of 0.05 mm in the centre of the sensitive area. The sensitive area is thinned down to a thickness of 75 μ m, while the surrounding parts of the ladder have a thickness of 525 μ m. This allows for a very low material budget in the sensitive area and a self-supporting frame around it. A simplified overview of the thinning and production steps, involved in producing a sensor, is shown in figure 4.9. At both ends of each ladder 8 ASIC chips are bump-bonded to the ladder: 4 DCDs and 4 DHPs. They read and pre-process the data from each sensor and send it over a 10 mm wide, multi-layer **Kapton cable** to a patch panel which is connected by a 15 mm wide InfiniBand cable with the Data Handling Hybrid (**DHH**)[131]. The DHH sends the data via optical fibre to the data acquisition system. The chips and the Kapton cables are placed such that only the sensitive area and the switcher chips are inside the detector acceptance. Everything else is located outside and does not disturb the passage of particles through the PXD. The mechanical design of the ladders for the inner and outer layer is illustrated in figure 4.10. Table 4.4 provides a summary of the most important values for the PXD ladder design.

	Radius [mm]	number ladders	overlap [pixel]	overlap [%]	thickness balconies [μ m]	thickness sensor [μ m]	ladder length [mm]	ladder width [mm]
Layer 1	14.0	8	11	4.43	525	75	136	15.4
Layer 2	22.0	12	11	4.41	525	75	170	15.4

Table 4.4: Summary of the numerical values for the PXD mechanical layout. In the case that the tolerances add up unfavourably, the overlap can become as small as 3-5 pixels. The overlap is measured for a single edge and not the full sensor.

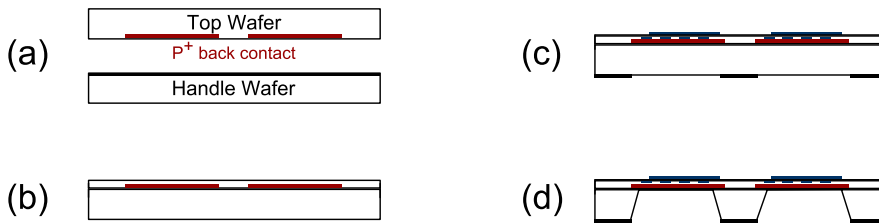


Figure 4.9: (a) Implant the p^+ contact onto the backside of the top wafer. (b) Bond the handle wafer from the bottom onto the top wafer. The handle wafer allows to thin the top wafer down to the required 75 μ m by standard wafer grinding and polishing techniques, without taking any special precautions for the protection of the p^+ backside contact. (c) Implant the DEPFET structures on the top wafer (d) Etch the handle wafer partially back, leaving a support frame that is large enough to provide mechanical stability.

4.3.6 Radiation damage

Every particle traversing the PXD can contribute to the sensor damage. The PXD suffers from two types of the damage effects: **surface damage** and **bulk damage**. Surface damage affects the pixel's signal over noise ratio by increasing the leakage current and consequently also the pedestal. The damage originates from defect sites located in the silicon dioxide very close to the silicon bulk. They might trap holes from the MOSFET channel and thus shift the pedestal value. Alternatively they degrade the mobility of the charge carrier in the channel, leading to a reduction of the internal amplification of the DEPFET. On the other hand, bulk damage arises from crystal displacement of the bulk's silicon atoms. The displacement is caused by traversing particles that collide with the silicon atoms in the crystal lattice [132]. The collision leads to a silicon atom being displaced from its original crystal position. This displaced atom might further displace other atoms, giving rise to several crystal defects such as vacancies and interstitials. Those defects create energy states in the middle of the forbidden band gap of the depleted silicon, leading to an enhanced thermal creation of electron-hole pairs. The electrons drift to the internal gate, degrading the signal over noise ratio. In addition, the defects might also trap or de-trap charge carriers in the bulk. This results in a fluctuation of the voltage required

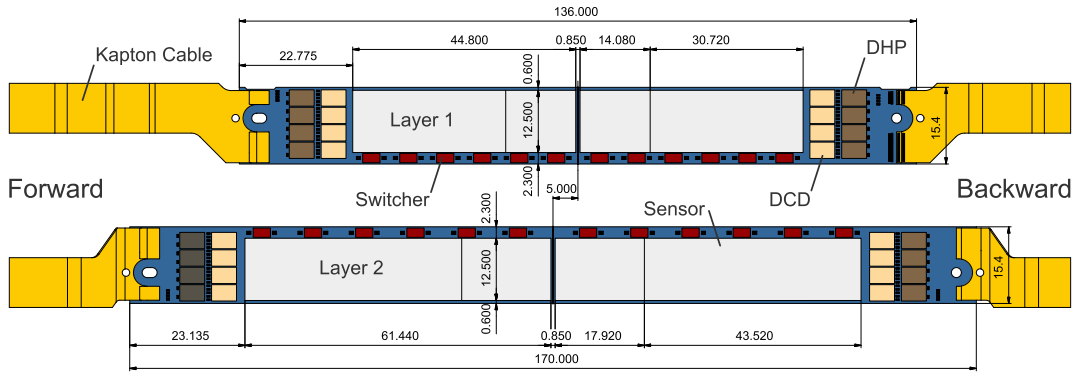


Figure 4.10: Mechanical layout of the PXD ladder for the inner and outer layer. The sizes of the chips are: DCD $3240 \mu\text{m} \times 4969 \mu\text{m}$, DHP $3280 \mu\text{m} \times 4200 \mu\text{m}$, Switcher $2030 \mu\text{m} \times 3600 \mu\text{m}$

to fully deplete the bulk [133]. Defects can also create a local change in the effective doping of the bulk, creating a local transition from the n-doped bulk to a p-doped region. The maximum radiation dose and neutron fluence the PXD is able to handle, before it suffers from the damage effects listed above, is 10 Mrad per snowmass year¹ and $10^{13} 1 \text{ MeV Neutron equivalent / cm}^2$ per snowmass year, respectively [80]. The expected values for the PXD are derived and explained in chapter 7.

4.3.7 Power consumption and Cooling

A DEPFET sensor only consumes power during the readout process. Thus, for a single sensor, the power consumption only depends on the number of readout columns N_{col} and the number of rows N_{read} that are read out simultaneously. Assuming an average pedestal current of $100 \mu\text{A}$ and the 4-fold readout, the total power consumption of a single sensor is

$$P_{sensor} = I \cdot V \cdot N_{col} \cdot N_{read} = 100 \mu\text{A} \cdot 5 \text{ V} \cdot 250 \cdot 4 = 0.5 \text{ W}$$

Each DCD or DHP chip dissipates about 1 W. The switcher chips are turned off most of the time, thus they only contribute about 1 W in average. The total power consumption of a single ladder is then 18 W and, for the whole PXD, 360 W. Since integrated circuits are very sensitive to temperature changes [134], the temperature of the DEPFET sensors and the chips has to be kept under control. For example, the noise in the DEPFET pixels depend on the sensor's temperature, especially if radiation damage is present. Thus, the temperature of the sensors should be kept stable around 30°C . For the chips, the temperature should be kept below 60°C to prevent electromigration [135]. In order to meet these goals, the PXD is actively cooled with

¹1 snowmass year = 10^7 s

CO_2 and N_2 . The PXD CO_2 cooling makes use of evaporative cooling [136] in order to achieve a high heat dissipation with a small CO_2 flux.

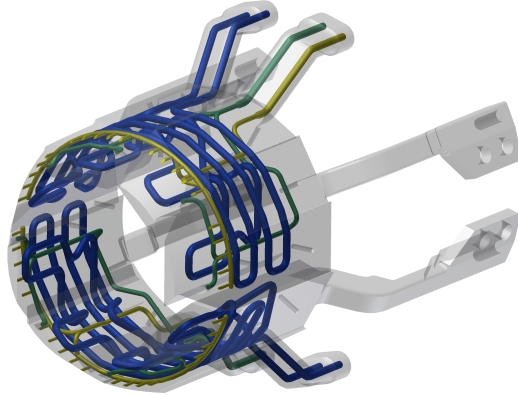


Figure 4.11: PXD support and cooling structure [122]. Fabricated with a 3D laser sintering technology. The blue channels contain the CO_2 , while the green and yellow channels blow nitrogen between the two PXD layers.

The PXD ladders are mounted on an integrated support and cooling structure made from stainless steel and are held by screws. The structure is cooled with CO_2 in order to dissipate the power that is produced by the ASICs on both ends of the ladders. Figure 4.11 illustrates the design of the support structure with the integrated cooling channels and capillaries. In addition to the CO_2 cooling, nitrogen is blown between the two PXD layers in order to generate a forced convection. The switchers of the inner layer are cooled by 1 mm thin carbon fibre tubes that connect to the cooling structure and span the whole ladder. Small 0.3 mm diameter holes in the tubes guide the cold gas to the switchers to prevent potential hot spots inside the small volume between the two layers. In order to electrically isolate the PXD ladders from the support, the support structure is covered with a 15 μm thick layer of Parylene [137]. The support structure itself is mounted on the beampipe, with the forward side being able to slide on the beampipe. This allows the structure to compensate for thermal expansion of the beampipe.

4.3.8 Naming convention

In order to address the constituents of the PXD unambiguously, the following naming convention has been introduced. It is based upon the PXD's geometric hierarchy, which is given as follows: the detector is subdivided into two **layers**; each layer consists of several **ladders**; each ladder hosts two **sensors**. The inner layer is given the ID 1 and the outer layer the ID 2. With an xy projection of the PXD in mind, the numbering of the ladders starts at the right side of the detector ($+x$). The innermost ladder intersecting the positive x axis is specified to carry the ID 1. The ladder ID is increased by one, following the ladders in mathematically positive (counter-clockwise) direction. Figure 4.12 shows the ladder numbering for the PXD.

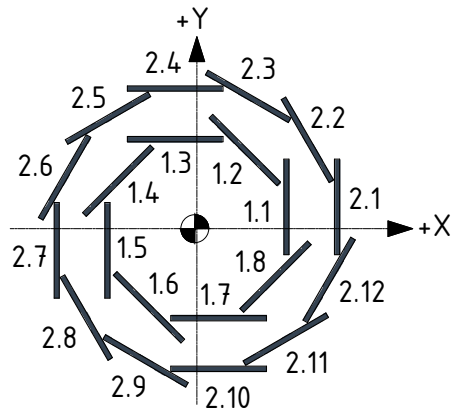


Figure 4.12: The ladder numbering for the *PXD*

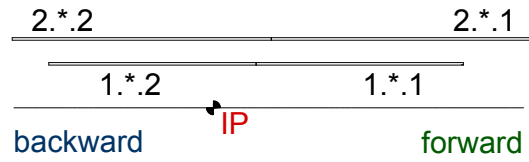


Figure 4.13: *The sensor numbering for the PXD*

Each ladder hosts two sensors, labelled in the following way: the first sensor starting from the forward part of a ladder (the part which is most positive in the z axis) is given the ID 1. The second sensor, located on the backward part of the ladder, is represented by ID 2. Figure 4.13 shows the sensor numbering for the PXD. Addressing a given sensor requires the three IDs for layer, ladder and sensor. The notation agreed upon is for the IDs to be listed in the order of layer, ladder and sensor using a point character (“. ”) as the delimiter. For example: “1.4.2” specifies the first layer, fourth ladder and second sensor. In this example this would be the backward sensor, which is located on the fourth ladder of the first (innermost) layer of the PXD. An asterisk can be used to address all layers, ladders or sensors. For example: “1.*.2” specifies all backward sensors of the first layer. To keep the notation short, trailing asterisks can be omitted: the notation “1.*.*” is equivalent to “1” and describes all ladders and sensors of the first layer. Figure 4.13 shows an example of the use of this notation.

4.4 The Silicon Vertex Detector

The Silicon Vertex Detector (SVD) surrounds the Pixel Vertex Detector and forms, together with the PXD, the **silicon tracking system** of Belle II. The silicon tracking system is complemented by the central drift chamber (see section 4.5) in order to provide an efficient full track reconstruction system. However, the silicon tracking system itself offers some unique features: It allows a stand-alone reconstruction of low- p_t tracks down to $\mathcal{O}(30 \text{ MeV})$. This capability increases, for example, the flavour tagging efficiency for B -mesons from daughters which originate from D^* decays, such as low momentum pions from $D^* \rightarrow D\pi$. In addition, the SVD is able to reconstruct the secondary vertices of long living particles that decay outside of the PXD, such as K_S mesons. Figure 4.14 shows an artistic rendering of the SVD detector, seen from the backward side.

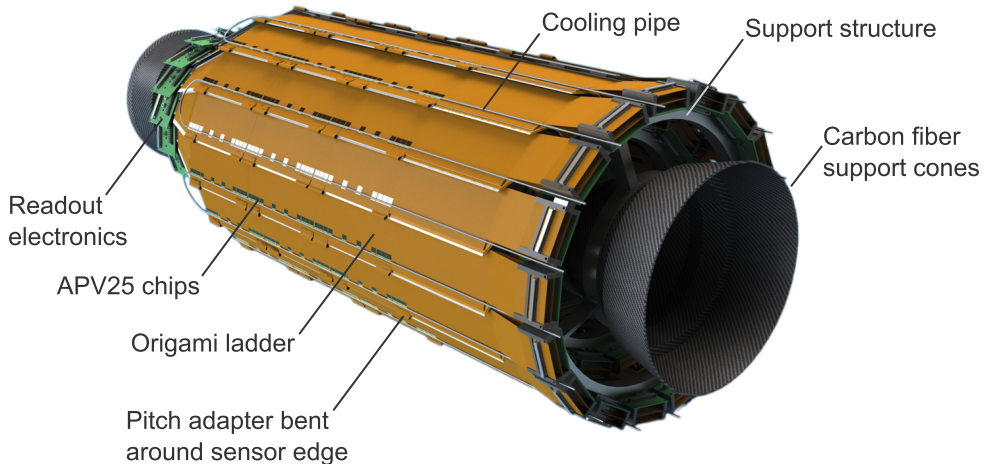


Figure 4.14: An artistic rendering of the SVD [138]. The picture shows the outermost layer of the SVD and the support structure.

4.4.1 Layout

The SVD consists of 4 layers of double-sided silicon strip detectors (**DSSD**) [139] and covers the full Belle II acceptance range of $17^\circ < \theta < 150^\circ$. Each layer consists of several ladders, arranged in a windmill-like structure, very similar to the PXD. However, due to the way the strips of the DSSDs are arranged (see 4.4.2), the orientation of the SVD's windmill structure is reversed with respect to the structure at the PXD. A listing of the layer radii and the number of ladders per layer is given in table 4.5.

The ladders are equipped with two different shapes of sensors. The innermost layer and the barrel part of the outer layers host **rectangular sensors**, while the sensors in the forward region of layer 4 to 6 are slanted (see figure 4.15) and host **trapezoidal sensors**. This decreases the

Layer	Radius [mm]	Number ladders	Windmill angle [°]	Overlap [%]
3	38	7	7.0	7.1
4	80	10	9.0	15.4
5	104	12	7.0	3.8
6	135	16	9.0	9.0

Table 4.5: Listing of the layer radii, number of ladders and the windmill angles for the SVD.

amount of material a forward-travelling particle has to cross. The average material budget per ladder is 0.57 % of radiation length.

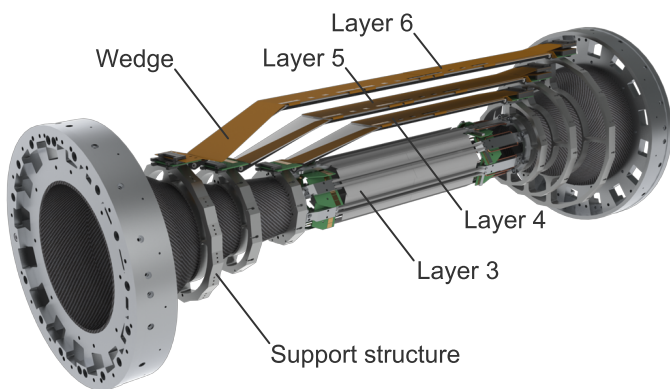


Figure 4.15: The mechanical design for the SVD layers [140]. The forward direction is on the left hand side of the picture. Following the naming convention (section 4.3.8), the innermost layer of the SVD is given the ID 3, as it follows layers 1 and 2 of the PXD.

The SVD is attached to the CDC structure, while the PXD is mounted on the beampipe. As a result, the PXD and SVD detectors move independently from each other. Therefore, the relative position of both detectors has to be determined frequently with an automated alignment procedure.

4.4.2 Sensors

A DSSD [139] is a semiconductor device that measures two coordinates of a traversing, charged particle at the same time. A depleted silicon bulk is sandwiched by a p-type and a n-type doped layer, which is segmented into strips. The strips are implanted into the bulk and oriented orthogonal to each other. A voltage is applied between the two strip layers in order to deplete the silicon. The sensors used for the Belle II SVD apply a voltage of ~ 120 V for the rectangular sensors and ~ 40 V for the trapezoidal sensors. Figure 4.16 illustrates the design and the measuring principle of a DSSD.

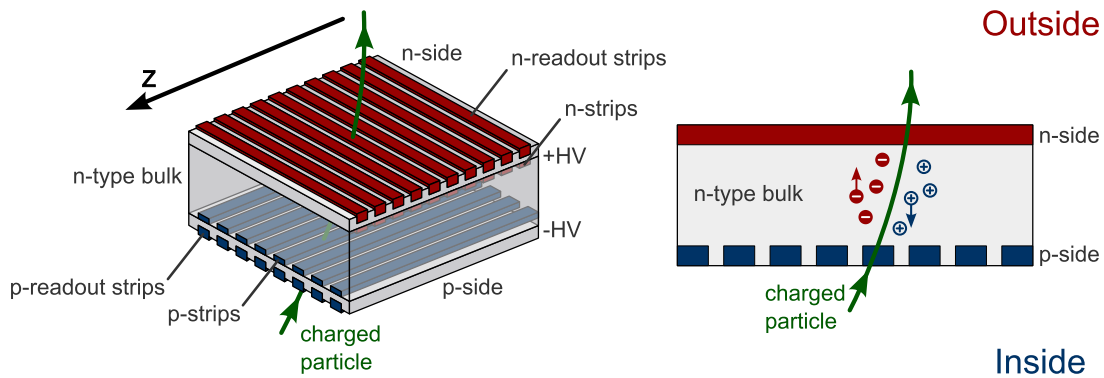


Figure 4.16: The measuring principle of a DSSD. A charged particle creates electron-hole pairs that drift to the appropriate strips: electrons to the strips on the n-side and holes to the strips on the p-side.

If a charged particle traverses the sensor, it creates electron-hole pairs in the bulk. Due to the applied voltage, the electrons drift to the n-type strips and the holes to the p-type strips. In order to avoid excess noise on the pre-amplifiers, the strips are capacitively coupled to metal strips and the signal is read from those. From the signals on the individual strips the position of the particle is deduced. A MIP generates about 24000 electron-hole pairs in 300 μm silicon and the average drift time is about 10 ns. However, if two or more particles traverse a DSSD within one readout period, a strip detector is not able to assign the hit positions unambiguously. In addition to the true hits, so-called **ghost hits** are created. This effect is illustrated in figure 4.17. As long as the number of hits is reasonable low, this is not a problem. But if the number of hits per readout period gets too large, a strip detector is not the optimal solution any more. This is the main reason why the two innermost layers of the Belle II silicon tracking system are equipped with pixel sensors.

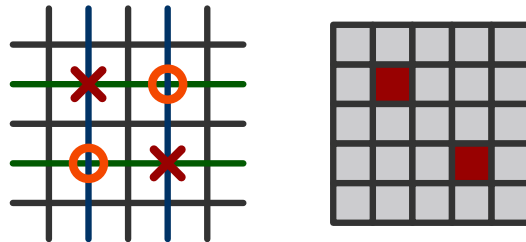


Figure 4.17: Left: True hits and ghost hits in a double sided strip detector in case of two particles traversing the detector. Right: Measured hits in a pixel detector in case of two particles traversing the detector.

The rectangular DSSD sensors used for the SVD at Belle II have the long strips on the p-side, parallel to the detector's z -axis. The short n-side strips along $r - \phi$ face towards the outside of the SVD, as it can be seen in figure 4.16. The slanted sensors are similar, with the long strips

pointing to the z -axis. Table 4.6 lists the types of sensors per ladder together with their strip pitches. It should be noted that the forward sensors have a variable strip pitch on the p-side, giving them a wedge-like shape. The strips on the n-side, though, are parallel with a constant strip pitch. They are arranged such that they are perpendicular to the central strip of the p-side.

Layer	Rectangular sensor			Wedge sensor		
	number per ladder	pitch [μm] n-side	pitch [μm] p-side	number per ladder	pitch [μm] n-side	pitch [μm] p-side
3	2	160	50	0		
4	2	240	75	1	240	75 to 50
5	3	240	75	1	240	75 to 50
6	4	240	75	1	240	75 to 50

Table 4.6: The pitch sizes for the rectangular and trapezoidal sensors.

There are two types of rectangular sensors. While layer 3 consists of smaller sensors, layer 4 to 6 are equipped with larger sensors. Both types have a thickness of 320 μm and 768 strips on the p-side. However, the smaller sensor has 768 strips and the larger sensor 512 strips on the n-side. The forward sensors are 300 μm thick and host 768 strips on the p-side and 512 strips on the n-side.

4.4.3 Readout

The DSSDs are read out with the APV25 chip [141], a radiation hard readout chip providing features such as low-noise amplification and fast waveform shaping. The chip was developed for the CMS silicon tracker. This results in a sensitive time window for the SVD of ~ 20 ns. In order to keep the noise level low, the APV25 chips are placed on top of the sensor. In the scheme developed for the SVD, called the **Origami scheme**, the APV25 are placed on a flexible circuit, mounted on the n-side of the sensor. The p-side strips are connected by a double layer flex cable which is wrapped around the sensor and connected to APV25 chips which are located on the same side as the chips for the n-side, hence the name of the scheme. The APV25 chips are cooled by CO_2 , supplied by the same system as the PXD.

4.5 The Central Drift Chamber

The central drift chamber (CDC) is a cylindrical wire chamber [113] that covers the full Belle II detector acceptance of $17^\circ < \theta < 150^\circ$. Its main tasks are the reconstruction and measurement of the momenta of charged tracks, the identification of particle types by measuring their energy loss (dE/dx) [142] and the supply of a trigger signal for charged particle tracks. The CDC is equipped with 14336, 30 μm thick, gold plated tungsten **sense wires**, surrounded by a **drift gas**. Each sense wire is surrounded by 8 aluminium **field wires**, forming a **drift cell**. If a charged particle travels through the gas volume, it ionizes the gas by kicking out electrons from the gas atoms. These free electrons drift to the sense wires, ionizing more gas atoms on their way. The electrons are then collected by the sense wires and the generated pulse is read by the electronics. The sense wires are arranged in 56 layers with a radial **cell size** of 10 mm for the innermost 8 layers and a cell size of ~ 18.2 mm for the outer layers. The smaller cell size for the inner layers allows them to keep their occupancy low, even under the harsh background conditions at Belle II. The layers of sense wires are grouped into so-called **superlayers**. The 8 innermost layers form an **axial superlayer (A)**. An axial superlayer consists of sense wires that run parallel to the Belle II solenoid and thus provide transverse momentum (p_t) information. The next 6 layers are tilted by ~ 45 mrad with respect to the solenoid axis, providing p_t and, in addition, information on the helix pitch (z). Depending on the sign of the tilt angle, this type of superlayer is either called an **U** or a **V stereo superlayer**. In total, the CDC consists of 9 superlayers, forming the superlayer configuration AUVAUAVA, as can be seen in figure 4.18. A summary for all superlayers is given in table 4.7.

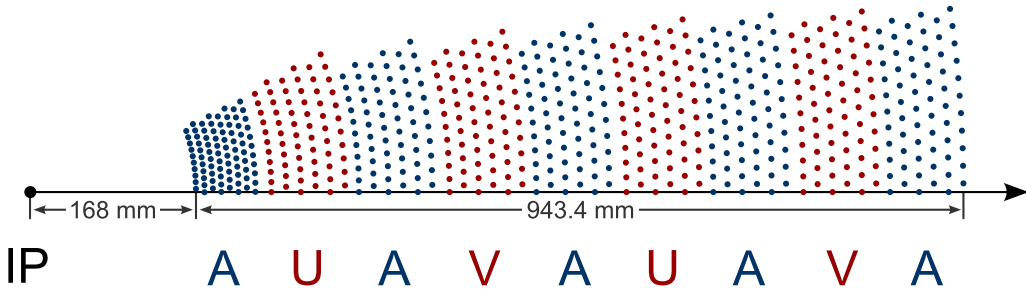


Figure 4.18: The sense wire configuration of the CDC. Axial superlayers are drawn in blue, stereo superlayers in red.

Since the majority of particles crossing the CDC have momenta lower than 1 GeV, multiple scattering is an important concern. Thus a low-Z gas mixture has been chosen. The mixture employed for the CDC is made from 50 % He and 50 % C_2H_6 . This mixture has a long radiation length of 640 m and the drift velocity saturates at 4 cm/ μs [143]. The energy a particle loses while travelling through the gas can be used to determine the type of the particle: since the

electric pulse measured at a sense wire is proportional to the energy a particle deposited in the gas, a dE/dx measurement can be performed. By applying the Bethe-Bloch formula [144, 145], which mainly depends on β , particles with equal momentum but different masses can be distinguished within a certain $\beta\gamma$ range.

Type	Layers	Drift cells per layer	Radius [mm]	Stereo angle [mrad]
1 Axial	8	160	168.0 to 238.0	0.0
2 Stereo U	6	160	257.0 to 348.0	45.4 to 45.8
3 Axial	6	192	365.2 to 455.7	0.0
4 Stereo V	6	224	476.9 to 566.9	-55.3 to -64.3
5 Axial	6	256	584.1 to 674.1	0.0
6 Stereo U	6	288	695.3 to 785.3	63.1 to 70.0
7 Axial	6	320	802.5 to 892.5	0.0
8 Stereo V	6	352	913.7 to 1003.7	-68.5 to -74.0
9 Axial	6	384	1020.9 to 1111.4	0.0

Table 4.7: The numerical values for the CDC wire configuration. The innermost superlayer has two additional layers with active guard wires.

4.6 The Time of Propagation Counter

The Time of Propagation Counter (TOP) [146] is part of the particle identification system in the barrel region of Belle II. In particular, it helps with the separation of K^\pm from π^\pm . The TOP covers the polar angle range of $32.5^\circ < \theta < 123^\circ$ and consists of 16 rectangular-shaped modules. The modules are radially arranged at a distance of 119 cm from the IP, thus surrounding the outer wall of the CDC. Each module consists of a 2.5 m long and 2 cm thick **quartz radiator**, as shown in figure 4.19.

The operation mode of the TOP detector is based on the Cherenkov principle. If the velocity of a charged particle travelling through the quartz radiator is faster than the speed of light in the quartz medium, the particle will emit **Cherenkov light** [147]. The light is emitted within a cone, the **Cherenkov cone**. The opening angle θ_C of the Cherenkov cone depends on the velocity of the particle and the material's refraction index

$$\cos \theta_C = \frac{1}{\beta n(\lambda)} \quad (4.1)$$

where β is the particle's velocity and $n(\lambda)$ the index of refraction of the quartz radiator for a given wavelength λ . A typical refraction index value for the synthetic fused silica quartz material used for the TOP is $n(\lambda = 390 \text{ nm}) = 1.47$. The emitted Cherenkov photons are confined

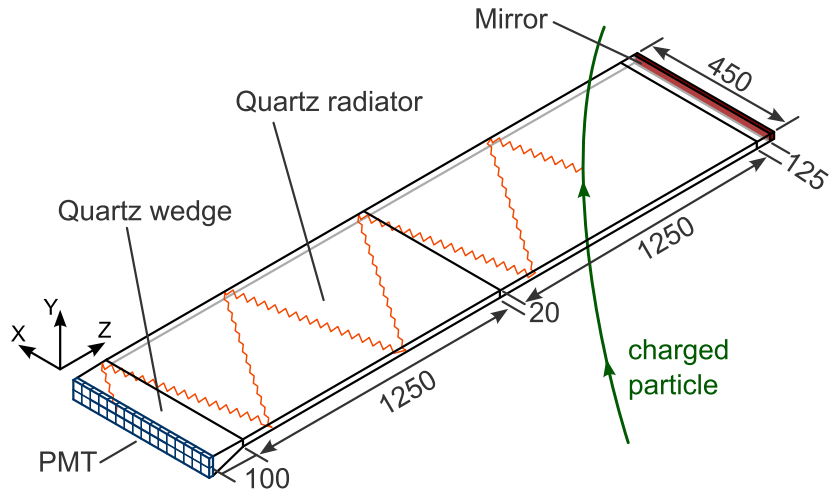


Figure 4.19: A single TOP module [80]. The module is made from two synthetic fused silica blocks which are glued together (0.5 mm glue thickness). The radius of the spherical mirror is 700 cm. All values in the drawing are given in [mm].

within the radiator by total internal reflection and are repeatedly reflected off the walls until they reach the **photo sensors** located at the end of the module (PMT in figure 4.19). The photo sensors are an array of 2×16 square shaped micro channel plate (MCP) photomultiplier tubes (PMT), developed in collaboration with Hamamatsu [148]. In order to achieve a better spatial distribution of the electrons and to allow for two rows of photo sensors, a **quartz wedge** is placed in front of the PMTs. Each PMT consists of 4×4 pixels. A photocathode in each pixel converts incident photons into electrons, which are then accelerated by an electric field. This field is generated by 2 MCP plates in the PMT, where the second plate is covered by an aluminium layer to prevent ion feedback. The accelerated electrons are guided by the field through $10 \mu\text{m}$ holes in each plate. Inside the hole, the electrons knock off additional electrons from the walls, thus amplifying the signal.

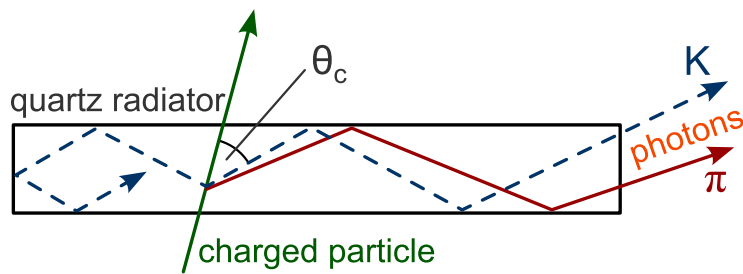


Figure 4.20: The K^\pm/π^\pm separation principle of the TOP [80].

The separation of π^\pm from K^\pm makes use of the fact that, according to equation 4.1 and the π^\pm/K^\pm mass difference, a π^\pm creates a wider Cherenkov cone than a K^\pm carrying the same momentum (see figure 4.20). This leads to a smaller number of reflections and, in turn, a shorter flight

path for the Cherenkov photons created by pions compared to those coming from kaons. By measuring the time it takes the Cherenkov photons to travel from the charged particle's incident location to the photo sensors and their spatial location on the photo sensors, a separation of π^\pm from K^\pm is achieved. The travel time is also called the **Time of Propagation**. A typical value for the Cherenkov photon path is 5 m and a typical number of internal reflections is 100. The measurement requires a precise determination of the incident angle and the impact position of the charged particle, which is delivered by the tracking detectors. Additionally, the arrival time of the Cherenkov photons at the photo sensors is measured relative to the event start time (time of e^+e^- collision), allowing for a further separation of the photons in time. The speed of propagation of the Cherenkov light inside the quartz radiator depends on the wavelength of the light (**chromatic dispersion**), limiting the time resolution that can be achieved. A significant improvement is made by introducing a concave mirror [149] at the end of the quartz radiator and reading both dimensions from the photo sensor array. The mirror focuses parallel rays of photons into a single channel of the photon sensor, leading to the detection of chromatically dispersed rays by separate channels instead of a single channel. From the y -coordinate of the photon's arrival position, the λ dependence can be estimated and corrected for. The expected performance is then a $\sim 4\sigma$ separation for 4 GeV π^\pm from K^\pm and a time resolution of ~ 40 ps.

4.7 The Aerogel Rich Detector

The particle identification system in the barrel region of the Belle II detector is complemented by the forward endcap system **ARICH**, a proximity-focusing Aerogel Ring-Imaging Cherenkov detector [150]. The ARICH covers the polar angle range of $14.78^\circ < \theta < 33.71^\circ$ and is located 1670 mm from the IP at the forward side of Belle II. Although the design of the ARICH is different from the one employed for the TOP detector, it uses the same Cherenkov principle in order to efficiently separate π^\pm from K^\pm up to 4 GeV. Additionally, the ARICH detector is able to discriminate between pions, muons and electrons below 1 GeV. The radiator material for the production of Cherenkov photons is **aerogel** [151]², a synthetic, jelly-like material. For the ARICH a highly transparent silica aerogel is used. When charged particles with a velocity exceeding the speed of light in aerogel travel through the aerogel radiator, they emit Cherenkov light. The emission angle θ_C depends on the refraction index of the aerogel material and on the particle's velocity as it can be seen from equation 4.1. In the thin radiator employed for the ARICH, the Cherenkov light is emitted as a cone. The Cherenkov cone then forms a ring image when it is projected onto the photon detector plane. Figure 4.21 illustrates this principle.

The ARICH particle identification system makes use of the ring's radius dependence on the particle type. Different particle types carrying the same momentum have different velocities and thus emit photons under different Cherenkov angles. This leads to rings with different

²More information can be found at: www.aerogel.org

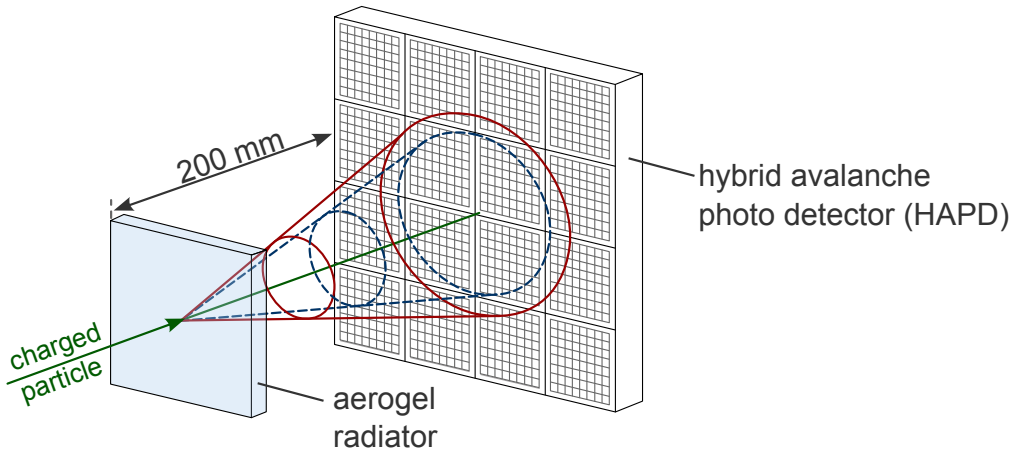


Figure 4.21: The π^\pm/K^\pm separation principle of the ARICH detector [152]. The red solid line represents a pion, the blue dashed line a kaon.

radii, as it is illustrated in figure 4.21. The typical Cherenkov angle difference between pions and kaons, achieved with the ARICH detector, is $\theta_\pi - \theta_K = 30$ mrad for 3.5 GeV particles. An efficient and reliable π^\pm/K^\pm separation requires an excellent resolution of the Cherenkov angle for each track. It is given as [153]

$$\sigma_{ring} = \frac{\sigma_C}{\sqrt{N_{photons}}} \quad (4.2)$$

where σ_C is the resolution of the Cherenkov angle for a single photon and $N_{photons}$ the number of photons seen in the photon detectors. In the **proximity focusing** ARICH detector, the radius of the ring depends on the Cherenkov emission angle and the distance between the point at which the Cherenkov light was emitted and the photon detector surface. This is a major disadvantage compared to a normal focusing scheme at which a spherical mirror focuses the photons, such that the radius of the ring is independent of the emission point. However, the proximity focusing scheme has the advantage that it can be realized as a very compact detector. Due to the tight space constraints found at Belle II, this scheme is adapted for the ARICH detector. According to equation 4.2, the Cherenkov angle resolution can be improved by increasing the number of detected photons ($N_{photons}$). This can be achieved by using a thicker aerogel radiator. However, a thicker radiator degrades the resolution of the single photon angle σ_C due to the increased uncertainty of the emission point. This problem is solved by splitting a thick radiator into two layers with different refraction indices [154]. For the Belle II ARICH each layer has a thickness of 20 mm and the refraction indices are $n_1 = 1.047$ for the first layer and $n_2 = 1.057$ for the second layer. By choosing $n_1 < n_2$, the Cherenkov cones, emerging from the same relative position with respect to each layer's boundary, are overlapping. This is shown in figure 4.22.

The detection of the Cherenkov photons is accomplished with an array of hybrid avalanche

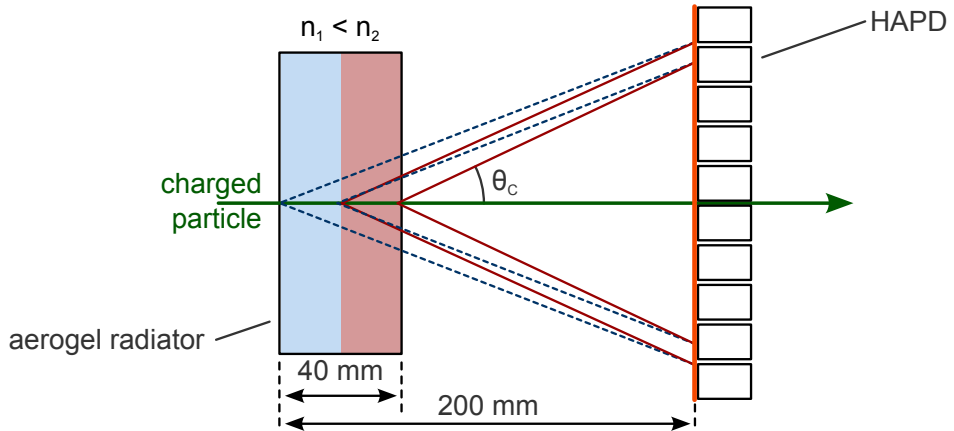


Figure 4.22: The resolution is improved by splitting the aerogel radiator [80]. The dashed, blue line represents a Cherenkov cone starting in the first layer. The solid, red line second a cone starting in the second layer.

photo detectors (**HAPD**) [155], developed in cooperation with Hamamatsu. A single HAPD is a $72 \text{ mm} \times 72 \text{ mm}$ vacuum tube that encloses a bi-alkali photocathode and an array of 12×12 solid state avalanche photo diodes. Each HAPD achieves a total gain of $\sim 10^4$ to 10^5 . The full ARICH detector consists of 420 HAPDs and 124 wedge-shaped aerogel radiator tiles, arranged in a 235 mm thick ring with an inner radius of 441 mm and an outer radius of 1115 mm. Each aerogel radiator tile has a length of ~ 175 mm. The expected performance of the ARICH detector is $\sim 4\sigma$ for the π^\pm/K^\pm separation for the momentum range $0.7 \text{ GeV} < p < 4.5 \text{ GeV}$.

4.8 The Electromagnetic calorimeter

The electromagnetic calorimeter (**ECL**) [156] surrounds the TOP and the ARICH detectors. It consists of 8736 CsI(Tl) crystals, where each crystal has a size of about $6 \text{ cm} \times 6 \text{ cm}$ and a depth of 30 cm corresponding to $16.1 X_0$. All crystals are oriented such that they point towards a narrow region around the IP as illustrated in figure 4.23. The ECL is subdivided into a forward, a barrel and a backward region. The 1152 crystals of the forward region are located at $z \approx 1.96 \text{ m}$ and cover the polar angle range of $12.4^\circ < \theta < 31.4^\circ$. The barrel region is 3 m long with an inner radius of 1.25 m and is made from 6624 crystals. Its polar angle range defines the barrel region of the Belle II detector and is $32.2^\circ < \theta < 128.7^\circ$. In the backward direction, 960 crystals, located at $z \approx -1.02 \text{ m}$, cover the polar angle $130.7^\circ < \theta < 155.1^\circ$. In summary, the ECL covers the full Belle II acceptance, apart from the 1° gaps between the barrel and the forward/backward regions.

The main purpose of the ECL is the detection and measurement of the energy and angular coordinates of photons. Photons at Belle II either originate from e^+e^- annihilation directly or

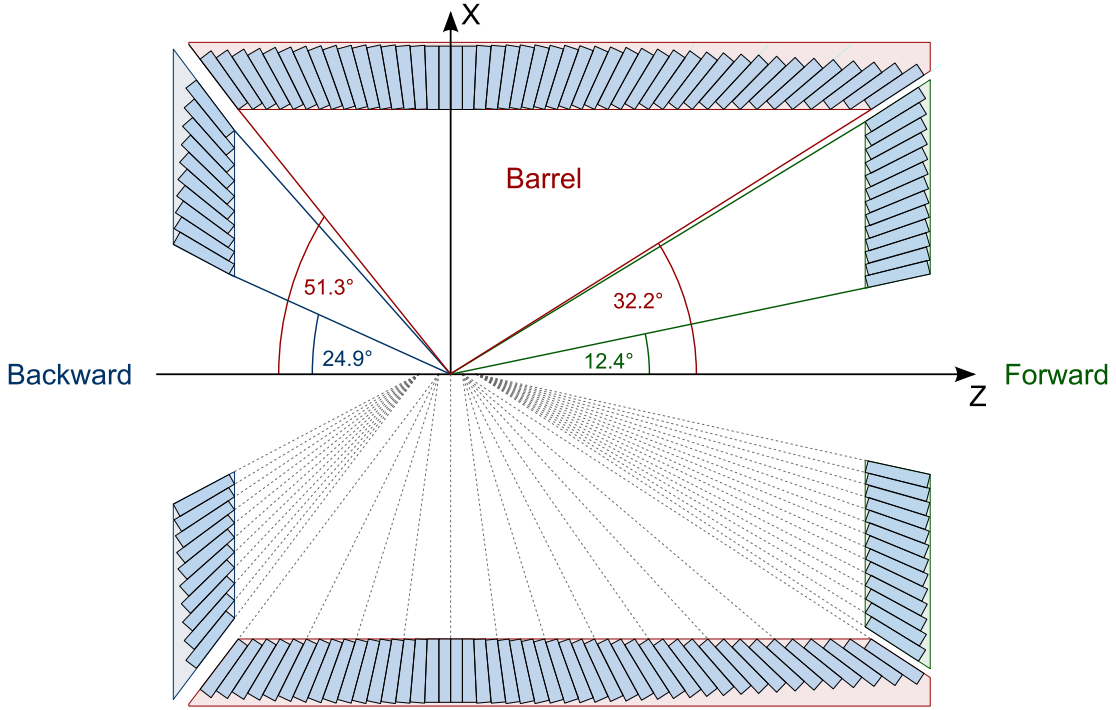


Figure 4.23: Schematic drawing of the CDC. Shown are the Forward, Barrel and Backward regions, together with their angles.

are the end product of decay chains. Thus, they cover a wide energy range from about 20 MeV up to 4 GeV. The ECL is built to work efficiently in this range. Additionally, it also provides an electron identification through the comparison of the deposited energy in the crystal and the momentum of the particle that hit the crystal. If a photon hits a crystal, it interacts with the material and converts into an electron-positron pair. High energetic electrons/positrons lose energy by emitting photons through the bremsstrahlung process. Those photons can then, in turn, interact with matter and convert into electron-positron pairs, giving rise to a particle shower. Low energetic electrons/positrons though dissipate their energy by ionization and excitation rather than by the generation of photons. The energy loss through ionization then produces scintillation light in the CsI(Tl) material, which is collected on each crystal's end by a pair of 10 mm \times 20 mm Hamamatsu S2744-08 photodiodes. The intrinsic energy resolution that is achieved by the ECL is [157]

$$\frac{\sigma_e}{E} = \sqrt{\left(\frac{0.066\%}{E}\right)^2 + \left(\frac{0.81\%}{\sqrt[4]{E}}\right)^2 + (1.34\%)^2} \quad (4.3)$$

where E is the energy in GeV. Showers that cannot be matched to a track in the tracking detectors are classified as a neutral shower. By measuring the lateral extent of the shower, it is possible

to identify showers that were caused by photons. In particular, the lateral extent of hadronic showers caused by neutrons for example is broader than those of electromagnetic showers. The ECL can therefore be used to assist the particle identification.

4.9 The Solenoid

The Belle II detector is surrounded by a superconducting solenoid in a cylindrical volume measuring 3.4 m in diameter and 4.4 m in length. It provides a constant magnetic field of 1.5 T which is parallel to the main detector axis. This magnetic field forces charged particles on a curved trajectory from which the particle's momentum is reconstructed within the tracking sub-detectors [113].

4.10 The KLM

The CDC, TOP, ARICH and ECL help to differentiate between different types of charged particles, such as π^\pm , K^\pm or e^\pm . However, these sub-detectors are not sensitive enough to provide an efficient particle identification for neutral K_L or muons: apart from the ECL, their interaction length is too small for K_L particles to interact with them and muons penetrate through the inner sub-detectors without leaving signal that could efficiently be used for particle identification. For this reason, the Belle II detector is equipped with the **KLM**, a detector specifically designed to identify K_L and muons with a momentum above ~ 0.6 GeV. The KLM can be divided into three regions: the **barrel**, the **forward endcap** and the **backward endcap**. The octagonal barrel covers the polar angle range of $45^\circ < \theta < 125^\circ$, while the forward endcap extends the range down to 20° and the backward endcap up to 155° . Each region consists of a sandwich of alternating layers of 4.7 cm thick **iron plates** and **active detector elements**. The iron plates are also used to return the magnetic flux of the Belle II solenoid. The iron plates provide an interaction length of $3.9 \lambda_I$, allowing the K_L to shower hadronically. It should be noted that the ECL provides an additional $0.8 \lambda_I$, thus contributing to the hadronic shower development. The charged particles that are generated in the hadronic showers are seen as hits in the active detector layers of the KLM.

The muon identification [158] makes use of the tracking data of the PXD, SVD and CDC. Each charged track is extrapolated from the tracking detectors to the last layer that the track reaches in the KLM. During the extrapolation through the KLM, a hit from each active layer in the KLM is associated to the track. The muon particle identification is then given by a likelihood ratio for a particle being a muon rather than a charged hadron. Two variables enter this likelihood ratio: the difference between the predicted and the measured last layer the particle hit and the goodness of a Kalman fit of the track to the hits under a muon hypothesis. This results in a

muon detection efficiency of about 89 % for muons above 1 GeV. For the K_L identification, hits that are within an opening angle of 5° measured from the IP are grouped into clusters. Performing a track extrapolation from the tracking detectors, the clusters created by charged tracks are identified and excluded as K_L cluster candidates. After a cluster size cut, the remaining, isolated clusters are considered to be K_L clusters and their direction is determined by drawing a line between each cluster's centroid and the IP. The large fluctuations in the hadronic shower development (size, depth etc.) do not allow a useful measurement of the K_L energy from the cluster hits, hence only the direction of the K_L is measured. The K_L detection efficiency reaches a plateau of 80 % at 3 GeV.

4.10.1 Barrel KLM

The barrel has an inner radius of 2.019 m and a length of 4.44 m. It consists of 15 active layers sandwiched by 14 iron plates. The 13 outer layers are equipped with glass resistive plate chambers (**RPC**)[159]. The two innermost layers use **strip scintillator detectors** instead of RPCs. The reason is the high neutron background that would produce an estimated charge deposit rate of 10 Hz/cm² if those layers were to be equipped with RPCs. On the other hand, resistive plate chambers have the advantage of being much cheaper than scintillators and they require only simple read-out electronics. An RPC[159] is constructed by two parallel plate electrodes of high bulk resistivity ($\sim 5 \cdot 10^{12} \Omega \text{ cm}$) and a gas volume between them. For the KLM RPCs, 2.4 mm thick glass (73 % silicon dioxide, 14 % sodium oxide, 9 % calcium oxide and 4 % other compounds) is used for the electrodes, which is covered with a thin layer of carbon-doped paint to distribute the high voltage. The gas layer is 2 mm thick and contains a gas mixture of 62 % HFC-134a, 30 % argon and 8 % butane-silver (70 % n-butane and 30 % isobutane). If a charged particle travels through the RPC, it creates a trail of electron-ion pairs in the gas volume by ionization (mainly of the argon). The constant and uniform electric field that is generated by the electrodes (4.3 kV/mm) accelerates the charge carriers. The accelerated particles in turn ionize the gas, which leads to an avalanche of charge carriers, causing a discharge on the electrodes. Using highly resistive materials (such as glass) as electrodes limits the discharge to an area around the primary avalanche. Because the high voltage drops only locally, the remaining RPC area is still sensitive to the passage of other charged particles. In addition, the voltage drop quenches the avalanche. During the avalanche process, photons are generated by recombination, which contribute to the spread of free charge carriers. By using isobutane as an organic gas with high ultra violet absorption capability, the charge diffusion is prevented. This allows to keep the actual area of the detector that suffers from the voltage drop localized around the primary ionization region.

The electric pulses generated by the charge displacement in the gas layer are picked up on 5 cm wide metallic strips. This coupling is possible because the high resistivity of the carbon-doped paint renders it transparent to the electric pulses. Two RPCs, a layer of 48 strips to measure z

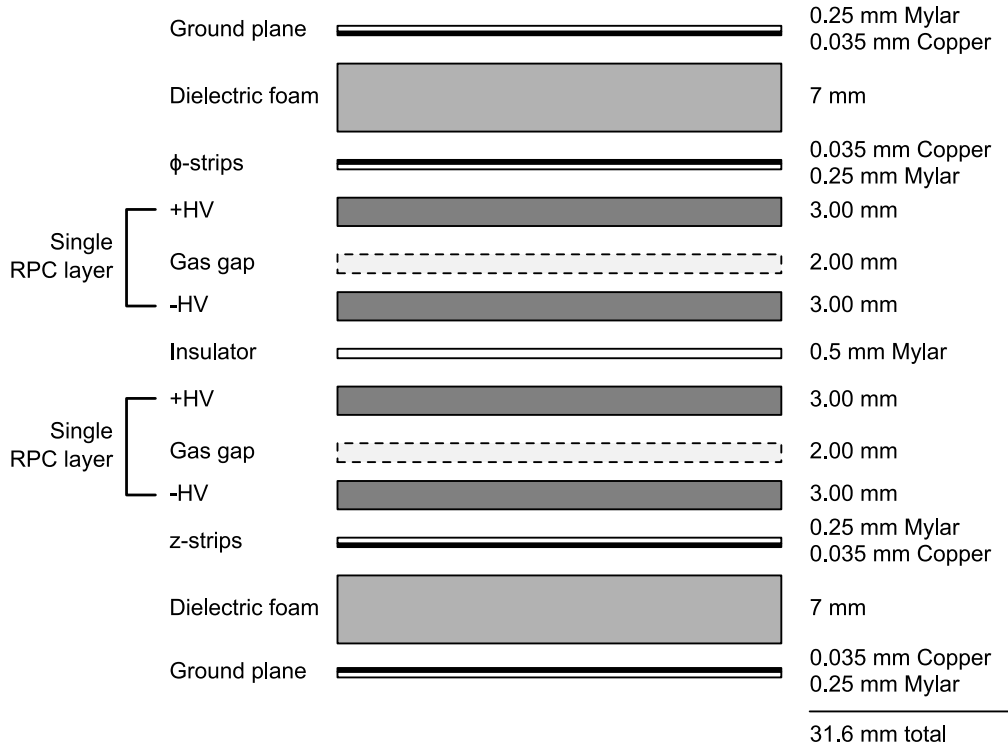


Figure 4.24: The constituents of a RPC superlayer of the BKLM [80].

and an orthogonal layer of 36 (48) strips in the first 5 layers (last 10 layers) to measure ϕ are combined into a **superlayer**, as illustrated in figure 4.24. The spatial resolution achieved for a superlayer is about 1.1 cm.

The two innermost superlayers are equipped with strip scintillators instead of RPCs. Each superlayer is built from two orthogonal planes of 40 mm wide and 10.6 mm high polystyrene scintillators. The inner scintillator superlayer consists of 54 z-strips and 38 ϕ -strips and the outer of 54 z-strips and 42 ϕ -strips. If a charged particle crosses the KLM scintillator, it emits blue scintillation light which is then transported to a SiPM (Hamamatsu MPPC S10362) photon detector. A wavelength-shifting fibre is embedded into each scintillator strip and takes care of collecting and transporting the light to the SiPM. Figure 4.25 shows the design of a single scintillator strip.

Another advantage of the scintillator superlayers over the RPC design, apart from their better performance under the high Belle II background, is that the scintillator z-strips and ϕ -strips are independent. This reduces the combinatorial background.

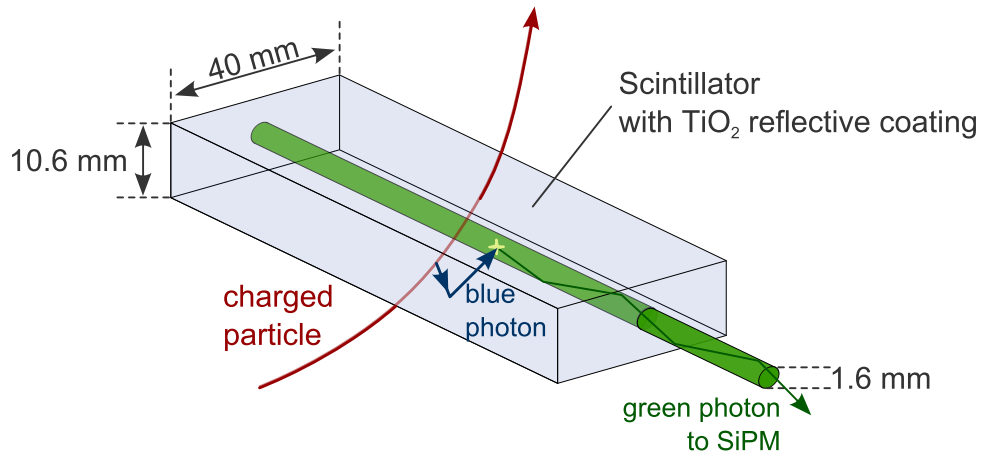


Figure 4.25: The operation mode of the BKLM scintillator. The polystyrene is covered with TiO_2 reflective coating and delivers blue light to an embedded WLS fibre (Kuraray Y11 MC, 1.2 mm diameter).

4.10.2 Endcap KLM

As for the innermost layers in the barrel region, the endcaps are subject to a high background flux, in particular from neutrons. This means that the long dead time of the RPCs during the recovery of the electric field after a discharge would render RPCs in the endcaps very inefficient. Therefore the endcaps are equipped with the same type of scintillator detectors as the innermost barrel layers. Each endcap consists of a sandwich of 14 scintillator superlayers and 14 iron plates composed into modules. A single scintillator superlayer contains 75 z-strips and 75 ϕ -strips.

4.11 Trigger

The Belle II trigger is responsible for starting the data readout of the whole detector for interesting events. The trigger bases its decision to start the readout on information that it receives from the sub-detectors. The trigger scheme is arranged in an hierarchical order where various sub-trigger systems send the trigger information from their specific sub-detector to a central trigger logic, the Global Decision Logic (**GDL**). The GDL is responsible for making the final decision of whether the event should be recorded. After a beam collision took place, the GDL makes a decision within 4.5 μ s, the fixed latency time of the GDL. The decision then starts the readout as described in the following section 4.12. Since the GDL is the first system to make this decision and is dead time free, it is also called a **Level 1 trigger**. Each sub-trigger logic is realized in an FPGA (Field-Programmable Gate Array) in order to maintain the speed of a hardware implementation while still being able to change the logic configuration at any time. The following sub-triggers are available:

- **CDC**

The CDC trigger performs a 2D track finding based on a conformal and a Hough transformation. It sends information from reconstructed tracks, such as a first estimate of the momentum, position, charge and track multiplicity to the GDL. In addition, a full 3D and a neural network based trigger are being developed which estimate the z -position of the primary vertex in order to reject background events that do not originate from the interaction point.

- **ECL**

The ECL measures the deposited energy of particles from their showers. The GDL is fed with information about clusters that exceed a certain energy threshold and with the number of isolated clusters. The information from the ECL is particularly used for identifying Bhabha and vetoing cosmic events.

- **TOP**

The TOP delivers precise timing and hit topology information to the GDL.

- **ARICH**

Like the TOP, the ARICH sends precise timing information to the GDL.

- **KLM**

The KLM is responsible for providing muon track information to the GDL.

The GDL makes the decision according to pre-defined selection configurations, which represent certain event signatures. Those configurations consist of different sub-trigger combinations. Table 4.8 gives a summary of the trigger configurations available at Belle II [160], together with their trigger rates.

Trigger	Process ($e^+ e^- \rightarrow$)	Cross-section [nb]	Rate [Hz] (at full lumi)
Physics	$\Upsilon(4S) \rightarrow B\bar{B}$	1.1	880
	Hadrons from continuum	3.4	2720
	$\tau^+ \tau^-$	0.9	720
Calibration	Bhabha	44	352
	$\gamma\gamma$	2.4	19
	$\mu^+ \mu^-$	1.1	880
	Random		

Table 4.8: The Belle II trigger channels [160]. The rates of Bhabha and $\gamma\gamma$ are pre-scaled by factor 100. The maximum average trigger rate for Belle II is 30 kHz.

The random trigger listed in table 4.8 starts the recording of data independently from the event signature. This is mainly used for recording background data. In particular, there are three types of random triggers: a periodical random trigger that is synchronized to the SuperKEKB bunch crossing signal, a pseudo-random trigger using an independent local clock and a delayed Bhabha trigger with a delay of $\sim 50 \mu\text{s}$ fired at the passage of a specific bunch.

4.12 Data Acquisition

As soon as the Level 1 trigger sends the signal for reading out the Belle detector signals, the data acquisition system (**DAQ**) takes over. Its main purpose is to read the data from the various sub-detectors, process and write it to the storage system. A schematic overview is shown in figure 4.26. Apart from the PXD, all sub-detectors are read out through a unified data link system, the **Belle2Link** [80]. An important part of the Belle2Link is the **COPPER** board, an electronic board that already existed at Belle and transforms the data format of each individual sub-detector into a common data format. The output of each COPPER board is sent to the **Event Builder**, which merges the data that belongs to the same collision into an **event**. Having the data from all detectors except the PXD collected and transformed into a common format, the full reconstruction of each event is performed. This is accomplished with the help of the High Level Trigger (**HLT**), a computing farm running **baf2** [161], the same reconstruction software as is used for physics analyses (see chapter 5). Based on the information from fully reconstructed events, the HLT is then able to make the final decision as to whether the event is kept or discarded. If the event is kept, the associated PXD data is merged with the existing data in a second Event Builder.

Due to the high data rate of 20.6 GB/s for the PXD, which is about 10 times the combined data rate of all the other sub-detectors, the PXD readout is treated separately from the other detectors. Additionally, a data reduction scheme is put in place in order to be able to handle this very

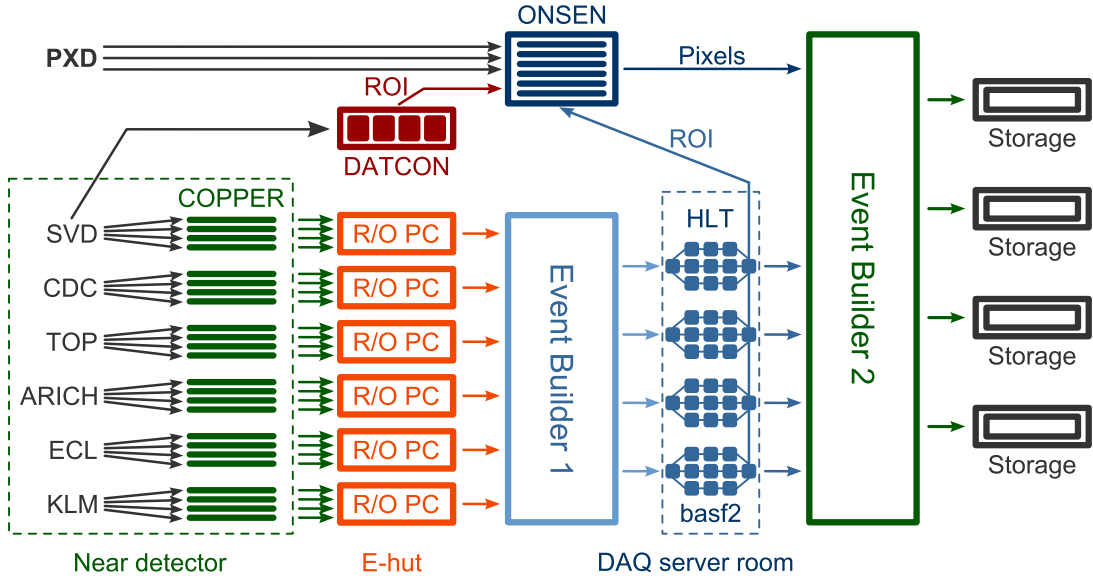


Figure 4.26: Schematic overview of the Belle II DAQ. About 300 COPPER boards take the data and transfer it to ~ 30 R/O PCs. The data is then merged in the Event Builder and the events are reconstructed in the HLT, which consists of $\mathcal{O}(10)$ units with ~ 400 cores per unit. The reconstructed data is merged with the PXD data and stored in ~ 10 storage units.

large data rate by stripping out all unnecessary PXD data originating from internal noise and machine/detector background. As soon as the PXD receives a trigger signal, its readout procedure, as discussed in section 4.3.3, is started. The data is read into the Online Selector Nodes (**ONSEN**), located in an ATCA crate [162]. The ONSEN stores the PXD data for up to 5 s, the maximum latency of the HLT. The HLT, in the meantime, performs the reconstruction of the events. The charged tracks that were reconstructed in the HLT with the information from the SVD and CDC are then propagated back to the PXD sensors, defining regions of interest (**ROI**). Figure 4.27 illustrates this principle.

Only the pixels of the PXD that are contained within a ROI are kept and sent to the second Event Builder. In addition to the HLT, another system, the Data Concentrator (**DATCON**), searches for ROIs. As can be seen in figure 4.26, the DATCON receives a copy of the SVD data. Using this data, the DATCON performs track finding on an FPGA, propagates the tracks back to the PXD sensors and defines a second set of ROIs. Both systems work complementary. The DATCON is optimised for low momentum tracks, while the HLT catches all high momentum particles. Both systems together with the ONSEN achieve a reduction of the PXD data rate by a factor 10. In order for both systems to work, a charged particle has to pass at least all layers of the SVD. But particles, such as slow pions from $D^{*+} \rightarrow D^0\pi^+$ decays, might not meet this criteria and would be lost. For those particles the ONSEN is equipped with a so-called hit recovery scheme, which makes use of the fact that low momentum particles have a large dE/dx due to the Bethe-Bloch formula [144] and requires only data from the PXD itself. By means of this

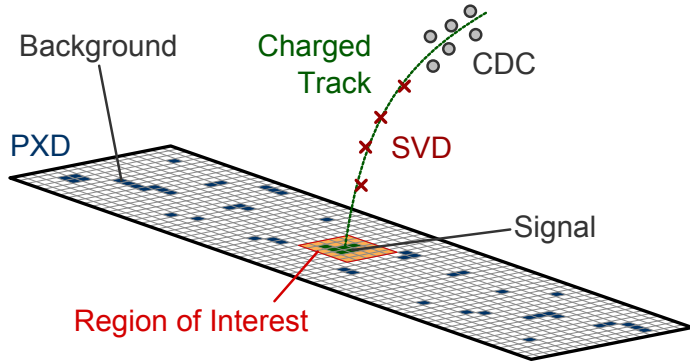


Figure 4.27: A charged track that has been identified and fitted with SVD and CDC information, is propagated back to the PXD. All pixels within an area (ROI) around the intersection point between the propagated track and a PXD sensor are kept. The size of the area depends mainly on the uncertainty of the track fit.

scheme, the hits and, in turn, clusters created by the large energy deposit of slow pions can be “rescued” and thus participate in the pattern recognition and particle tracking algorithms.

5 The Belle II Software Framework

The Belle II software framework comprises all software tools that are required to record, store and process the data taken by the Belle II detector. It is a crucial element of the Belle II experiment as it will be used for the whole of the data processing. Its application starts with the HLT, where the data taken by the various sub-detectors is used to decide whether the event contains interesting physics and should therefore be stored on disk (section 4.12). This decision process requires an analysis of the data in real-time and is performed by using the Belle II software framework. The same software framework is then used to read the stored data and reconstruct the events. Furthermore it is employed by the user to perform the final physics analysis. Its application as a real-time tool is often referred to as the **online** use of the software framework, while the **offline** use describes all processing steps that happen after the HLT has made its decision and the DAQ has written the data to disk.

Belle II adopts the successful software scheme of its predecessor experiment Belle [156], which used the same reconstruction and data handling tools for online as well as offline purposes. The software framework used successfully for over 10 years at Belle is called **BASF** [163] (**Belle AnalysiS Framework**). In order to reflect the changes made in the Belle II detector upgrade in the existing software framework BASF, major modifications of nearly all parts of the software would have been necessary. The vast amount of required modifications and the lack of object oriented persistency (BASF uses Fortran based Panther tables to store data) led to the decision to completely rewrite the software framework. This decision was initiated by the author of this thesis. The new software framework, called **baf2** [161], incorporates concepts from other HEP experiments, such as ILC [164], LHCb [165], CDF [166] and ALICE [167], into its design, but primarily follows concepts proven in BASF. In addition, the reuse of well-written algorithms of BASF is encouraged in order to maintain the excellent work done in the past 10 years at Belle. To facilitate and accelerate the development, established third-party libraries such as ROOT [168], boost [169], CLHEP [170] and libxml [171] are used throughout the entire software.

All physics analyses at Belle II require the generation and analysis of Monte Carlo events in addition to the analysis of the real detector data. This leads to a scheme of typically two types of processing paths as shown in figure 5.1. The first path represents the creation of physics events by means of Monte Carlo methods. A Monte Carlo **generator** creates events with each event containing the outgoing particles of a particle collision. Those events are then passed to a **full detector simulation**, simulating the passage of the particles through the detector material of the

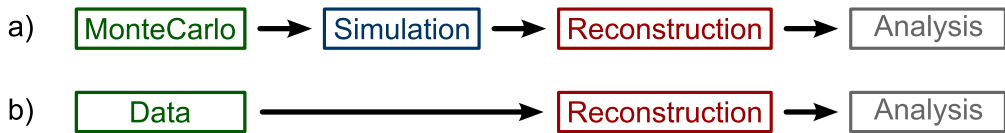


Figure 5.1: The typical data processing chains for a physics analysis. a) The Monte Carlo simulation chain, b) The detector data processing chain

various sub-detectors. Each sub-detector has a **digitiser** assigned, that uses the input of the full detector simulation in order to perform a realistic detector response simulation. The output of the digitiser should then resemble the output of the real sub-detector as closely as possible. The digitised data is then passed to the **reconstruction** stage, where the input data for the physics analyses is created. Among the various reconstruction procedures are, for example, the **clustering** of pixels and strips, **track finding** and **track fitting**. The last step in the processing chain is then the physics analysis. The real data processing chain, however, skips the Monte Carlo and simulation steps and feeds the real detector data directly to the reconstruction stage. The Monte Carlo chain and the real data chain share the same reconstruction and analysis procedures. This chapter presents the software and methods employed for the generation, simulation and reconstruction of Belle II events, as briefly outlined above, in more detail.

5.1 The Framework Core

The design of the Belle II software framework is based on the fact that the processing of events can be split into multiple, independent steps. The granularity of this subdivision is chosen such that each step represents a very specific task of the processing chain. Typical steps are the reading of event data, the clustering of pixels, strips or showers, the finding of charged tracks, the precision fitting of those tracks, particle identification etc. In the Belle II software framework such a processing step is implemented as a so-called **module**. A collection of modules, laid out in a linear order, represents the processing chain that should act on the events at hand. The modules are arranged linearly within a container, the **path**, and are executed exactly in the order in which they are present in the path. Figure 5.2 shows a schematic view of 4 modules. The initial implementation of this core functionality of basf2 was done in C++ by the author of this thesis.

The event processing starts with the first module on the left. It executes the module by calling the module's processing function. Depending on the specific task of the module, it might require input data such as detector hits, tracks etc. This data is maintained and provided by the **DataStore**. The DataStore is the common data storage for the whole framework. Modules can read, modify and write data from and to the DataStore. Thus, the DataStore represents an always up-to-date snapshot of the data at any processing step. After having executed a module,

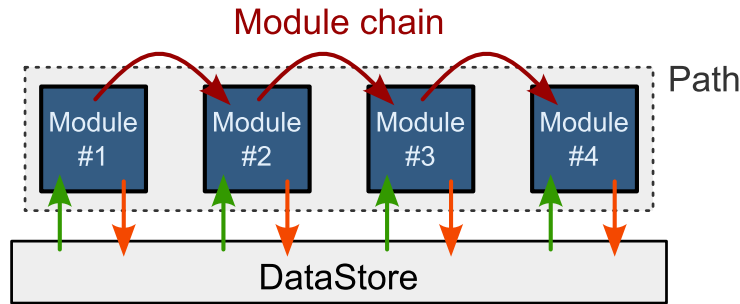


Figure 5.2: The core architecture of the Belle II software framework. Modules, encapsulating a particular functionality, are arranged in a linear order. The event data enters the chain on the left and progresses to the right, using the DataStore to feed data from one module to another.

the framework proceeds to the next module in the chain. This procedure is continued until the end of the chain of modules is reached. At this point, the processing of a single event is finished. The framework clears its DataStore and starts the processing of a new event with the first module. Internally, the framework is actually running in an endless loop: it iterates over the modules and starts from the beginning as soon as it reached the last module. In order to break the endless loop, a single module is chosen to become the **master module**. The first module in the module chain that changes the framework's event counter is picked by the framework as the master module. This module then tells the framework to stop processing events, as soon as, for example, the limit of an internal counter is reached, no input data is available anymore etc. The event processing is not confined to a single path, though. Multiple paths, each containing a chain of modules, can be linked with each other. There are two types of linking available. The **simple linking** of paths allows to attach a new path to an existing one, chaining two paths together. This is particularly useful for pre-defining paths for certain tasks. For example, there are pre-defined paths for the full reconstruction of events, containing all the required modules for particle tracking, particle identification and energy measurement of neutral particles. Without knowing the internal details, a user is then able to build a whole data processing chain from those larger “building blocks”. The second type of linking is **conditional linking** and is illustrated in figure 5.3.

Each module can return either a numeric or a boolean value. Based on this return value and a specified condition, the framework continues the execution of modules on a different path. This is helpful, for example, for applying different processing chains to events selected by a user-written selection module.

One of the key aspects of the framework design is the reuse of code. Therefore, the implementation of a particular processing step is divided into the development of a **library** and a module. The library hosts all functionality that might not only be used by a single module but will also be of interest to other modules. A typical example is the code for propagating a track through the

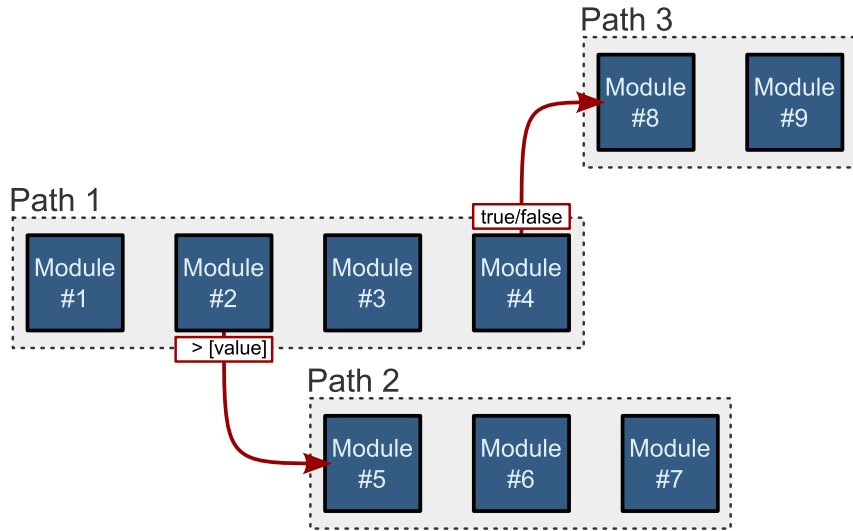


Figure 5.3: Conditional linking of paths in basf2: Three paths are connected by conditions. Both possible condition types are shown: An integer value and a simple boolean value.

detector. This code has been developed for the track fitting module, but is also used in the TOP particle identification module. This avoids the problem of modules implicitly including other modules, which has led to various issues in the past. A module should always be independent from other modules and use libraries to perform its task. Technically, modules are written in C++ and compiled into shared libraries [172]. If a specific module is requested, the framework loads the associated shared library from the disk and registers all modules contained in it to a common **module pool**. For future module requests, the framework first checks the module pool to see if the module has already been loaded. This optimises the amount of memory used by the framework. Figure 5.4 shows a schematic drawing of the on-demand loading plugin architecture of basf2.

The users interact with the framework via Python [173] scripts, called **steering files**. A typical steering file contains Python code to create paths and modules, add modules to paths, connect paths with each other, set module parameters and start the event processing. However, the use of Python as a scripting language allows to extend the typical usage by adding calculations of module parameters, analysis code, plot drawing code etc. to a steering file. It is even possible to write basf2 modules in Python and add them to the event processing chain. This is especially useful for prototyping modules and interactive plotting.

With the advent of multi-core computers and its usage as an online tool in the HLT, the software framework has to be able to make use of **parallel processing** techniques in order to accelerate the event processing. The scheme employed in basf2 is based on forking [174] and is illustrated in figure 5.5. Because recorded or simulated events from particle collisions are not correlated with each other, the parallelisation takes place on the event level. This means that incoming

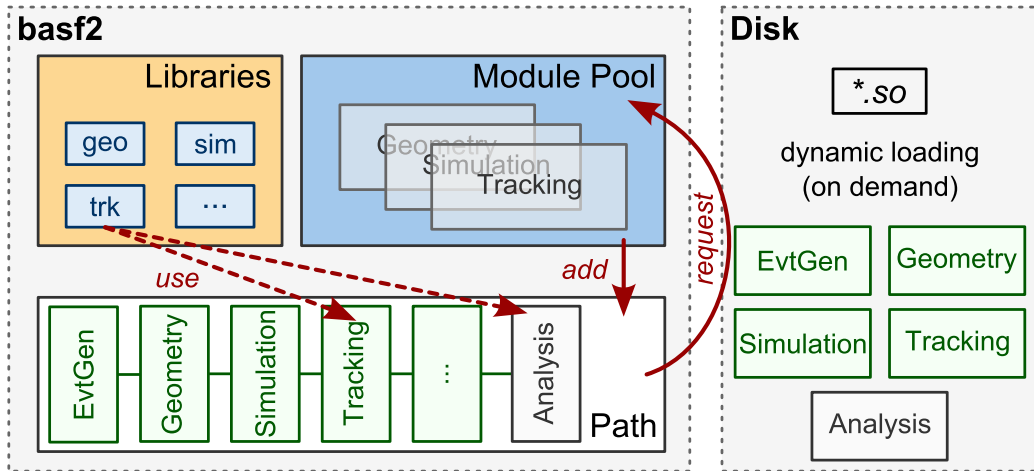


Figure 5.4: Modules and libraries are separated in basf2, allowing to share a library among multiple modules. Modules are loaded on-demand from shared object files by a user request.

events are distributed to multiple and independent processing chains and processed in parallel. Before processing events, the software framework analyses the paths and modules of the given processing chain. All modules that are able to perform their processing in parallel without causing any side-effects carry a special flag. The framework groups all modules according to this flag into an input, parallel and output group. While the modules of the input and output group are executed in single processing mode, the modules of the parallel group are processed in parallel. The number of parallel processing chains is specified in the steering file. The connection between the input/output group and the parallel group is accomplished with two **ring buffers**. The first ring buffer stores the incoming data from the input group and distributes it to the various paths of the parallel group. The second ring buffer collects the data from the parallel paths and sends it to the output group. In order to use the parallel processing scheme efficiently, the parallel processing paths should contain the computation-intensive modules. Typical examples are the full detector simulation module and the reconstruction modules.

5.2 Event and Particle Generation

Unlike most other software frameworks in high energy physics, basf2 employs the module concept for all tasks and data processing methods within the framework. Even the reading and creation of data is done through modules. There are various modules available for reading in event data from files, creating simple events by shooting single particles and for generating complex events by means of Monte Carlo methods. Among the file reading modules are modules for reading the full content of the DataStore into the memory, which had, at an earlier point, been saved to disk. Other modules allow the reading of HepEvt [175] ASCII files (a com-

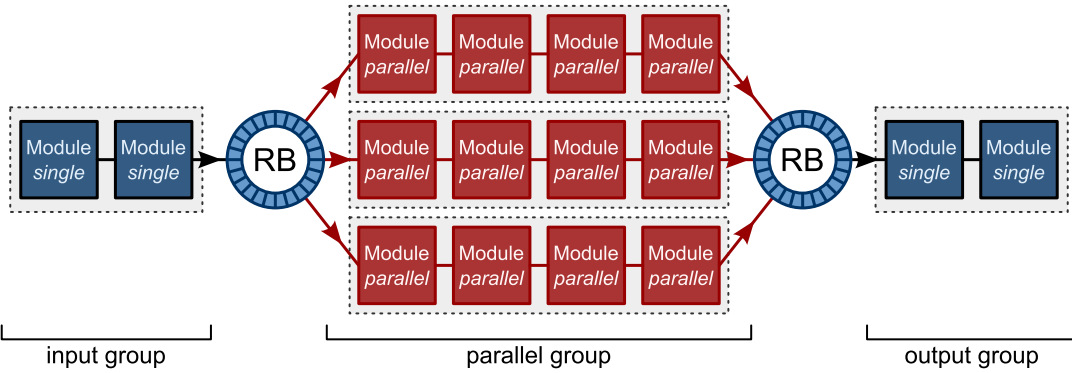


Figure 5.5: The parallel processing architecture of basf2. The module chain is divided into a single processing input and output group and a parallel processing group. The groups are connected by ring buffers (RB), taking care of the event distribution and collection.

mon event exchange file format in the high energy physics community) or SAD files (developed by the author of this thesis in order to exchange data with the SuperKEKB accelerator group). Simple events can be generated with the **particle gun** module. This module generates events with a specified number of particles per event, where their PDG particle codes, momenta, polar and azimuthal angles and vertex positions can either be fixed values or randomly sampled from flat or Gaussian distributions. The particle gun module is particularly useful for testing and debugging simulation and reconstruction algorithms. In order to generate complex physics events, a number of Monte Carlo generators have been implemented as modules into basf2.

For background and luminosity measurement studies, two Bhabha Monte Carlo generators are available: BHWide [176], providing large angle Bhabha scattering, and BBBrem [177] which covers radiative Bhabha scattering in the very forward direction. While the first generator is mainly used for luminosity studies, the second generator plays an important role for the estimation of the expected background at Belle II. The largest background for the PXD, however, originates from the two-photon process (see section 6.2). Several Monte Carlo generators are available for this process. KoralW [178], as a promising candidate, has been implemented in basf2 for this thesis.

The main Monte Carlo generator for *B*-physics events is EvtGen [179]. It is widely used among *B*-physics experiments, such as Belle, Babar [180] and LHCb. However during the last 10 years the aforementioned experiments have modified EvtGen to suit their own needs and did not communicate their changes. In order to consolidate those changes and make EvtGen ready for the next decade of *B*-physics analyses, it was decided to develop EvtGen centrally and move its source code from Fortran to C++, making use of the latest C++ version of Pythia [181]. The Belle II software framework incorporates this new, centrally hosted version of EvtGen.

5.3 Geometry Handling

Nearly all the tools of the software framework need a geometrical description of the Belle II detector, starting from the Monte Carlo based simulation of the passage of particles through the detector, to the simulation of the response of the sub-detector hardware, to the final reconstruction (e.g. tracking) algorithms. To make sure that all tools of the framework have access to the same version of the detector geometry description, it must be managed centrally. The geometry handling system of basf2 stores the parameter values needed to fully describe the Belle II detector in a central repository. The concrete geometry is then created using C++ source code from the parameters. Storing parameter values instead of concrete geometry objects allows for a simple and generic way of handling time varying geometry. For example, the position of the sensors of the PXD have to be known to a high precision. Various effects, such as temperature variations, may change the position of these parts over time. By measuring the position of the sensors at a given time, the deformation of the geometry can later be taken into account for the reconstruction of the particle tracks.

Name	Standard Unit	C++ Code
Length	Centimeter	Unit::cm
Time	Nanosecond	Unit::ns
Energy	GeV	Unit::GeV
Momentum	GeV	Unit::GeV
Mass	GeV	Unit::GeV
Angle	Radian	Unit::rad
Magnetic field	Tesla	Unit::T
Temperature	Kelvin	Unit::K
Density	g/cm ³	Unit::g_cm3

Table 5.1: The standard units of the Belle II software. All other units in basf2 are based on those. In general, units are implemented in the framework such that multiplying a unit to a value automatically converts the value from the specified unit to the standard unit.

The central repository for the Belle II detector parameters is realised using XML documents [182]. XML documents have the advantage of being human readable and highly extendable. Furthermore, they are widely used in both particle physics and industry, leading to the availability of high quality libraries, tools and software (both Open Source and commercial) to write, read and manage XML documents. The central parameter repository stores the parameters for each sub-detector in a separate XML document. In order to describe the full Belle II detector they are combined into a single document using the XInclude technology [183]. This keeps the size of each sub-detector XML document reasonable small and allows the definition of different detector configurations with each configuration being given by a specific set of sub-detectors.

The access to the parameters describing the Belle II detector is handled by a user-friendly library called Gearbox, initially developed by the author of this thesis. Using the XPath query language [183], a standardised language developed by the W3C, the user sends a request for a parameter via the Gearbox library and gets the value of the parameter back. Special care is taken to handle the unit of parameters (e.g. length) consistently. The user is able to attach the unit in which a parameter is specified in the XML file. Upon request of a parameter the library automatically performs the correct unit conversion from its specified unit to the standard unit of the basf2 software framework. Table 5.1 lists the standard units of basf2.

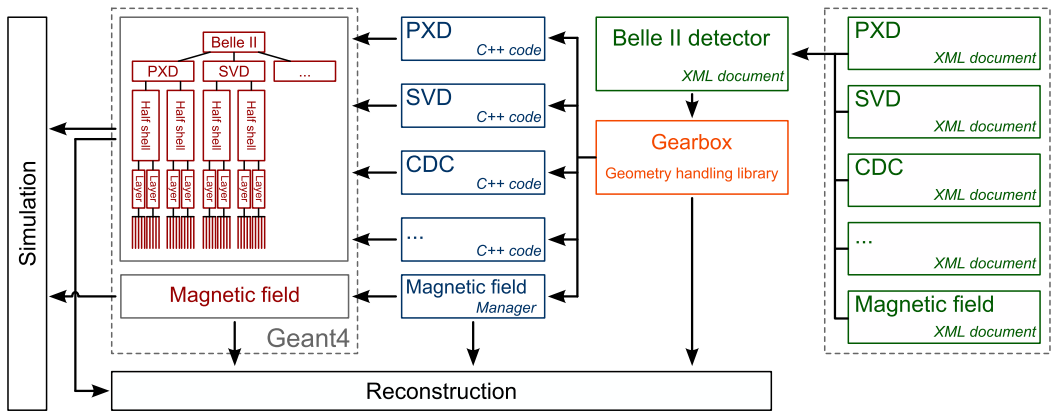


Figure 5.6: The architecture of the geometry handling system in basf2. If needed, the Geant4 geometry can be converted to a ROOT TGeo [168] geometry.

The link between parameter values and the actual geometry of a sub-detector is filled by C++ code. Each sub-detector has associated C++ code that is aware of the available parameters for its specific sub-detector. The C++ code requests the parameter values from the Gearbox library and uses them to create the geometry. This allows each sub-detector to store only a minimal set of parameters for its description and use C++ to build the geometry in an efficient way. Figure 5.6 illustrates the basic architecture of the basf2 geometry handling system. The geometry is created within the full detector simulation toolkit Geant4 [184], which is described in more detail in the next section. Geant4 uses the Constructive Solid Geometry (CSG) paradigm [185] for describing complex geometry. In CSG geometry is composed from geometry primitives (such as boxes, tubes, spheres, etc.) and Boolean operators to combine them. This leads to a tree-like geometry hierarchy with nodes representing Boolean operators and leaves representing primitives. In addition, Geant4 assigns material properties like radiation length and specific energy loss to single primitives and combined primitives, which are then called **volumes**. The number of volumes required to build a sub-detector in Belle II depends on the sub-detector and ranges from $\mathcal{O}(10)$ up to $\mathcal{O}(10^5)$. Figures 5.7, 5.8 and 5.9 show renderings of the geometry implementation of the inner detectors in basf2. For the reconstruction algorithms the geometry can be converted to a ROOT TGeo [168] geometry and is therefore also available for the processing of real data.

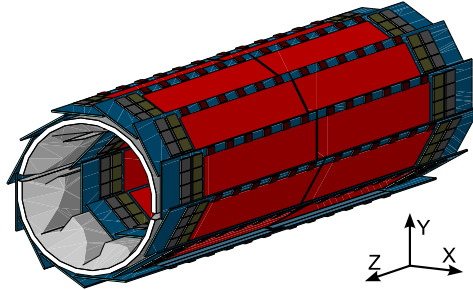


Figure 5.7: The Geant4 PXD detector geometry. Shown is the outer layer and the support.

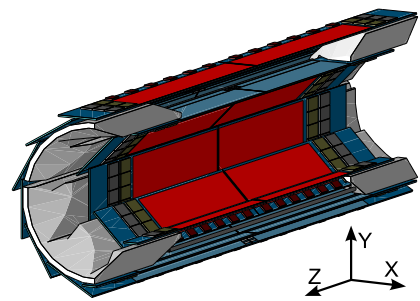


Figure 5.8: Cut through the Geant4 PXD geometry to reveal the inner layer.

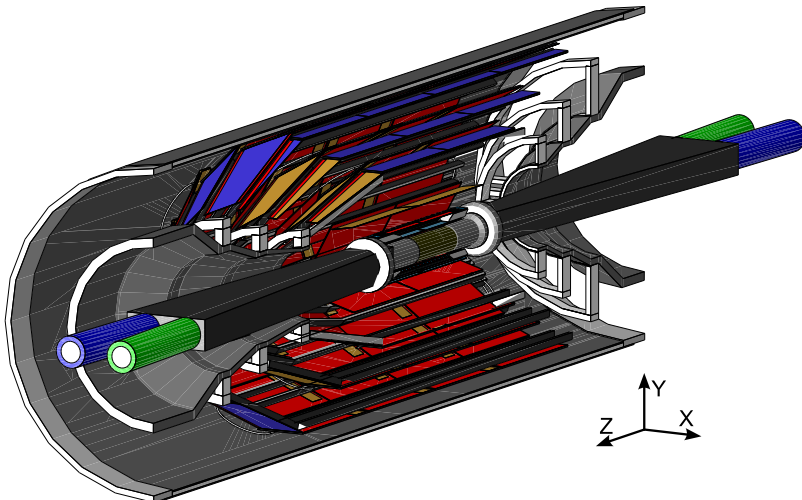


Figure 5.9: Cut through the Geant4 geometry of the silicon tracking detectors (PXD, SVD), their support structures and the Beampipe.

The implementation of the Belle II geometry in Geant4 focuses on the correct description of its basic geometry components and material definitions, rather than on modelling each little screw or hole. The detector geometry is mainly used to simulate the passage of particles through the detector, which requires a material description that resembles reality as closely as possible. A material budget scan of the detector is usually used to check the material description. Figures 5.10 and 5.11 show a material budget scan of the PXD and the full Belle II detector, respectively. The scan is performed with Geant4 and measures the material budget as it is seen from the IP for the full Belle II acceptance. The two-layer PXD contributes with only 0.6 % of a radiation length to the total material budget of Belle II. The material budget of the PXD itself is dominated by the sensor (0.46 % X_0), followed by the switchers (0.079 % X_0), the reinforcement (0.027 % X_0) and other material such as the glue joining the modules can be neglected. The peak in the distribution at a polar angle of about 50° is due to the ZnO_2 reinforcement between the two

halves of a PXD ladder. See section 4.3.5 for a more detailed description of the PXD.

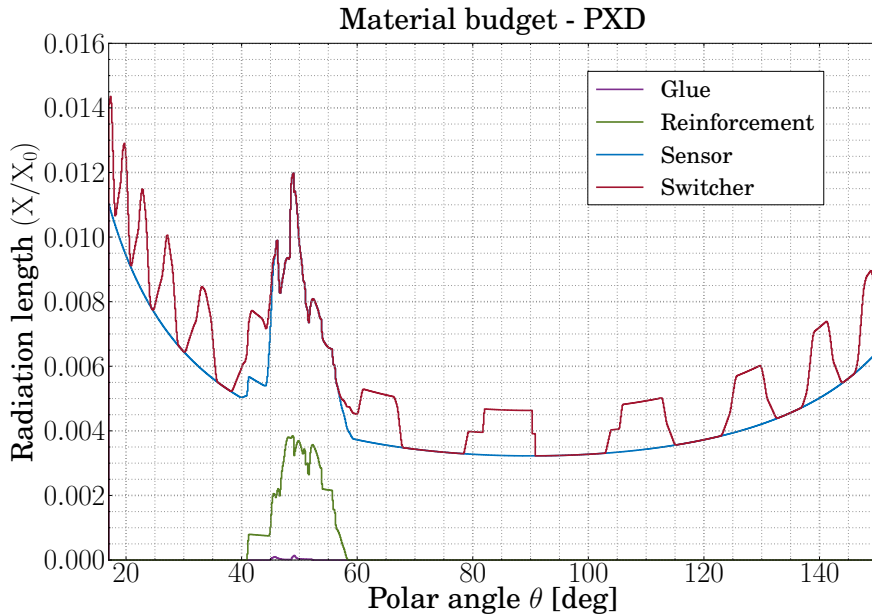


Figure 5.10: Stack plot of a spherical material budget scan of the PXD. The x-axis is the polar angle, with the forward direction being on the left and the backward direction on the right. The y-axis measures the radiation length X in units of X_0 .

The geometry handling system is not only responsible for building the detector geometry. It also manages and provides the values for the magnetic field of Belle II (see figure 5.6). The simulation as well as the reconstruction use the magnetic field values to propagate charged particles through the detector and to extrapolate reconstructed tracks. Three different types of magnetic field values are available in basf2: a constant magnetic field of 1.5 T, which is useful for fast detector simulations; a two-dimensional, cylindrical field map, which assumes a rotation symmetric detector around the z-axis; and a three-dimensional field map. The two-dimensional field map defines a discretised vector field of the Belle II magnetic field with one axis being z and the other the radius measured from the z -axis. This field map is usually good enough for most simulation purposes, the exception being studies that require particles to travel along the beam, because the in- and outgoing beampipes are not rotation symmetric around the z -axis. The three-dimensional magnetic field combines the two-dimensional field map of the Belle II detector with three-dimensional magnetic field maps for the focusing magnets and the beampipes. This field map is, for example, used to study the synchrotron radiation at Belle II. The two-dimensional as well as the three-dimensional magnetic field maps are the result of a finite element simulation. The values for the three-dimensional magnetic field map in the zx -plane are drawn in figures 5.12 and 5.13. As the figures show, the magnetic field throughout the whole detector (but particularly in the inner region) is sufficiently uniform and can often be approximated by a constant 1.5 T field if simulation speed is an issue.

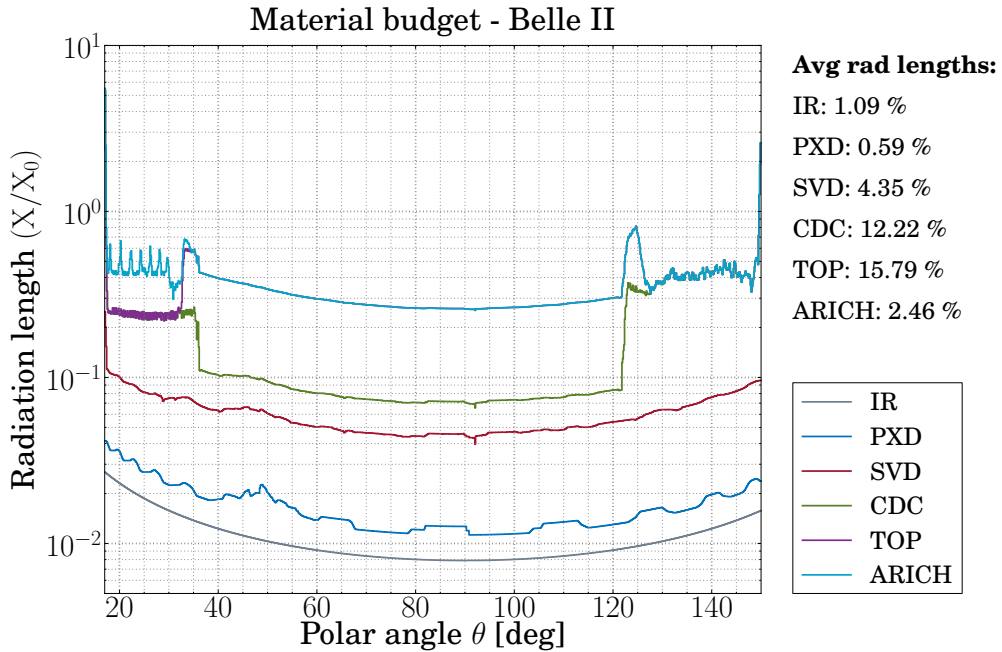


Figure 5.11: Stack plot of a spherical material budget scan of the full Belle II detector. The forward direction of the detector is on the left and the backward direction on the right.

5.4 Full Detector Simulation

The full detector simulation in basf2 is based on Geant4 [184], the standard toolkit for the simulation of particles traversing matter in the high energy physics community. Taking the detector geometry, the magnetic field and a list of particles as input, Geant4 performs the simulation by tracking the particles, one at a time, through the geometry. It takes into account the effect of the magnetic field on the particle, the energy loss and multiple scattering the particle experiences while traversing material and various other electromagnetic and hadronic effects. If a particle decays, the decay products are added to the list of particles. The initial particles given to Geant4 (see section 5.2) are called **primary** particles, while all particles created from interactions or decays during the simulation are called **secondary** particles. The tracking of the particles is accomplished by breaking the particle's trajectory into smaller steps. For each step, Geant4 calculates the probability for a particle to decay or to interact with the detector material. Geant4 creates a new step if either the boundary between two volumes is reached, an interaction or decay happened or the length of the step exceeds the maximum step length. The maximum length of a step can be set for each geometry volume separately, where the value usually depends on the density or the thickness of the material. Geant4 incorporates a feedback system which allows certain actions to be taken if a particle steps through a volume. By attaching a special piece of source code to a volume it is made **sensitive** and the parameters of all steps located in this volume, such as step length, position and the energy deposited can be accessed and

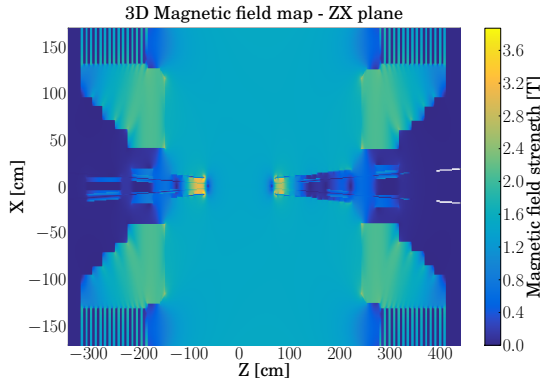


Figure 5.12: The 3D magnetic field map of the Belle II detector in the zx -plane.

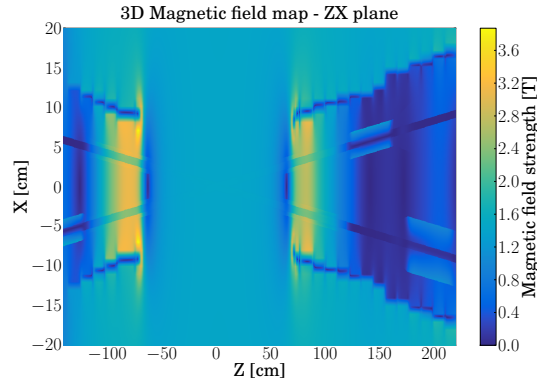


Figure 5.13: The 3D magnetic field map in the inner region of the Belle II detector in the zx -plane.

stored for later usage. Typically, the step information collected in a sensitive volume is used to perform a realistic simulation of the response of a sub-detector. The simulation of the detector response is called **digitisation** and is explained in more detail in the next section. In the case of the PXD, the default step size is $5\text{ }\mu\text{m}$, resulting in several steps per particle and per sensor. The information for each step in the PXD sensor is stored as a DataStore object called **PXDSimHit**. However, for optimisation and counting purposes, one might want exactly one hit representing the “true” location where the particle traversed the PXD sensor. This is accomplished by defining a virtual plane, the **zero plane**, parallel to the sensor and located in its centre. Each time a particle traverses the zero plane a so-called **PXDTrueHit** is created. Two scenarios are possible and illustrated in figure 5.14 and 5.15.

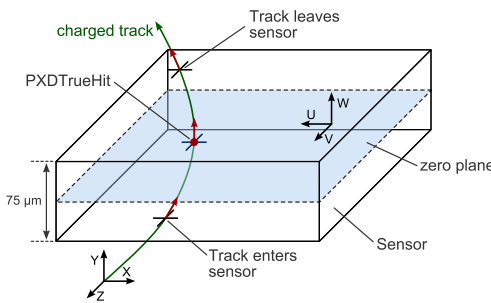


Figure 5.14: A particle enters the sensor at one side and leaves it on the other. The **PXDTrueHit** is then the position at which the particle crossed the zero plane.

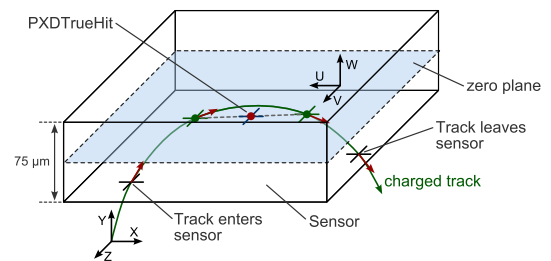


Figure 5.15: A particle enters and leaves the sensor on the same side. In this case the positions of the two crossing points are averaged.

If a particle enters the sensor at one side and leaves it on the other, the **PXDTrueHit** is simply

the location where the particle crossed the zero plane. The energy that the particle deposited in the sensor is accumulated and assigned to the true hit. In rare cases though, the particle might enter and leave the sensor on the same side. If this happens the two locations on the zero plane are averaged and this average position becomes the `PXDTrueHit`.

5.5 Digitisation for the PXD

The realistic simulation of the sub-detector hardware response is called **digitisation**. It takes the recorded Geant4 step information from the simulation as an input and produces an output which should resemble the output of the real sub-detector as closely as possible. The digitisation is the last step in the processing chain used solely for Monte Carlo data. After the digitisation, all data processing steps are the same for Monte Carlo and real data. Since the implementation of the digitisation method varies heavily from sub-detector to sub-detector, the implementation for the PXD is presented in the following.

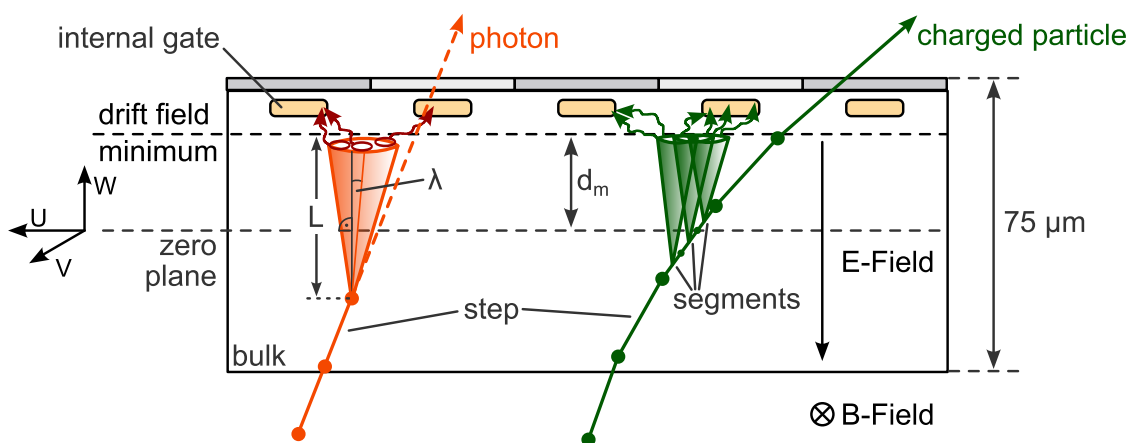


Figure 5.16: The PXD digitisation procedure. Electron clouds drift from the position where they have been generated to the drift field minimum. There, they perform a random walk to the internal gates. The local coordinate system of the PXD sensors is a right-handed Cartesian coordinate system (u , v , w), where v is parallel to the global z axis of the Belle II detector and w is the normal vector of the sensor surface.

The digitisation starts by taking the Geant4 step information that was recorded in the sensitive volume of the PXD sensor as `PXDSimHits`. After having verified that the timestamp for a `PXDSimHit` is within the readout (integration) time of the PXD, the number of electron-hole pairs were created by the particle along the Geant4 step is calculated

$$N_{eh} = \frac{E_{dep}}{3.65 \text{ eV}}$$

where E_{dep} is the energy that the particle deposited along the Geant4 step and 3.65 eV the average energy needed to produce an electron-hole pair in silicon. From the created electron-hole pairs only the electrons contribute to the signal in the PXD. Therefore, the generated holes are not used in the digitisation procedure. If the particle is a photon, all electrons are created at the end of the step. If the particle is not a photon, the step is subdivided into segments with a length of 5 μm , the number of electrons is evenly distributed across all segments and the electrons are created at each segment's centre. Since the default step size is set to 5 μm in basf2, there is usually only one segment per step. The method of generating more than one step is applied if the step length is either set to a value larger than 5 μm or Geant4 was configured to set the step length automatically. Then the electrons are drifted to the drift field minimum and are collected in the internal gate. Figure 5.16 illustrates the PXD digitisation procedure and introduces the local coordinate system of the sensor. The simulation of the electron drift is split into a **vertical** and a **lateral** part. The electrons drift vertically in the bulk upwards to the plane of the drift field minimum, performing a random-walk. This spreads the initial small cloud of electrons, an effect called **diffusion** [186]. The width of the electron cloud is given by the well-known equation [187]

$$\sigma = \sqrt{2Dt} \quad (5.1)$$

where σ is the electron cloud width, D is the electron diffusion coefficient, and t the drift time. This equation holds as long as the diffusion coefficient and, in turn, the electron mobility and drift velocity is constant over the whole drift volume. However, for the drift model of the DEP-FET a more general and detailed approach is used. Equation 5.1 can be written as

$$\sigma^2 = 2 \int_0^L \frac{D(w)}{v_d(w)} dw \quad (5.2)$$

where the diffusion coefficient $D(w)$ and the drift velocity $v_d(w)$ depend on the location inside the drift volume. The integral runs over the drift path with length L (see figure 5.16).

The diffusion coefficient is then given by the Nernst-Einstein relation [188]

$$D(w) = \mu(w) \frac{k_B T}{e} \quad (5.3)$$

with $\mu(w)$ being the position dependent electron mobility, k_B the Boltzmann constant, e the electron charge and T the absolute temperature. The numerical integration of equation 5.2 is performed with a 5-point Gauss-Legendre quadrature [189]. The drift velocity depends on the electric and magnetic fields acting on the electrons and the electron mobility μ in the silicon bulk [190]

$$\vec{v}_d = \frac{\mu \vec{E} + \mu \mu_H (\vec{E} \times \vec{B}) + \mu \mu_H^2 (\vec{E} \cdot \vec{B}) \vec{B}}{1 + \mu_H^2 |\vec{B}|^2} \quad (5.4)$$

where the electric and magnetic fields, and thus the velocity, depend on the current position \vec{p} of the electrons. The value for the magnetic field is provided by the geometry handling system of basf2. In equation 5.4, $\mu_H = r_H \mu$ is the Hall mobility which differs from the electron mobility by the Hall scattering factor r_H . This factor describes the influence of the magnetic field on the mean scattering time of the electrons. The electron mobility can be described as a function of the electric field E [187]

$$\mu = \frac{v_s/E_c}{\left[1 + (E/E_c)^\beta\right]^{1/\beta}} \quad (5.5)$$

with the parameters

$$\begin{aligned} v_s &= 1.53 \cdot 10^9 \cdot T^{-0.87} \\ E_c &= 1.01 \cdot T^{1.55} \\ \beta &= 2.57 \cdot 10^{-2} \cdot T^{0.66} \end{aligned} \quad (5.6)$$

where T is the temperature in Kelvin and E is the absolute value of the electric field, given as

$$\vec{E} = \left(0, 0, \frac{2 \cdot V_{dep} \cdot \overbrace{(p_w - d_m)}^{\text{distance of } \vec{p} \text{ to field min}}}{(d_s)^2} \right) \quad (5.7)$$

with d_m the distance between the field minimum and the centre of the sensor (zero plane), V_{dep} the depletion voltage and d_s the thickness of the sensor. The default values for these parameters are listed in table 5.2. The integration of equation 5.2 yields the value for the cloud width σ at the plane of the drift field minimum. By integrating \vec{v}/v_w at the same time, the position of the electron cloud on the plane is estimated, too. From the position the **Lorentz angle** [188] λ is calculated. The Lorentz angle is the angle by which particles moving in an electric field are deflected due to the effect of a magnetic field. Since the integration of equation 5.2 is performed without the Lorentz angle in mind, the cloud widths have to be corrected by scaling them with a factor $f_{u,v}$, deduced from the Lorentz angle

$$\begin{aligned} f_{u,v} &= \frac{1}{\cos_{u,v} \lambda} = \sqrt{1 + \tan_{u,v}^2 \lambda} \\ \sigma_u &= \sqrt{f_u \cdot \sigma^2} \\ \sigma_v &= \sqrt{f_v \cdot \sigma^2} \end{aligned} \tag{5.8}$$

After having simulated the vertical drift of the electrons, the digitisation algorithm divides the electron cloud into smaller groups of electrons. Those groups are placed randomly on the plane of the drift field minimum according to a 2D Gaussian distribution with the mean being the position of the drifted electron cloud and the sigma values being σ_u and σ_v . The groups then execute a **lateral random walk**, where each step in the walk is a combination of a random step, modelling diffusion, and a Hall effect [191] step due to the magnetic field. The direction of the random step is calculated using a 2D Gaussian distribution with a sigma value given by equation 5.1. The random walk of a group is stopped as soon as it reaches an internal gate. The total charge of the group is then assigned to the pixel associated with the internal gate. The presented algorithm has been verified in testbeam experiments to correctly describe the DEPFET [192].

Name	Variable	Value	Unit
Temperature	T	300	K
Hall scattering factor (at 300 K)	r_H	1.151	
Thickness sensor	d_s	75	μm
Depletion voltage	V_{dep}	42.767	V
Distance drift field minimum	d_m	15.5	μm
Size Source		3.0	μm
Size Clear		3.0	μm
Size Drain		3.0	μm
Number of electrons per group		100	
Step size for random walk		1	ns
Step number limit for random walk		200	

Table 5.2: The default input values for the PXD Digitiser.

5.6 Clustering in the PXD

If the charge of an electron cloud is shared between adjacent pixels, a single particle will cause multiple pixels to fire. Figure 5.16 illustrates this charge sharing effect. For the subsequent data processing steps the pixels belonging to a single particle have to be identified. This is done by means of a **clusteriser**, which groups together adjacent pixels into so-called **clusters**. The clustering is performed for both real data and Monte Carlo data in the same way. The approach that the clusteriser takes is illustrated in figure 5.17.

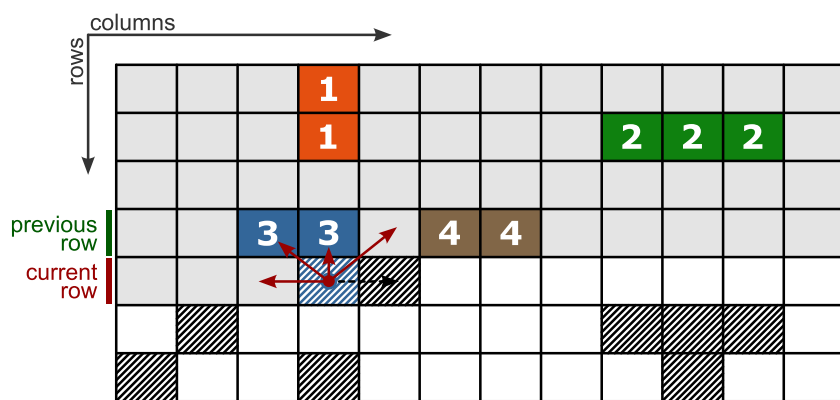


Figure 5.17: The PXD clustering method. Clusters 1, 2, 3 and 4 have already been found. The current pixel under investigation is added to cluster 3. The next pixel to the right will fill the gap between cluster 3 and 4. This will lead to clusters 3 and 4 being merged to a large cluster.

The clustering of the PXD pixels is done in a row-wise manner, with increasing values for the column index and the row index. Starting with the pixel in the upper left corner, the clusteriser checks each pixel to make sure that the ratio of its charge over a common noise level is above a given threshold (see table 5.3). If it is, the left neighbour in the same row and the direct neighbours in the previous row are investigated. If one or more clusters have already been found in those neighbouring pixels, the clusters are merged and the pixel is assigned to this cluster. Otherwise, a new cluster is created and the pixel becomes its first member. The clusteriser proceeds with the pixel to the right of the current pixel or, if the pixel is the last pixel in the current row, with the first pixel of the next row. The procedure is repeated until the last pixel in the last row has been processed. This clustering scheme investigates each pixel only once and requires only the current and the previous pixel row to be stored in memory, making it an efficient and memory-saving pixel clustering method. After having grouped all pixels into clusters, the position of each cluster is determined: if the size of the cluster, defined by the number of pixels belonging to the cluster, exceeds a given threshold, the **head-tail** algorithm [193] is used to calculate its position. The default threshold in basf2 is set to 3 pixels. The head-tail algorithm calculates the position of the cluster by using the outermost pixels of a cluster.

The following formula is applied to the column and the row pixels separately

$$x_{ht} = \frac{x_R + x_L}{2} + \frac{q_R - q_L}{2 \bar{q}} \cdot pitch$$

where x_R and x_L are the positions of the right- and leftmost pixels, q_R and q_L the charges of the right- and leftmost pixels, \bar{q} the average charge of the pixels between the right- and leftmost pixels and *pitch* the pixel size. If the size of the cluster is smaller than the threshold, the **center-of-gravity** algorithm provides the better position measurement [193]. This algorithm calculates the position of the cluster by means of an average of the pixel positions with each pixel being weighted with its charge

$$x_{cog} = \frac{\sum_{cluster} x_i q_i}{\sum_{cluster} q_i}$$

After having calculated the position of the cluster with one of the two algorithms, the position is corrected for the influence of the magnetic field by using a specified value for the Lorentz angle. The pixel that carries the largest charge of all pixels within a cluster, is called the **seed** and its charge becomes the **seed charge** of the cluster. If the ratio of the seed charge over the noise level and the ratio of the total cluster charge over the noise level are above their respective thresholds, the cluster is kept and stored in memory for subsequent data processing steps.

Name	Value
Noise level	200 electrons
Cluster size limit for head-tail	3 pixels
Signal over noise threshold (for pixel)	3
Signal over noise threshold (for seed pixel)	3
Signal over noise threshold (for cluster)	3
Tangent of the Lorentz angle	0.25

Table 5.3: The default input values for the PXD Clusteriser.

5.7 Data Persistency and the PXD Event Model

During the processing of events, a basf2 module reads the required data from the DataStore, processes the data and writes modified or new data back to the DataStore. The DataStore itself is divided into two categories: one for data which should be stored only for one single event and one for data which is stored over a complete run. The module can decide which data should be written into which category. The framework clears the event category after each event has

been processed and the run category as soon as a new run is started. The data is realised as **objects** instantiated from C++ classes. Objects of the same type are grouped into lists, called **collections**. The DataStore uses ROOT [168] for the object persistency. This allows writing the DataStore content into a file that is compatible with any ROOT based tool.

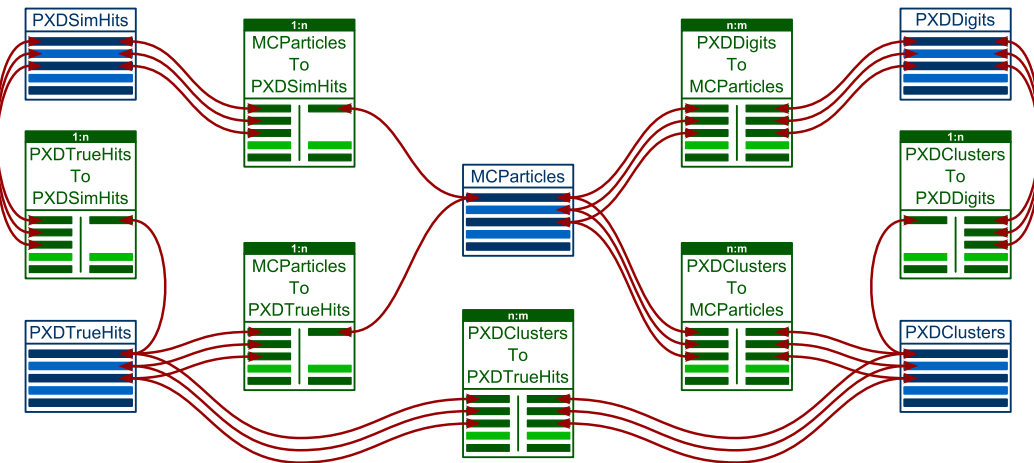


Figure 5.18: The PXD Event model. Relations connect collections with each other. A $1:n$ relation connects one object of the first collection with n objects of the second collection, while $n:m$ Relations connect n objects of the first collection with m objects of the second collection.

Figure 5.18 shows the content of the DataStore for the PXD related data after a full Monte Carlo simulation. The **MCParticles** collection contains a list of all particles that were created by a Monte Carlo generator. The **PXDSimHits** represent the information collected for all Geant4 steps in the PXD sensitive volumes, and the **PXDTrueHits** provide a single location measurement for a sensor (see section 5.4). While the **PXDTrueHits** are usually directly used for various studies, the **PXDSimHits** are meant as an input to the PXD Digitiser. The Digitiser converts the **PXDSimHits** to **PXDDigits**, which represent the fired pixels of the sensor. The **PXDDigits**, in turn, are the input to the Clustering. The result are **PXDClusters**. For real detector data, the simulation stage is skipped and the input are the fired pixels (**PXDDigits**). The different collections in the DataStore can be connected with each other. For example, the **PXDTrueHits** are connected to the **MCParticles**, which allows users or algorithms to access the Monte Carlo particle that created a specific **PXDTrueHit**. Figure 5.18 shows all connections that are available for the PXD DataStore objects. The framework offers the generic concept of **Relations** to set up a network of connections. Relations are keeping record of the relationship between one or more objects of one collection to one or more objects of another collection. Thus, the Relations in basf2 allow for $n:m$ relationships, very similar to a relational database [194]. In addition, each connection between two objects in a Relation can carry a **weight**. This is useful to specify “how much” a connection contributes to a relation. Relations are particularly useful for Monte Carlo data, as they allow to calculate efficiencies or validate reconstruction algorithms.

5.8 Impact parameter resolution

The investigation of CP -violation at Belle II relies on the measurement of the time-dependent asymmetry of the B -meson decay rate, where the time is determined from the difference between the positions of the B -meson pair decay vertices. The reconstruction of charged tracks with a high precision is crucial for measuring the decay vertices and has a significant influence on the physics analyses and their systematic errors. One of the most relevant measures for the track reconstruction precision is the **impact parameter resolution**. The impact parameters measure the distance of a track at its point of closest approach to a reference point, usually the IP or a decay vertex. Figure 5.19 illustrates the definition of the impact parameters at Belle II, where the origin (ideal IP) has been chosen as the reference point.

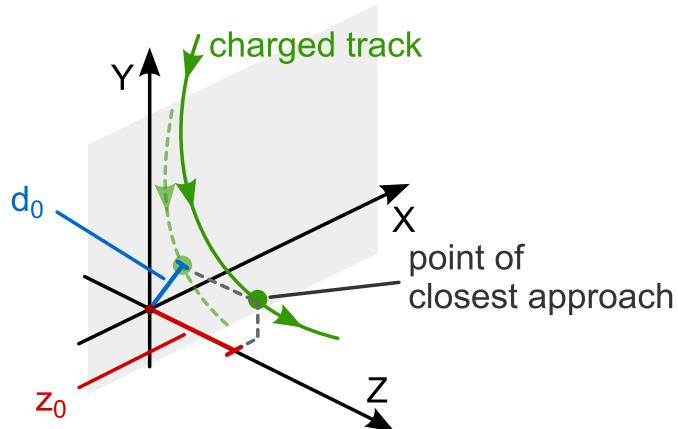


Figure 5.19: The solid green line represents the particle trajectory, while the dashed green line the projection of the trajectory onto the xy plane. The definition of the impact parameter of a track is as follows: d_0 is the signed distance between the origin and the point of closest approach of the projected track to the origin; z_0 is the z coordinate of the track at the point of closest approach.

The point of closest approach is determined by extrapolating a particle track to the global detector z -axis. The distance between the origin and the projection of the point of closest approach onto the xy plane provides the impact parameter d_0 . It is a signed value, with the sign convention being defined as follows: moving along the track into the direction of the particle's momentum, the sign is positive (negative) if the origin is to the right (left) of the track at the point of closest approach. The z position of the track at the point of closest approach defines the impact parameter z_0 . The accuracy, or resolution, that can be achieved for d_0 and z_0 consists of two independent components. The first, σ_{int} , originates from the intrinsic detector resolution and is independent of the particle momentum. The second component, σ_{ms} , describes the effect of multiple scattering that a particle experiences while traversing the material in the beampipe and the detectors. It depends on the particle momentum and the thickness of the material.

The total impact parameter resolution can be written as

$$\sigma^2 = \sigma_{int}^2 + \sigma_{ms}^2$$

Assuming that the beampipe and the tracking detectors have a cylindrical shape, aligned along the z -axis, the component σ_{ms} is given by the width Φ_{ms} of the multiple scattering angle distribution, the polar angle θ of the particle track and the distance $\frac{r}{\sin \theta}$ from the scattering point to the IP

$$\sigma_{ms} = \frac{r}{\sin \theta} \cdot \Phi_{ms} \quad (5.9)$$

In general, the multiple scattering distribution Φ_{ms} is well described by Molière theory [195]. However, for small deflection angles the central 98 % of the distribution can be approximated by a Gaussian distribution with a width given by [42]

$$\Phi_{ms} = \frac{13.6 \text{ MeV}}{\beta c p} z \sqrt{\frac{x}{X_0}} \left[1 + 0.038 \ln \left(\frac{x}{X_0} \right) \right] \quad (5.10)$$

where p is the momentum in [MeV/c], βc the speed, z the charge of the particle, x the material thickness and X_0 the radiation length of the material. This approximation is accurate to 11% for $10^{-3} < \frac{x}{X_0} < 100$ [42]. By introducing a factor $\frac{x}{\sin \theta}$ in order to correct for the actual traversed material thickness and by omitting the weak dependence of the logarithmic term on $\sin \theta$, the d_0 impact parameter resolution for electrons due to multiple scattering can be written as

$$\sigma_{ms}^{d_0} \approx \frac{1}{c p \cdot \sin^{\frac{3}{2}}(\theta)} \underbrace{r \cdot 13.6 \text{ MeV} \sqrt{\frac{x}{X_0}}}_b \quad (5.11)$$

The same scattering angle changes the impact parameter z_0 by an additional factor $\frac{1}{\sin \theta}$, which yields the z_0 impact parameter resolution

$$\sigma_{ms}^{z_0} \approx \frac{1}{c p \cdot \sin^{\frac{5}{2}}(\theta)} \underbrace{r \cdot 13.6 \text{ MeV} \sqrt{\frac{x}{X_0}}}_b \quad (5.12)$$

The denominators in equations 5.11 and 5.12 are often referred to as **pseudo-momentum**.

The total impact parameter resolutions, including the intrinsic detector resolution, are then given by

$$\sigma^{d_0} = \sqrt{\sigma_{int}^2 + \frac{b^2}{[\beta p \cdot \sin^{\frac{3}{2}}(\theta)]^2}} \quad \sigma^{z_0} = \sqrt{\sigma_{int}^2 + \frac{b^2}{[\beta p \cdot \sin^{\frac{5}{2}}(\theta)]^2}} \quad (5.13)$$

where σ_{int} is the intrinsic detector resolution and b in [GeV μm] the multiple scattering coefficient. Equations 5.13 are used as a figure of merit to quantify the expected track reconstruction resolution at Belle II and compare it to the achieved resolution at the previous Belle detector. In order to get a more conservative estimate, μ^- particles are used for studying the impact parameter resolution. They are minimum ionising particles and therefore deposit very little energy in the tracking detectors. This leads to small clusters in the PXD and SVD, reducing the accuracy of the cluster position measurement. An advantage of their minimal interaction with matter is drawn from the fact that muons travel usually through the whole detector. This makes them ideal particles for testing the performance of the tracking detectors.

The inputs for the study are single track events, where each event contains exactly one μ^- . The particle gun is used to produce the particles. Their momentum is taken randomly from the range of values between 0.1 to 3.0 GeV. The muons cover the full detector acceptance of $17^\circ < \theta < 150^\circ$ for the polar angle and the full 2π for the azimuthal angle. The generated events are passed to the Geant4 detector simulation, using the full detector geometry and a constant magnetic field of 1.5 T. The output of the simulation is given to the PXD, SVD and CDC digitisers in order to simulate the realistic sub-detector response. The fired pixels in the PXD and the fired strips in the SVD are clusterised. The PXD/SVD clusters and the fired CDC wires are then the input for the particle track reconstruction. The track reconstruction consists of two steps, the **track finding** and the **track fitting** step. During the track finding step the clusters from the PXD/SVD and the fired wires in the CDC that belong to the same track are identified. For the impact parameter study, a track finding procedure based on Monte Carlo information is used. This means that for each Monte Carlo particle the associated clusters and wires are found by following links between the particle and the clusters/wires that have been generated during the detector simulation. Therefore, in this study the track finding procedure is not tested and its efficiency is always 100 %. The identified clusters and wires are passed to the track fitting, which estimates the optimal track parameters. The track fitting in basf2 is based on the Genfit tracking framework [196] and a Kalman filter [197, 198] that has been optimised for Belle II.

Each track is then extrapolated to the z -axis and the impact parameters d_0 and z_0 are calculated according to figure 5.19. From the track's polar angle and momentum its pseudo-momentum is derived. The impact parameters d_0 and z_0 are then collected in bins of the pseudo-momentum. The impact parameter resolution is estimated for each pseudo-momentum bin by fitting a Gaussian function to its d_0 and z_0 distributions. The σ value of the fitted Gaussian defines the impact

parameter resolution. In order to reduce the influence of outliers, the fit is limited to the core of the distribution defined by a region that contains 90 % of the data and is centred around the distribution's mean value. The impact parameter resolution values are then plotted against the associated pseudo-momentum. Figure 5.20 and 5.21 show the expected impact parameter resolutions for Belle II. The green, dashed line represents the resolution achieved at the Belle detector [199]. The figures also show the impact parameter resolution for the case that the data from the PXD is not available for the track reconstruction.

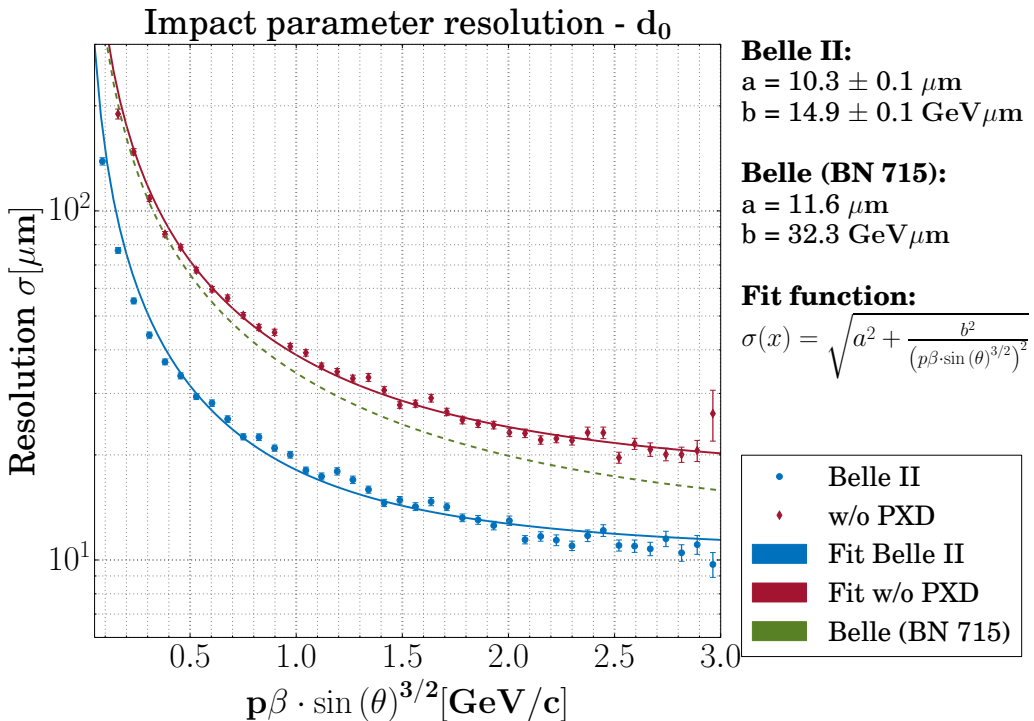


Figure 5.20: Impact parameter resolution for d_0 . The lower curve represents the Belle II detector, the dashed, green curve the Belle detector and the upper curve the Belle II detector without the PXD.

In order to extract the values for the intrinsic detector resolution and the multiple scattering coefficient, the impact parameter resolution data for d_0 and z_0 is fitted with equations 5.13. The d_0 resolution σ^{d_0} for the full Belle II detector is

$$\begin{aligned} a &= \sigma_{int} = (10.3 \pm 0.1) \mu\text{m} \\ b &= (14.9 \pm 0.1) \text{ GeV } \mu\text{m} \end{aligned}$$

and for the z_0 resolution σ^{z_0}

$$\begin{aligned} a &= \sigma_{int} = (12.9 \pm 0.1) \mu\text{m} \\ b &= (15.4 \pm 0.1) \text{ GeV } \mu\text{m} \end{aligned}$$

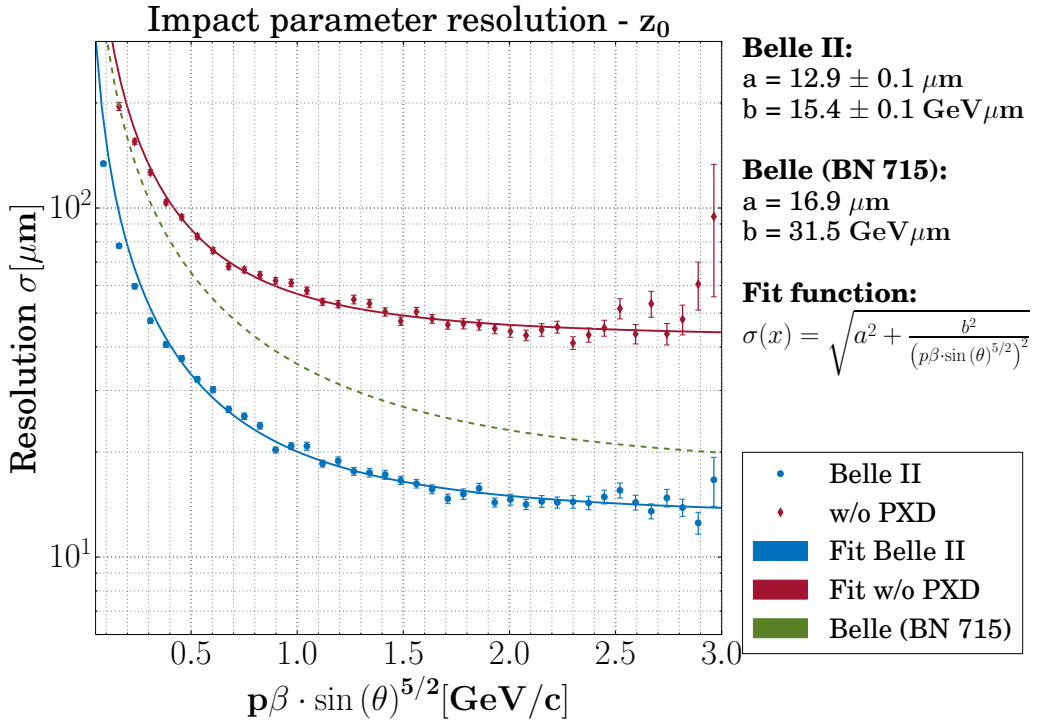


Figure 5.21: Impact parameter resolution for z_0 . The lower curve represents the Belle II detector, the dashed, green curve the Belle detector and the upper curve the Belle II detector without the PXD.

Figures 5.20 and 5.21 show that the expected impact parameter resolution of Belle II improves by roughly a factor of two compared to Belle. Without the PXD, the resolution is comparable to the one at Belle (d_0) or even worse (z_0). This proves that the PXD is crucial for achieving an excellent impact parameter resolution and that the PXD is essential for the precise reconstruction of vertices and, in turn, the precise measurement of the time-dependent asymmetry of the B -meson decay rate.

6 Measurement of e^+e^- pairs from the two-photon process

6.1 Introduction

The SuperKEKB accelerator will produce particle beams with a vertical size of only 48 nm, a size that has never been reached in a particle collider before. While this will allow SuperKEKB to reach unprecedented luminosity values and, in turn, will open the door to study physics beyond the Standard Model, it will also produce a much higher background at Belle II in comparison to that at Belle. This is particularly true for the PXD, as this sub-detector is located very close to the interaction point. The amount of background, however, is largely unknown as there is no experience with a pixel detector at such a high luminosity accelerator. In order to estimate the expected amount of background, Monte Carlo techniques have to be employed. Of particular interest is the amount of background contributed by the two-photon QED process

$$e^+e^- \rightarrow e^+e^-\gamma\gamma \rightarrow e^+e^-e^+e^-$$

This process has a very large cross-section and dominates all other production processes found at SuperKEKB. While its physics is of minor interest at Belle II, its large cross-section in combination with the high luminosity at SuperKEKB makes it one of the most important background processes at the Belle II experiment. Almost all outgoing particles carry a very low transverse momentum which confines them to the innermost region around the IP. This means that this process does not contribute to the backgrounds of most of the Belle II sub-detectors. Moreover, as a QED process originating from the IP, its particle density is expected to scale roughly like r^{-2} where r is the radius from the IP, reducing its impact on the outer detectors even further. In fact, it turns out that this background process is only relevant for the PXD at SuperKEKB. On the other hand, it is by far the largest PXD background contribution, as it is shown in the next chapter. It is apparent that the dominant nature of this process requires a thorough investigation of the reliability of the event generators that are used for the Monte Carlo production, especially those at Belle II, as the Monte Carlo generators at hand have been developed for and tested at e^+e^- colliders running at a much higher centre-of-mass energy, such as LEP [200].

This chapter is devoted to the examination of the validity of the Monte Carlo $e^+e^- \rightarrow e^+e^-e^+e^-$ generators for the Belle II centre-of-mass energy. For this purpose special data was taken at the Belle experiment in 2010, shortly before the KEKB accelerator and the Belle detector were shut down. After an introduction to the importance of the two-photon process and a brief overview of the experiment at which the data was taken, the chapter presents two analyses of the data and their results. The first analysis focuses on the dominating, low p_t region of two-photon events, while the second analysis explores the high p_t nature of the two-photon process at hand. Two different Monte Carlo generators are studied and their output is compared to the result of the data analyses.

6.2 Two-photon processes

The interaction of photons with each other cannot be described by the classical Maxwell theory of electromagnetism because of the linear nature of the Maxwell equations. However, in the framework of quantum electrodynamics (QED), photons can interact by fluctuating into charged particle pairs. The lifetime of the intermediate state follows from the Heisenberg uncertainty principle

$$\Delta t = \frac{2E_\gamma}{m_{pair}^2}$$

where E_γ is the energy of the photon and m_{pair} the mass of the intermediate state particles. This allows for **elastic** as well as **inelastic** scattering of two photons, illustrated by the Feynman diagrams in figure 6.1.

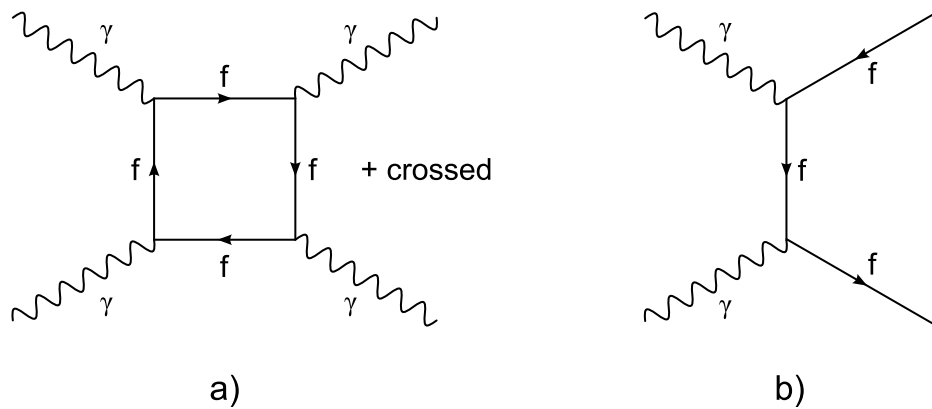


Figure 6.1: The Feynman diagrams for $\gamma\gamma$ scattering in QED: **a)** elastic $\gamma\gamma$ scattering, **b)** inelastic $\gamma\gamma$ scattering.

For low energetic photons, $E_\gamma \ll m_e c^2$, the cross-section for these processes becomes very small [201]. For example, for visible light ($E_\gamma \sim 1\text{eV}$), the cross-section is $\sim 10^{-65}\text{cm}^2$ and thus too small to be measured. If the energy of each photon is $E_\gamma > mc^2$, where m is the mass of a charged particle, two photons are able to produce a pair of charged particles x^+x^-

$$\gamma\gamma \rightarrow x^+x^-$$

The cross-section for the production of a charged lepton or hadron pair x^+x^- from two photons is

$$\sigma_{\gamma\gamma \rightarrow x^+x^-} = \frac{4\pi\alpha^2}{s} \ln \frac{s}{m_x^2 c^4} \quad (6.1)$$

where s is the square of the centre-of-mass energy of the system \sqrt{s} and m_x is the mass of the lepton/hadron. The highly energetic photons required for this process are available at e^+e^- colliders such as SuperKEKB because the relativistic beam particles are accompanied by electromagnetic fields, causing the radiation of quasi-real photons [202]. Those photons collide and can produce a pair of charged particles x^+x^- via

$$e^+e^- \rightarrow e^+e^-\gamma\gamma \rightarrow e^+e^-x^+x^-$$

This is the **two-photon process**, a pure QED process which was discovered experimentally 1971 at the VEPP-2 experiment in Novosibirsk [203]. The kinematics in the centre-of-mass system are illustrated in figure 6.2.

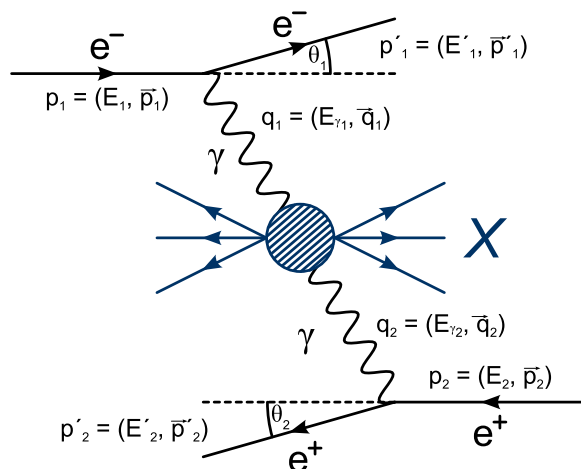


Figure 6.2: The kinematics of the two-photon process $e^+e^- \rightarrow e^+e^-\gamma\gamma \rightarrow e^+e^-X$ in the centre-of-mass system.

The incoming electron has the 4-vector $p_1(E_1, \vec{p}_1)$ and the positron the 4-vector $p_2(E_2, \vec{p}_2)$, with their energies given by the beam energy $E_b = \sqrt{s}/2 = E_1 = E_2$. After the interaction the **scattered electron** leaves under the angle θ_1 and the **scattered positron** under θ_2 with the respective 4-momenta $p'_1(E'_1, \vec{p}'_1)$ and $p'_2(E'_2, \vec{p}'_2)$. The 4-momenta of the two photons are given by

$$q_1 = p_1 - p'_1 \quad q_2 = p_2 - p'_2$$

The squared photon mass can be expressed as

$$\begin{aligned} q_i^2 &= (p_i - p'_i)^2 \\ &= 2m_e^2 - 2E_b E'_i \left(1 - \sqrt{1 - \left(\frac{m_e}{E_b} \right)^2} \sqrt{1 - \left(\frac{m_e}{E'_i} \right)^2} \cos \theta_i \right) \\ &\approx -2E_b E'_i (1 - \cos \theta_i) \end{aligned}$$

with the approximation being valid as long as $E'_i \gg m_e$, which is the case at SuperKEKB. The **virtuality** of the photons is defined as

$$Q_i^2 \equiv -q_i^2$$

where a photon is called **quasi-real** if its Q_i^2 value is close to zero, meaning that the photon is produced nearly on mass shell. For a high Q_i^2 value, the photon is produced off mass shell and thus called **virtual**. Due to the Bremsstrahlung nature of the two-photon process, the small momentum transfer region of the reaction dominates the cross-section. Thus, the scattered electrons (positrons) peak very strongly in the forward (backward) direction. In the Belle II experiment most of them disappear undetected in the beampipe. Based on their kinematics, the detection capabilities of two-photon processes can be divided into the following categories:

- **No-Tag (untagged):**

Neither the scattered electron nor the scattered positron is detected. The analysis presented in this chapter studies events of this kind.

- **Single-Tag:**

Either the scattered electron or the scattered positron is detected. This can be used to reconstruct the virtuality of one photon, if the other photon is assumed to be quasi-real. At high energies this type of process can be regarded as deep inelastic electron-photon scattering.

- **Double-Tag:**

Both scattered particles are detected, which allows the full reconstruction of both photons

and, in turn, the kinematics of the event. This requires the electron and the positron to scatter under large angles, which makes the produced photons highly virtual and this type of event strongly suppressed.

The calculation of the Feynman graphs of the two-photon process is straightforward but tedious [204]. The cross-section for the two-photon production of a lepton pair l^+l^- in a e^+e^- collision was calculated by Landau and Lifshitz [205, 206]

$$\sigma_{e^+e^- \rightarrow e^+e^- l^+l^-} = \frac{28\alpha^4}{27\pi m_l^2} \left(\ln \frac{s}{m_e^2} \right)^2 \ln \frac{s}{m_l^2} \quad l \equiv e \text{ or } \mu \quad (6.2)$$

The cross-section scales $\propto m_l^{-2}$ where m_l is the mass of the lepton. Since the mass of the muon is roughly a factor 205 larger than the mass of the electron, the cross-section for the process $e^+e^- \rightarrow e^+e^- e^+e^-$ is about $4 \cdot 10^4$ larger than that of the process $e^+e^- \rightarrow e^+e^- \mu^+\mu^-$. This means that the production of electron-positron pairs dominates the two-photon processes. A more accurate cross-section calculation for the two-photon production of electron-positron pairs has been carried out in [207]

$$\sigma_{e^+e^- \rightarrow e^+e^- e^+e^-} = \frac{\alpha^4}{27\pi m_e^2} [28L^3 - 178L^2 + (490 - 82\pi^2)L] \quad (6.3)$$

where $L = \ln(s/m_e^2)$. Using the centre-of-mass energy of 10.58 GeV at SuperKEKB, the total cross-section for the two-photon electron-positron pair production is estimated to ~ 5 mb.

In general there are two ways for an e^+e^- collider to produce a final state X : either via annihilation or via two-photon interactions. Figure 6.3 shows the Feynman diagrams of both processes.

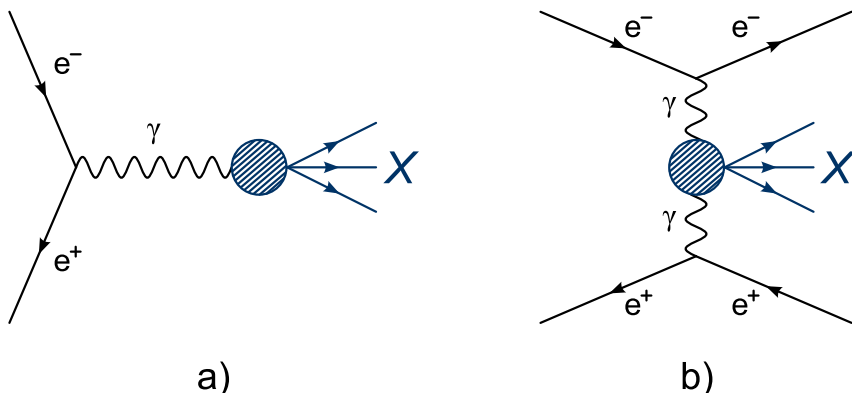


Figure 6.3: The production of a final state X in e^+e^- collisions at SuperKEKB: **a)** production via the annihilation process, **b)** production via the two-photon process.

The cross-section of the annihilation process scales like [201]

$$\sigma_{e^+e^- \rightarrow X} \sim \alpha^2 \frac{\hbar^2 c^4}{s} \quad (6.4)$$

The annihilation cross-section is proportional to α^2 compared to the two-photon process which scales with α^4 (equation 6.2). This seems to result in a small two-photon cross-section. However, the two-photon cross-section increases like $\ln(s)$ with the centre-of-mass energy, while the annihilation cross-section decreases like s^{-1} . The dependence of the cross-sections on the centre-of-mass energy is plotted in figure 6.4. In addition, the cross-section for the production of hadrons via annihilation and two-photon processes is shown. As can be seen from the figure, the two-photon processes dominate for centre-of-mass energies above a few GeV. The two-photon process provides a test of QED to α^4 at large momentum transfers and offers a wide field of research. However, due to its large cross-section and its dominant nature, the process $e^+e^- \rightarrow e^+e^- + e^+e^-$ is considered a major background rather than a signal at Belle II.

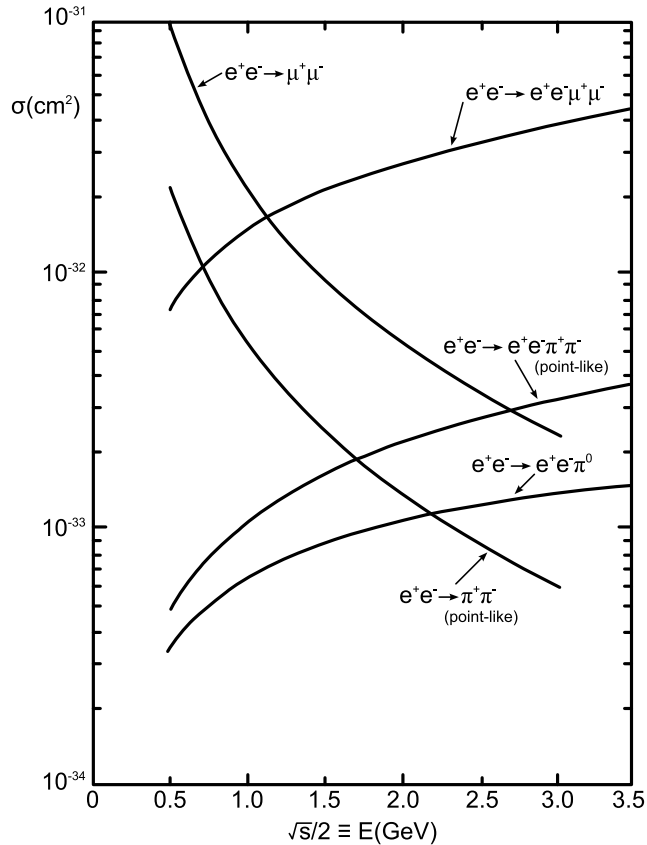


Figure 6.4: The production cross-sections for colliding e^+e^- particles [206]: $e^+e^- \rightarrow e^+e^-\pi^+\pi^-$, $e^+e^- \rightarrow e^+e^-\mu^+\mu^-$, $e^+e^- \rightarrow e^+e^-\pi^0$ (two-photon production) and $e^+e^- \rightarrow \pi^+\pi^-$, $e^+e^- \rightarrow \mu^+\mu^-$ (annihilation)

6.3 Generation of Monte Carlo events

The analyses presented in this chapter revolve around the four fermion final state reaction $e^+e^- \rightarrow e^+e^-l^+l^-$ where the leptons in the final state are e^\pm . The lowest order Feynman diagrams, contributing to this pure QED process, are shown in figure 6.5.

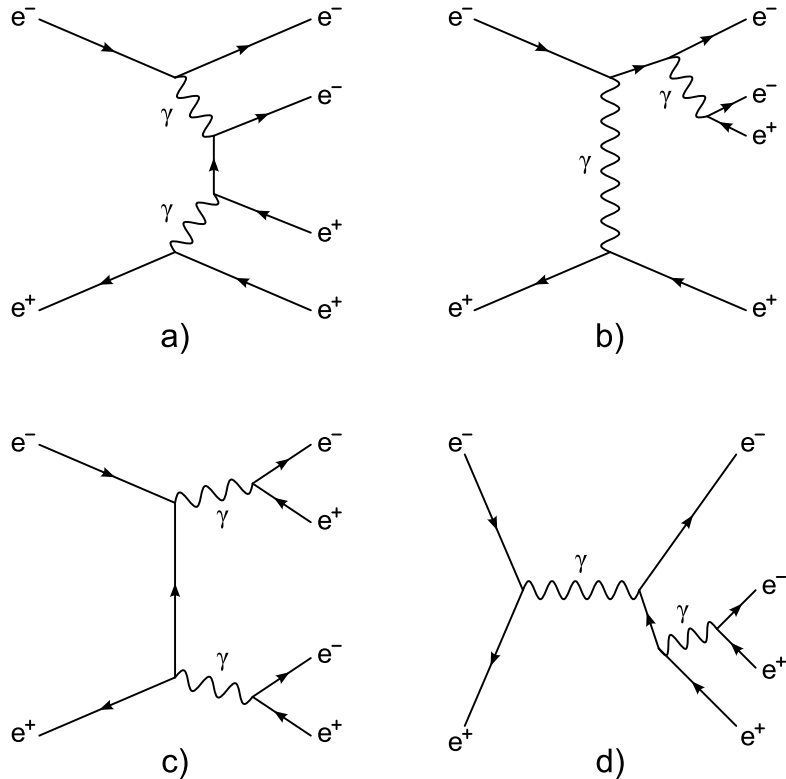


Figure 6.5: The lowest order Feynman diagrams for the process $e^+e^- \rightarrow e^+e^-e^+e^-$: **a)** multiperipheral, **b)** bremsstrahlung, **c)** conversion and **d)** annihilation. **a)** and **b)** are *t*-channel diagrams, **c)** and **d)** involve *s*-channel diagrams.

In the previous section it was shown that the dominating contribution to the total cross-section originates from the multiperipheral, two-photon Feynman diagram (diagram *a* in figure 6.5). The contribution of the other diagrams is small due to either their annihilation nature or because they are suppressed by photon propagators. Therefore, in the following, the process $e^+e^- \rightarrow e^+e^-e^+e^-$ will often be called the **two-photon process**. In order to compare experimental measurements with predictions from theory, distributions of various observables are studied. Usually, those distributions are gained by performing a multi-dimensional integration over a set of probability distributions. However, often it is not possible to find an analytic solution for the integrals and Monte Carlo methods are employed. This leads to the term **Monte Carlo generator**, describing a software tool that generates events for one or more specific processes.

6.3.1 The generators

In the following, the three Monte Carlo generators that are used throughout the analyses are presented.

KoralW

KoralW [178] is a powerful Monte Carlo generator for the simulation of every possible 4-fermion final state in a e^+e^- collision. It covers all lowest order

$$e^+e^- \rightarrow 4f + n\gamma \quad (n = 0, 1, 2, \dots)$$

processes and includes radiative corrections such as initial-state radiation (ISR) and the Coulomb effect. The event generation makes use of the exact Born-level matrix element, which was generated using the GRACE system of the MINAMI-TATEYA collaboration [208]. An efficient event generation is accomplished by employing two independent 4-fermion phase-space pre-samplers [209] that account for all kinematic singularities in the 4-fermion processes. The simulation of the ISR is based on the Yennie-Frautschi-Suura (YFS) procedure [210, 211] and the Coulomb correction is implemented according to [212, 213]. The analyses use version 1.53.3 of KoralW [178, 214] which has been modified by the KoralW authors for this thesis to use quadruple precision for its calculations.

BDK

BDK¹ [215] is an earlier Monte Carlo generator for the simulation of the process

$$e^+e^- \rightarrow e^+e^-l^+l^-$$

where l^+l^- is a lepton pair. It takes into account all Feynman diagrams shown in figure 6.5. For the process $e^+e^- \rightarrow e^+e^-e^+e^-$ this results in a total number of 36 diagrams. What makes the two-photon process special is the fact that it gives rise to 657 different peaks in a seven-dimensional phase-space. BDK treats those by dividing the 36 Feynman diagrams into four groups. Each group gets a separate Monte Carlo generator assigned whose phase-space variables are chosen such that the peaking structure is properly described. The interference between the groups is taken care of by imposing a weight to the events. The BDK generator is optimised for no-tag events, which makes it particularly suited for the analysis at hand. A disadvantage

¹Also known as **DIAG36** in the literature.

of BDK though, when compared to KoralW, is its lack of radiative corrections. However, the contribution of radiative corrections, especially in the case of no-tag events, is considered to be small. The Belle software BASF [163] contains an implementation of BDK, called **aafhb**, which has been optimised for Belle. The analyses presented in this chapter make use of this version of BDK.

BHWide

Unlike KoralW and BDK, BHWide [176] is not a 4-fermion final state Monte Carlo generator. It is a large angle Bhabha generator, widely used in the high energy physics community for the simulation of radiative Bhabha scattering. BHWide is based on the YFS procedure [210] and the Monte Carlo generator BHLUMI [216]. Within the second analysis presented in this chapter, its purpose is to provide the Monte Carlo data for the measurement of the luminosity value and the normalisation factor for the two-photon result from reconstructed Bhabha events. Moreover, Bhabha scattering is considered a background processes for the two-photon analysis and BHWide is employed to estimate the Bhabha contamination in the final analysis result. The BHWide generator was implemented as a module into the Belle II software framework basf2 by the author of this thesis.

6.3.2 The two-photon event production

The production of Monte Carlo data for the two-photon analyses is split into two steps. In the first step a Monte Carlo generator produces a list of events, where each event contains the 4-vector description of the outgoing particles. In the second step the 4-vector data is handed over to the full detector simulation, which simulates the response of the Belle detector to the traversing particles. Due to limitations in the simulation software of BASF², all particles with a polar angle outside the detector acceptance are removed from the event prior to the simulation. This section presents the details of the Monte Carlo production of KoralW and BDK events.

The first generator, KoralW, can produce events with equal probability upon user request. Internally, however, events are not generated with equal probability. Instead, each event gets a **weight** value assigned. This value states how probable the event is. To be more precise, this value is defined as the ratio of the matrix element squared over the phase space Jacobian [217]. The total cross-section is then computed as the average of the weights of all generated events. Figure 6.6 shows the distribution of the KoralW event weights and indicates the value of the **maximum weight**.

In order to obtain events that respect the correct distributions of kinematic variables and thus resemble real events taken at a detector, the events have to be “unweighted”. This is accomplished

²finite size of the array for secondary particles in GEANT

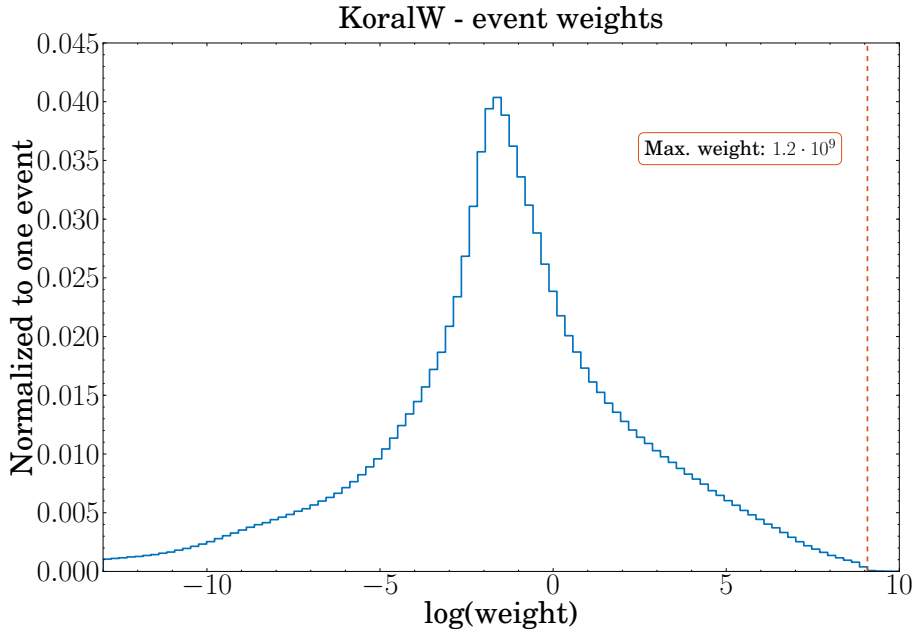


Figure 6.6: The KoralW event weights. The dashed line indicates the maximum weight.

with a simple event rejection method. The method starts by requesting an event, including its weight, from KoralW. A random number is generated from a flat distribution in the interval $[0, 1)$. If the ratio of the event weight to the maximum weight is smaller than the random number, the event is rejected and the steps of the method are repeated. Otherwise the event is taken and its weight is set to 1.0. After having generated the events, KoralW provides the total cross-section together with its statistical error. The version of KoralW [214] employed for the low p_t analysis uses double precision but for the high p_t analysis the generator has been modified by its authors to use quadruple precision in order to achieve numerical stability under the challenging phase space beyond $p_t > 250\text{MeV}$. It is found, however, that the speed with which KoralW generates unweighted events suffers from the quadruple precision. Therefore, a set of low-level cuts, restricting the polar angle of the outgoing leptons, is introduced before the matrix element calculations in KoralW. This helps to reduce CPU consumption. In order to find the optimal values for the cuts, a visible cross-section stability test for the detector acceptance is performed. The visible cross-section is defined as the cross-section that is seen after a number of cuts. Since the polar angle cuts have no effect on the maximum weight, which is verified by producing weighted events for each polar angle configuration, the maximum weight from figure 6.6 is valid for all configurations. Table A.1 in the appendix lists the polar angle configurations used for the visible cross-section stability test.

Figure 6.7 shows the visible cross-section for different polar angle configurations. The visible cross-section starts descending around the configuration representing the detector acceptance.

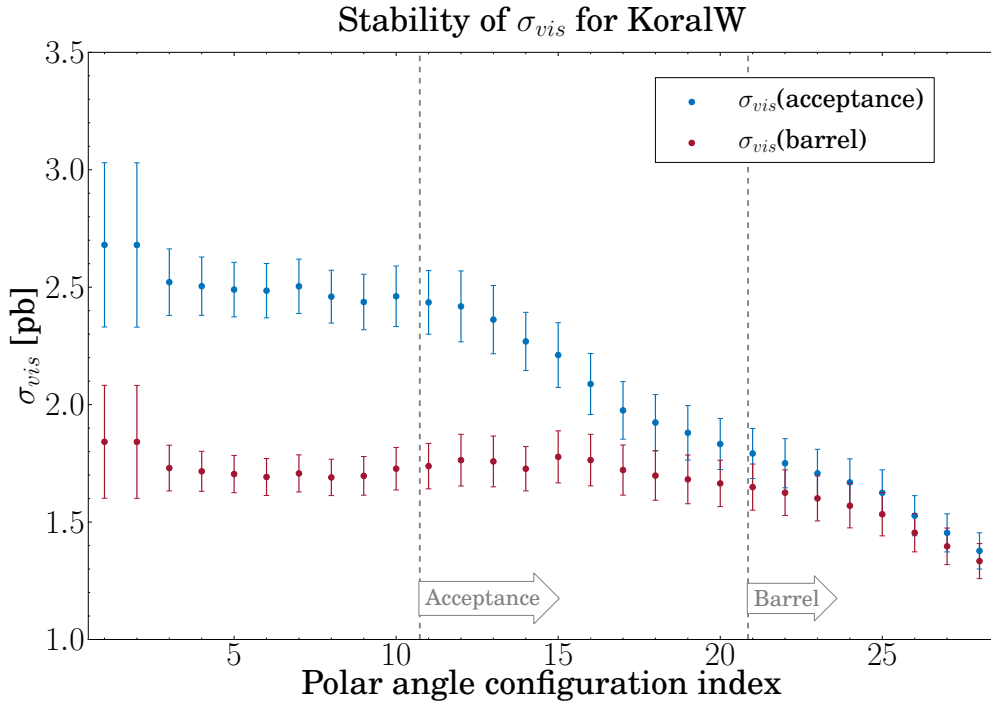


Figure 6.7: Stability of σ_{vis} (KoralW) for different polar angle configurations.

Choosing configuration 8 and the settings listed in table A.2 in the appendix for the KoralW Monte Carlo data generation results in a total cross-section of

$$\sigma_{KW} = (2.66 \pm 0.13) \cdot 10^9 \text{ pb} \quad (6.5)$$

As can be seen from table A.1, the time per event for configuration 8 is very close to the minimum, resulting in a speed gain of about 37 % when compared to a Monte Carlo production without any cuts. BDK generates internally weighted events as well. It contains the exact same event rejection method as explained above and delivers unweighted events together with the total cross-section for the settings listed in table A.3 in the appendix

$$\sigma_{BDK} = 7.337 \cdot 10^9 \text{ pb} \quad (6.6)$$

6.3.3 4-vector comparison

In order to gain a preliminary understanding of the differences between KoralW and BDK, the momentum spectra and the event topology of both generators are compared. Three different cuts are applied and the behaviour of the Monte Carlo generators under those cuts is studied. The cuts are executed in the following order:

1. Detector acceptance cut

Only particles that make it into the detector are kept. This means the polar angle θ_{lab} of the particle, measured in the laboratory system, has to be within the Belle detector acceptance

$$17^\circ < \theta_{lab} < 150^\circ$$

Particles have to leave the beampipe and enter the detector volume. This is accomplished by accepting only those particles that have a minimum transverse momentum³ p_t , measured in the laboratory system, of:

$$p_t > 2.25 \text{ MeV}$$

Events passing this cut are candidates for the low p_t analysis described in section 6.5.

2. Transverse momentum cut

An additional p_t cut of 300 MeV is applied, in order to make sure the particles reach the outer sub-detectors of the Belle detector as they are important for identifying the particle type.

3. Barrel polar angle cut

The barrel polar angle cut restricts the polar angle of the accepted particles even further. The barrel part of the detector, given by the polar angle range

$$46.742^\circ < \theta_{CMS} < 145.715^\circ$$

is known to provide the best tracking resolution and particle identification efficiency and thus is of particular interest for the high p_t analysis in section 6.6.

All events which have no electron or positron left after a cut are removed. For the 4-vector comparison described in this section, $1.34 \cdot 10^7$ KoralW events are generated, which corresponds to a luminosity of

$$L_{KW} = 5.03 \cdot 10^{-3} \text{ pb}^{-1} \quad (6.7)$$

³The transverse momentum p_t of a particle with momentum $\vec{p} = (p_x, p_y, p_z)$ is defined as:

$$p_t = \sqrt{p_x^2 + p_y^2}$$

Using the settings listed in table A.3 in the appendix, a total number of $1.51 \cdot 10^9$ BDK events are generated, representing a generated luminosity of

$$L_{BDK} = 2.06 \cdot 10^{-1} \text{ pb}^{-1} \quad (6.8)$$

By using the luminosity values, the visible cross-section σ_{vis} after each cut is calculated and, together with the number of events, listed in table 6.1.

	Generator	Input	Acceptance	p_t	Barrel
Events	KoralW	$1.34 \cdot 10^7$	326958	1138	899
	BDK	$1.51 \cdot 10^9$	9318532	437	216
σ_{vis} [pb]	KoralW	$2.67 \cdot 10^9$	$6.50 \cdot 10^7$	$2.26 \cdot 10^5$	$1.79 \cdot 10^5$
	BDK	$7.33 \cdot 10^9$	$4.53 \cdot 10^7$	$2.12 \cdot 10^3$	$1.05 \cdot 10^3$

Table 6.1: The table summarises the number of events after each cut and the calculated values for the visible cross-section.

Since the initial cross-sections given by each generator depend on internal generator cuts and settings, they cannot be compared directly. However, the visible cross-sections after the acceptance cut should agree as both generators describe the same physics process. From table 6.1 it can be seen that for the acceptance cut both generators show a “good agreement” in the visible cross-section. However, starting with the 300 MeV p_t cut the values of the visible-cross section differ by two orders of magnitude between KoralW and BDK. The main source for the deviation is the p_t cut as the barrel cut does not worsen the difference in the visible cross-sections. This leads to the conclusion that for larger values of p_t the transverse momentum spectra for KoralW and BDK should show a significant deviation. This is indeed the case as figure 6.8 shows. The left plot shows the transverse momentum for the full p_t range, while the right plot shows the range up to 100 MeV. In both cases the transverse momentum of the e^-/e^+ with the highest p_t after the acceptance cut is plotted.

It is obvious from the left plot that for larger p_t the KoralW spectrum saturates and exhibits a plateau, while the BDK spectrum falls rapidly. On the other hand, for the dominating p_t range below 20 MeV, which is of particular interest for the PXD at Belle II, both spectra show a very similar behaviour. Thus, one can conclude that both generators are good enough in order to provide the data required for the estimation of the PXD background. However, it should be noted that additional contribution to the PXD background may come from back-scattered particles originating from large p_t particles. In addition, the background in the outer sub-detectors is caused by particles with a large p_t . Therefore it is important to make sure that the selected two-photon generator also performs correctly in the higher p_t regions. It is interesting to see that on the generator level KoralW and BDK already differ quite significantly for

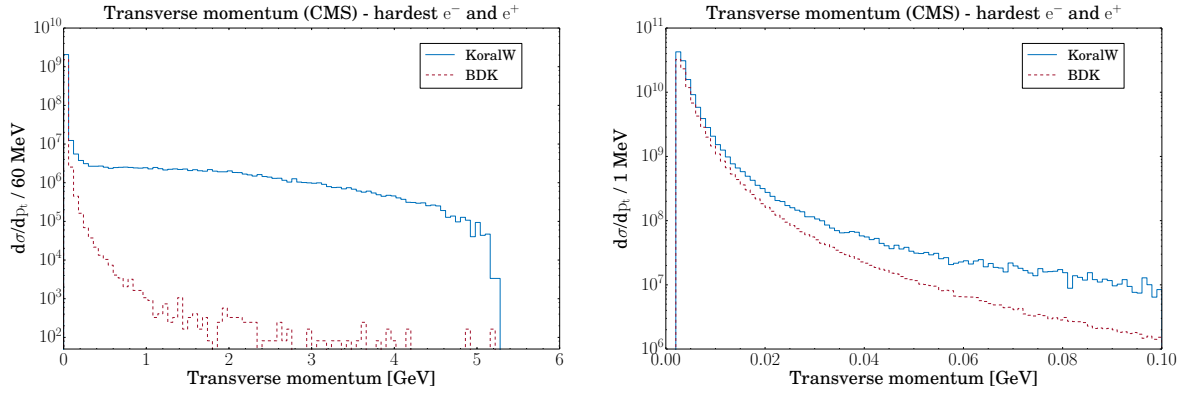


Figure 6.8: The transverse momentum of KoralW (solid line) and BDK (dashed line) in the centre-of-mass system after the acceptance cut. The left plot shows the momentum up to 6 GeV and the right plot up to 100 MeV.

larger values of p_t . This shows clearly that only the comparison with real data allows the validation of the two-photon Monte Carlo generators at hand. The validation is performed for the low p_t and the high p_t region separately, as both regions demand a different analysis approach. Section 6.5 and 6.6 explain the analyses in detail.

6.4 The QED Experiment at Belle

The experimental data for the two-photon analyses was taken at the Belle detector, the predecessor of Belle II, at the KEKB accelerator in Japan. In the following, the KEKB accelerator and the Belle detector are briefly introduced. A complete description can be found in [74] and [156].

6.4.1 The KEKB asymmetric electron-positron collider

The **KEKB** accelerator [74] is the predecessor of the SuperKEKB accelerator. It started operation in December 1998 and was shut-down in June 2010. During its operational life, it delivered about 1052 fb^{-1} of data and set the luminosity world-record of $2.11 \times 10^{34} \text{ cm}^{-2} \text{ s}^{-1}$. Since SuperKEKB is an upgrade to KEKB, both accelerators have a lot in common. The most important differences that play a role in this analysis between both accelerators are listed in table 6.2.

	Belle	Belle II	
E_{HER}	7.998 GeV	7 GeV	Beam energy of HER
E_{LER}	3.499 GeV	4 GeV	Beam energy of LER
ϕ	22 mrad	83 mrad	Crossing angle of beams
ψ	0	41.5 mrad	Angle between detector z-axis and LER
β	0.391	0.276	
$\beta\gamma$	0.425	0.287	

Table 6.2: Comparison of the beam parameters of KEKB and SuperKEKB and their respective boosts.

6.4.2 The Belle detector

The Belle II detector presented in chapter 4 is based on the Belle detector [156], which successfully took data for more than 10 years. Although the overall structure stays the same, Belle II contains so many changes compared to Belle that it can be considered a new detector. Therefore, the Belle detector will be introduced with a little bit more detail than the KEKB accelerator.

A two-wall beryllium **beampipe** with an inner radius of 15 mm surrounds the interaction point. A 2.5 mm gap between the two walls allows for a helium-gas flow to cool the beampipe. The innermost detector is a four layer silicon strip detector, called the **SVD2** [218]. Its four layers are at radii of 20 mm, 43.5 mm, 70 mm and 88 mm and cover the full polar angle acceptance of $17^\circ < \theta < 150^\circ$. Unlike the SVD in Belle II, it does not contain slanted parts in the forward direction. The **CDC** of Belle is composed of 50 cylindrical layers and filled with the same helium

and ethane gas mixture as the Belle II CDC. Its inner radius is 294 mm and its outer radius is 880 mm. This complements the tracking system of Belle.

The PID system uses an aerogel Cherenkov counter (**ACC**) [219] in the forward endcap and a time-of-flight counter (**TOF**) [220] in the barrel part of the detector. The main goal of the ACC is to efficiently distinguish pions from kaons by means of an array of silica aerogel threshold Cherenkov counters. The measurement principle is exactly the same as for the ARICH in Belle II. The TOF, however, is a sub-detector that is not present at Belle II anymore. It has been replaced by the TOP. The TOF covers Belle's barrel polar angle region of $33^\circ < \theta < 121^\circ$ and measures the time of flight of a particle from the interaction point to a TOF module. The signal of the TOF is used to distinguish pions and kaons with momenta lower than 1.2 GeV as well as an input for the trigger system.

The electromagnetic calorimeter (**ECL**) [221] and the **KLM** [222] remain almost unchanged at Belle II, thus section 4.8 and 4.10 apply to Belle as well. The whole Belle detector is immersed in a 1.5 T magnetic field, which is generated by the same superconducting solenoid coil as at Belle II.

The coordinate system at Belle is a right-handed, Cartesian coordinate system with the x -axis pointing to the outside of the ring and the y -axis vertically upwards. This definition is in accordance with the one at Belle II. Unlike the Belle II system, however, the z -axis at Belle is aligned with the LER and points in the opposite direction of the positron momentum. This is the reason for the introduction of the angle ψ in table 6.2.

6.4.3 The dedicated background experiment

On May 28th, 2010, one month before the accelerator and the detector was shut down forever, a series of special experiments were conducted at Belle. The author of this thesis was involved in the planning and preparation (e.g. DAQ histograms, triggers) of the experiments and took the data during his detector shifts. The aim of those experiments was to collect data that can be used to validate the output of the Monte Carlo generators KoralW and BDK. From the 22 runs⁴ that were taken, 17 contain valid data and are used for the analyses described in this chapter. Table A.4 in the appendix lists the official Belle run summary for those 17 valid runs. As it will be shown in the upcoming section, most leptons originating from the two-photon process have a transverse momentum of less than about 100 MeV. This means, most particles hardly ever reach the centre of the CDC or any detector further outward. Since the central trigger system of Belle is based on sub-detector trigger signals from the CDC, TOF, ECL, KLM and EFC [156], Belle would only be able to capture a very small fraction of the two-photon events with its standard trigger configuration. The trigger system at Belle did not have the capability to trigger on events

⁴The measurements are divided into periods, the so-called runs. The duration of a single run depends on the experiment at hand, but was limited to eight hours for physics runs at Belle.

that are relevant for the PXD background. Thus, a new trigger was introduced specifically for this experiment: a (truly) **random trigger**. It starts the readout cycle of the Belle detector at random times and is therefore independent of a specific event signal in the detector. This leads to the fact that physics events, consisting mostly of high energetic particles, are not dominating the recorded data, as it would be the case with the standard trigger configuration. The random trigger frequency was set to 400 Hz, close to the maximum trigger rate possible with the Belle trigger system. The trigger was labelled *random_ev* and carried the internal trigger bitmask 77. Thus, it will be called **Trg77** in the following. Almost all standard Belle triggers were set inactive for the time of the experiment. Among those still being active was the *brl_bhabha* trigger (bitmask 42, **Trg42**), which triggered on Bhabha-like events in the barrel region of the detector. The recorded data triggered by Trg42 is used in the high p_t analysis in order to calculate the luminosity for each run. Table 6.3 summarises the number of recorded events per trigger and per run for experiment 73.

Run	total	Trg77	Trg42	time [s]	L deliv [pb^{-1}]	L accum [pb^{-1}]	Experiment
401	502384	433721	54119	990.9	11.235	10.270	Type B:
403	509040	450420	43867	1029.3	9.089	8.280	Beam size
408	502680	453377	35034	1036.9	7.192	6.670	
409	443944	411137	20147	939.9	4.191	3.800	
411	512914	462426	35623	1057.1	7.392	6.750	
414	485416	419097	51771	958.1	10.723	9.860	Type A:
416	509021	449210	45118	1026.8	9.373	8.500	Separate
417	502004	455144	32898	1041.0	6.866	6.270	beams
418	510625	470788	25930	1077.7	5.352	4.910	
419	300234	291674	235	667.8	0.0	0.0	
420	100314	97592	75	223.5	0.0	0.0	
421	424769	366934	45176	838.3	9.419	8.570	Type C:
422	440175	385012	44723	879.7	9.333	8.450	Bunch
424	433993	385190	38783	880.5	8.051	7.280	current
425	429069	385446	33822	882.0	7.069	6.340	
426	424003	385654	28818	882.5	5.984	5.410	
427	200160	184635	11097	422.4	2.305	2.070	
Total	7230745	6487457	547236	14834.4	113.57	103.43	

Table 6.3: Run summary - Experiment 73. For each run the following information is shown: the total number of events, the number of events from the random trigger (Trg77), the number of Bhabha-like events (Trg42), the time the detector measured (total run time - detector dead time), the luminosity delivered from the accelerator, the accumulated luminosity by the detector. The runs are grouped according to the type of the sub-experiment, explained in detail in the text.

In order to differentiate between QED events, such as the two-photon events which scale with the luminosity, and beam background events, which scale with the beam conditions, the luminosity delivered from the accelerator has been varied on a run by run basis. By counting the hits in the SVD for each luminosity setup, one can then extrapolate to a zero luminosity scenario under which only beam background is present. Removing the zero luminosity contribution from the counted number of hits in the SVD for full luminosity, results in the SVD hit contribution of QED only, which can be compared to Monte Carlo data. This concept is summarised in figure 6.9 and is discussed in more detail in section 6.5 and in [223].

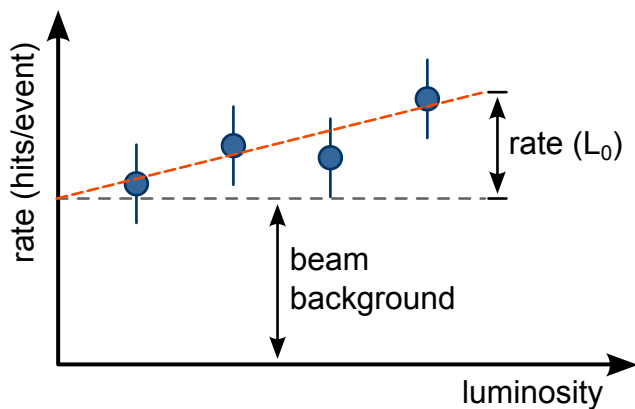


Figure 6.9: The concept behind the low p_t analysis: measure the SVD hits per event for different values of the luminosity. Then extrapolate to zero luminosity in order to retrieve the beam background contribution. The difference is then the rate of the luminosity dependent processes for full luminosity.

The variation of the luminosity has been accomplished by dividing the experiment into three (sub-)experiments, each employing a different method for tuning the luminosity. In each sub-experiment, the accelerator started with the Belle nominal luminosity and then decreased its value in several steps. The three sub-experiments were labelled A, B, C and have been executed in the following way:

(Sub-)experiment A - Separate beams

The luminosity scales linearly with the number of particles that collide. Thus, a way to decrease the luminosity is to reduce the number of colliding particles by introducing a transverse offset between the colliding beams. During the experiment, the beams were separated starting from their nominal position, to a complete separation at which the beams weren't colliding anymore. This can be seen in the decrease of the luminosity from $\sim 10 pb^{-1}$ to zero for the runs 414 to 420 in table 6.3.

(Sub-)experiment B - Beam size

The luminosity is also inversely proportional to the size of the beams. By expanding the height of the HER beam compared to the LER beam (except for run 409), the luminosity was reduced in steps of $\sim 2nb^{-1}s^{-1}$. The LER beam was not expanded as the LER is the dominating source for the Touschek beam background (see section 7.4.1) and the aim of the experiment was to not alter the beam background level. Table 6.4 lists the beam size changes for each run of sub-experiment B.

Run	401	403	408	409	411
HER width [μm]	460.8	443.3	428.6	432.0	420.6
HER height [μm]	2.1	2.4	2.7	3.4	2.8
LER width [μm]	264.4	265.8	274.1	277.3	271.1
LER height [μm]	2.4	2.4	2.5	3.8	2.5

Table 6.4: The increase of the beam size per run. Due to the squeezing of the beams, the change in height has a much larger influence on the luminosity than the change of the width of the beam.

(Sub-)experiment C - Beam current

The circulating bunches in the accelerator are subject to a continuous loss of particles due to scattering with the residual gas in the beampipe and intra-bunch interactions that kick the particles out of their nominal orbit. By injecting new bunches into the accelerator the loss of particles is compensated (see section 3.8). For sub-experiment C, the injection of new bunches was stopped leading to a decrease of the stored beam current over time. Because the luminosity scales linearly with the beam current the luminosity dropped as well. Table 6.5 summarises the development of the beam currents for each run of experiment 73.

The order of the (sub-)experiments was chosen such that the tasks that seemed easier to accomplish by the accelerator have been performed first. This means that sub-experiment **B** has been conducted before **A** and **C**.

Run	421	422	424	425	426	427
HER start [mA]	849.0	845.1	786.8	742.7	701.8	666.9
HER stop [mA]	848.9	796.2	744.5	705.0	668.5	651.6
LER start [mA]	1451.3	1438.9	1240.7	1094.6	965.2	822.8
LER stop [mA]	1447.4	1272.8	1100.5	975.3	827.6	657.8

Table 6.5: The beam currents for sub-experiment C in [mA]. The values for both, the start and the stop time of the run are given for HER and LER.

6.5 Analysis of low p_t two-photon events

The cross-section of the two-photon process peaks strongly towards small values of p_t as the spectrum in figure 6.8 shows. This means only a small number of particles make it into the CDC and can therefore be fully reconstructed using the information from Belle's tracking detectors. Most particles entering the detector are confined to the inner layers of the SVD. With the hits from the inner layers of the SVD only, a reliable, standalone reconstruction of the traversing particles is not possible. Thus, the analysis presented in this section performs a hit counting measurement in order to validate the Monte Carlo generators KoralW and BDK with recorded data in this dominating, low p_t region. The concept behind the analysis was motivated in section 6.4.3 and is summarised in figure 6.9. A detailed discussion can be found in Belle II Note 0012 [223].

6.5.1 SVD hit multiplicity measurement

The SVD2 sub-detector of the Belle detector uses the same measurement principle as the SVD of the Belle II detector (see chapter 4.4). It records two coordinates, also referred to as hits, of a traversing, charged particle. One coordinate in the detector's $r - \phi$ plane, and one in the $r - z$ plane. For the analysis at hand the location of each hit is not relevant, only the number of hits per event is counted. For each run of experiment 73 the number of hits per event is filled into a histogram and its mean is taken as the reading for the average hits per run. This is done for the $r - \phi$ and $r - z$ plane separately. Tables 6.6 and 6.7 list the result for all runs. From the tables one can see how the number of hits decline for decreasing values of the luminosity. Additionally, the number of hits also depend on the radius, as the declining values for each layer of the SVD2 show. This can be taken as a first hint that the data contains indeed two-photon events for which such a behaviour is expected. It should be noted that the innermost layer of the SVD2 was suffering from an increased noise level induced by an ageing VA1TA readout chip [224]. This lead to occupancy values of up to 10 % and explains part of the unproportionally large number of hits in the first layer of the SVD2 in comparison to the second layer. Another reason for the larger value lies in the nature of the low p_t particles. For the inner layer the chances are much higher that a particle is bent by the magnetic field in such a way that it travels through the inner layer multiple times.

Run	L [pb^{-1}]	Layer 1 <hits/event>	Layer 2 <hits/event>	Layer 3 <hits/event>	Layer 4 <hits/event>	Experiment
401	10.270	108.4 ± 0.2	48.7 ± 0.1	44.5 ± 0.1	39.2 ± 0.1	Type B:
403	8.280	103.2 ± 0.1	47.1 ± 0.1	43.7 ± 0.1	38.3 ± 0.1	Beam size
408	6.670	98.7 ± 0.1	46.0 ± 0.1	42.9 ± 0.1	37.6 ± 0.1	
409	3.800	86.2 ± 0.1	41.9 ± 0.1	38.9 ± 0.1	33.8 ± 0.1	
411	6.750	99.8 ± 0.1	46.5 ± 0.1	42.9 ± 0.1	38.2 ± 0.1	
414	9.860	108.3 ± 0.2	48.5 ± 0.1	44.2 ± 0.1	38.9 ± 0.1	Type A:
416	8.500	92.0 ± 0.1	42.9 ± 0.1	39.0 ± 0.1	34.1 ± 0.1	Separate
417	6.270	81.9 ± 0.1	39.8 ± 0.1	36.2 ± 0.1	31.6 ± 0.1	beams
418	4.910	76.6 ± 0.1	38.1 ± 0.1	35.1 ± 0.1	30.6 ± 0.1	
421	8.570	107.5 ± 0.2	48.2 ± 0.1	43.4 ± 0.1	38.3 ± 0.1	Type C:
422	8.450	100.5 ± 0.2	45.1 ± 0.1	40.1 ± 0.1	35.4 ± 0.1	Bunch
424	7.280	89.0 ± 0.1	40.8 ± 0.1	36.5 ± 0.1	31.9 ± 0.1	current
425	6.340	79.9 ± 0.1	37.2 ± 0.1	33.6 ± 0.1	29.1 ± 0.1	
426	5.410	73.2 ± 0.1	34.9 ± 0.1	31.4 ± 0.1	27.4 ± 0.1	
427	2.070	67.2 ± 0.2	32.9 ± 0.1	30.2 ± 0.1	26.1 ± 0.1	

Table 6.6: Hit multiplicity in the $r - z$ plane for all runs and all layers of the SVD2.

Run	L [pb^{-1}]	Layer 1 <hits/event>	Layer 2 <hits/event>	Layer 3 <hits/event>	Layer 4 <hits/event>	Experiment
401	10.270	103.7 ± 0.1	49.2 ± 0.1	38.3 ± 0.1	38.2 ± 0.1	Type B:
403	8.280	98.0 ± 0.1	47.5 ± 0.1	38.6 ± 0.1	37.5 ± 0.1	Beam size
408	6.670	92.9 ± 0.1	46.1 ± 0.1	37.9 ± 0.1	36.9 ± 0.1	
409	3.800	79.8 ± 0.1	41.2 ± 0.1	34.1 ± 0.1	33.2 ± 0.1	
411	6.750	93.8 ± 0.1	46.6 ± 0.1	36.7 ± 0.1	37.1 ± 0.1	
414	9.860	103.7 ± 0.1	49.1 ± 0.1	37.9 ± 0.1	38.0 ± 0.1	Type A:
416	8.500	87.4 ± 0.1	42.4 ± 0.1	33.5 ± 0.1	33.1 ± 0.1	Separate
417	6.270	77.0 ± 0.1	38.7 ± 0.1	31.7 ± 0.1	30.8 ± 0.1	beams
418	4.910	71.5 ± 0.1	36.8 ± 0.1	30.7 ± 0.1	29.8 ± 0.1	
421	8.570	102.9 ± 0.2	48.9 ± 0.1	37.3 ± 0.1	37.5 ± 0.1	Type C:
422	8.450	96.1 ± 0.1	45.6 ± 0.1	35.3 ± 0.1	34.8 ± 0.1	Bunch
424	7.280	84.9 ± 0.1	40.6 ± 0.1	32.3 ± 0.1	31.4 ± 0.1	current
425	6.340	75.9 ± 0.1	36.7 ± 0.1	29.6 ± 0.1	28.6 ± 0.1	
426	5.410	69.3 ± 0.1	33.9 ± 0.1	27.8 ± 0.1	26.9 ± 0.1	
427	2.070	63.1 ± 0.2	31.8 ± 0.1	26.7 ± 0.1	25.5 ± 0.1	

Table 6.7: Hit multiplicity in the $r - \phi$ plane for all runs and all layers of the SVD2.

6.5.2 CDC correction

The particles from low p_t two-photon events are not able to reach the CDC, thus the CDC can be used to suppress the contribution from luminosity dependent background processes, such as Bhabha scattering. The rate of the remaining luminosity dependent background processes that leave a signal in the SVD but not the CDC are considered to be negligible compared to the rate of the two-photon process. Plotting the average number of CDC hits per event and the CDC current for the different luminosity values results in figure 6.10.

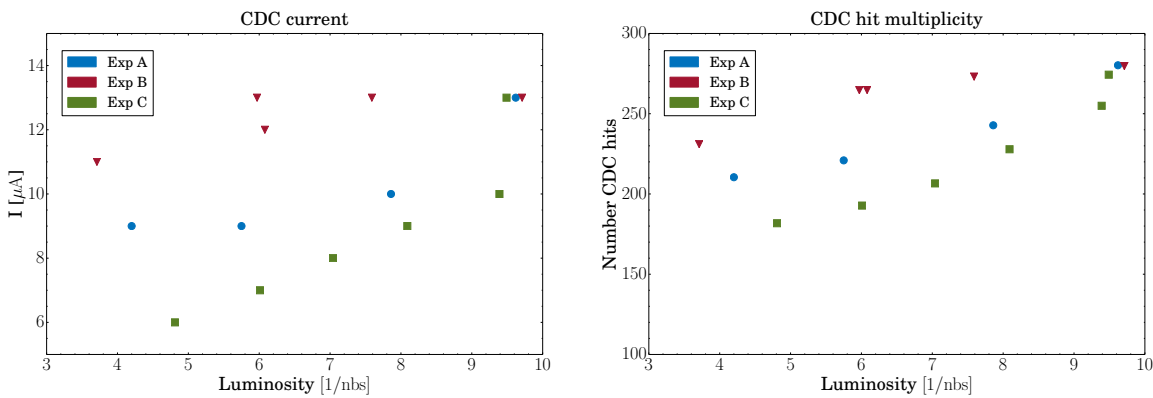


Figure 6.10: The CDC current (left) and CDC hit multiplicity as a function of the instantaneous luminosity.

The values are listed in table 6.8. From the figure it is apparent that both the number of hits and the current change with the luminosity. However, the change depends on the approach taken to reduce the luminosity. This means that the majority of events seen in the CDC are machine induced and do not originate from QED. The hits in the SVD are therefore produced by three types of processes: luminosity independent machine processes, luminosity dependent QED processes and luminosity dependent machine processes. In order to remove the contribution from luminosity dependent machine processes a correction based on the observed activity in the CDC is performed. The CDC current cannot be used for the correction as it shows large, periodic fluctuations that are related to the injection of the beam. Therefore the sum of the hit multiplicities for all 50 CDC layers is used. The correction is based on a reference luminosity L_{ref} and carried out as follows

$$N_{corr}^{SVD}(L_i) = N_{rec}^{SVD}(L_i) \cdot \frac{N^{CDC}(L_{ref})}{N^{CDC}(L_i)} \quad (6.9)$$

where $N_{corr}^{SVD}(L_i)$ is the corrected SVD hit multiplicity, $N_{rec}^{SVD}(L_i)$ the SVD hit multiplicity recorded for the luminosity L_i , $N^{CDC}(L_{ref})$ the CDC hit multiplicity for the reference luminosity and $N^{CDC}(L_i)$ the CDC hit multiplicity for the luminosity L_i . For the experiments A and B the highest luminosity is chosen as the reference luminosity, for experiment C the second highest.

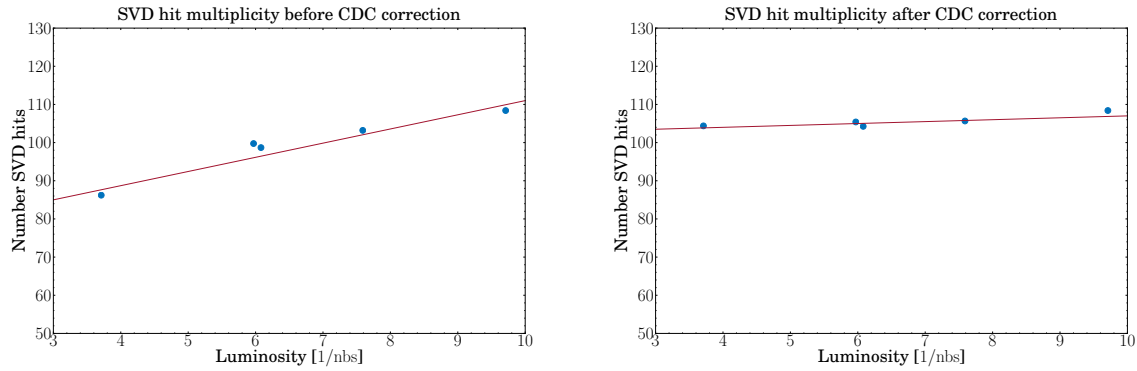


Figure 6.11: The hit multiplicities in the first SVD layer (rz -plane) for experiment B. Left: before the CDC correction; Right: after the CDC correction.

Figure 6.11 shows a comparison of the SVD hit multiplicities for the first SVD layer before and after the CDC correction. In order to estimate the QED contribution to the number of SVD hits for each run, the average number of SVD hits per event is corrected according to equation 6.9 for each run. Then, for each possible pair of runs within an experiment, the number of SVD hits is extrapolated to zero luminosity. The result for the three experiments is shown in figure 6.12. The distribution shows two peaks, one at about 0 hits and one at 12 hits. The peak at 12 hits originates from the first layer and is the result of the high background noise in the innermost layer of the SVD and the low p_t particles traversing the layer multiple times, as mentioned above. Table 6.9 lists the estimated QED contribution for all experiments and all layers of the SVD.

Run	L (run) [pb^{-1}]	L (inst) [1/nbs]	Hits <hits/event>	Current < μA >	Experiment
401	10.270	9.71	279.68	13	Type B:
403	8.280	7.59	273.15	13	Beam size
408	6.670	6.08	264.75	12	
409	3.800	3.71	231.02	11	
411	6.750	5.97	264.67	13	
414	9.860	9.62	280.19	13	Type A:
416	8.500	7.86	242.79	10	Separate
417	6.270	5.75	220.93	9	beams
418	4.910	4.20	210.43	9	
421	8.570	9.49	274.32	13	Type C:
422	8.450	9.39	254.95	10	Bunch
424	7.280	8.09	227.86	9	current
425	6.340	7.04	206.59	8	
426	5.410	6.01	192.77	7	
427	2.070	4.81	181.77	6	

Table 6.8: Hit multiplicity and current in the CDC for all runs.

Layer	Experiment A	Experiment B	Experiment C	All experiments
1	15.66 ± 0.47	13.65 ± 1.89	13.86 ± 2.20	14.27 ± 1.96
2	-2.07 ± 2.66	0.38 ± 1.74	-0.32 ± 2.45	-0.54 ± 2.48
3	-4.55 ± 0.55	-3.13 ± 1.75	-4.48 ± 0.53	-4.01 ± 1.32
4	-2.48 ± 0.63	-1.96 ± 1.00	-2.09 ± 0.25	-2.15 ± 0.73

Table 6.9: Estimated QED background contribution in each SVD layer.

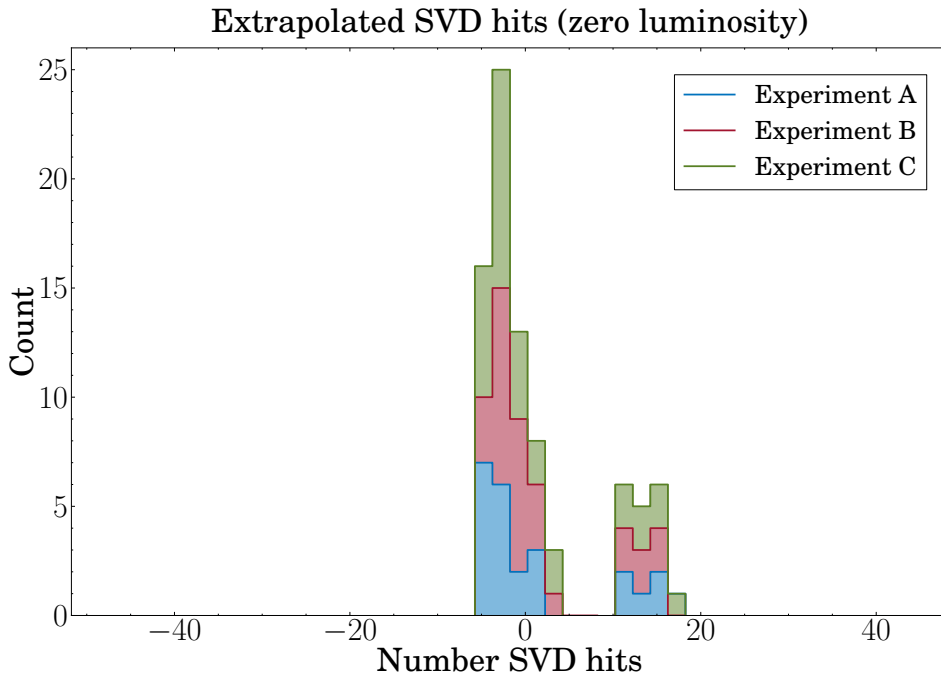


Figure 6.12: Stack plot for the three experiments of the number of hits extrapolated to zero luminosity.

6.5.3 Systematics

The correction of the average number of SVD hits recorded in the four SVD layers with the activity measured in the CDC introduces the largest systematic uncertainty for this analysis. In order to verify that the CDC correction method is robust under the selection of CDC layers, the correction factor is recalculated for various subsets of CDC layers. In table 6.10 the impact on the QED contribution result by dividing the 50 layers of the CDC into 5 subsets of 10 CDC layers each is listed. For further details see [223]. Another approach is to start with the full set of layers and incrementally reduce the number of layers by 10. The result is shown in table 6.11. The values are consistent with each other and the conclusion is drawn that the CDC correction method is reliable.

SVD layers	CDC layers	Experiment A	Experiment B	Experiment C	All
1 ($r - z$)	1 - 10	20.96 ± 1.90	16.41 ± 2.08	25.76 ± 0.71	21.05 ± 4.32
	10 - 20	6.85 ± 2.89	13.97 ± 2.56	1.73 ± 5.96	7.58 ± 6.71
	20 - 30	13.83 ± 0.52	11.56 ± 1.36	6.08 ± 3.24	10.19 ± 3.87
	30 - 40	16.07 ± 1.15	10.21 ± 1.31	7.96 ± 1.29	10.99 ± 3.49
	40 - 50	14.57 ± 0.63	9.90 ± 1.55	7.89 ± 0.96	10.45 ± 2.90
2-4	1 - 10	-0.73 ± 2.13	-0.37 ± 2.21	2.77 ± 2.51	0.67 ± 2.79
	10 - 20	-6.85 ± 2.20	-1.44 ± 2.28	-7.43 ± 2.72	-5.19 ± 3.69
	20 - 30	-3.82 ± 1.93	-2.45 ± 1.95	-5.61 ± 2.22	-3.98 ± 2.45
	30 - 40	-2.86 ± 2.00	-3.06 ± 1.93	-4.83 ± 2.16	-3.65 ± 2.23
	40 - 50	-3.51 ± 1.95	-3.19 ± 2.00	-4.87 ± 2.17	-3.89 ± 2.18

Table 6.10: Systematic study of the QED contribution for correction factors derived from different subsets of CDC layers.

SVD layers	CDC layers	Experiment A	Experiment B	Experiment C	All
1 ($r - z$)	10 - 50	12.02 ± 0.86	11.82 ± 1.78	5.36 ± 3.28	9.52 ± 3.90
	20 - 50	14.78 ± 0.51	10.62 ± 1.37	7.25 ± 1.88	10.53 ± 3.30
	30 - 50	15.34 ± 0.89	10.06 ± 1.42	7.93 ± 1.11	10.72 ± 3.19
	40 - 50	14.57 ± 0.63	9.91 ± 1.55	7.89 ± 0.96	10.45 ± 2.90
2-4	10 - 50	-4.61 ± 1.93	-2.37 ± 2.06	-5.92 ± 2.21	4.27 ± 2.58
	20 - 50	-3.42 ± 1.94	-2.88 ± 1.95	-5.13 ± 2.14	-3.84 ± 2.25
	30 - 50	-3.18 ± 1.97	-3.12 ± 1.96	-4.85 ± 2.16	-3.77 ± 2.19
	40 - 50	-3.51 ± 1.95	-3.19 ± 2.00	-4.87 ± 2.17	-3.89 ± 2.18

Table 6.11: Systematic study of the QED contribution for correction factors derived from different group sizes of CDC layers.

6.5.4 Comparison with Monte Carlo data

As both Monte Carlo generators agree nicely in the low p_t momentum range, it is sufficient to compare the recorded data with the KoralW generator only. Using the KoralW Monte Carlo generation explained in section 6.3, KoralW events are produced. They are given to the full detector simulation in the BASF software framework [163] and the hit multiplicity for each layer of the SVD is recorded. The result is listed in table 6.12 together with the measured results from the analysis.

Layer	Experiment 73	KoralW Monte Carlo
1	12.69 ± 1.52	11.31
2	-0.54 ± 2.48	3.99
3	-4.01 ± 1.32	1.84
4	-2.15 ± 0.73	1.32

Table 6.12: Comparison between the measured SVD hit multiplicity and the KoralW Monte Carlo simulation.

6.6 Reconstruction and analysis of high p_t two-photon events

The previous section described the analysis of recorded data and its comparison with Monte Carlo data for the dominating, low p_t region of the two-photon process. In this region both Monte Carlo generators under test, KoralW and BDK, agree nicely with each other as section 6.3.3 shows. However, for larger values of p_t ($p_t > 20$ MeV) the generators differ substantially. This section aims at comparing the recorded data with Monte Carlo data for large values of p_t by performing a full reconstruction of two-photon events.

6.6.1 Normalisation of the random trigger events

The random nature of Trg77 results in a different event signature to the physics events that are usually taken at Belle. The physics triggers at Belle only allow the recording of events that have been identified as physics events by the GDL. This means the recorded data contains the full signature of an event, from the hits in the SVD to the showers in the ECL and the signals collected in the KLM. On the other hand, the random trigger simply triggers the readout of the sub-detectors at random times. This leads to effects such as incomplete events, where sub-detectors either missed or only recorded parts of an event. Although the random trigger seems to be very

restrictive on the data analysis at a first glance, it offers two advantages: It allows the recording of events that would otherwise have been missed by the standard physics triggers; Scaling the number of reconstructed events recorded by the random trigger to the number of events that could have been collected theoretically if the detector was perfect and it was recording during an entire run is straight forward. The latter advantage is based on the fact that the recorded data can be regarded as an independent subset of the full data taken during a run. Thus, the scaling or **normalisation factor** is determined by the duration of a single run and the time period the detector spent to collect data after the random trigger had fired. The normalisation factor is then used to scale the two-photon Monte Carlo data such that it can be compared with the measured data from the detector, this is explained in the following sections.

The memory time

The time period the detector takes to record an event after a random trigger initiated the recording is called **memory time** (t_{mem}). It can be measured by analysing a well-understood physics process, such as Bhabha scattering. Due to the truly random nature of the random trigger the fraction of events of a specific type found in a run is equal to the fraction of the same kind of events found in a subset of the full run sampled by the random trigger

$$\frac{N_{run}}{t_{run}} = \frac{N_{rand}}{t_{rand}} \quad (6.10)$$

where N_{run} is the number of events that could have been measured theoretically during the run, t_{run} the recording time of the run, N_{rand} the number of events in the random trigger subset and t_{rand} the total time the detector was collecting data due to the random trigger. The number of events N_{run} is given by the measured luminosity of the run and the theoretical cross-section of the process estimated from Monte Carlo

$$N_{run} = L_{run} \cdot \sigma_{th} \quad (6.11)$$

The number of events N_{rand} is counted by reconstructing the randomly triggered data. However, due to the detector acceptance, imperfections in the detector and limitations of the reconstruction algorithms a reconstruction efficiency ϵ_{rec} is introduced

$$N_{rec} = \epsilon_{rec} \cdot N_{rand} \quad (6.12)$$

N_{rec} is the number of reconstructed random trigger events.

The total time t_{rand} that the detector was recording due to the random trigger can be written as

$$t_{rand} = N_{trg} \cdot t_{mem} \quad (6.13)$$

where N_{trg} is the number of times the random trigger fired during the run and t_{mem} the memory time of the detector. Combining all equations yields the memory time, which depends only on quantities that can either be measured or are calculated from Monte Carlo data

$$t_{mem} = \frac{N_{rec} \cdot t_{run}}{N_{trg} \cdot L_{run} \cdot \sigma_{th} \cdot \epsilon_{rec}} \quad (6.14)$$

The normalisation factor

The normalisation factor is then given as the fraction of the time the detector was measuring due to the random trigger

$$f = \frac{N_{trg} \cdot t_{mem}}{t_{run}} \quad (6.15)$$

with equation 6.14 it simplifies to

$$f = \frac{N_{rec}}{L_{run} \cdot \sigma_{th} \cdot \epsilon_{rec}} \quad (6.16)$$

The normalisation factor allows the direct comparison of the number of expected events from recorded data with the number of events obtained from Monte Carlo data. It will be used in equation 6.21 to calculate the expected number of events from the reconstructed events. Equation 6.16 does not require the explicit measurement and calculation of the memory time value. However, it was found that the comparison of the measured value of the memory time with the expected value ($\sim 1 \mu\text{s}$) provides a good validation of the reconstruction procedure used for the normalisation.

Bhabha scattering as the normalisation physics process

The memory time and, in turn, the normalisation factor for a single run is determined by counting the number of reconstructed events from a well-understood physics process. This allows to

minimise systematic errors arising from Monte Carlo generation and event reconstruction. The ideal physics process for the analysis at hand is (radiative) Bhabha scattering

$$e^+e^- \rightarrow e^+e^- (\gamma)$$

This process has a large cross-section, a simple event topology and is used extensively at Belle for measuring the luminosity delivered by KEKB. In addition, the available Monte Carlo generators were validated at other accelerators over a wide range of center-of-mass energies. The measurement is confined to the barrel region of the Belle detector. This ensures that the detector part is used at which both, CDC and ECL, have the best resolution and efficiency and at which the detector simulation works reliably. The polar angle range for the barrel part is $32^\circ < \theta < 130^\circ$ in the laboratory system and $46.7^\circ < \theta < 145.7^\circ$ in the CMS frame. Choosing this angular range avoids hitting the gaps in the ECL that separate the barrel and the endcap regions. In order to generate Monte Carlo events efficiently for the barrel region, the wide-angle Bhabha Monte Carlo generator BHWide (see section 6.3.1) is chosen. Most input parameters for BHWide are either defined by physics quantities, the experimental setup, or are recommendations from the authors of the generator. Examples are the centre-of-mass energy or the type of the random number generator. The polar angle range for the outgoing leptons can be freely chosen. Since the analysis is only performed in the barrel region of the detector, the aim is to select an optimal set of values such that the generated events cover the whole barrel region while, at the same time, the number of events with outgoing leptons outside of the barrel is kept minimal. An optimal set of polar angles is found by a stability test of the visible cross-section $\sigma_{vis}(\text{BHWide})$. The visible cross-section is defined as the cross-section that is seen after one or more of cuts. For this test $5 \cdot 10^4$ BHWide events are generated, simulated and reconstructed for several polar angle configurations. The details for the reconstruction procedure are given in the following section. Table A.5 in the appendix summarises the polar angle configurations used for the $\sigma_{vis}(\text{BHWide})$ stability test, the resulting BHWide cross-sections and the final values for $\sigma_{vis}(\text{BHWide})$. The result of the stability test is shown in figure 6.13. It can clearly be seen how the visible cross-section drops from configuration 9 onwards, due to the smaller polar angle coverage of the generator compared to the barrel region limitation used in the reconstruction procedure. Thus the conclusion is drawn to use the angle configuration 8 ($28.0^\circ, 132.0^\circ$) for the final BHWide generation.

The settings for the final BHWide production are listed in table A.6 in the appendix. The final radiative Bhabha sample contains 10^7 events and yields a theoretical cross-section, given by BHWide, of

$$\sigma_{th}(\text{BHWide}) = 10.47 \text{ nb} \quad (6.17)$$

The generated events are then boosted to the laboratory frame, using the method explained

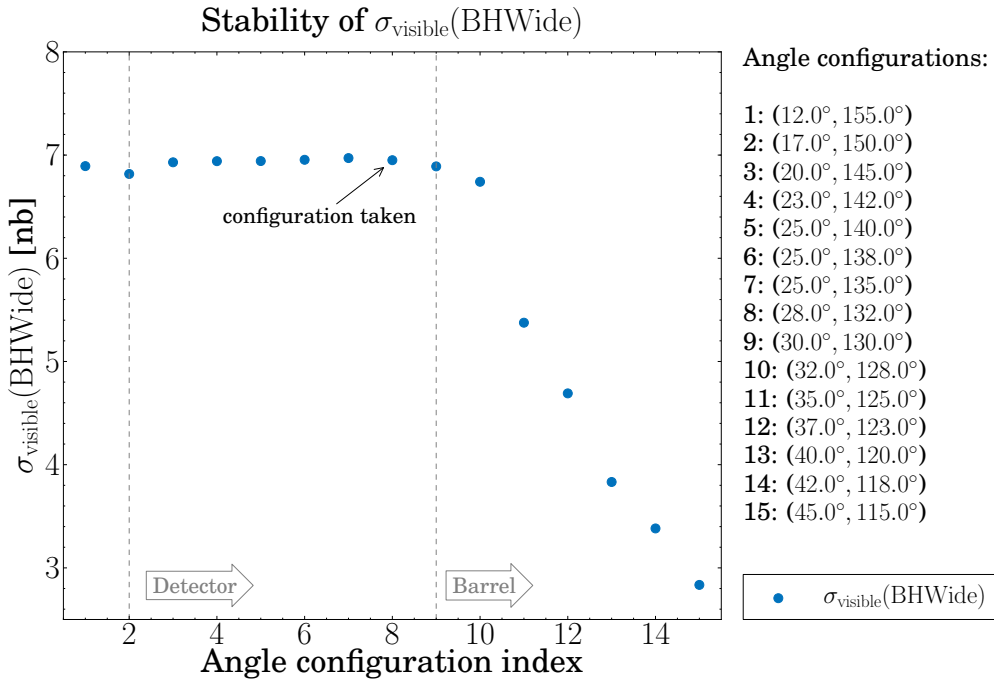


Figure 6.13: Stability of $\sigma_{\text{vis}}(\text{BHWide})$ for different BHWide angle configurations. See table A.5 in the appendix for a detailed listing of the configurations.

in section A.3. The momentum spectrum of the resulting events is shown in figure 6.14. In an ideal world the IP would be located exactly at the point (0, 0, 0), however in reality the position of the IP is statistically distributed around the nominal IP position. Therefore, before handing the Monte Carlo events over to the full detector simulation, the origin of each event is randomly displaced with the position and uncertainties taken from measurements performed during experiment 73. Table 6.13 lists the values. The full detector simulation is then carried out within the Belle software library BASF [163].

x	y	z	σ_x	σ_y	σ_z	unit
0.05603	-0.02268	0.001981	0.009729	0.0002323	0.3782	[cm]

Table 6.13: Beamspot position and width values for the MonteCarlo simulation of experiment 73.

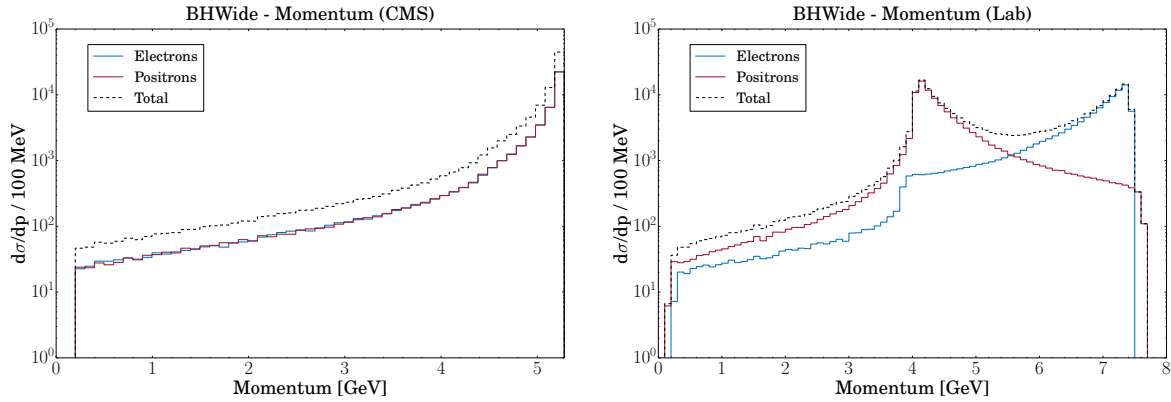


Figure 6.14: Momentum spectrum of the generator BHWide events before and after the boost. The left figure shows the momentum spectrum in the centre-of-mass frame. The right figure the momentum spectrum after applying the boost to the lab frame. Electrons are drawn in blue, positrons in red and their sum in black.

Reconstruction of radiative Bhabha scattering events

The reconstruction of Bhabha events follows the approach that is used for the calculation of the luminosity at Belle. It is described in detail in [225] and revolves around a sequence of cuts on particle energies and event topologies. Only events that pass the procedure outlined below are considered to be radiative Bhabha events.

1. Track collection

Before applying cuts to the whole event, all successfully reconstructed charged tracks are collected in each event. A track is regarded as being successfully reconstructed if it complies with the following criteria (standard values for Belle analyses):

- its impact parameter values (dr, dz as defined by Belle) are within:

$$\begin{aligned} |dr| &< 2.0 \text{ cm} \\ |dz| &< 4.0 \text{ cm} \end{aligned}$$

- its transverse momentum p_t is greater than 100 MeV
- the confidence level of the track fit is greater than 10^{-25}

Those criteria make sure only those tracks are taken into consideration that originate from the IP (impact parameter), can reliably be found by the pattern recognition (p_t) and pass the track fitting procedure.

2. ECL cluster collection

Similarly, only well reconstructed clusters in the ECL are collected. For this purpose BASF

provides a quality flag for each cluster and only clusters carrying the flag “good cluster” are taken into account.

3. Creation of lists

All steps following this step will act upon the content of three lists that were created during the collection steps above: the first containing the negatively charged tracks, the second the positively charged tracks and the third list contains the ECL clusters. If any of the charged track lists is empty or the ECL cluster list has less than two entries, the event cannot be a Bhabha event and is therefore rejected. Otherwise the charged track lists are sorted according to the track’s momentum and the ECL cluster list according to the cluster energy.

4. Barrel region

By restricting events to be contained within the barrel region of the detector, it is made sure that the part of the Belle detector is used where the CDC and the ECL provide their best resolution and efficiency. The polar angle in the CMS of the positive and negative track with the highest momentum is calculated. The event is kept if both angles lie inside the barrel region: $46.742^\circ < \theta_{CMS} < 145.715^\circ$

5. Reject events with a hard radiation photon

In order to reconstruct Bhabha events reliably, events containing a high energetic photon are rejected. From each charged track list, the track with the highest momentum is taken and its CMS momentum is calculated. The event is kept if each CMS momentum is larger than half the beam energy (2.645 GeV).

6. Event topology

Bhabha events can easily be distinguished from other events by the typical back-to-back topology of the two outgoing leptons in the centre-of-mass system. Thus, the acollinearity angle between the highest momentum track from the positively and the negatively charged track list is calculated and only if the angle is smaller than 10° the event is kept. In addition, this step ensures that hard radiation photon events are rejected.

7. Event energy

The Bhabha event topology cuts are complemented by energy cuts that ensure that the event contains highly energetic leptons. The event is kept, and thus considered to be a Bhabha event, if the ECL cluster with the highest energy has an energy greater than 2 GeV and the sum of all ECL clusters is larger than 4 GeV.

The cuts and their impact on the BHWide Monte Carlo data is listed in table A.7 in the appendix. From the table the reconstruction efficiency $\epsilon_{rec}(\text{BHWide})$ is read to be 65.6 %. This efficiency is a combined efficiency and contains the effects imposed by the acceptance and imperfections of the detector and the efficiencies of the reconstruction software, such as tracking and ECL clustering efficiencies.

The visible cross-section for the barrel region is then

$$\sigma_{barrel}(\text{BHWide}) = \epsilon_{rec}(\text{BHWide}) \cdot \sigma_{th}(\text{BHWide}) = (6.867 \pm 0.001) \text{ nb} \quad (6.18)$$

Luminosity measurement

The calculation of the memory time (equation 6.14) and, in turn, the normalisation factor (equation 6.16) requires the value of the luminosity for each run. Although the luminosity for each run can be retrieved from the Belle runinfo table [226], an independent measurement offers a good opportunity to validate the Bhabha reconstruction code that will later be used to estimate the memory time and the normalisation factor. For the luminosity measurement the data recorded due to the barrel Bhabha trigger of experiment 73 (brl_bhabha) is used. This trigger is activated by Bhabha-like events in the barrel region of the detector. It carries the trigger bit **42** and has a pre-scale value of **2**, which means only every second triggered barrel Bhabha event is recorded. This helps to reduce the amount of recorded data. Applying the reconstruction method outlined in section 6.6.1 to all 17 runs results in the number of reconstructed Bhabha events listed in table A.8 in the appendix. Runs 419 and 420 do not contain enough events in order to measure the luminosity and will therefore be omitted for the calculation of the memory time and the normalisation factor. The overall reconstruction efficiency is 64.9 %. This value is very similar to 65.6 %, the value obtained from the Monte Carlo data, indicating that the Belle barrel Bhabha hardware trigger does an excellent job.

The luminosity value for each run is then calculated by

$$L_{run} = \frac{s \cdot N_{rec}(\text{trg42})}{\sigma_{barrel}(\text{BHWide})}$$

where s is the pre-scale factor (2 for experiment 73). The results can be found in table 6.14, which compares the measured luminosity values with the official Belle values taken from [226].

As can be seen from table 6.14 the measured values agree within less than 1 % for almost all runs with the official values.

Run	trigger 42	official	rel. error
401	10.258	10.270	0.116%
403	8.290	8.280	0.124%
408	6.613	6.670	0.860%
409	3.821	3.800	0.556%
411	6.753	6.750	0.049%
414	9.791	9.860	0.701%
416	8.549	8.500	0.576%
417	6.238	6.270	0.505%
418	4.854	4.910	1.147%
419			
420			
421	8.558	8.570	0.140%
422	8.491	8.450	0.482%
424	7.342	7.280	0.847%
425	6.417	6.340	1.208%
426	5.450	5.410	0.737%
427	2.087	2.070	0.817%
Total	103.511	103.430	0.078%

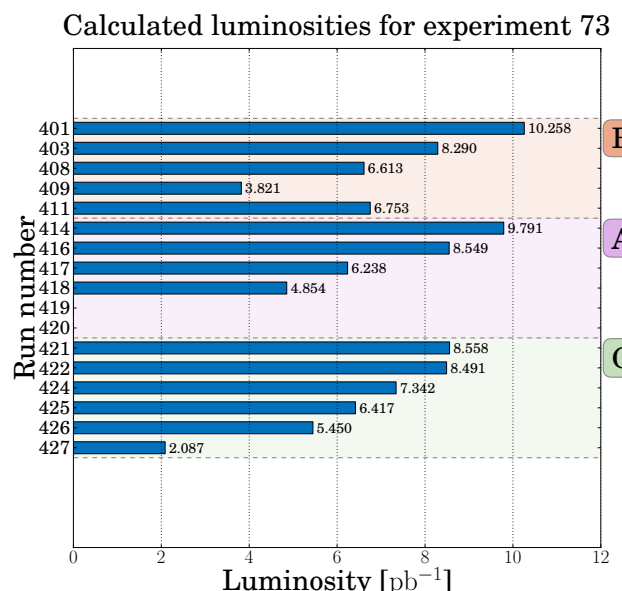


Table 6.14: Luminosity in pb^{-1} calculated from radiative Bhabha events from experiment 73, trigger 42.

Memory time measurement

Having measured the luminosity for each run and calculated the Bhabha reconstruction efficiency from Monte Carlo, the final step in estimating the memory time is to count the number of Bhabha events in the random trigger recorded data. Therefore, the reconstruction process explained in section 6.6.1 is applied to the data that was recorded due to trigger 77 (the random trigger random_ev). The result of the reconstruction process is summarised in table A.9 in the appendix, listing the effect of each cut on the number of events.

The memory time is then calculated using equations 6.14 together with 6.18. Table 6.15 lists the calculated memory time for each run. As expected, the memory time is roughly 1 μ s.

Run	memory time [μ s]
401	1.589
403	1.204
408	1.209
409	1.307
411	1.676
414	1.190
416	1.596
417	1.869
418	1.511
419	-
420	-
421	1.594
422	1.646
424	1.270
425	1.195
426	1.162
427	0.958
Avg	1.398

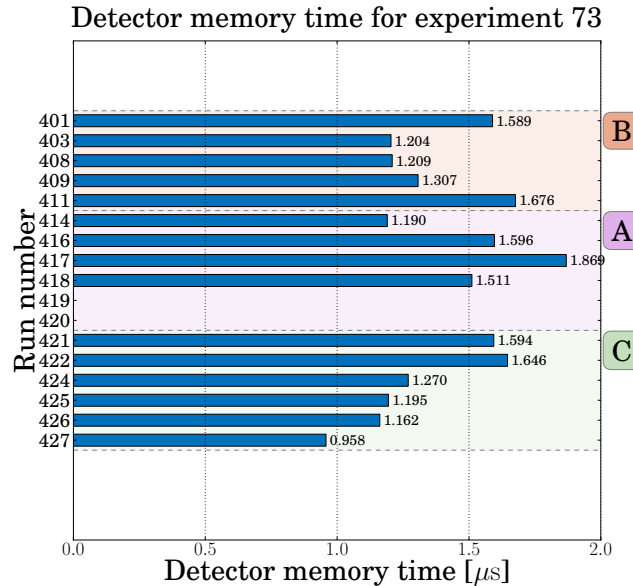


Table 6.15: Memory time of the detector in [μ s], calculated from experiment 73, trigger 77

6.6.2 Monte Carlo generation

For the high p_t analysis the KoralW and BDK Monte Carlo data generated in section 6.3.2 is used. In total, $1.34 \cdot 10^7$ KoralW events are generated, which correspond to a luminosity of

$$L_{KW} = 5.03 \cdot 10^{-3} \text{ pb}^{-1} \quad (6.19)$$

and for BDK a total number of $1.51 \cdot 10^9$ events are generated with a total generated luminosity of

$$L_{BDK} = 2.06 \cdot 10^{-1} \text{ pb}^{-1} \quad (6.20)$$

It is not sufficient, however, to only produce the Monte Carlo data for KoralW and BDK. The data recorded by the random trigger contains a myriad of different physics processes and the reconstruction algorithm faces the task of picking the two-photon events and rejecting everything else. In order to test the performance of the algorithm to reject events that aren't two-photon events, the Monte Carlo data for various **background** processes is generated as well. The selection of background processes focuses on processes that share a similar event topology with the two-photon process that is analysed in this chapter and exhibit a large cross-section. An obvious candidate is radiative Bhabha scattering. But there are also two two-photon processes that have a large cross-section at the Belle centre-of-mass energy as can be seen in figure 6.4. Those processes have, in addition to the electron-positron pair, either two muons or two pions in their final state

$$e^+ e^- \rightarrow e^+ e^- \pi^+ \pi^- \quad e^+ e^- \rightarrow e^+ e^- \mu^+ \mu^-$$

For the radiative Bhabha scattering, the same Monte Carlo data that is used for the estimation of the luminosity and memory time is taken (see section 6.6.1). The Monte Carlo data for the process $e^+ e^- \rightarrow e^+ e^- \pi^+ \pi^-$ is generated using TREPS-WCONTPIPI⁵ [227, 228]. In total, 1019054 events for the invariant mass spectrum $0.5 < M(\pi^+ \pi^-) < 3.0$ GeV are generated. The cross-section is

$$\sigma_{\pi^+ \pi^-} = 2807.31 \text{ pb}$$

corresponding to a luminosity of about $L = 363 \text{ pb}^{-1}$. The two muon data is generated using

⁵Two-photon REsonance Production Simulator applied for W (inv.mass) of a CONTinuous range for PI+PI-

the BDK (aafhb) Monte Carlo generator explained in section 6.3.1. It is configured to generate a $\mu^+\mu^-$ pair instead of a e^+e^- pair in the final state, but otherwise uses the settings listed in table A.3. The cross-section returned by the Monte Carlo generator is

$$\sigma_{th}(\mu^+\mu^-) = 6.79 \cdot 10^4 \pm 6 \text{ pb}$$

The generated $9.39 \cdot 10^7$ events represent a luminosity of $L = 1380 \text{ pb}^{-1}$. The simulation of the background Monte Carlo data is carried out in the same way as for the KoralW and BDK data.

6.6.3 Reconstruction of the two-photon events

The main goal of the reconstruction is the production of a very clean sample of two-photon events. Thus, the analysis puts the focus on the reconstruction of electron-positron pairs and limits itself to no-tag events where the scattered electron and positron disappear in the beampipe and only the generated electron-positron pair is measured. The procedure outlined below is inspired by the Bhabha reconstruction and comprises topology and momenta cuts to select events with electron-positron pairs, inverted Bhabha reconstruction cuts to reject Bhabha contamination and particle identification cuts in order to remove multi-hadron events.

1. Track collection

Before applying cuts to the whole event, all successfully reconstructed charged tracks are collected in each event. A track is regarded as being successfully reconstructed if it complies with the following criteria:

- its impact parameter values (dr, dz as defined by Belle) are within

$$\begin{aligned} |dr| &< 2.0 \text{ cm} \\ |dz| &< 4.0 \text{ cm} \end{aligned}$$

- the confidence level of the track fit is greater than 10^{-25}
- its transverse momentum p_t is greater than 340 MeV

Those criteria make sure that only those tracks are taken into consideration that originate from the IP (impact parameter), can reliably be found by the pattern recognition (p_t) and perform well in the track fitting procedure (confidence level). The particular value for the p_t cut is motivated by the particle identification system as will be explained below.

2. Creation of lists

All steps following this step will act upon the content of two lists that were created during the collection steps above: the first containing the negatively charged tracks and the second the positively charged tracks. If any of the lists is empty, the event cannot be a

two-photon event and is therefore rejected. Otherwise the lists are sorted according to the track's momentum.

3. Barrel region

By restricting events to be contained within the barrel region of the detector, it is made sure that the part of the Belle detector is used where the CDC and the particle identification detectors provide the best resolution and efficiency. The polar angle in the CMS of the positive and negative track with the highest momentum is calculated. The event is kept if both angles lie inside the barrel region

$$46.742^\circ < \theta_{CMS} < 145.715^\circ$$

4. Pair constraint

This step makes sure only clean electron-positron pair events are selected. It requires that each particle list contains exactly one particle, thus forming a single e^+e^- pair. While this criterion seems to be quite restrictive, it turns out to have only a small effect.

5. Reject high momentum tracks

In order to remove any contamination from Bhabha events, only events where both charged tracks have a CMS momentum of less than half the beam energy (2.645 GeV) are kept.

6. Event topology

Similarly to the previous step, this cut helps to reject Bhabha events by inverting the associated criterion in the Bhabha selection algorithm outlined in section 6.6.1. The acollinearity angle between the two tracks is calculated and the event is kept if the angle is greater than 10° .

7. Invariant mass

Another source of background events mimicking low momentum e^+e^- pairs is photon conversion. In this process a photon interacts with the material of the detector and is converted into a e^+e^- pair. This contamination can be efficiently removed by introducing a cut on the invariant mass of the e^+e^- pair

$$m_{inv} = \sqrt{(E_{e^+} + E_{e^-})^2 - \|\vec{p}_{e^+} + \vec{p}_{e^-}\|^2}$$

If the invariant mass m_{inv} is smaller than 100 MeV, the event is discarded.

8. Particle identification

So far any existing background has only been removed by means of cuts on the particle momenta and the event topology. However, at this point multi-hadron processes such as $e^+e^- \rightarrow e^+e^-\pi^+\pi^-$ might still be present. In order to make sure only events containing e^+e^- pairs in their final state are selected, the particle identification sub-detectors of Belle are used. In particular, the electron identification system [229] of BASF is applied.

The decision to reject an event is based on three qualifiers provided by the system:

- the combined likelihood excluding the TOF information
- the confidence level estimated from the energy deposition in the CDC (dE/dx)
- the confidence level taken from the ratio of the cluster energy measured in the ECL and the charged track momentum measured in the CDC (E/p)

In the electron identification process used for this analysis only the two sub-detectors CDC and ECL contribute. Therefore, the tracking cuts and, in particular, the p_t cut have to make sure both tracks reach the ECL. The ECL covers the p_t range from about 281 MeV to 369 MeV. Electrons with a p_t larger than 281 MeV enter the ECL and give rise to electromagnetic showers. In order to make sure that the electrons reach the ECL over the whole polar angle range of the barrel region, a p_t cut of 340 MeV is chosen. Finally, the event is kept, and thus considered to be a two-photon event, if any of the following criteria hold:

- the combined likelihood for each tracks is greater than 0.01
- the combined likelihood for the e^- track is greater than 0.01 **and**
 - the dE/dx confidence level of the e^+ track is greater than 0.5
 - **or** the E/p confidence level of the e^+ track is greater than 0.5
- the combined likelihood for the e^+ track is greater than 0.01 **and**
 - the dE/dx confidence level of the e^- track is greater than 0.5
 - **or** the E/p confidence level of the e^- track is greater than 0.5

6.6.4 Results from data

The reconstruction chain outlined above is applied to the simulated Monte Carlo data and the recorded data from the detector. The Monte Carlo data comprises the signal event samples from KoralW and BDK and the background data samples for Bhabha scattering, two pion and two muon final states. This section describes the result of the reconstruction, compares the expected event numbers from Monte Carlo with the event number gained from the measured data and explains the contribution of background events in the final data sample.

Signal

The output of the reconstruction process is a list of events that are considered to be two-photon events. From the number of reconstructed Monte Carlo events the number of events that are

expected to be found in the measured data can be calculated. Using the normalisation factor f (equation 6.16) the number of expected events is given by

$$N_{ex} = \underbrace{\left(f \cdot \frac{L_{runs}}{L_{gen}} \right)}_{\text{scaling factor}} \cdot N_{\gamma\gamma} \quad (6.21)$$

where L_{runs} is the total luminosities of all 17 runs, L_{gen} the generated luminosity from the Monte Carlo generators and $N_{\gamma\gamma}$ is the number of reconstructed two-photon Monte Carlo events. The normalisation factor together with the fraction of the run and generated luminosity is called the Monte Carlo to data **scaling factor**. Plugging in the numerical values, the normalisation factor is found to be

$$f = 6.12 \cdot 10^{-4}$$

The numerical values of the scaling factors for the two signal and the three background Monte Carlo samples are listed in table 6.16.

KoralW	BDK	Bhabha	$\pi^+\pi^-$	$\mu^+\mu^-$
12.59	0.31	$6.62 \cdot 10^{-5}$	$1.74 \cdot 10^{-4}$	$4.58 \cdot 10^{-5}$

Table 6.16: The Monte Carlo to data scaling factors for the signal and background Monte Carlo samples.

The individual cuts and their values in the two-photon event reconstruction chain are given by the detector geometry, motivated by inverting the Bhabha reconstruction or are default values used for most analyses performed at Belle. The exception, however, is the value for the p_t cut. Its primary function is to make sure the particles reach the sub-detectors that are responsible for the electron identification, in particular the CDC and the ECL. Changing the value for the p_t cut has a significant impact on the number of events in the final sample and, in turn, the predicted number of events from Monte Carlo. Therefore, by varying the p_t cut value and measuring the expected number of events, the robustness of the reconstruction chain can be tested. Starting with 210 MeV, the p_t cut is increased in 10 MeV steps up to 450 MeV. For each step the detector and Monte Carlo data is fully reconstructed and the number of expected events is calculated. Table A.10 in the appendix lists the number of expected events for each p_t cut. For the BDK Monte Carlo generator the result of the p_t cut scan is drawn in figure 6.15. As expected, increasing the value of p_t leads to a decrease in the number of expected events. The ratio between the expected events from BDK and the reconstructed events from the detector data shows that the Monte Carlo data does not agree very well with the detector data below ~ 320 MeV. But above this value the agreement is quite good and stays constant. This can be explained with the ECL.

Although particles with a p_t value above 281 MeV are able to reach the ECL, its electron identification power does not come into effect until the particles left a measurable signal in the ECL. This is the case for particles with a momentum above ~ 300 MeV [229]. The ratio plotted in figure 6.15 shows that the reconstruction is robust under changes of p_t above a p_t of 320 MeV and that the expected number of events from BDK matches the measured number of events from the Belle detector quite well.

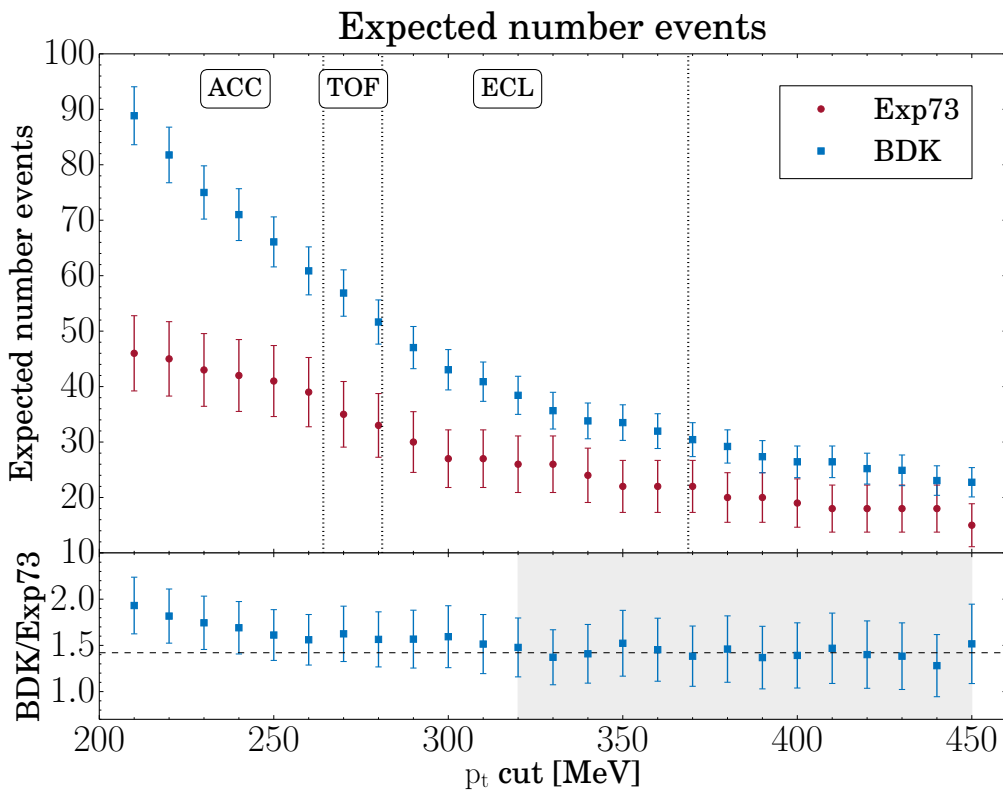


Figure 6.15: Impact of the p_t cut on the number of expected events. The dashed lines in the upper plot illustrate the boundaries of the ACC, TOF and ECL. The dashed line in the lower plot is the average of the values within the grey area.

In order to make sure the electron identification works reliably, the p_t cut value is set to 340 MeV for the final reconstruction. The result is summarised in table A.11 for the Monte Carlo data and in table A.12 for the experiment 73 detector data. Both tables can be found in the appendix and list the number of reconstructed and expected events after each reconstruction step. The final number of reconstructed events from the data recorded during the random trigger runs of experiment 73 is

$$N_{exp} (\text{Exp73}) = 24$$

The expected number of events predicted by the Monte Carlo generators are, for BDK

$$N_{exp}(\text{BDK}) = 33.8 \pm 3.2$$

and for KoralW

$$N_{exp}(\text{KoralW}) = 793.4 \pm 99.9$$

The specified errors are the statistical errors originating from the number of available Monte Carlo events. The result for the BDK Monte Carlo generator is consistent with the measured data within 3.1σ . For the KoralW Monte Carlo generator, on the other hand, the result is consistent within 7.7σ . This means the BDK Monte Carlo generator agrees reasonable well with the experimental data taken during the random trigger runs at Belle over the full p_t range, especially considering that systematic errors from the reconstruction process haven't been taken into account. The KoralW generator is not able to produce data that describes the two-photon process correctly for values of p_t larger than 20 MeV. It should be noted that the comparison drawn in section 6.3.3 between the 4-vector data of the Monte Carlo generators already suggested a significant deviation between BDK and KoralW for large p_t . Looking into the momentum spectra for BDK and KoralW (see figure 6.16), the comparison with the measured data reveals a nice agreement between BDK and data, and the expected large deviation between KoralW and data.

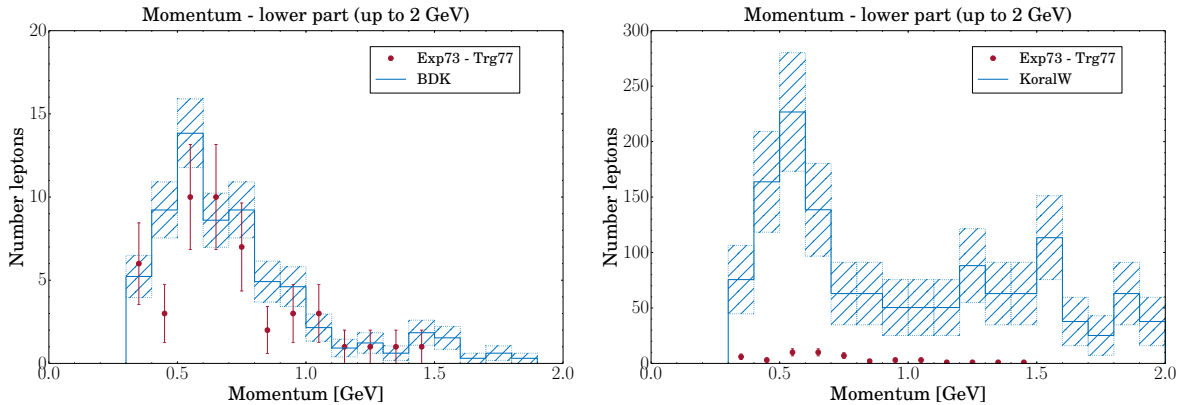


Figure 6.16: Momentum of the two outgoing leptons after the last reconstruction step. The left plot shows the result for BDK, the right plot for KoralW. The measured data is drawn as red dots, while the histogram represents the Monte Carlo data.

The same picture is found for the topology of the events. The $\cos(\theta)$ distribution for BDK matches the one for the data (see figure 6.17), while KoralW does not agree with the data.

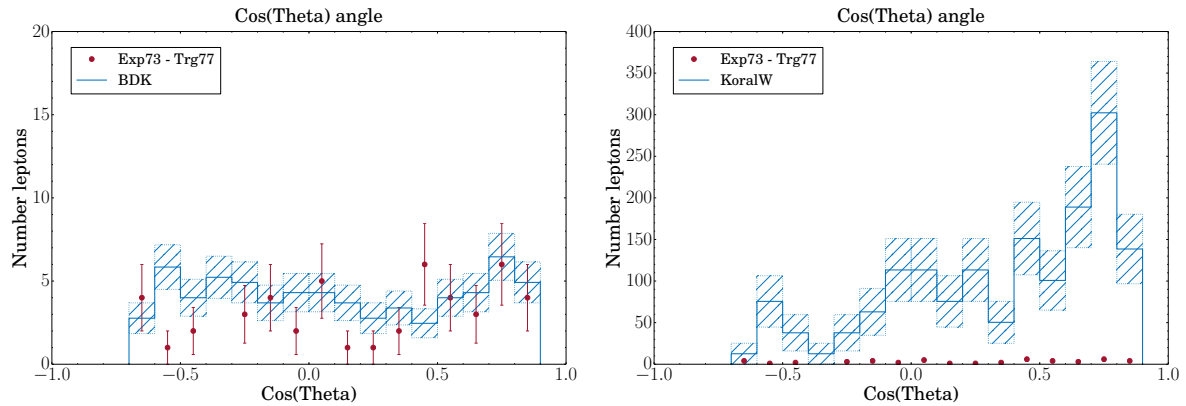


Figure 6.17: $\text{Cos}(\theta)$ of the two outgoing leptons after the last reconstruction step, with the BDK data on the left and the KoralW data on the right.

The opening angle, measured between the two outgoing leptons, shows a peak for very small opening angles for KoralW but none for BDK and data (see figure 6.18). It turns out that this peak originates from photon conversions. For BDK this can be explained with the absence of photons from the generator, the data, however, does not show this peak either. It seems KoralW produces too many photons which turn into e^+e^- pairs and thus mimic a two-photon event signature.

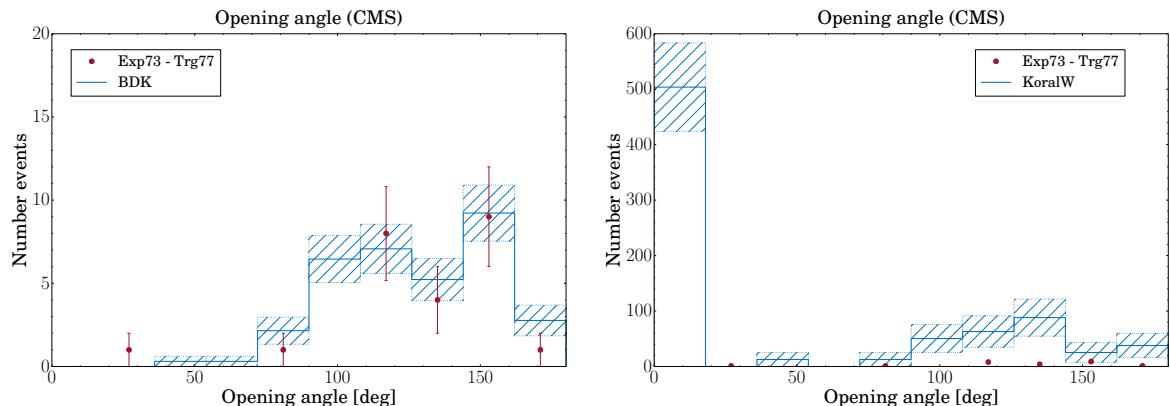


Figure 6.18: Opening angle in the centre-of-mass system of the two outgoing leptons after the last reconstruction step. The BDK result is shown in the left plot, the KoralW result in the right plot.

Background

The simulated background Monte Carlo data is reconstructed using exactly the same reconstruction process as the signal data. Table A.13 in the appendix summarises the result. It lists the event number together with its associated normalised event number after each cut for the

three background processes under consideration. The values for the Bhabha scattering events are only moderately reduced by the tracking, barrel acceptance and track pair cuts. However, the cuts rejecting high momentum tracks and back-to-back events (acollinearity cut) are very efficient and reduce the Bhabha background by more than 99.99 %. This shows that the cuts aimed at the rejection of Bhabha scattering events work very well. In the final data sample only

$$N_{Bhabha} = 0.01$$

Bhabha scattering events are expected to contribute. The transverse momentum spectra in figure 6.19 illustrate the effect of the acollinearity cut. The left plot shows the spectrum before the cut. The prominent peak at around 4.5 GeV originates almost exclusively from Bhabha scattering events. By rejecting events with a back-to-back track topology, the Bhabha contamination is removed, as it can be seen from the missing peak in the right spectrum of figure 6.19.

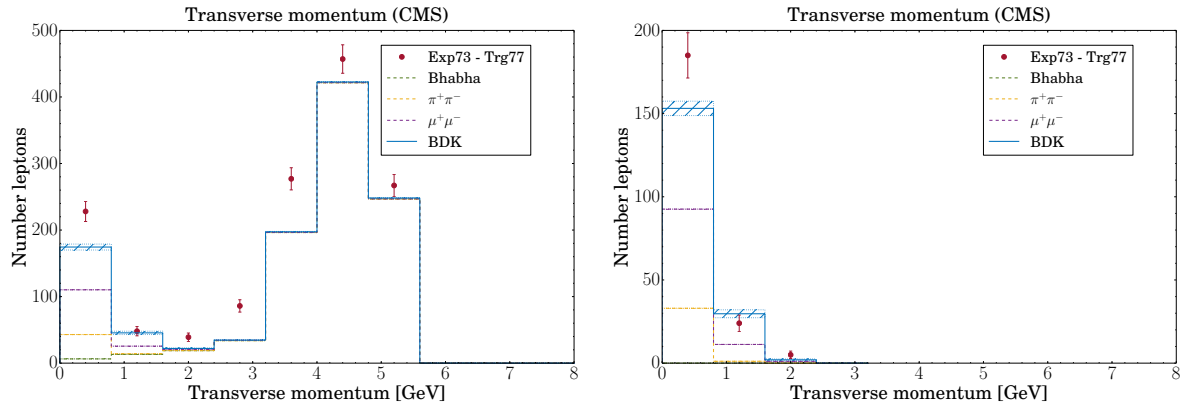


Figure 6.19: Transverse momentum spectrum before (left) and after (right) the acollinearity cut.

The $\pi^+\pi^-$ and $\mu^+\mu^-$ processes see only a gradual reduction for all but the last cut. This is to be expected as the events of those two background processes are very similar to the signal events. The real discrimination power, however, lies in the particle identification. By rejecting non-electron tracks, the $\pi^+\pi^-$ Monte Carlo data is reduced by 99.86 % and the $\mu^+\mu^-$ data by 99.97 %. This leads to the following number of events in the final data sample

$$N_{\pi^+\pi^-} = 0.02 \quad N_{\mu^+\mu^-} = 0.01$$

The momentum distribution of the background components and the BDK signal after the invariant mass cut is shown in the stack plot of figure 6.20. The plot shows that the selected background processes cover indeed the majority of the background and the background + signal is in nice agreement with the measured data.

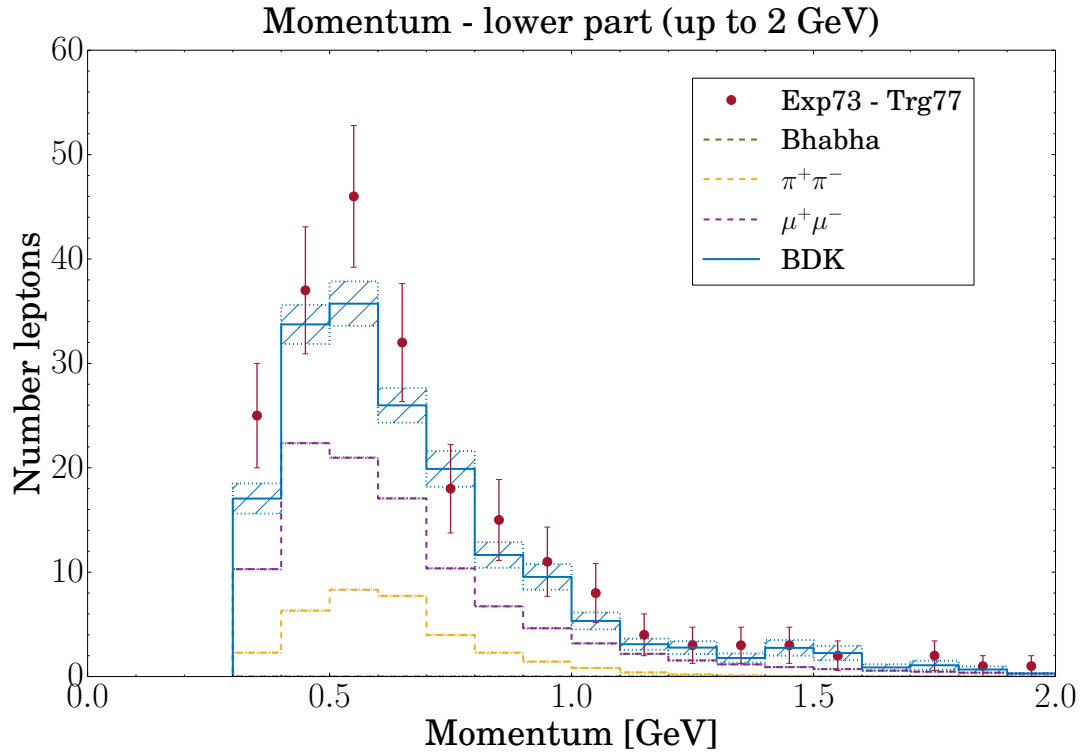


Figure 6.20: Momentum distribution of the background and the BDK signal after the invariant mass cut and before the electron ID cut.

6.7 Conclusion

The goal of the two-photon analyses described in this chapter was the validation of the two-photon Monte Carlo generators KoralW and BDK with data taken at the Belle experiment. The data used for the validation was recorded in 2010 specifically with the analyses in mind and used a random trigger instead of normal physics triggers. This allowed the recording of two-photon events that would otherwise have been missed by the detector. By analysing the number of hits in the SVD for different luminosity settings, the contribution of two-photon QED events to the total number of SVD hits was estimated and compared to the Monte Carlo prediction. It was found that the Monte Carlo generators agree with the recorded data. While this analysis focused on the dominating low p_t region of the two-photon process, the second analysis presented in this chapter dealt with the high p_t region. It aimed at fully reconstructing two-photon events and on producing a clean data sample from the recorded data. The normalisation between Monte Carlo and measured data was accomplished with the help of Bhabha events.

The number of expected events in the reconstructed Belle data for all recorded runs of experiment 73 was estimated from KoralW and BDK Monte Carlo and was found to be

$$N_{exp} (\text{BDK}) = 33.8 \pm 3.2$$
$$N_{exp} (\text{KoralW}) = 793.4 \pm 99.9$$

The measured number for all 17 recorded runs of experiment 73 was

$$N_{exp} (\text{Exp73}) = 24$$

The contribution of three major backgrounds was studied and found to be negligible. From the results the conclusion was drawn that both Monte Carlo generators agree very nicely for low values of p_t , where the cross-section peaks, but differ significantly for larger values. The analysis proved that for larger p_t the behaviour of BDK is correct and agrees reasonable well with the measured data within 3.1σ . The comparison of the 4-vector data between KoralW and BDK already showed a large discrepancy for values of p_t above 20 MeV. This discrepancy was then found in the comparison with data, too. Since the KoralW generator has been developed for and validated at LEP, it seems that KoralW is not optimised for the centre-of-mass energies found at KEKB. During the development of the analysis procedure the KoralW generator was modified by its authors due to early results from this analysis, but the discrepancies remained. On the other hand, BDK is a well established two-photon Monte Carlo generator, even if it does not offer important features such as initial state radiation and final state radiation. The lack of those features might contribute to the differences found between the measured data and the BDK Monte Carlo data.

The goal of validating the two-photon Monte Carlo generators was achieved. In the next chapter the impact of the two-photon process on the expected background for the Pixel Vertex Detector at Belle II is presented in detail. In general, only the low momentum region below 20 MeV is crucial for the PXD. In this momentum region both, KoralW and BDK, agree with each other and could be used to produce the Monte Carlo data for the background studies. However, due to performance advantages and possible contributions from back-scattered particles originating from high p_t tracks, albeit a very small contribution, BDK will be used as the Monte Carlo generator.

7 Expected background for the PXD

7.1 Introduction

With the increase of the luminosity, by decreasing the transverse beam size by a factor 20 and doubling the beam currents at SuperKEKB in comparison to KEKB (section 3.6), the amount of background will increase significantly at Belle II. In general, the individual processes contributing to the background can be categorised into two types: **beam-induced** and **luminosity-dependent** processes. The beam-induced processes originate from the collisions of beam particles with residual gas in the beampipe, bending magnets or particles within a bunch, whereas luminosity-dependent processes comprise electron-positron collisions leading to “non-interesting” physics processes such as Bhabha scattering or two-photon processes. This chapter introduces the dominating beam-induced and luminosity-dependent background processes at Belle II and estimates their individual contribution to the total PXD background. The main objective of this study is to understand the expected occupancy of the PXD at full luminosity, which will serve as an important criterion for the construction principles of the pixel detector and its usefulness for the upcoming physics analyses.

7.2 Detailed simulations of the PXD background

The simulation of each background process studied in this chapter results in a dataset consisting of the 4-vector information for individual particles. The number of particles per dataset depends on the type of background being simulated. Each particle in the dataset is described by its type, the vertex from which it originated and its momentum. This information is given to basf2 in order to perform the Geant4-based full detector simulation (see section 5.4). The simulation settings follow the standard basf2 settings, except for the choice of the physics processes (“physics list”) to be studied. For the background studies the Geant4 physics list QGSP_BERT_HP is used. This list extends the standard QGSP_BERT physics list by a data driven, high precision neutron package and allows for the transport of neutrons below 20 MeV down to thermal energies. This is of particular interest for the PXD neutron studies presented in section 7.3.6. The simulation is carried out for the range of -8 m to 8 m along the global z -axis in order to incorporate any effects that far-beamline components might have on the PXD background. Although

all sub-detectors are present in the full detector simulation, only the PXD is set to record data. This helps to keep the simulation time and file size small, while still incorporating the physical effects the other detectors have on the PXD into the simulation, such as back-scattering or particle showers.

As it will be shown in the upcoming sections, almost all particles given to the full detector simulation originate either from the IP and hit the PXD directly or come from particle showers/back-scattered particles with their origin outside the beampipe. Therefore, the two-dimensional magnetic field map (see section 5.3) is accurate enough for a realistic full detector simulation. The output of the simulation are the Geant4 steps recorded by the PXD, referred to as PXDSimHits and the locations where a particle traversed the PXD sensors, called PXDTrueHits (see section 5.4 and 5.7).

7.2.1 Relative normalisation of backgrounds

The number of particles within a single dataset does not correspond to an event as it will be recorded by the PXD, yet. In order to be able to compare the results of the different backgrounds with each other, a common normalisation is introduced. The readout cycle of the PXD (see section 4.3.3) implies to normalise the various background contributions to one **readout frame** (ROF), which represents a time window of $20\ \mu\text{s}$. This is accomplished by merging the content of multiple datasets into a single ROF event where the number of datasets used, and thus number of particles, depends on the background type at hand. For the SAD-based background types it is sufficient to simply merge all datasets into one single event, as the normalisation can be done during the loading of the SAD file. By setting the SAD integration time to the PXD readout time, a single SAD file is converted to the correct number of datasets, representing exactly one ROF. For the luminosity-dependent processes, the number of datasets that have to be merged into a single ROF event is given by

$$N_{evt} = \sigma \cdot \mathcal{L} \cdot 20\ \mu\text{s}$$

where σ is the cross-section of the particular process and $\mathcal{L} = 0.8 \frac{1}{pb\ s}$ the design luminosity of SuperKEKB. The number of events for the synchrotron radiation is taken from the number of hits recorded in the beamline multiplied by $1 \cdot 10^3$. The factor converts the 20 ns of events from the simulation to the ROF time of $20\ \mu\text{s}$. Table 7.1 summarizes the number of datasets that represent a single ROF event for all backgrounds after relative normalisation.

7.2.2 PXD simulation and reconstruction

After the normalisation, each event corresponds to an integration time of $20\ \mu\text{s}$, representing the amount of background the PXD will see during its readout time. The PXDSimHits of each event are then taken as an input to the simulation of the PXD response (see section 5.5), with the settings given by table 5.2. The output of the PXD response simulation are the fired pixels of the PXD, referred to as PXDDigits (see section 5.4 and 5.7). The PXDDigits are then clustered using the clustering method described in section 5.6. The PXDTrueHits and the clustered pixels, called PXDClusters, are the input for the Belle II background analysis and characterisation studies, presented in the next sections.

Generator	number datasets [10^3]
Touschek LER	13.25
Touschek HER	4.43
Beam-Gas LER	2.02
Beam-Gas HER	0.02
Radiative Bhabha LER	1008
Radiative Bhabha HER	310.1
Synchrotron radiation HER	$3979 \cdot 10^3$
Synchrotron radiation LER	$2250 \cdot 10^3$
Two-photon	118

Table 7.1: Summary of the number of datasets that represent one ROF event

7.3 Figures of merit

The various backgrounds contributing to the total background of the PXD are analysed and compared with each other using several figures of merit. This section introduces the figures of merit and explains how each of them is computed.

7.3.1 Particle flux

The particle flux measures the number of particles that traverse the PXD sensors per second and per area. Of particular interest is the distribution of the particle flux along the global z -axis. Any sensor areas with an increased particle flux compared to the rest of the sensors are a hint of an increased radiation damage in this confined area, a scenario the hardware developers would like to avoid. The particle flux is estimated by counting the PXDTrueHits inside a PXD

sensor for one ROF and plotting the result with respect to the global z -axis. In addition the spatial and angular distributions of the traversing particles for each background are studied.

7.3.2 Origin of particles

The particle flux explains in detail the angles and locations of the background particles traversing the PXD. But where does the background actually come from? The answer to this question is of great relevance for the mechanical design of the interaction region. For example, changing the size of the apertures and the radii of the IR beampipes directly influences the amount of background found in the PXD. The origin of the background particles is evaluated by tracing back the production chain for each particle to the beginning of the chain.

7.3.3 Occupancy

The occupancy is one of the most important figures of merit for the PXD. It is defined as the number of pixels fired within one ROF divided by the total number of pixels of the PXD. Due to limitations imposed by the DAQ (DHP bandwidth) and its impact on the track finding performance, the maximum allowed value for the PXD occupancy is 3 %. Ideally, the average occupancy is below 2 % in order to allow for some headroom. For each background the number of PXDDigits is counted separately for each ladder and each ROF and divided by the number of pixels in a ladder. The result of multiple ROFs for the same ladder is filled into a histogram. The mean of the distribution is taken as the occupancy value for the particular ladder and the standard deviation as its error.

7.3.4 Cluster analysis

The large data rate expected for the PXD demands the implementation of an online data reduction scheme, as described in section 4.12. In addition to the propagation of the track onto the PXD, a hit recovery scheme will help in the rescue of low momentum particles. In order for the hit recovery scheme to work efficiently, a separation between signal and background induced pixels is necessary. If clusters created by background pixels exhibit certain features that clusters from signal pixels do not have, a neural network or a similar technique could be trained to differentiate between the pixels that should be kept and those that can be removed safely. The cluster analysis figures of merit aims at comparing the spatial features of pixel clusters created by different background types with each other.

The clustering method from section 5.6 is used to group pixels into clusters. An example is given in figure 7.1, which shows the result of the clustering algorithm for the two-photon background.

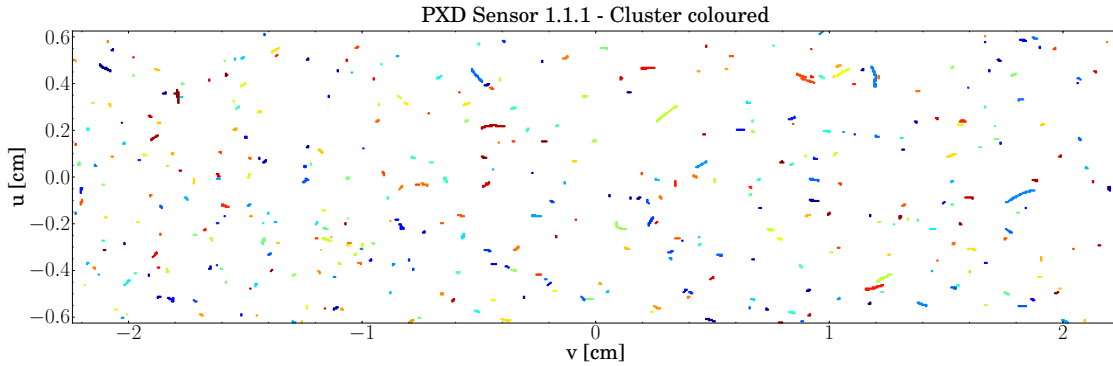


Figure 7.1: Result of the clustering algorithm applied to one ROF of the two-photon background on sensor 1.1.1.

The number of pixels that are contained in a single cluster is called the **cluster size**. The cluster size, however, does not contain any information about the geometrical pattern of the pixel clusters, which allows for a more refined comparison of the different background types. This is especially the case for clusters containing 3 or more pixels, where the same cluster size can look very differently. Two figures of merit are investigated: the angle of a cluster and the length of a cluster. The angle of a cluster is defined as the angle of the major axis of the cluster with respect to the global z -axis. Figure 7.2 illustrates the definition of the major cluster axis and shows how the angle is measured.

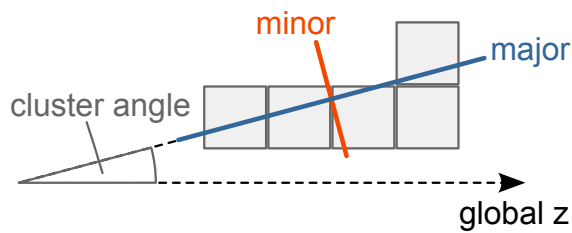


Figure 7.2: The angle of a cluster is defined as the angle between the major axis of a cluster and the global z -axis of Belle II (which is also the global z -axis of the PXD).

The major axis of a cluster is calculated using the **principle component analysis** method (PCA) [230, 231]. The PCA is a robust way to reduce the dimensionality and extract specific features of a given dataset. It uses the correlation between the variables of the data to convert the data into a set of values of linearly uncorrelated variables called **principal components**. The input data for the PCA are the pixel positions of a single cluster. By calculating the mean value for the pixel positions in x and y independently, the cluster's 2×2 covariance matrix is gained. This matrix contains the full information of the relationship between the x and y dimensions of the

clusters. Finding the eigenbasis of the covariance matrix provides a way to reduce the complexity of a cluster down to its two principal components: the major and minor axis of the cluster. The eigenbasis is obtained by calculating the eigenvalues and eigenvectors of the covariance matrix. The eigenvectors are then ordered by their associated eigenvalue. The eigenvector with the largest eigenvalue corresponds to the major cluster axis, the remaining eigenvector to the minor cluster axis. Measuring the angle between the major axis and the global z -axis yields the cluster angle. In order to illustrate the method visually, the PCA algorithm is applied to figure 7.1 and the result is drawn in figure 7.3. For each cluster the major axis (red), the minor axis (blue) and the number of pixels contained in the cluster is presented.

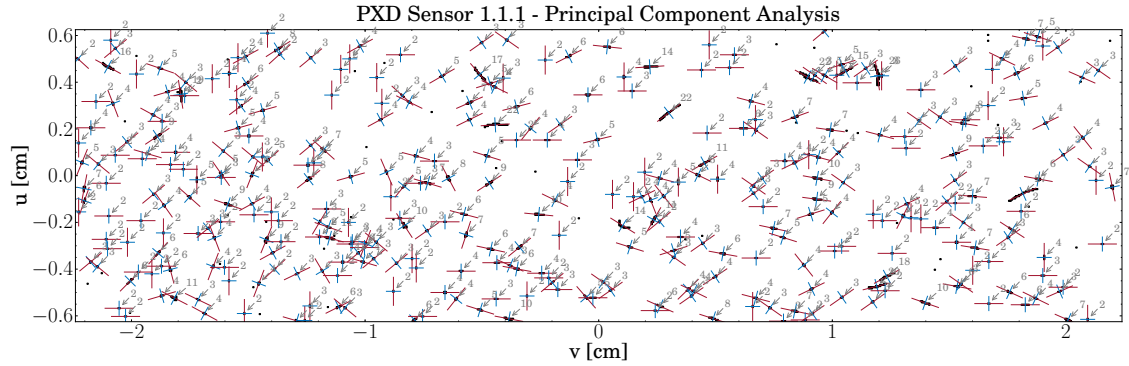


Figure 7.3: The result of the PCA after applying it to the data of figure 7.1. For each cluster the major axis (red), the minor axis (blue) and the number of pixels contained in the cluster is shown.

While the PCA provides a robust way to estimate the angle of a cluster, it does not allow the measurement of the length of a cluster. The length of a cluster is defined as the distance a cluster spans along its major axis. This is different to the cluster size as, for example, it takes curved clusters into account. A robust way to measure the length of a cluster is achieved by finding the **smallest enclosing ellipse** for each cluster. The length of the cluster is then given by the length of the major axis of the ellipse. The left drawing in figure 7.4 illustrates the method.

The estimation presented in this chapter makes use of an implementation of [232] from the CGAL library [233] in order to calculate the smallest enclosing ellipse. The library returns the fitted ellipse as a conic in linear form, which is the set of points $p = (x, y)^T$ satisfying the quadratic equation

$$rx^2 + sy^2 + txy + ux + vy + w = 0 \quad (7.1)$$

The output of the algorithm is a set of parameters (r, s, t, u, v, w) . Although this fully describes

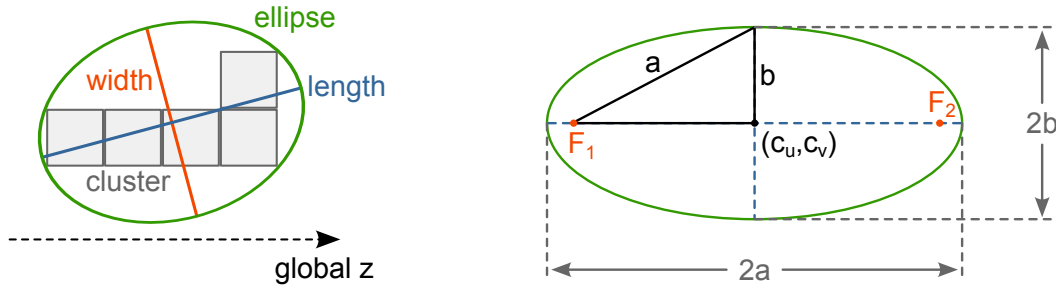


Figure 7.4: Definition of the length of a cluster. The left drawing illustrates the smallest enclosing ellipse fitted around a pixel cluster. The major axis of the ellipse is then defined as the length of the cluster. The right drawing shows the definition of the centre of the ellipse (c_u, c_v) and the semi-major axis a and the semi-minor axis b . The major axis is then $2 \cdot a$ and the minor axis is $2 \cdot b$.

the ellipse, the parameters of interest are the major and minor axis and the centre of the ellipse. From the matrices

$$M_0 = \begin{pmatrix} w & u/2 & v/2 \\ u/2 & r & t/2 \\ v/2 & t/2 & s \end{pmatrix} \quad M = \begin{pmatrix} r & t/2 \\ t/2 & s \end{pmatrix} \quad (7.2)$$

the semi-major axis a and semi-minor axis b (illustrated on the right hand side of figure 7.4) are given by

$$a = \sqrt{-\det(M_0) / (\det(M) \cdot \lambda_1)} \quad (7.3)$$

$$b = \sqrt{-\det(M_0) / (\det(M) \cdot \lambda_2)} \quad (7.4)$$

where $\lambda_{1/2}$ are the eigenvalues of the matrix M . The length of the cluster is then $2 \cdot a$. The centre of the matrix is

$$c_u = \frac{tv - 2su}{4rs - t^2} \quad (7.5)$$

$$c_v = \frac{tu - 2rv}{4rs - t^2} \quad (7.6)$$

As an example, figure 7.5 draws the result of the ellipse fitting method after it is applied to the data of figure 7.1.

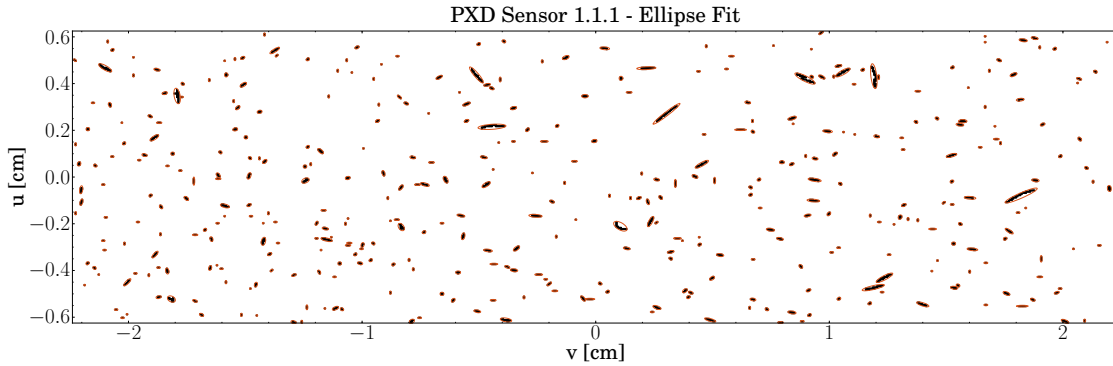


Figure 7.5: The result of the ellipse fitting algorithm applied to the two-photon data of figure 7.1. For each cluster the fitted ellipse is drawn.

7.3.5 Radiation dose

The definition of **radiation dose**, used in this thesis, follows the definition given in [188, 234]

$$D = \frac{d\bar{\epsilon}}{dm} \quad (7.7)$$

where $d\bar{\epsilon}$ is the mean energy deposited in a volume with the mass dm . The sensitive area of each PXD ladder is subdivided into 2 mm slices along the global z -axis. For each slice, the energy that traversing particles deposit over the time span of a single readout frame (20 μ s) is summed up. This procedure is performed for multiple readout frames. The mean value of all sums is calculated and divided by the mass of the slice. In order to estimate the expected radiation dose for a typical one-year run period of the PXD the value is normalised to one snowmass year.

7.3.6 Neutron flux

Radiation damage can originate from two types of processes: ionisation processes and non-ionisation energy loss (NIEL) processes. The first process is responsible for the radiation dose discussed in the previous section. In the case of the latter one, however, the deposited energy either results in atomic displacements or dissipates in lattice vibrations of the silicon material [132]. For all particles except neutrons, the energy deposition by non-ionising processes is much lower than that of ionising processes. As discussed in section 4.3.6 bulk damage in the PXD is mostly the result from atomic displacement deposition mechanisms. As neutrons play a crucial role for those mechanisms, the expected neutron flux and energy distribution arising from the various background types are studied. Experimental observations suggest that damage effects

in silicon can be described as being proportional to a displacement damage cross-section, D , defined to be equivalent to the NIEL. This proportionality is also called the **NIEL scaling hypothesis**. The value of D depends on the particle type and its energy, which allows the comparison of damage caused by different particle types or energies. The damage cross-section for a 1 MeV neutron is used as the normalisation value [235]

$$D(1\text{MeV}) = 95\text{MeVmb} \quad (7.8)$$

Figure 7.6 draws the normalised NIEL values as a function of energy.

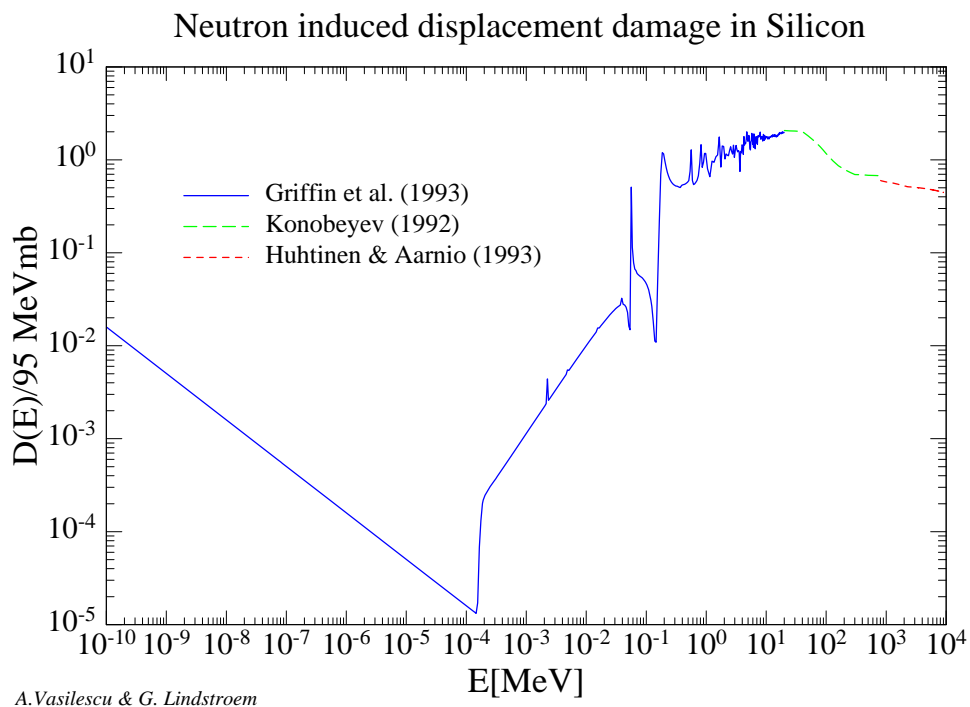


Figure 7.6: Normalised NIEL damage cross-section $D(E)$ for neutrons in silicon [236].

Another important figure of merit for neutrons is the fluence rate, defined as [188]

$$\Sigma = \frac{d^2N}{da dt} \quad (7.9)$$

where dN is the number of particles traversing the area da during the time interval dt .

7.4 Beam-induced processes

The beam travelling in a storage ring, such as SuperKEKB, is subject to a constant loss of particles. Of course, the beam loses particles from the collisions at the interaction point, but, to a much greater extent, particles are lost because they leave the spatial or momentum acceptance of the accelerator. This means that the tails of a 3-dimensional Gaussian-like particle bunch are truncated by the ring acceptance as the bunches travel through the ring. Due to the loss of particles, the beam will disappear after a finite time, called the **beam-lifetime**, and has to be refilled. SuperKEKB employs a continuous injection scheme (section 3.8) in order to replace the lost particles. The beam-lifetime is defined as the time after which the beam is reduced by a factor of e . The beam-lifetime is composed of several components and is summed as follows [91]

$$\frac{1}{\tau} = \frac{1}{\tau_{Touschek}} + \frac{1}{\tau_{Beam-Gas}} + \dots$$

A listing of the beam-lifetime values for SuperKEKB were given in table 3.2. Particles that have left the beam's nominal trajectory and thus are outside the accelerator's acceptance will collide with the beampipe wall or a beam-mask. As with most collisions of high-energy particles with matter, a particle shower is created. If this shower happens to be generated in the vicinity of the Belle II detector, shower particles might enter the detector and will be seen as background in the various sub-detectors. The PXD, for example, will then record additional hits on top of the hits produced by a physics event.

7.4.1 Touschek effect

SuperKEKB achieves its high luminosity by squeezing the particles into tiny bunches leading to a high particle density within the bunch (section 3.6). During their journey around the accelerator, the particles within the bunches oscillate perpendicular to the beam direction (see section 3.4). This oscillation, particularly in areas of high bunch densities, results in a high collision rate of the particles within the bunch. Coulomb scattering causes two types of collisions, both

affecting the beam. Multiple collisions at small angles, called **intra-beam scattering**, degrade the beam quality by increasing the emittance and worsening the beam size in all three directions. However, they are not responsible for an immediate loss of particles. Single large angle collisions that cause an exchange of energy between the longitudinal and the transversal motion of the colliding particles can kick them out of their bunch. Eventually they hit a beampipe wall or beam-mask and are lost. This process is called the **Touschek effect**, named after the Austrian physicist Bruno Touschek. The effect has been observed for the first time at AdA in Frascati, Italy in 1963 [237], which was also the first e^+e^- storage ring ever built¹.

The Touschek effect can reduce the beam lifetime considerably, especially at a low energy, low emittance accelerator, such as SuperKEKB. Theoretical calculations have been carried out in [237, 239] for the non-relativistic case. An extension to the ultra-relativistic case can be found in [240] and one for arbitrary energies in [241]. A non-relativistic calculation for round beams, which means a full strength coupling between horizontal and vertical betatron oscillations, has been performed in [242]. In the following, the process that transfers energy from the transverse motion of the colliding particles to their longitudinal motion [243] is presented in more detail.

Theory

Before the collision, the particles' momenta are given in the laboratory system as

$$\vec{p}_{1,2} = \begin{pmatrix} p_{x1,2} \\ p_{y1,2} \\ p_{z1,2} \end{pmatrix} \quad (7.10)$$

where the coordinate system follows the definition in section 3.2, with the difference that the z-axis points into the beam direction. In order to simplify the calculations, a new coordinate system $\{j, k, l\}$ is chosen, such that both colliding particles lie in a plane defined by the normal vector

$$\begin{pmatrix} e_x \\ e_y \\ e_z \end{pmatrix} \rightarrow \begin{pmatrix} \vec{p}_1 \times \vec{p}_2 \\ (\vec{p}_1 + \vec{p}_2) \times (\vec{p}_1 \times \vec{p}_2) \\ \vec{p}_1 + \vec{p}_2 \end{pmatrix} \quad (7.11)$$

Figure 7.7 shows the colliding particles in the new coordinate system. The particles collide with each other under the angles χ_1 and χ_2 , defined with respect to the l -axis.

¹The AdA e^+e^- storage ring has been proposed by Bruno Touschek in 1960 [238]. In his proposal for AdA, Touschek uses the term *luminosity* for the interaction rate. It appears that Touschek has been the first to use this term. It was probably inspired by his proposal to use $e^+e^- \rightarrow 2\gamma$ as the monitor for the event rate.

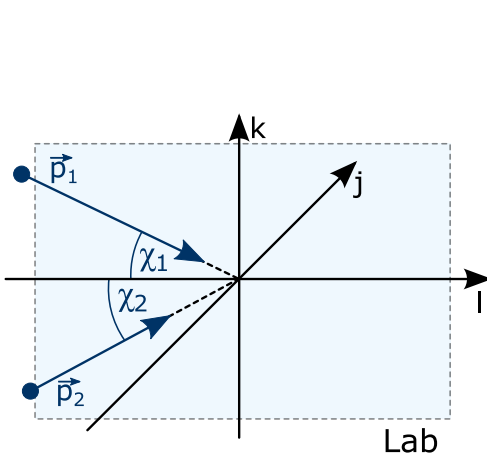


Figure 7.7: The $\{j, k, l\}$ laboratory coordinate system in which the colliding particles lie in the plane spanned by the k -axis and the l -axis.

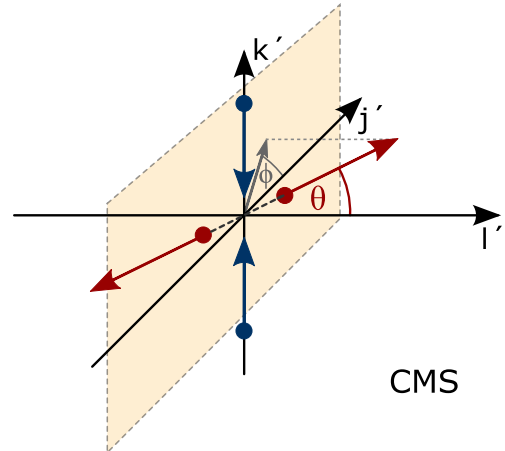


Figure 7.8: The coulomb scattering in the center-of-mass system of the bunch. Blue are the incoming particles and red the scattered particles.

The momenta of the particles in the new coordinate system are then

$$\vec{p}_{1,2} = p_{1,2} \cdot \begin{pmatrix} \cos \chi_{1,2} \\ 0 \\ \pm \sin \chi_{1,2} \end{pmatrix} \quad (7.12)$$

In order to transform the particle from the laboratory system into the centre-of-mass system of the particle's bunch, a Lorentz transformation is applied

$$\begin{pmatrix} 0 \\ \pm p_{1,2} \sin \chi_{1,2} \\ p_{1,2} \gamma \cos \chi_{1,2} - \gamma \beta E_{1,2} \\ \gamma E_{1,2} - p_{1,2} \gamma \beta \cos \chi_{1,2} \end{pmatrix} = \begin{pmatrix} 1 & 0 & 0 & 0 \\ 0 & 1 & 0 & 0 \\ 0 & 0 & \gamma & -\gamma \beta \\ 0 & 0 & -\gamma \beta & \gamma \end{pmatrix} \cdot \begin{pmatrix} 0 \\ \pm p_{1,2} \sin \chi_{1,2} \\ p_{1,2} \cos \chi_{1,2} \\ E_{1,2} \end{pmatrix} \quad (7.13)$$

where β is the relative velocity of the bunch, γ the Lorentz factor and $E_{1,2}$ the energies of the colliding particles. The beams at SuperKEKB are considered to be flat (see section 3.6). Thus, it is safe to assume that the angles $\chi_{1,2}$ are small and can be approximated by

$$\sin \chi_{1,2} \approx \chi_{1,2} \quad \cos \chi_{1,2} \approx 1$$

With $E_{1,2} = \frac{p_{1,2}}{\beta}$ the 4-momenta of the particles in the centre-of-mass system are then given by

$$P'_{1,2} = p_{1,2} \cdot \begin{pmatrix} 0 \\ \pm \chi_{1,2} \\ 0 \\ \frac{1}{\beta \gamma} \end{pmatrix} \quad (7.14)$$

Figure 7.8 shows the single coulomb scattering, responsible for the Touschek effect, in the centre-of-mass system of the bunch. The incoming particles (blue in fig. 7.8) scatter elastically and leave under the polar angle θ and the azimuthal angle ϕ (orange in fig. 7.8). The momenta of the particles change as follows

$$\pm p_{1,2} \chi_{1,2} \begin{pmatrix} 0 \\ 1 \\ 0 \end{pmatrix} \longrightarrow \pm p_{1,2} \chi_{1,2} \begin{pmatrix} \sin \theta \cos \phi \\ \sin \theta \sin \phi \\ \cos \theta \end{pmatrix} \quad (7.15)$$

Performing the same Lorentz transformation as in equation 7.13 with $-\beta \rightarrow \beta$, returns the 4-momenta of the scattered particles in the laboratory system

$$P_{1,2} = \begin{pmatrix} \pm p_{1,2} \chi_{1,2} \sin \theta \cos \phi \\ \pm p_{1,2} \chi_{1,2} \sin \theta \sin \phi \\ p_{1,2} \pm \gamma p_{1,2} \chi_{1,2} \cos \theta \\ E_{1,2} \pm p_{1,2} \gamma \beta \chi_{1,2} \cos \theta \end{pmatrix} \quad (7.16)$$

From equation 7.16 follows that the Touschek effect changes the energy of the particles

$$E_{1,2} \longrightarrow E_{1,2} \pm p_{1,2} \gamma \beta \chi_{1,2} \cos \theta$$

As one particle gains energy the other one loses energy. The gain or loss is amplified by the Lorentz factor γ , meaning that even small amounts of energy being transferred from the transverse to the longitudinal motion is usually enough to kick the particles out of their nominal orbit and the energy acceptance of the accelerator. The rate at which the Touschek effect scatters particles in a single bunch, is given by the formula from Piwinski [243]. It is the most general description of the Touschek scattering rate

$$R_{Touschek}^{Piw} = \frac{r_e^2 c \beta_x \beta_y \sigma_h N^2}{8 \sqrt{\pi} \beta^2 \gamma^4 \sigma_x^2 \beta \sigma_y^2 \beta \sigma_s \sigma_p} \int_{\tau_m}^{\infty} \left(\left(2 + \frac{1}{\tau} \right)^2 \left(\frac{\tau/\tau_m}{1 + \tau} - 1 \right) + 1 - \frac{\sqrt{1 + \tau}}{\sqrt{\tau/\tau_m}} - \frac{1}{2\tau} \left(4 + \frac{1}{\tau} \right) \ln \frac{\tau/\tau_m}{1 + \tau} \right) e^{-B_1 \tau} I_0(B_2 \tau) \frac{\sqrt{\tau} d\tau}{\sqrt{1 + \tau}} \quad (7.17)$$

with

$$B_1 = \frac{\beta_x^2}{2\beta^2\gamma^2\sigma_{x\beta}^2} \left(1 - \frac{\sigma_h^2 \tilde{D}_x^2}{\sigma_{x\beta}^2} \right) + \frac{\beta_y^2}{2\beta^2\gamma^2\sigma_{y\beta}^2} \left(1 - \frac{\sigma_h^2 \tilde{D}_y^2}{\sigma_{y\beta}^2} \right)$$

and

$$B_2^2 = B_1^2 - \frac{\beta_x^2 \beta_y^2 \sigma_h^2}{\beta^4 \gamma^4 \sigma_{y\beta}^4 \sigma_{y\beta}^4 \sigma_p^2} \left(\sigma_x^2 \sigma_y^2 - \sigma_p^4 D_x^2 D_y^2 \right)$$

In formula 7.17, r_e is the classical electron radius, β_x, β_y the Twiss parameters for the horizontal and vertical beam size (see section 3.6), N^2 the number squared of particles per bunch, σ_x, σ_y the horizontal and vertical beam size, σ_p the relative momentum spread, σ_s the bunch length, I_0 the modified Bessel function and σ_h is given by

$$\frac{1}{\sigma_h^2} = \frac{1}{\sigma_p^2} + \frac{D_x^2 + \tilde{D}_x^2}{\sigma_{x\beta}^2} + \frac{D_y^2 + \tilde{D}_y^2}{\sigma_{y\beta}^2}$$

where $\sigma_{x\beta}$ and $\sigma_{y\beta}$ are the standard deviations for the horizontal and vertical betatron distribution

$$\sigma_{x\beta} = \sqrt{\epsilon_x \beta_x} \quad \sigma_{y\beta} = \sqrt{\epsilon_y \beta_y}$$

The dispersion (dependence of the orbit on the energy) enters the formula as D_x, D_y and \tilde{D}_x, \tilde{D}_y with

$$\tilde{D}_{x,y} = \alpha_{x,y} D_{x,y} + \beta_{x,y} D'_{x,y}$$

The integral runs over all angles of all particles with $\tau = \beta^2 \gamma^2 \chi^2$, starting with

$$\tau_m = \beta^2 \delta_m^2$$

where δ_m describes the maximum, stable relative momentum spread $\Delta p/p$ [243] the accelerator allows, referred to as the momentum acceptance. This means that the integration in equation 7.17 is performed for all particles which are above that limit and are therefore lost after scattering.

As can be seen from equation 7.17, the Touschek scattering rate is **proportional** to the number of particles per bunch squared ($R_{Touschek} \propto N^2$) and **inversely proportional** to the square of the beam size ($R_{Touschek} \propto \sigma_{x,y}^2$). Therefore, at SuperKEKB, the nano-beam scheme leads to a

large Touschek scattering rate about 20 times larger for the LER and 28 times larger for the HER compared to KEKB [244]. The time after which the number of particles in the beam drops to half of the initial number as a result of the Touschek effect is called the **Touschek lifetime**

$$\frac{1}{\tau_{Touschek}} = \left\langle \frac{R_{Touschek}}{N_0} \right\rangle \quad (7.18)$$

with $R_{Touschek}$ the Touschek rate from equation 7.17 or 7.19, N_0 the number of particles in the bunch and the brackets denoting the average over the circumference of the SuperKEKB accelerator. At SuperKEKB, the expected Touschek lifetime is about 600 s (see section 3.2).

Simulation

The Monte Carlo simulation of the Touschek effect is carried out by combining the accelerator tracking software SAD (see section 3.10) with the Touschek scattering rate formula. So-called **macro-particles**, representing a fraction of the beam and as such many “real” particles, are distributed uniformly along the ideal orbit of the whole accelerator ring. Each macro-particle is then propagated through the ring using SAD. At each propagation step the Touschek scattering rate is calculated. It is found, however, that the implementation of the general Touschek equation imposes difficulties due to numerical and computational issues. Thus, an approximation assuming flat beams and particles having a non-relativistic transverse momentum is used. The calculation for this approximation of the Touschek scattering rate has been carried out by Brück [245]

$$R_{Touschek}^{Br} = \frac{r_e^2 c \beta_x N^2}{8\pi\beta\gamma^3 \tilde{\sigma}_x \sigma_x \sigma_y \sigma_z} \int_{\tau_m}^{\infty} \left(\frac{\tau}{\tau_m} - 1 + \frac{1}{2} \ln \frac{\tau_m}{\tau} \right) \exp^{-\frac{\tau_m}{\tau}} \frac{d\tau}{\tau^2} \quad (7.19)$$

where $\tilde{\sigma}_x^2 = \sigma_{x\beta}^2 + \sigma_p^2 (D_x^2 + \hat{D}_x^2)$. From equation 7.19 one can see another, important feature of the Touschek effect. Due to the relation $R_{Touschek} \propto \frac{1}{\gamma^3}$ the Touschek rate **scales with the beam energy** like E^{-3} , making the Touschek effect larger in the LER than in the HER.

The macro-particles that are subject to Touschek scattering undergo a change of their momentum according to the formulas above. If a macro-particle hits the beampipe or a mask, it is considered to be lost and taken out from the simulation. The **loss position** together with the macro-particle’s momentum vector is recorded. The rate with which particles are lost at this position is calculated from the scattering rate and is called the **loss rate**. The result of the SAD simulation is a file, in the following referred to as the SAD file, containing the loss positions, momenta and loss rates of the macro-particles.

For the next stage, the full detector simulation, the SAD file has to be read into basf2. A special SAD reader module was developed within this thesis for that purpose. For each macro-particle

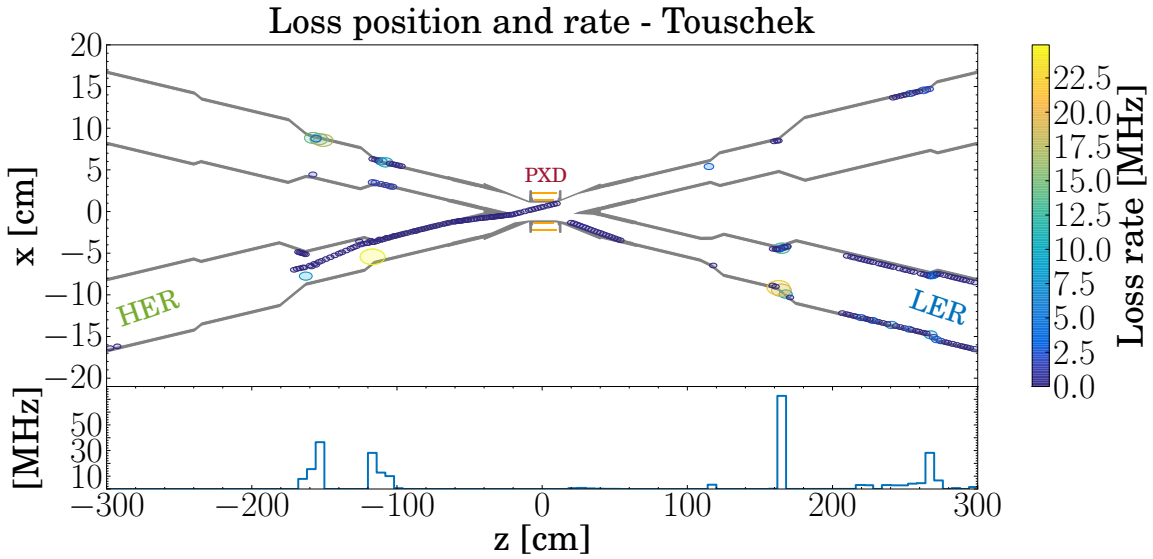


Figure 7.9: The locations and loss rates for the Touschek particles after the SAD accelerator simulation. The bottom plot shows the loss rate in [MHz].

in the SAD file multiple “real” particles are generated, where the number is given by the loss rate and the detector readout time ($20\ \mu\text{s}$ for the PXD). Each newly generated particle gets the loss position and the momentum of the macro-particle assigned and is added as a 4-vector particle to the list of Monte Carlo particles. If the number of “real” particles per macro-particle is below one, a random generator decides whether a particle should be created. By applying this reading scheme it is ensured that the output is automatically normalised to the readout time of a particular sub-detector. The loss positions and loss rates obtained from the simulation of the LER and HER Touschek effect are shown in figure 7.9. Of particular interest are the positions of the high loss rate regions within a range of about 3 m from the PXD. While the HER exhibits only one high loss rate region, the LER has multiple regions, upstream as well as downstream from the IP. In order to answer the question of which regions contribute to the background of the PXD and by how much, a detailed full detector simulation study is performed.

Particle flux

Figure 7.10 illustrates the angular and spatial distributions of the electrons and positrons traversing the PXD that emerged from the Touschek LER background. The left plots show the $z\text{-}\phi$ distribution for the inner layer (top plot) and the outer layer (bottom plot). A clear peak is visible in the forward part of the PXD sensor and for the azimuthal angle area around 0° . The increased exposure in the forward part can be explained by the direction from which the LER enters the IR, while the angular distribution is the result of the beam crossing angle. The peak is confined to the sensor area and affects the ASICs only moderately. Measuring the polar angle

of the particles at the location where they traverse the PXD produces the right hand side plots of figure 7.10. The distribution peaks strongly at 172° with the inner layer being only slightly more exposed to the background particles than the outer layer. This shows that the Touschek LER background enters the inner region of the Belle II detector under a shallow angle w.r.t. the global z -axis from the upstream direction. Since the background particles are produced by showers, both layers are affected similarly.

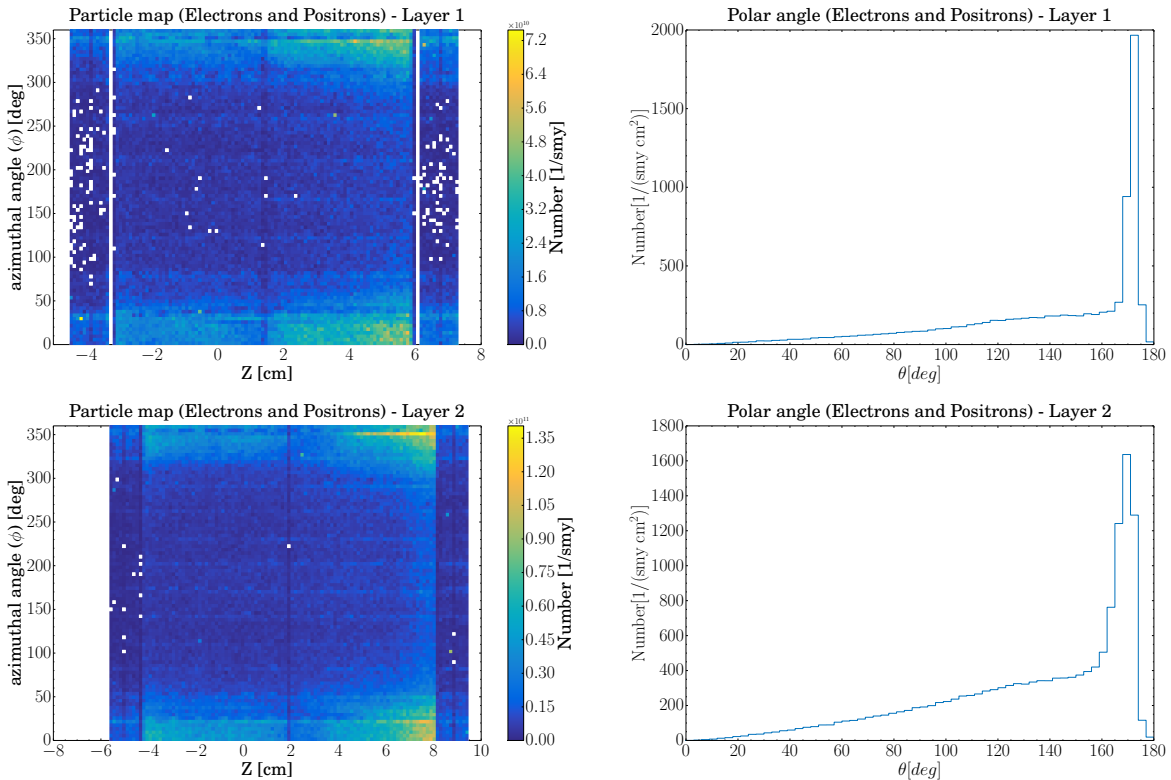


Figure 7.10: Angular and spatial distributions of the electrons and positrons traversing the PXD from Touschek LER per area during one snowmass year. The top row represents the inner layer and the bottom row the outer layer. The left plots show the z - ϕ distributions of electrons and positrons traversing the sensor area, the backward ASICs and the forward ASICs. The plots on the right hand side show the polar angle distribution.

The polar angle distribution of the Touschek HER background (see figure 7.11) is mirrored compared to the distribution from the LER background, with the peak being at 7° due to the upstream direction of the HER. The statistics in the z - ϕ distribution is too low to make a statement about possible peaks. However, it seems that the inner layer shows no pronounced peaks, while the outer layer has peaks for the forward and backward direction at the azimuthal angle of 0° .

Background particles do not necessarily traverse the sensors of the inner/outer PXD layer only once. Charged background particles are bent in the Belle II solenoid magnetic field and can return to the PXD if their transverse momentum (p_t) is low enough. In fact very low p_t particles

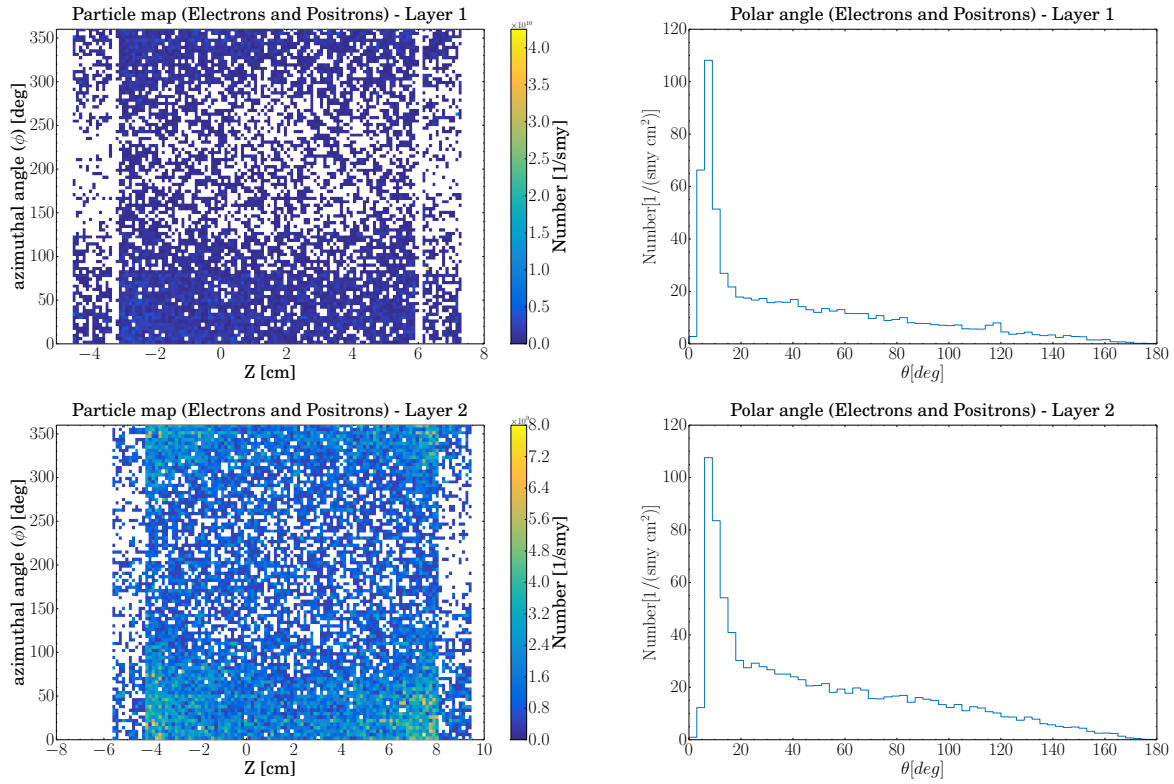


Figure 7.11: Angular and spatial distributions of the electrons and positrons traversing the PXD from Touschek HER per area during one snowmass year. The top row represents the inner layer and the bottom row the outer layer. The left plots show the $z\text{-}\phi$ distributions of electrons and positrons traversing the sensor area, the backward ASICs and the forward ASICs. The plots on the right hand side show the polar angle distribution.

are subject to **curling** in the magnetic field and might traverse the PXD multiple times before being stopped by material (usually the beampipe). These particles are often referred to as **curlers** and can contribute significantly to the particle flux. In order to understand the contribution of curlers to the total particle flux, the number of times a particle traverses a layer is counted and plotted with respect to the global z -axis in figure 7.12.

For both layers the single crossings in the forward part of the sensor dominates, with a minor contribution of two crossings. In the backward part of the sensor the curlers from multiple crossings play a larger role, contributing about 50 % to the overall particle flux.

Origin of particles

The two plots in figure 7.13 show the origin of the Touschek background (red: LER, orange: HER). This background is the result of particles lost at beampipe walls due to intra-beam scattering. The majority of the Touschek background is produced by particles from the LER beam

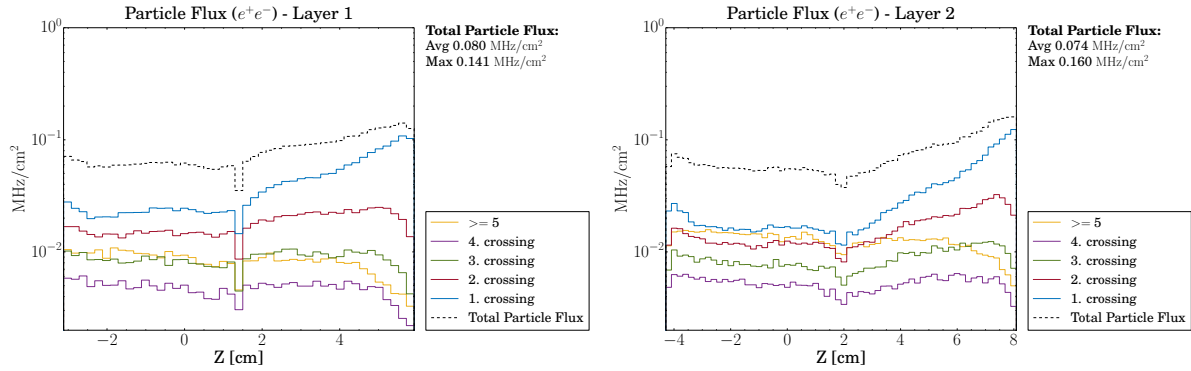


Figure 7.12: Distribution of the number of times a particle traverses a layer. The left plot shows the result for the inner layer and the right plot for the outer layer. Due to the low statistics of the Touschek HER, the plots only show the result for the LER.

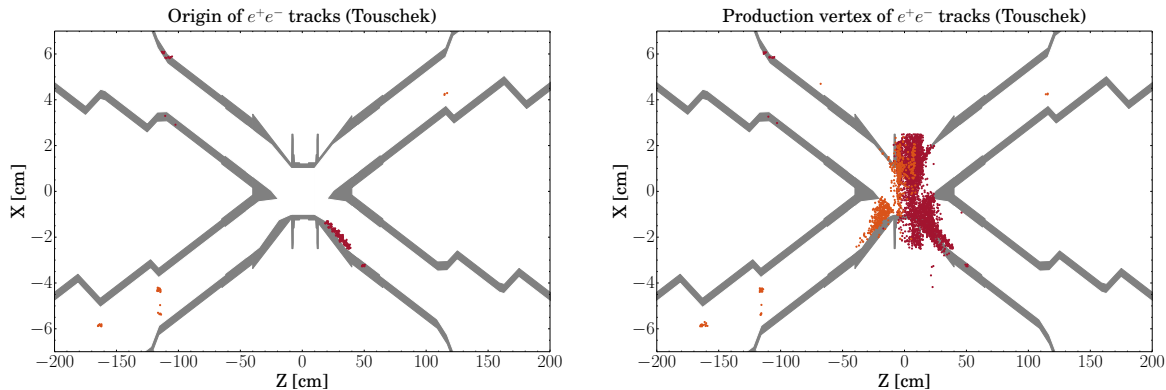


Figure 7.13: The left plot shows the distribution of the origin of all e^+e^- particles that spark the creation of particles that, further down the chain, hit the PXD sensors. The right plot shows primary as well as secondary particles that hit the PXD sensors, thus helping to identify the areas within the interaction region that contribute to the background of the PXD.

hitting the upstream, “inside”² wall between 18 cm and 40 cm where the beampipe radius is reduced. Minor contributions come from backscattered LER particles (at -110 cm) and HER particles. The Touschek particles lost at the beampipe wall interact with the material of the beampipe and give rise to particle showers that can hit the PXD, as the right Touschek plot shows. Of particular significance are the apertures closest to the IP and the material of the “inner” beampipe walls.

²as defined by the coordinate system in section 4.1

Occupancy

For the Touschek background, 1000 ROFs are simulated for both the HER and the LER. The top plot of figure 7.14 illustrates what a Touschek LER ROF looks like for sensor 1.1.1. The long pixel clusters, typical for the Touschek background, can be seen nicely. Looking at the xy -projection of the fired pixels an asymmetry in x is noticeable, exposing the ladder 1.1 to almost all particles originating from the Touschek LER background. This asymmetry is the result of the beam crossing-angle. The distribution of the fired pixels along z (bottom right plot of figure 7.14) shows a flat distribution for both, the inner and the outer layer of the PXD.

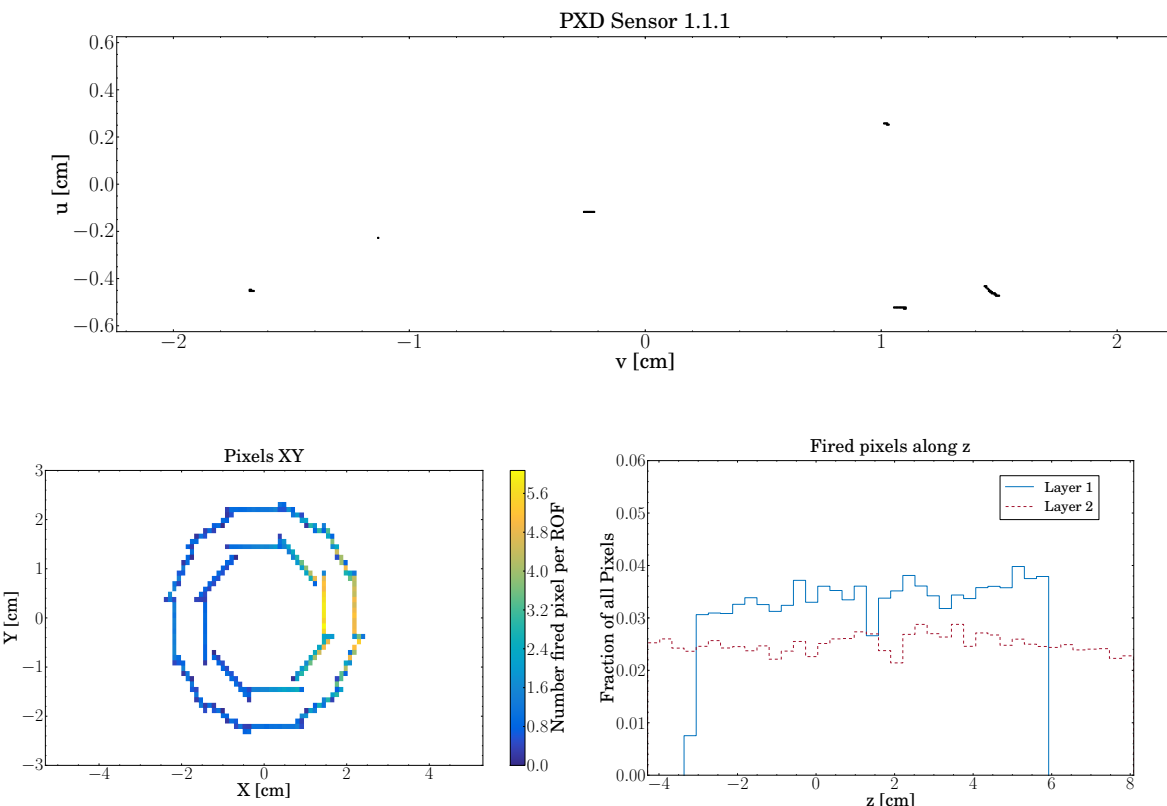


Figure 7.14: The fired pixels from the Touschek LER background. The top plot presents the content for one ROF of sensor 1.1.1. The bottom left plot shows the xy -projection where the asymmetry is caused by the beam-crossing angle. The distribution of the fired pixels along z in the bottom right plot is fairly flat.

The result of the Touschek simulation for the HER (figure 7.15) shows a similar pattern as for the LER. An asymmetry in both x and y is visible, exposing the upper right corner of the PXD to the HER Touschek. Again, the distribution along z is flat. A summary of the occupancy values of the Touschek background for each ladder of the PXD is given in figure 7.16 with the detailed values listed in table 7.2. The largest occupancy value is found in sensor 1.1.1 with $(17.8 \pm 6.8) \cdot 10^{-3}$

for the inner layer and in sensor 2.1.1 with $(14.8 \pm 5.7) \cdot 10^{-3}\%$ for the outer layer. The occupancy values for both layers are very similar, which can be explained by the fact that the background is created outside the interaction region. The particles created by secondary showers traverse the PXD in a shallow polar angle, thus affecting both layers in the same way.

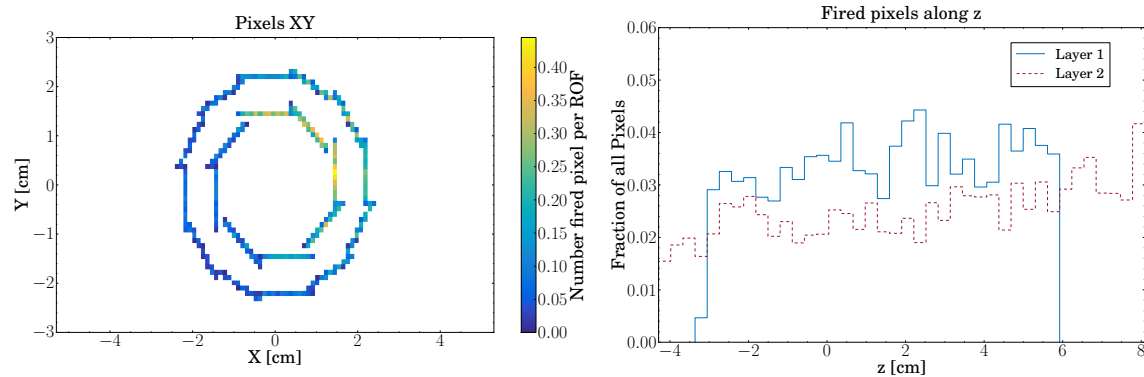


Figure 7.15: The fired pixels from the Touschek HER background. The left plot shows the xy -projection where the asymmetry is caused by the beam-crossing angle. The distribution of the fired pixels along z in the right plot is fairly flat with a slight rise in the forward direction.

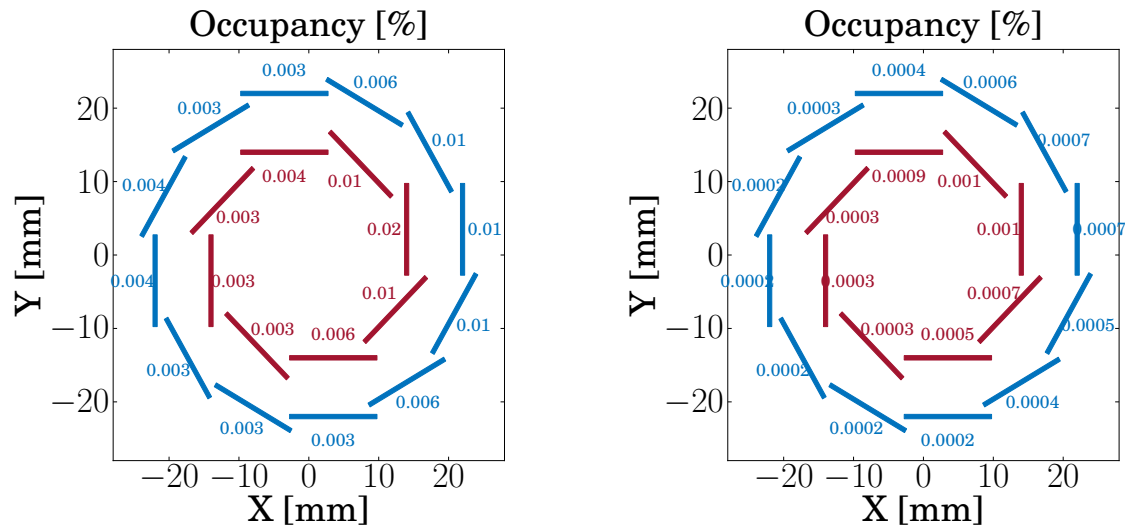


Figure 7.16: Summary of the PXD occupancy values for the Touschek LER (left) and Touschek HER (right) background.

Cluster analysis

Figure 7.17 plots the cluster angles for different cluster sizes of the Touschek background. It shows an equal amount of parallel and perpendicular 2-pixel clusters, with a tendency for larger

Layer 1 [%] $\cdot 10^{-3}$			Layer 2 [%] $\cdot 10^{-3}$		
Sensor	LER	HER	Sensor	LER	HER
1.1.1	17.8 ± 6.8	1.0 ± 0.2	2.1.1	14.8 ± 5.7	0.8 ± 0.2
1.1.2	15.9 ± 7.0	1.0 ± 0.3	2.1.2	13.8 ± 5.7	0.5 ± 0.05
1.2.1	11.3 ± 4.7	1.2 ± 0.4	2.2.1	11.5 ± 4.9	0.8 ± 0.1
1.2.2	10.3 ± 5.0	1.0 ± 0.3	2.2.2	10.9 ± 4.7	0.6 ± 0.04
1.3.1	4.2 ± 2.2	0.8 ± 0.1	2.3.1	5.9 ± 2.7	0.6 ± 0.2
1.3.2	4.5 ± 2.3	0.9 ± 0.2	2.3.2	6.0 ± 3.3	0.6 ± 0.2
1.4.1	2.7 ± 1.4	0.4 ± 0.03	2.4.1	3.4 ± 1.7	0.4 ± 0.05
1.4.2	3.1 ± 1.6	0.3 ± 0.04	2.4.2	3.6 ± 1.9	0.4 ± 0.05
1.5.1	2.4 ± 1.4	0.3 ± 0.05	2.5.1	2.6 ± 1.4	0.4 ± 0.05
1.5.2	2.8 ± 1.6	0.2 ± 0.04	2.5.2	2.8 ± 1.5	0.2 ± 0.02
1.6.1	3.2 ± 1.7	0.4 ± 0.08	2.6.1	3.8 ± 2.0	0.2 ± 0.03
1.6.2	3.3 ± 1.8	0.2 ± 0.04	2.6.2	3.4 ± 1.8	0.2 ± 0.03
1.7.1	6.1 ± 3.0	0.5 ± 0.03	2.7.1	4.2 ± 2.2	0.2 ± 0.03
1.7.2	5.5 ± 2.9	0.4 ± 0.04	2.7.2	4.2 ± 2.1	0.2 ± 0.05
1.8.1	13.7 ± 5.8	0.8 ± 0.1	2.8.1	3.3 ± 1.7	0.2 ± 0.03
1.8.2	11.9 ± 5.3	0.7 ± 0.2	2.8.2	3.4 ± 1.8	0.1 ± 0.03
			2.9.1	2.8 ± 1.5	0.2 ± 0.03
			2.9.2	2.8 ± 1.5	0.1 ± 0.03
			2.10.1	3.5 ± 1.9	0.3 ± 0.04
			2.10.2	3.4 ± 1.9	0.2 ± 0.03
			2.11.1	6.5 ± 2.9	0.4 ± 0.03
			2.11.2	6.5 ± 3.4	0.4 ± 0.04
			2.12.1	11.7 ± 4.9	0.6 ± 0.2
			2.12.2	11.9 ± 5.4	0.5 ± 0.04
Max	17.8 ± 6.8	1.2 ± 0.4	Max	14.8 ± 5.7	0.8 ± 0.2

Table 7.2: The detailed occupancy values for the Touschek background split into their individual contributions for each sensor.

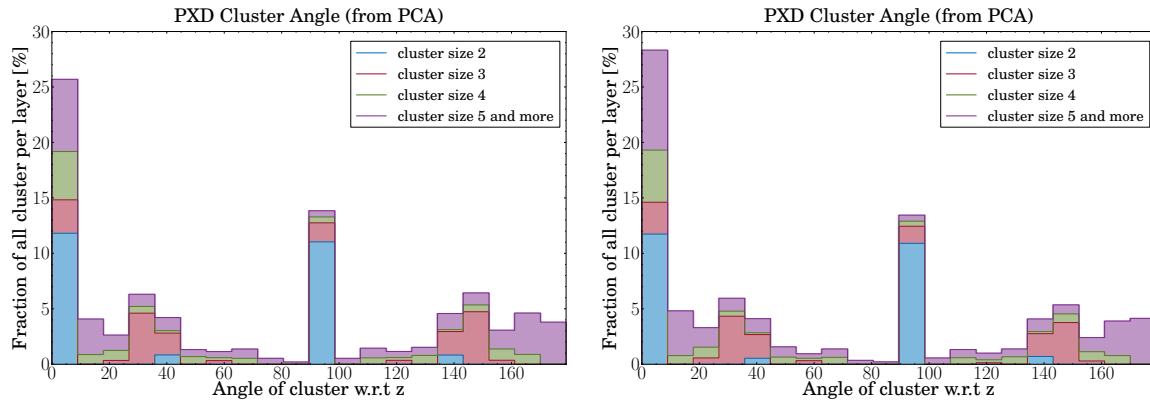


Figure 7.17: Cluster angle distributions for Touschek LER (left) and Touschek HER (right). The plots differentiate the different cluster sizes by colours and stack them to provide an overall distribution of the cluster angle. Starting with the cluster size 2 (blue), there are only four possible pixel arrangements with respect to the global z -axis: parallel (0°), perpendicular (90°), diagonal “upward” (45°) and diagonal “downward” (135°).

clusters to be aligned to the global z -axis. This can be explained by the main contribution of particles to the clusters that arise from showers and thus mainly travel from the outside to the inside of the detector (machine background). The result are long clusters that are mainly parallel to the global z -axis.

7.4.2 Beam-Gas

Even under the best conditions, ideal vacuum inside the beampipe cannot be achieved technically. There are always gas molecules left inside the beampipe. For SuperKEKB, the primary constituents of the residual gas are H_2 and *Carbon monoxide* (CO) [79, 246]. Particles travelling on their design orbit through the accelerator can collide with the residual gas. This process is called **Beam-Gas scattering** and might lead to particles which are kicked off their nominal orbit and the momentum acceptance of the accelerator. The scattered particles give rise to particle showers that might reach the Belle II detector. The two most important processes, contributing to Beam-Gas scattering, are **elastic Coulomb scattering** and **inelastic Bremsstrahlung**. While in the first case the scattered particle simply changes its direction, the latter decreases the energy of the particle by the emission of a photon. Figure 7.18 and 7.19 show the Feynman diagrams for Beam-Gas Coulomb scattering and Beam-Gas Bremsstrahlung, respectively.

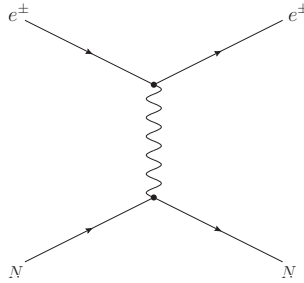


Figure 7.18: Feynman diagram for Beam-Gas Coulomb scattering.

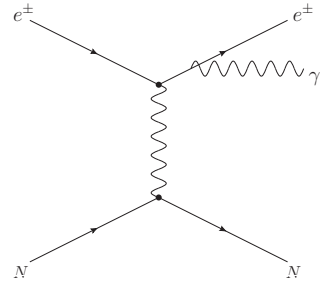


Figure 7.19: Feynman diagram for Beam-Gas Bremsstrahlung scattering.

Theory

The differential cross-section for the **elastic scattering** of the electron/positron on the residual gas nucleus is given by the Mott-scattering formula [10]

$$\frac{d\sigma}{d\Omega} = \frac{Z^2 \alpha^2 \hbar^2}{4p^2 \beta^2 \sin^4\left(\frac{\theta}{2}\right)} \left(1 - \beta^2 \sin^2\left(\frac{\theta}{2}\right)\right) \quad (7.20)$$

where Z is the atomic number of the nucleus, and p is the momentum of the incoming electron/positron and θ the scattering angle. Under the assumption that the scattering angles are small and the beam particles relativistic, meaning $\sin\left(\frac{\theta}{2}\right) \approx \frac{\theta}{2}$ and $\beta = 1$, the differential cross-section simplifies to

$$\frac{d\sigma}{d\Omega} = \frac{Z^2 \alpha^2 \hbar^2}{4p^2 \left(\frac{\theta}{2}\right)^4} \left(1 - \left(\frac{\theta}{2}\right)^2\right), \quad d\Omega = 2\pi\theta d\theta \quad (7.21)$$

As can be seen from this equation, the Coulomb term $1/\theta^4$ dominates, which is the reason why elastic Beam-Gas scattering is usually referred to as Coulomb scattering. Integrating equation 7.21 over the solid angle from θ_{min} to θ_{max} yields the Beam-Gas elastic scattering total cross-section

$$\sigma_{Elastic} = \frac{4\pi Z^2 \alpha^2 \hbar^2}{p^2} \left(\frac{1}{\theta_{min}^2} - \frac{1}{\theta_{max}^2} - \frac{1}{2} \ln \frac{\theta_{max}}{\theta_{min}} \right) \quad (7.22)$$

Using the typical values for $\theta_{min} \approx 1$ mrad and $\theta_{max} \approx \pi$, the contribution of the second and third term inside the brackets of equation 7.22 is less than 0.001%.

Skipping these terms and setting $\beta = 1$ and $r_e = \alpha \hbar / m_e c$ the equation then simplifies to

$$\sigma_{Coulomb} = \frac{4\pi Z^2 r_e^2}{\gamma^2 \theta_{min}^2} \quad (7.23)$$

Particles scattering at angles that exceed the beam divergence are lost and thus might become relevant for the background production. Hence the minimal angle can be approximated by

$$\theta_{min} = \sqrt{\frac{\epsilon}{\beta_y}}$$

where ϵ is the vertical emittance and β_y the local vertical beta function. Equation 7.23 then yields the local Beam-Gas Coulomb scattering total cross-section for lost particles

$$\sigma_{Loss}^{Coulomb} = \frac{4\pi Z^2 r_e^2 \beta_y}{\epsilon \gamma^2} \quad (7.24)$$

The total Beam-Gas loss rate is dominated by the elastic Coulomb scattering, described above. The most important **second order process**, with respect to the Beam-Gas loss rate, is Bremsstrahlung. As this process is not used for the Beam-Gas background simulation at Belle II an introduction to the theory of its cross-section can be found in annex B.1. For independent events, the total Beam-Gas cross-section is the sum of the Coulomb and the Bremsstrahlung cross-section is

$$\sigma_{Loss} = \sigma_{Loss}^{Coulomb} + \sigma_{Loss}^{Brem} \quad (7.25)$$

By plugging in equations 7.24 and B.3 in 7.25, it can be seen that the total cross-section depends strongly on the atomic number ($\propto Z^2$). Hence, the scattering at *Carbon monoxide* (CO) dominates and the contribution of H_2 can safely be ignored. The number of particles dN that scatter per unit time, is proportional to the Beam-Gas cross-section σ_{Loss} , the density ρ of the gas and the number of beam particles N

$$dN = -N \sigma_{Loss} \rho ds \quad (7.26)$$

With ds given by figure 7.20, equation 7.26 is written as

$$\frac{dN}{N dt} = -\sigma_{Loss} \rho \beta c \quad (7.27)$$

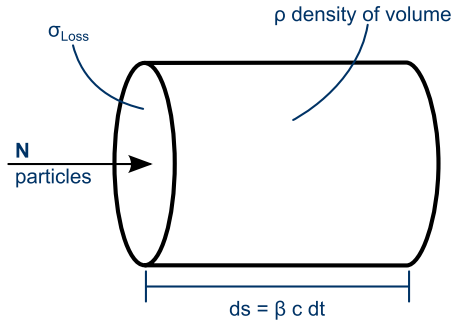


Figure 7.20: Definition of the quantities for the Beam-Gas rate calculation.

Integrating equation 7.27, yields the well-known exponential decay for a number N_0 of initial beam particles

$$N = N_0 e^{-t/\tau} \quad (7.28)$$

with τ being the lifetime of the beam due to Beam-Gas scattering

$$\tau = \frac{1}{\sigma_{Loss} \rho \beta c} \quad (7.29)$$

The density is calculated from the ideal gas law [247]

$$P V = n R_{gas} T$$

$$\rho = \frac{M P}{R_{gas} T}$$

where P is the pressure, V the volume, n the number of moles, M the molar mass, T the temperature of the gas and R_{gas} the ideal gas constant³. The number of beam particles stored in the SuperKEKB accelerator ring is

$$N_0 = \frac{I L}{e \beta c}$$

with I the beam current, L is the circumference of the SuperKEKB ring and e the electric charge.

³ $R_{gas} = 8.314 J K^{-1} mol^{-1}$

Those N_0 particles, travelling with the velocity βc , pass N_{gas} atoms per m^3

$$N_{gas} = 2 \frac{P}{k_B T}$$

where the factor two represents the dominance of two-atomic gas (e.g. CO) in the accelerator. The **Beam-Gas loss rate** is then

$$R_{BeamGas}^{Loss} = N_0 \cdot \underbrace{(N_{gas} \beta c)}_{\text{flux of gas molecules}} \cdot \sigma_{Loss} = 2 \frac{I L P}{e k_B T} \cdot \sigma_{Loss} \quad (7.30)$$

Simulation

The previous Beam-Gas studies, performed for the Belle detector, have been carried out with the TURTLE generator [248]. For Belle II the accelerator tracking software SAD is used (see section 3.10). Building upon the same setup as for the Touschek simulation (see section 7.4.1), the Touschek scattering rate formula is replaced by the formula for Beam-Gas scattering. A homogeneous distribution of the gas under the SuperKEKB design vacuum pressure (see section 4.2) is assumed. The result of the SAD simulation is a file containing the loss positions, momenta and loss rates of the Beam-Gas macro-particles. The SAD reader module loads the Beam-Gas data into basf2 for the full detector simulation. The output of the SAD simulation is illustrated in figure 7.21. Compared to the Touschek background, the loss rates of the Beam-Gas background are in general about 50 % smaller and the number of regions is significantly reduced. Thus, the contribution of Beam-Gas to the total background of the PXD is expected to be small.

Particle flux

The Beam-Gas background is expected to behave similarly to the Touschek background. Due to its very low statistics (see table 7.1) the Beam-Gas HER background is omitted and the following studies focus on the LER background. Like the Touschek background the Beam-Gas background particles enter the inner detector region under a shallow angle from the LER upstream direction. This can be seen from the right plots of figure 7.22. Unlike the Touschek, however, the outer layer is more exposed to the background as the inner layer and there is no distinctive peak for the azimuthal angle.

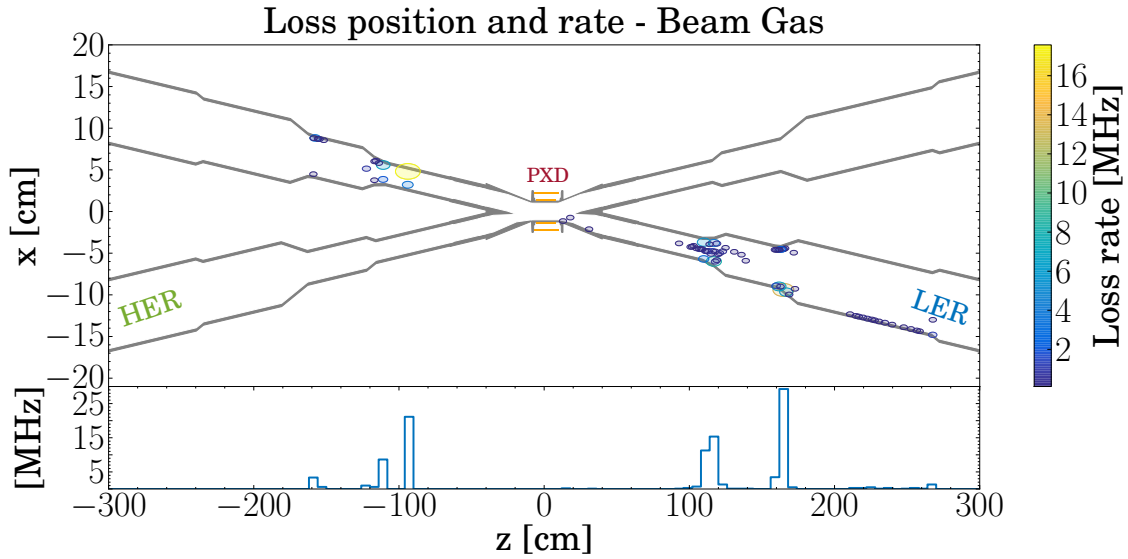


Figure 7.21: The locations and loss rates for the Beam-Gas particles after the SAD accelerator simulation.

The particle flux in the forward part of the sensors is dominated by single particle crossings (see figure 7.23), while the particle flux in the backward part of the sensors is mostly the result of particles traversing the sensors more than four times. In the inner layer the contribution of multiple crossings to the total particle flux in the backward sensor regions is more than 60 %. The backward area of the outer layer, on the other hand, is dominated by particles with more than five crossings. The reason being that the forward parts of the PXD sensors are directly hit by the Beam-Gas shower particles while the backward areas are traversed by less energetic, back-scattered particles created by secondary processes.

Origin of particles

The Beam-Gas background is produced upstream and leads to three main areas where the particles are lost (see figure 7.24): at 110 cm and -95 cm for the LER; at -120 cm for the HER. The main contribution to the background in the PXD arises from particles lost upstream at beampipe walls. The overall contribution to the total background, however, is negligible.

Occupancy

For the Beam-Gas background 1000 ROFs are simulated for each ring. Comparing figure 7.25 with figure 7.26 it is obvious that the main contribution to the Beam-Gas occupancy originates from the LER. Although there is an asymmetry in x for the fired pixels in the LER, it is much less pronounced compared to the Touschek LER asymmetry. Again, the occupancy is flat along

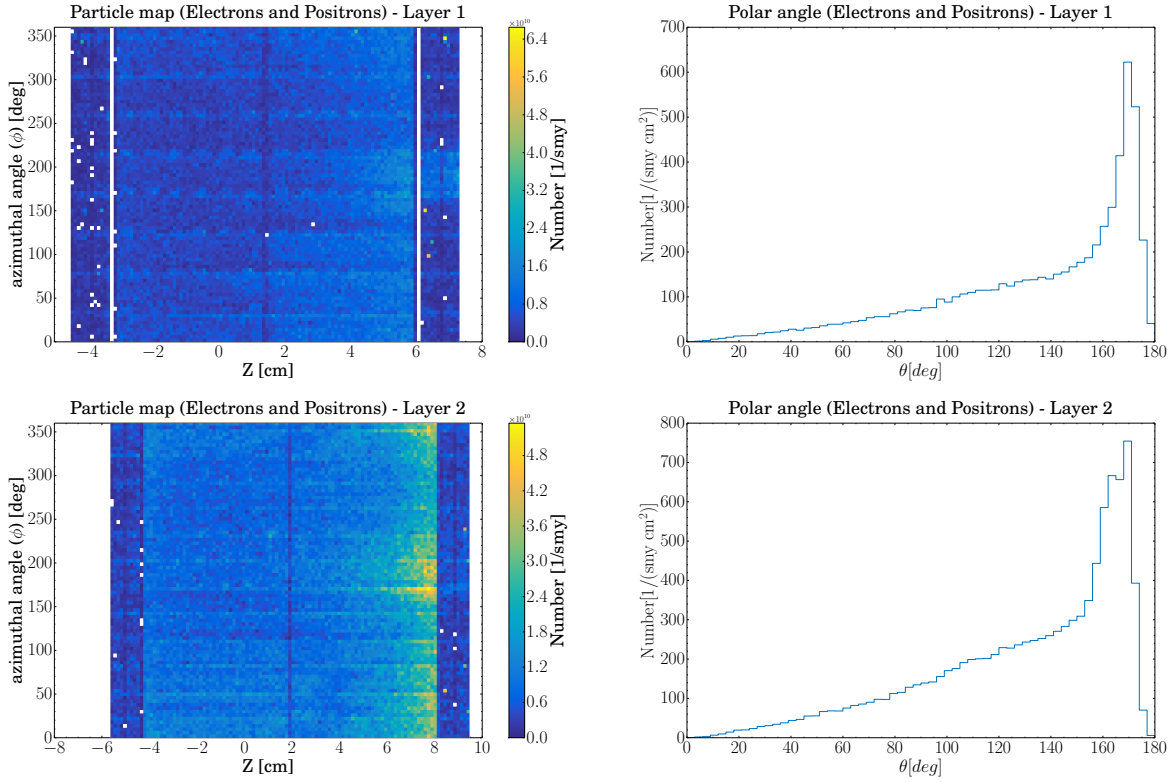


Figure 7.22: Angular and spatial distributions of the electrons and positrons traversing the PXD from Beam-Gas LER per area during one snowmass year. The top row represents the inner layer and the bottom row the outer layer. The left plots show the $z\phi$ distributions of electrons and positrons traversing the sensor area, the backward ASICs and the forward ASICs. The plots on the right hand side show the polar angle distribution.

z for both layers, which is good news for the hardware developers. In summary, the occupancy contribution from Beam-Gas is negligible compared to the other backgrounds as figure 7.27 shows. The largest occupancy is found in the 1.5.1 sensor with $(9.1 \pm 5.0) \cdot 10^{-3}\%$ for the inner layer and in sensor 2.7.2 with $(5.4 \pm 2.7) \cdot 10^{-3}\%$ for the outer layer.

Cluster analysis

Figure 7.28 shows the distribution of the cluster angles for the Beam-Gas LER background. The statistics for the HER were too low to be plotted. As for Touschek induced backgrounds, the Beam-Gas background shows an equal amount of parallel and perpendicular 2-pixel clusters, with a tendency for larger clusters to be aligned to the global z -axis.

Layer 1 [%] $\cdot 10^{-3}$			Layer 2 [%] $\cdot 10^{-3}$		
Sensor	LER	HER	Sensor	LER	HER
1.1.1	5.3 ± 2.9		2.1.1	3.7 ± 1.9	
1.1.2	5.7 ± 3.2		2.1.2	3.8 ± 2.1	
1.2.1	5.1 ± 2.8		2.2.1	3.1 ± 1.6	0.002 ± 0.07
1.2.2	5.8 ± 3.2		2.2.2	3.7 ± 2.0	
1.3.1	5.9 ± 3.2	0.002 ± 0.002	2.3.1	3.2 ± 1.6	
1.3.2	6.0 ± 3.4		2.3.2	3.8 ± 2.1	0.009 ± 0.01
1.4.1	6.8 ± 3.6		2.4.1	2.8 ± 1.5	
1.4.2	6.0 ± 3.4		2.4.2	4.0 ± 2.1	0.02 ± 0.02
1.5.1	9.1 ± 5.0		2.5.1	3.2 ± 1.6	0.005 ± 0.009
1.5.2	7.1 ± 3.6	0.002 ± 0.003	2.5.2	4.0 ± 2.1	0.004 ± 0.007
1.6.1	6.6 ± 3.6		2.6.1	4.4 ± 2.3	
1.6.2	6.1 ± 3.3		2.6.2	4.4 ± 2.3	
1.7.1	5.9 ± 3.2		2.7.1	5.0 ± 2.7	
1.7.2	6.2 ± 3.4		2.7.2	5.4 ± 2.7	0.002 ± 0.002
1.8.1	5.3 ± 2.8	0.002 ± 0.003	2.8.1	4.8 ± 2.6	
1.8.2	6.6 ± 3.6		2.8.2	5.1 ± 2.6	
			2.9.1	3.8 ± 2.1	
			2.9.2	4.1 ± 2.2	
			2.10.1	2.9 ± 1.5	
			2.10.2	3.8 ± 2.2	
			2.11.1	2.9 ± 1.6	0.002 ± 0.002
			2.11.2	3.6 ± 2.0	
			2.12.1	3.2 ± 1.6	
			2.12.2	3.7 ± 2.0	
Max	9.1 ± 5.0	0.002 ± 0.002	Max	5.4 ± 2.7	0.02 ± 0.02

Table 7.3: The detailed occupancy values for the Beam-Gas background split into their individual contributions for each sensor.

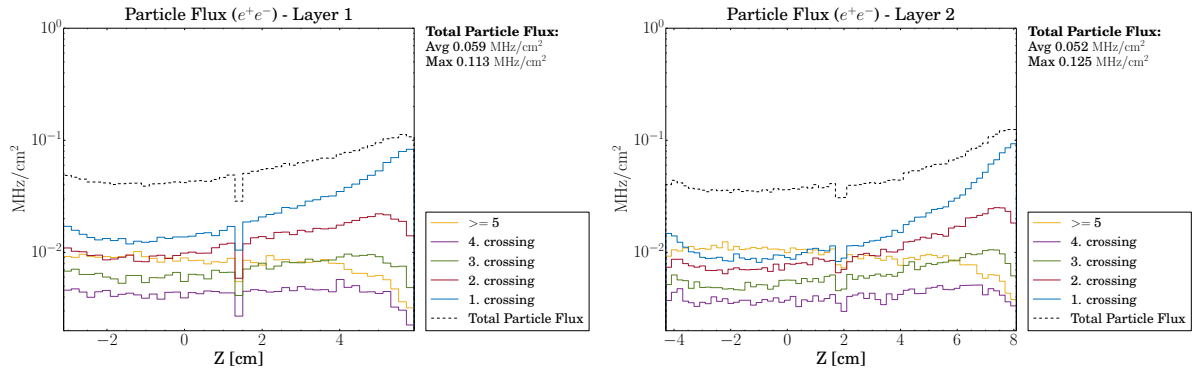


Figure 7.23: Distribution of the number of times a Beam-Gas generated particle traverses a PXD layer. The left plot shows the result for the inner layer and the right plot for the outer layer.

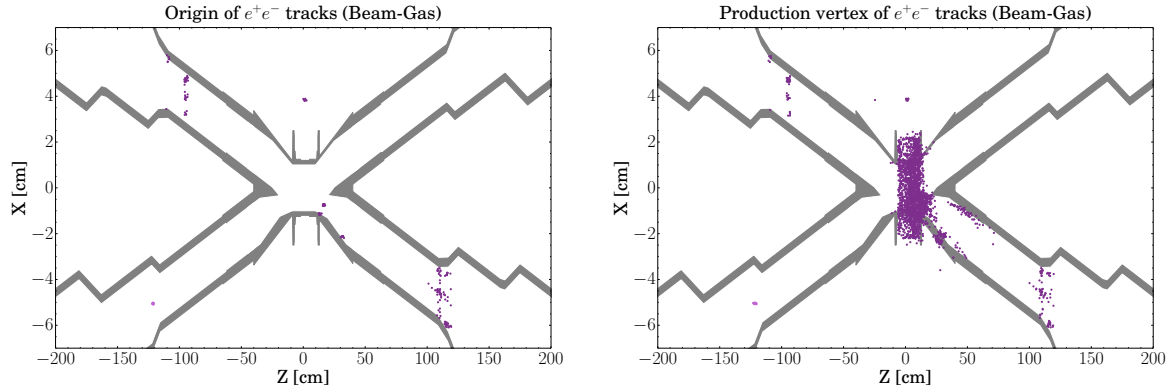


Figure 7.24: The left plot shows the distribution of the origin of all e^+e^- particles that spark the creation of particles that, further down the chain, hit the PXD sensors. The right plot shows primary as well as secondary particles that hit the PXD sensors, thus helping to identify the areas within the interaction region that contribute to the background of the PXD.

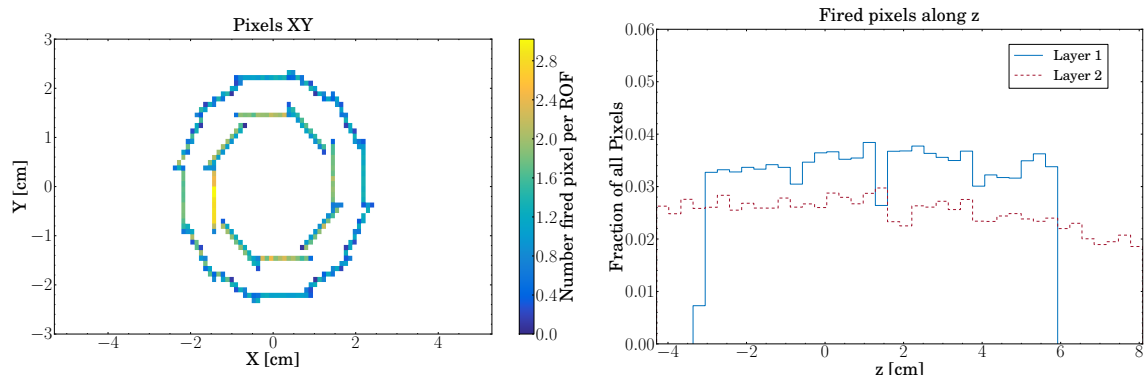


Figure 7.25: The fired pixels from the Beam-Gas LER background. The left plot shows the x - y -projection where an asymmetry in x is visible. The distribution of the fired pixels along z in the right plot is fairly flat.

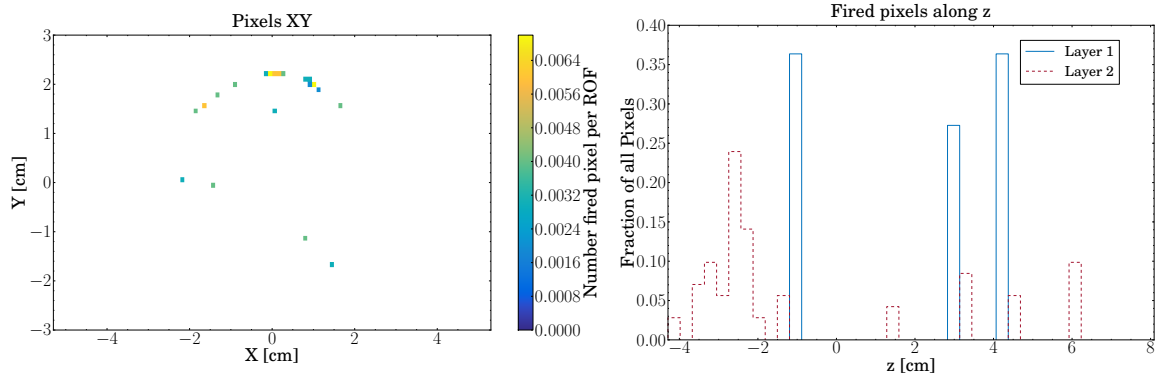


Figure 7.26: The fired pixels from the Beam-Gas HER background. The left plot shows the xy -projection and the right plot the distribution of the fired pixels along z .

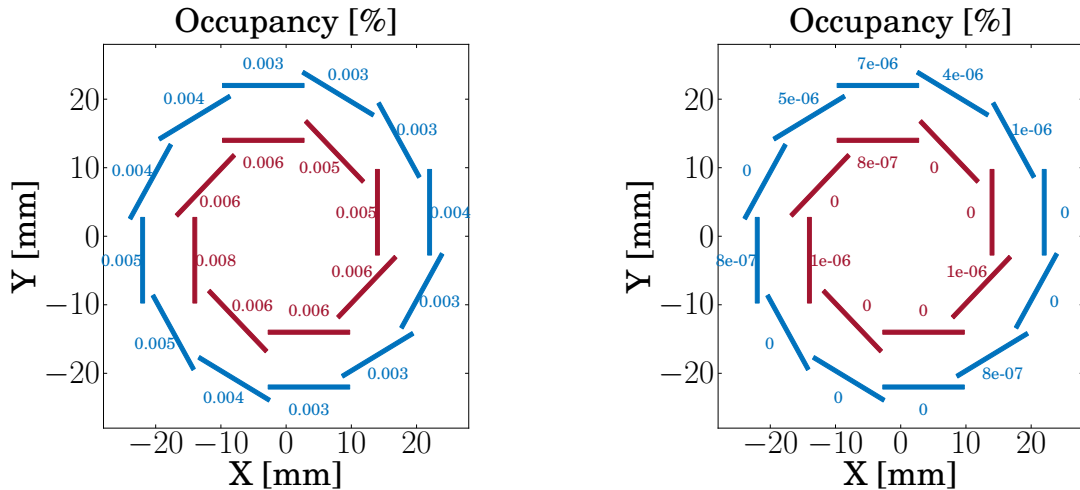


Figure 7.27: Summary of the PXD occupancy values for the Beam-Gas LER (left) and Beam-Gas HER (right) background.

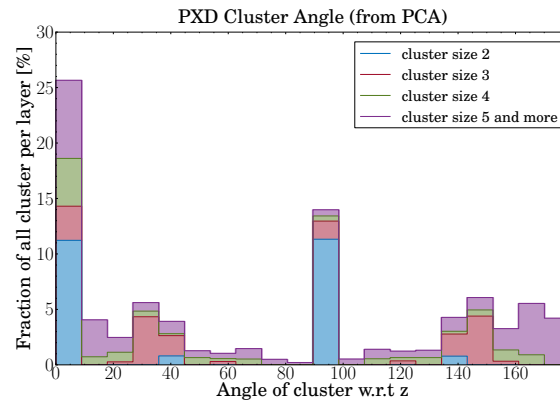


Figure 7.28: Cluster angle stack plot for Beam-Gas LER.

7.4.3 Synchrotron radiation

The circulating electrons and positrons in SuperKEKB undergo transverse acceleration through the accelerator's bending and focusing magnets. This acceleration leads to the emission of radiation, known as **synchrotron radiation**. The concept was first described by Liénard [249] and Wiechert [250]. Further theoretical work followed by Ivanenko, Pomeranchouk and Schwinger [251, 76]. Finally, synchrotron radiation was experimentally discovered for the first time on April 24, 1947 at General Electric's 70 MeV synchrotron [252]. While the synchrotron radiation caused by bending magnets imposes a limit on the achievable energies at a circular accelerator, it does not reach the interaction region and, in particular, the PXD, under normal conditions. But the QCS and beam correction magnets are located close to the IP and can deflect the beam in such a way that the emitted synchrotron radiation reaches the interaction region and the PXD.

Theory

Electromagnetic radiation occurs wherever electric and magnetic fields exist with components orthogonal to each other such that the Poynting vector

$$\vec{S} = \frac{c}{4\pi} [\vec{E} \times \vec{B}]$$

is non-zero [85]. In the following, a single point charge, undergoing a uniform motion, is considered. In the rest frame of the moving charge, the charge is stationary and its Coulomb fields extend radially to infinity. However, in the laboratory system, the moving charge creates a current that, in turn, gives rise to a magnetic field. Thus, the Poynting vector is non-zero and radiation is possible. The electric and magnetic fields of a moving point charge can be calculated using the Liénard-Wiechert potentials and yield [7]

$$\vec{E} = \frac{q}{4\pi\epsilon_0} \left(\underbrace{\frac{1}{R^2 u^3} (\hat{n} - \vec{\beta}) (1 - \beta^2)}_{\text{Coulomb}} + \underbrace{\frac{1}{R c u^3} \hat{n} \times [(\hat{n} - \vec{\beta}) \times \dot{\vec{\beta}}]}_{\text{Radiation}} \right) \quad (7.31)$$

$$\vec{B} = \frac{1}{c} \hat{n} \times \vec{E} \quad (7.32)$$

with

$$u = 1 - \hat{n} \cdot \vec{\beta}$$

where $\vec{\beta} = \vec{v}/c$, q is the charge of the point charge, \hat{n} is the unit vector pointing from the charge to the observer and R is the distance between both. The electric field, given by equation 7.31, consists of two terms: The first term is called the **generalized Coulomb field** and drops like R^{-2} . It dominates the near-field region and does not contribute to radiation. The second term, the **radiation field**, drops like R^{-1} . Hence, it dominates the far-field and is responsible for the radiation emitted by the point charge. Because it contains the acceleration $\vec{\beta} = \vec{a}/c$, only accelerated charges emit radiation. In order to accelerate the charge, a uniform movement in its rest frame is applied to the charge. Figure 7.29 illustrates this. A point charge, initially resting at location A, moves during the time Δt to location B. Due to the finite velocity of light, the purely radial electric field gets distorted within a radius $c \Delta t$ from the original location A. It is this distortion that is responsible for the emission of radiation. Two types of acceleration are possible: acceleration **parallel** to the flight direction of the charge or acceleration **perpendicular** to it. The left drawing in figure 7.29 represents the parallel (longitudinal) case and the right figure the perpendicular (transversal) case. In the longitudinal case the perturbation of the electric field varies like $\sin \Theta^*$, where Θ^* is the angle between the line of observation and the flight direction of the charge. An asterisk indicates that the quantity is given in the rest frame of the point charge. With the electric charge q , the acceleration a^* and the observation distance R , the electric field perturbation perpendicular to the direction of observation is [85]

$$E_{\perp} = \frac{q a^*}{c^2 R} \sin \Theta^* \quad (7.33)$$

As can be seen from equation 7.33, the radiation for longitudinal acceleration is emitted in a direction that is primarily perpendicular to the flight direction of the charge. However, the more interesting case is the acceleration of the charge transversal to its flight direction, as this is the case for the deflection of the charge in magnetic fields. It is this acceleration that gives rise to synchrotron radiation.

The electric field perturbation due to transversal acceleration can be written as [85]

$$E_{\perp} \propto \frac{q a^*}{c^2 R} \cos \Theta^* \quad (7.34)$$

In the rest frame of the charge the distribution of the radiation is similar to the distribution of an oscillating dipole with the maximum intensity emitted perpendicular to the acceleration. This is illustrated in the left drawing of figure 7.30. In the laboratory system (for relativistic charges) the emission gets highly collimated into the direction of motion of the charge due to the Lorentz transformation [85]

$$\sin \Theta = \frac{\sin \Theta^*}{\gamma (1 + \beta \cos \Theta^*)} \quad \cos \Theta = \frac{\cos \Theta^* + \beta}{1 + \beta \cos \Theta^*} \quad (7.35)$$

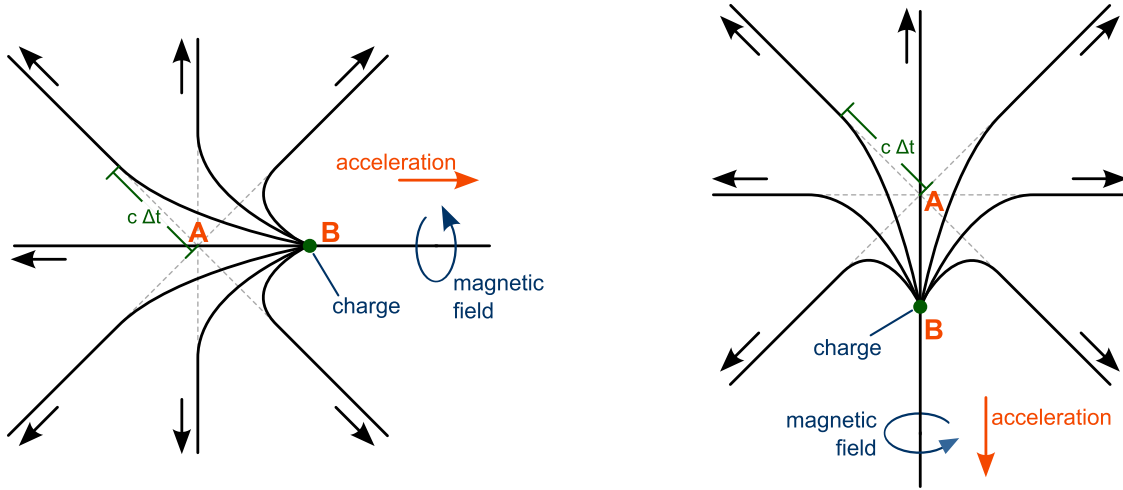


Figure 7.29: The left figure illustrates the deformation of the electric field of a point charge due to a parallel (longitudinal) acceleration of the charge. The right figure shows the deformation for a perpendicular (transversal) acceleration. Figure adapted from [85].

For charges at relativistic energies, $\beta \approx 1$, the peak of the dipole emission pattern in the charge rest frame, $\theta^* = 90^\circ$, transforms to

$$\Theta \approx \frac{1}{\gamma} \quad (7.36)$$

in the laboratory frame. This means synchrotron radiation is emitted within a narrow cone with a half-opening angle of γ^{-1} , as illustrated in the right drawing of figure 7.30. For the highly relativistic particles at SuperKEKB, this leads to a highly collimated beam of photons.

In order to calculate the radiation power of a single charge, the Poynting vector is integrated over a closed surface, enclosing the point charge. This leads to the synchrotron radiation power, given separately for the longitudinal and transversal acceleration in the following. For the longitudinal acceleration the radiation power is [85]

$$P_{\parallel} = \frac{2}{3} \frac{q^2}{m^2 c^3} \left(\frac{d\vec{p}_{\parallel}}{dt} \right)^2 \quad (7.37)$$

where $d\vec{p}_{\parallel}/dt$ is the accelerating force imposed by SuperKEKB on the particles and m the rest mass of the beam particle. It should be noted that the synchrotron radiation power for longitudinal acceleration is independent of the energy of the particle. This is the reason why linear accelerators do not suffer from synchrotron radiation.

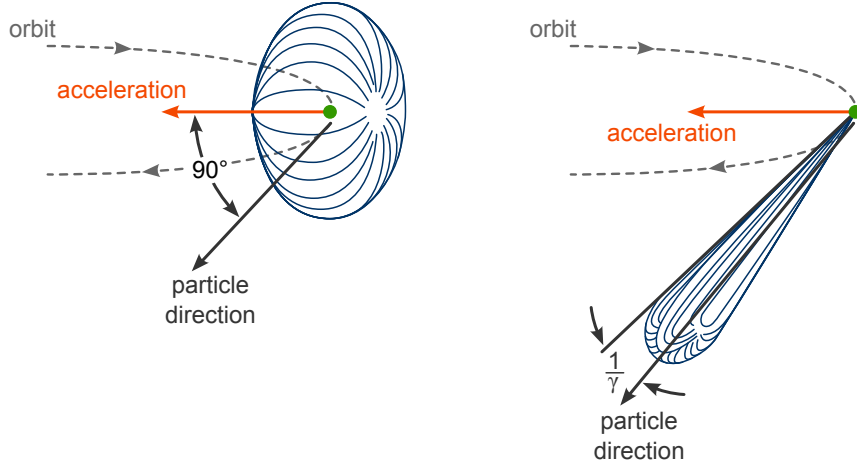


Figure 7.30: The left figure shows the emission of synchrotron radiation due to a transversal accelerated charge in the rest frame of the charge. The right figure illustrates the narrow cone with a half-opening angle of γ^{-1} for the synchrotron radiation in the laboratory frame. Figure adapted from [253]

On the other hand, the radiation power for transversal acceleration is

$$P_{\perp} = \frac{2}{3} \frac{q^2}{m^2 c^3} \gamma^2 \left(\frac{d\vec{p}_{\perp}}{dt} \right)^2 \quad (7.38)$$

with $d\vec{p}_{\perp}/dt$ being the transversal force acting on the particle. In comparison with equation 7.37, the additional factor γ^2 leads to a much higher radiation power, making it by far the dominating synchrotron radiation process for electron energies above a few MeV. From equation 7.38 one can see that the energy loss, defined as the radiated power per turn in a circular accelerator, scales with the fourth power of the particle's energy. This imposes the limitation to the maximum energy achievable at a circular accelerator. Restricting equation 7.38 to singly charged particles $q = e$ and omitting longitudinal acceleration, the equation can be written as [85]

$$P_{\gamma} = \frac{4\pi}{\mu_0} \frac{2r_e^2 c}{3(mc^2)^2} B^2 E^2$$

where the force in equation 7.38 has been replaced by the Lorentz force. This equation describes the instantaneous synchrotron radiation power of a single electron. If the deflecting magnetic field is replaced by the local bending radius ρ , the equation becomes

$$P_\gamma = \frac{2}{3} r_e m c^3 \frac{\beta^4 \gamma^4}{\rho^2} \quad (7.39)$$

or

$$P_\gamma = \frac{c C_\gamma}{2\pi} \frac{E^4}{\rho^2} \quad (7.40)$$

where

$$C_\gamma = \frac{4\pi}{3} \frac{r_e}{(mc^2)^3} = 1.41733 \cdot 10^{-14} \frac{msW}{GeV^4}$$

The energy spectrum of synchrotron radiation spans over a huge range, from the infrared region, via the visible portion of the electromagnetic spectrum, up to energies of the order of 10's of keV. An important quantity that characterises the energy or frequency spectrum of synchrotron radiation is the **critical photon frequency**. In the following this quantity will be motivated. Figure 7.31 shows a particle travelling along a trajectory and emitting synchrotron radiation which is, of course, confined to a cone with an opening angle of $2/\gamma$. A detector is placed in order to capture the radiation.

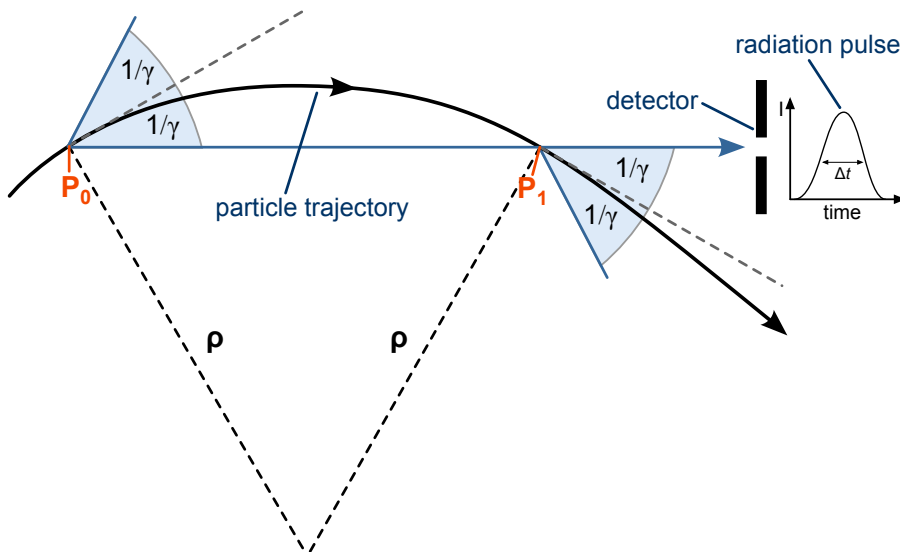


Figure 7.31: A particle travelling from P_0 to P_1 emits synchrotron radiation. The radiation is collected by a detector as a radiation pulse with duration Δt . Figure adapted from [85].

The detector starts receiving the emitted synchrotron radiation photons as soon as the lower edge of the cone comes into sight of the detector. This happens at location P_0 .

The detector is exposed to synchrotron radiation until the cone passes out of sight for the detector at location P_1 . The detector records a very short light pulse with the duration of the pulse being given by the difference between the time the particle took to travel from P_0 to P_1 and the time the light spent between these two points

$$\Delta t = t_{particle} - t_\gamma \approx \frac{4 R}{3 c \gamma^3} \quad (7.41)$$

where the approximation is carried out by using the first two terms of the Taylor-expansion of $\sin 1/\gamma$ and an approximation⁴ for $1/\beta$. The particle's travel time is given by the arc-length between P_0 and P_1 and the particle's velocity

$$t_{particle} = \frac{2 R}{\beta c \gamma}$$

The light's travel time is given by the time it took the light to go from P_0 to P_1

$$t_\gamma = \frac{2 R \sin \frac{1}{\gamma}}{c}$$

The duration of the electromagnetic pulse given in equation 7.41 is very short and scales inversely proportional to the third power of γ . Due to the shortness of the pulse, the detector observes a broad spectrum of frequencies. Using only half the pulse length for the effective pulse duration the spectrum reaches a maximum frequency of about

$$\omega_c \approx \frac{1}{\frac{1}{2} \Delta t} \approx \frac{3 c \gamma^3}{2 R} \quad (7.42)$$

which is called the **critical frequency** or **critical energy** $u_c = \hbar \omega_c$ of synchrotron radiation. It has the property that one-half of the power is radiated above this frequency and one-half below. For electrons, numerical expressions are [85]

$$u_c \text{ (eV)} = 2.2183 \frac{E^3 \text{ (GeV}^3)}{R \text{ (m)}} = 0.66503 E^2 \text{ (GeV}^2) B \text{ (T)}$$

For example, the bending sections leading into into the Fuji (LER) and Oho (HER) straight sections at SuperKEKB (see section 3.1), have bending radii of 177.4 m and 580 m respectively [254]. This leads to critical energies of u_c (LER) = 0.8 keV and u_c (HER) = 1.3 keV.

⁴ $\sin \frac{1}{\gamma} \approx \frac{1}{\gamma} - \frac{1}{6\gamma^3}$, $\frac{1}{\beta} = \frac{1}{\sqrt{1-1/\gamma^2}} \approx \frac{1}{1-1/(2\gamma^2)} \approx 1 + \frac{1}{2\gamma^2}$

The instantaneous radiation power from equation 7.39 can also be expressed as an integral over the radiated power spectrum $\mathcal{P}(\omega)$ [255]

$$P_\gamma = \int_0^\infty \mathcal{P}(\omega) d\omega \quad (7.43)$$

leading to the following form of the power spectrum

$$\mathcal{P}(\omega) = \frac{P_\gamma}{\omega_c} S\left(\frac{\omega}{\omega_c}\right) \quad (7.44)$$

where the spectral function $S(\xi)$ with $\xi = \frac{\omega}{\omega_c}$ can be written as

$$S(\xi) = \frac{9\sqrt{3}}{8\pi} \xi \int_\xi^\infty K_{5/3}(x) dx \quad (7.45)$$

with $K_{5/3}$ being a modified Bessel function. It should be noted that from equation 7.44 it follows that S is normalised

$$\int_0^\infty S(\xi) d\xi = 1 \quad (7.46)$$

The total rate of the emission of photons is [256]

$$N = \frac{P_\gamma}{u_c} \int_0^\infty \underbrace{\frac{S(\xi)}{\xi}}_{F(\xi)} d\xi \quad (7.47)$$

where $F(\xi)$ represents the photon number spectrum and calculates to [255]

$$\int_0^\infty F(\xi) d\xi = \frac{15\sqrt{3}}{8} \quad (7.48)$$

Both functions, $S(\xi)$ and $F(\xi)$, are drawn in figure 7.32.

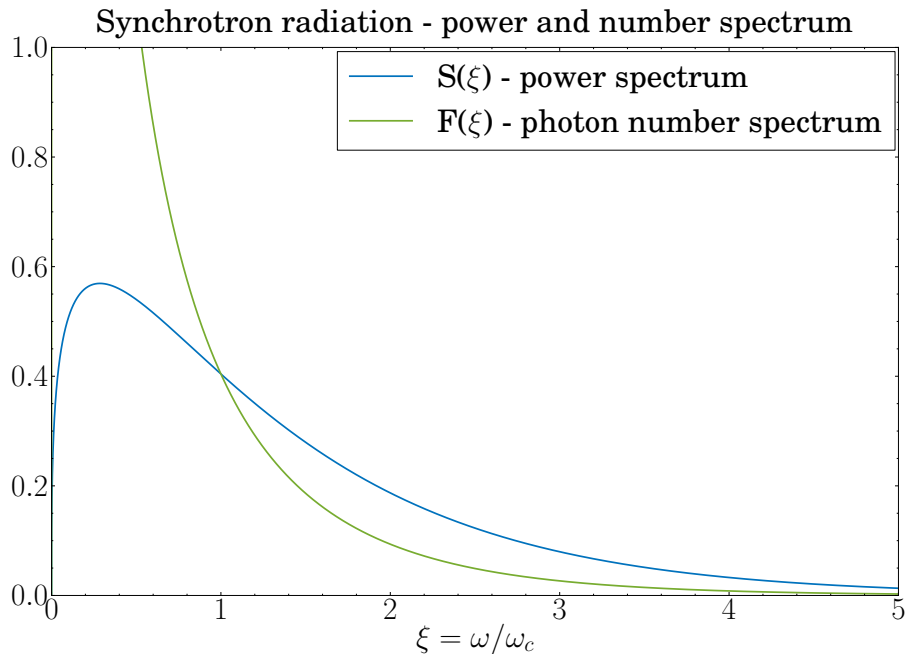


Figure 7.32: The power spectrum function S and the number spectrum function F of synchrotron radiation.

Simulation

The synchrotron radiation studies conducted at Belle the predecessor experiment of Belle II used the simulation package **SRGEN** [257, 258]⁵. SRGEN propagates the profile of the beam, defined at a starting point, through the magnets of the accelerator. The implementation performs the propagation in a step-wise manner and models the magnets as hard-edged magnetic fields using the formulas described in section 3.4. The dynamics of the beam is updated at the entrance and the exit of each magnet taking into account the magnet's properties, such as length, bending angle and strength. At each step SRGEN integrates over the horizontal and vertical dimensions of the beam, calculates the number of photons that are emitted and determines their direction. This approach to simulate synchrotron radiation has not only been used successfully at Belle [258] but also at the CLEO experiment [259]. Previous synchrotron radiation studies at Belle II, on the other hand, used Geant4 to track single electrons/positrons through the three dimensional magnetic field of the accelerator structure. While this allows to take local variations of the magnetic field into account coming from, for example, fringe and leak fields ⁶, it is a time and resource intensive approach limiting the simulation to only a fraction of the total number of particles in a bunch.

⁵ SRGEN was written by Stuart D. Henderson, but the source code was never released to the public.

⁶ In fact, there are ways to include fringe fields into the SRGEN approach, see [85]. However, often they are just simple approximations.

The goal of the study presented here is the simulation of the total amount of synchrotron radiation that hits the PXD during its readout time of 20 μ s. In order to achieve this goal computationally, a hybrid approach is employed, bringing together the advantages of the Belle and the Belle II synchrotron radiation simulations. The result of this effort is a newly developed synchrotron radiation generator, called **PySynRad**, which has been written by the author of this thesis using Python and made publicly available [260]. It uses the main concepts of SRGEN to create the 4-vectors of the synchrotron radiation photons and leaves the simulation of the photon interaction with the beampipe material to Geant4. Thus, it does not need to know about the beampipe geometry, as opposed to SRGEN which requires a simplified model of the beampipe as input. In order to capture the details of the magnetic field of the accelerator PySynRad relies on the magnet lattice of the SAD accelerator simulation (see section 3.10) instead of the simplified magnet description of SRGEN. The SAD magnet lattice describes the accelerator's magnetic field as a series of steps along the design orbit. Each step provides the following information (see section 3.4 for the definition of the magnetic field strength):

- k_0 The dipole magnet field strength per unit length
- sk_0 The skewed (rotated by 90° w.r.t. k_0) dipole magnet field strength per unit length
- k_1 The quadrupole magnet field strength per unit length, where a positive sign means horizontal focusing
- sk_1 The skewed quadrupole magnet field strength per unit length, where a positive sign means horizontal focusing
- dx The horizontal offset of the magnet with respect to the design orbit
- dy The vertical offset of the magnet with respect to the design orbit
- dl The step length
- ϕ The rotation of the magnet around the design orbit

The magnetic field value at a position (x, y) is given by

$$B_x = sk_0 + k_1 \cdot y_m + sk_1 \cdot x_m \quad (7.49)$$

$$B_y = k_0 + k_1 \cdot x_m - sk_1 \cdot y_m \quad (7.50)$$

with

$$\begin{pmatrix} x_m \\ y_m \end{pmatrix} = \begin{pmatrix} \cos(-\phi) & -\sin(-\phi) \\ \sin(-\phi) & \cos(-\phi) \end{pmatrix} \cdot \begin{pmatrix} x - dx \\ y - dy \end{pmatrix} \quad (7.51)$$

where B_x is the horizontal and B_y the vertical magnetic field component, using the SuperKEKB coordinate system introduced in section 3.2. Effects from leak fields or additional magnetic fields, such as the solenoid field of the Belle II detector, are taken into account by summing the $B_{x/y}$ values for all fields that are present at a position (x, y) . By modelling each lattice step as a hard edge magnet, PySynRad retains the speed of SRGEN, while the subdivision of the lattice allows to capture local variations of the magnet field as well as fringe and leak fields. The field information is loaded from separate ASCII files for the accelerator lattice, the leak field lattice (HER only) and the Belle II solenoid lattice. From the loaded field values the regions exhibiting a magnetic field and the vacuum regions between them are identified. The regions will later be used to decide whether synchrotron radiation is emitted or not. A start position is specified and the values of the Twiss parameters (see section 3.5) of the beam at this location are given to PySynRad.

For the study at hand, the IP is chosen as the start position because the Twiss parameters at the IP are well-defined from table 3.1. Further input required by PySynRad are the beam energy and current, the crossing angle of the beams at the IP and the desired timespan for which the synchrotron radiation should be generated. Apart from the last parameter, all values can be found in table 3.1. The timespan is set to 20 ns in order to keep the Geant4 simulation of the synchrotron photons, performed later, within a reasonable time. Starting the synchrotron radiation generation tells PySynRad to track the beam profile in a step-wise manner along the orbit through the SAD magnet lattice. The beam profile is tracked from the IP upstream for a distance of 3 m. Beyond this point no significant amount of synchrotron radiation hitting the PXD region is produced, as will be shown later. The orbit step length is set to 10 μm , but is shortened dynamically by PySynRad at magnet-vacuum borders. For each step the beam is propagated along the s -coordinate and the magnetic field values at this new position are calculated from equations 7.49 and 7.50. The effect of the magnetic fields on the trajectory of the beam is computed as a horizontal and vertical deviation of the beam position from the ideal orbit using the formulas from [255]. Figure 7.33 compares the horizontal and vertical deviation values along s calculated by PySynRad with those obtained from SAD. The values agree nicely for both rings, showing that the computation of the beam orbit is correct in PySynRad.

Next, the Twiss parameters for the current step are evolved (see [255] for the formulas). See figure 7.34 for a comparison of the values for the β Twiss parameter between PySynRad and SAD. The size of the beam is calculated from the Twiss parameters using equation 3.15 and a comparison is shown in figure 7.35. The plots nicely show the vertical focusing (and horizontal defocusing) properties of the QC1RP and QC1LE quadrupole magnets and the horizontal focusing (and vertical defocusing) properties of QC2RP and QC2LE (see table 4.2).

In summary, the values for the β Twiss parameter and beamsize obtained from PySynRad agree nicely with those from the SAD simulation, although a discrepancy for small (LER) and large (HER) values of s can be seen. This is due to the fact that the Twiss parameter propagation starts at the IP where the Twiss parameters have their smallest value. This in turn leads to

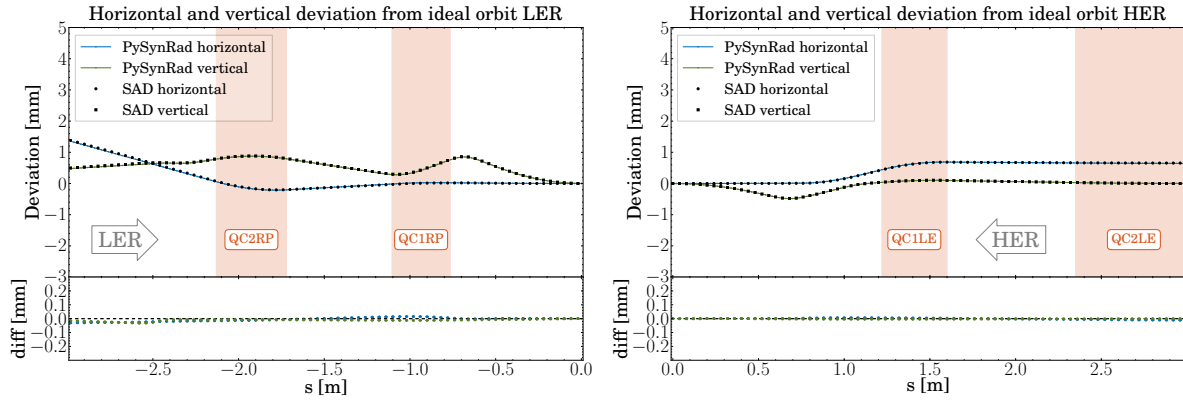


Figure 7.33: Deviation of the beam position from the ideal orbit for the LER (left) and the HER (right). The result from PySynRad is compared with the values obtained from SAD.

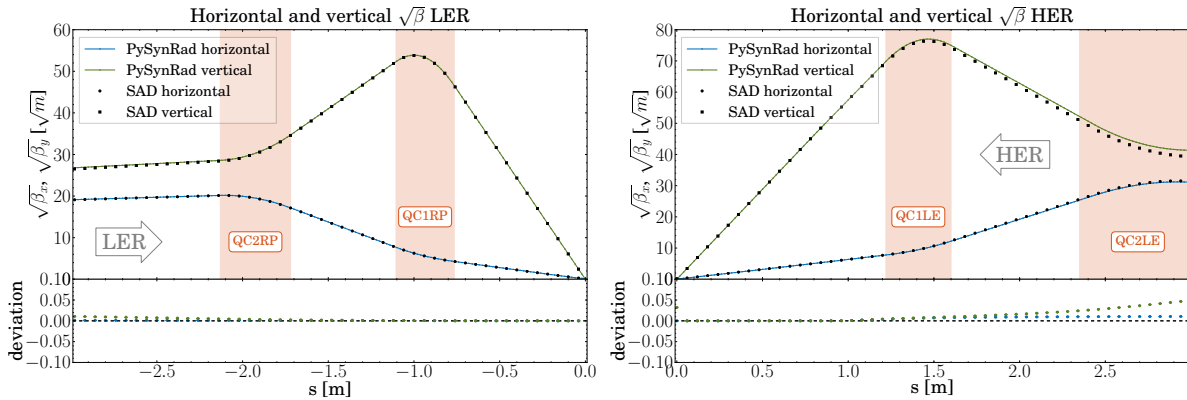


Figure 7.34: The horizontal and vertical β Twiss parameters for the LER (left) and the HER (right). Shown is a comparison between the results from PySynRad and SAD.

computational inaccuracies adding up during the beam profile stepping from the IP outwards to smaller/larger values of s . However, the discrepancies are very small and therefore acceptable.

For each step along the orbit that does not lie within a vacuum region PySynRad integrates over the beam profile in order to estimate the number of radiated photons. The beam profile is approximated by a normalised 2D Gaussian distribution with the width set to the size of the beam. The distribution is subdivided into a grid of 200x200 cells, covering 10σ of the beam profile. For each cell the local radius ρ and the value from the Gaussian distribution, denoted w , is calculated. Using those values, the number of photons radiated by each cell can be estimated.

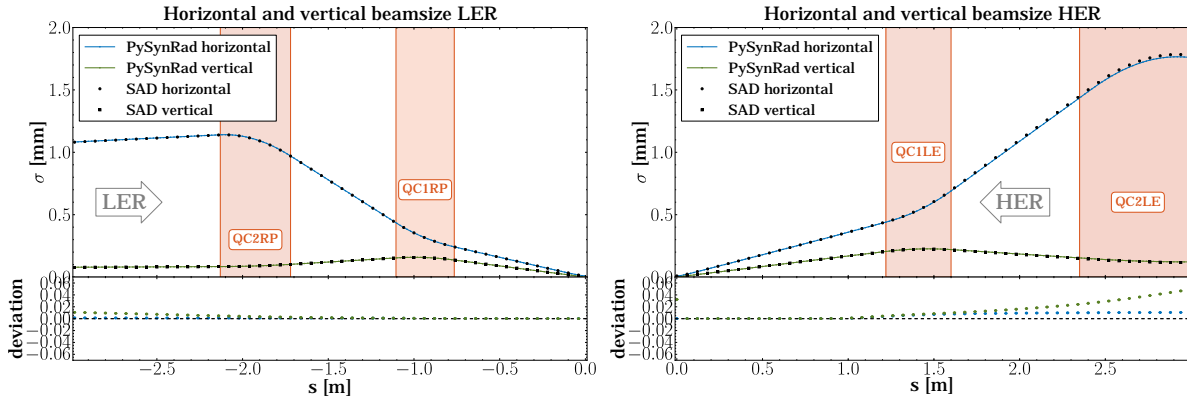


Figure 7.35: The size of the beam along s for the LER (left) and the HER (right). Both results, from PySynRad and from SAD are drawn.

The total number of photons emitted by a single electron is given from equation 7.47 with 7.48 is

$$N_{ph} = \frac{15\sqrt{3}}{8} \frac{P_\gamma}{u_c} \quad (7.52)$$

Since the electrons at SuperKEKB are ultra-relativistic ($\beta \approx 1$), equation 7.39 can be simplified to

$$P_\gamma = \frac{2}{3} r_e m_e c^3 \frac{\gamma^4}{\rho^2}$$

Plugging P_γ and the critical energy from equation 7.42 into equation 7.52 gives

$$N_{ph} = \frac{5}{2\sqrt{3}} \underbrace{\frac{r_e m_e c^2}{\hbar} \frac{\gamma}{\rho}}_{\alpha} \quad (7.53)$$

Thus, the total number of photons that are radiated from an integration cell is

$$N_{ph} = \frac{5}{2\sqrt{3}} \cdot \frac{\alpha \gamma}{\rho} \cdot I \cdot t \cdot w \cdot dl \quad (7.54)$$

where $I \cdot t$ is the number of charged particles that traverse the integration cell for the orbit step length dl during the specified timespan (in this study 20 ns) due to the beam current I . Having determined the position, critical energy and amount of the synchrotron radiation for each cell, the next step is the calculation of the emission direction of the synchrotron radiation

photons. The direction is given as the tangent on the trajectory of the cell, pointing towards the IP. In order to prepare the emission direction and the spatial position of each cell for the next phase of the synchrotron radiation generation, the Geant4 simulation, the direction and position values are transferred from the accelerator coordinate system to the Belle II detector coordinate system. Under the assumption that only photons that directly reach the vicinity of the PXD will be able to contribute to the background of the PXD, the emission direction can be used to reduce the number of photons that have to be simulated in Geant4. For each cell, a tube with an inner radius of 1 cm, an outer radius of 4 cm and a length spanning from -10 cm to 15 cm is intersected with the synchrotron radiation cone (see section 7.4.3) defined by the emission direction of the cell. If both intersect, the critical energy for the cell, its position, the emission direction and number of photons is written to disk.

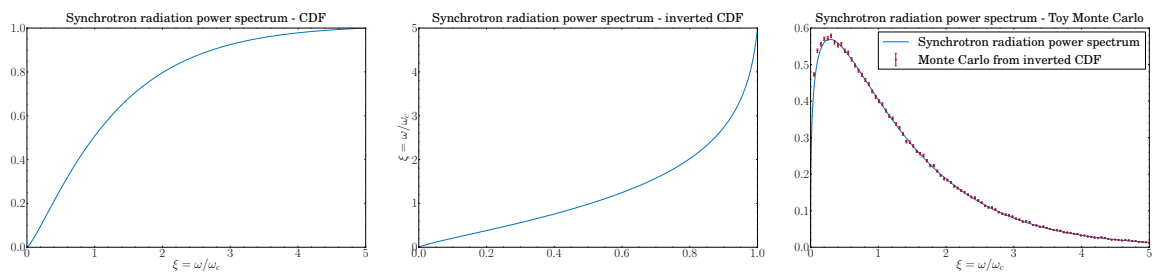


Figure 7.36: Sampling the synchrotron radiation energy spectrum. The left plot shows the CDF gained from the synchrotron power spectrum of figure 7.32, the middle plot the inverted CDF and the right plot compares samples drawn from the inverted CDF with the original synchrotron power spectrum.

The interaction of the synchrotron radiation photons with the beampipe geometry is simulated using Geant4 and basf2. This makes sure that all the details of the interaction region geometry are taken into account. For each integration cell of PySynRad, the basf2 framework reads the number of photons that are emitted by the cell from disk and simulates each photon separately. The start location of the photon is the location of the cell, while the photon direction is smeared uniformly around the cell emission direction within an opening angle of $2/\gamma$. This simulates the typical synchrotron radiation emission cone as explained in section 7.4.3. The energy for each photon is randomly sampled from the synchrotron energy spectrum, using equation 7.45 and the critical energy value from the cell. There are various ways to implement a random selection process for a given probability distribution, most notably methods based on the von Neumann method⁷ [261] and methods based on the inverse transform sampling method [262]. For sampling the synchrotron radiation spectrum in basf2 the latter method is chosen as it has been successfully applied to synchrotron radiation in the past [263]. In short, the method works by creating a cumulative distribution function (**CDF**) of the probability distribution at hand and by inverting it. A random number sampled from a uniform distribution in the range $]0,1[$ is

⁷also called “rejection sampling” or the “acceptance-rejection method”

then used to pick a value from the inverted distribution to return a random number according to the original probability distribution function. The implementation in basf2 uses look-up-tables for the inversion compared to the analytical description based on simple transformations and Chebyshev polynomials in [263]. The left plot of figure 7.36 shows the cumulative distribution function gained from the synchrotron power spectrum of figure 7.32, the middle plot the inverted CDF and the right plot compares samples drawn from the inverted CDF with the original synchrotron power spectrum. In order to avoid simulating the large number of low energetic photons that won't be able to travel through the gold layer and the beampipe material, all photons with a sampled energy below 5 keV are rejected. The resulting energy spectrum of the emitted photons is drawn in figure 7.37.

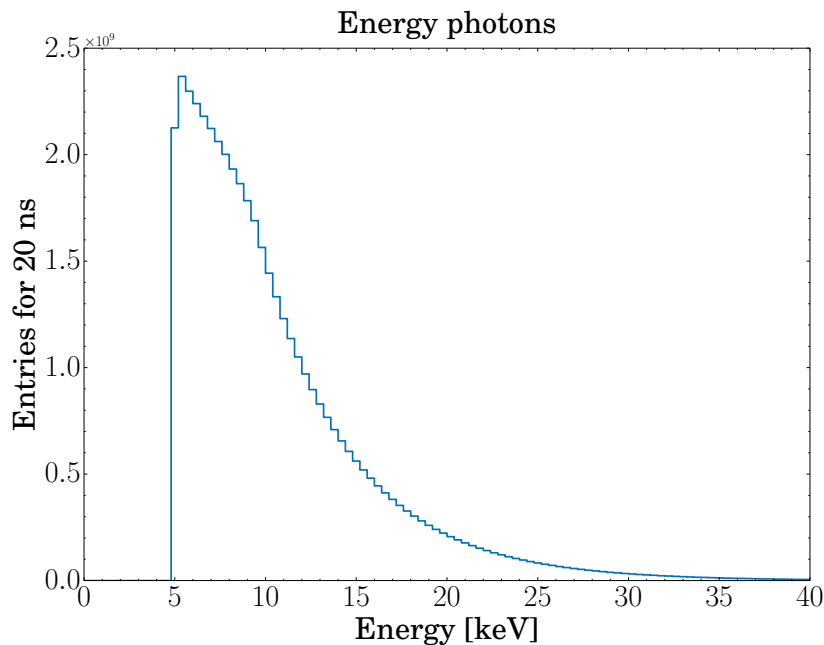


Figure 7.37: The energy spectrum of the emitted photons from synchrotron radiation in the LER. The rejection cut of 5 keV is clearly visible on the left hand side.

The Geant4 simulation is set up to record any hit of a particle in the gold layer and the forward/backward tantalum part of the beampipe. The distribution of the recorded hits along the z -coordinate caused by a photon are shown in figure 7.38 for the LER on the left and the HER on the right, respectively. The range covered by the inner layer of the PXD is drawn in red, indicating possible areas of synchrotron radiation flux in the PXD. While the PXD covers mostly a low-flux area in the LER, the overlap of the PXD with the high-flux region in the HER for z values above 5 cm is not negligible. The distribution of the azimuthal angle ϕ of the synchrotron radiation inside the beampipe is illustrated in figure 7.39. The synchrotron radiation hits the beampipe almost exclusively around $\phi = 0$, as one would expect from the crossing-angle of the beams.

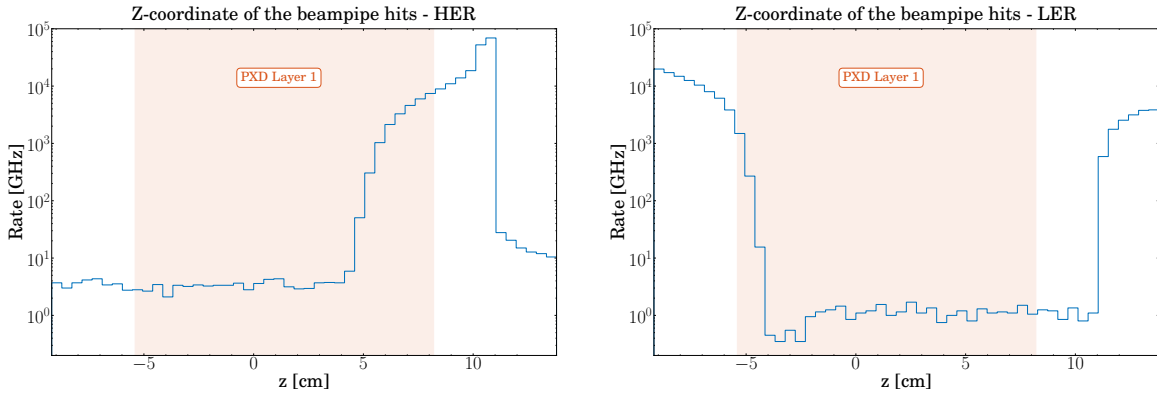


Figure 7.38: The distributions illustrate the regions that are hit by the synchrotron radiation inside the beampipe. The coverage along z of the inner PXD layer is drawn in red.

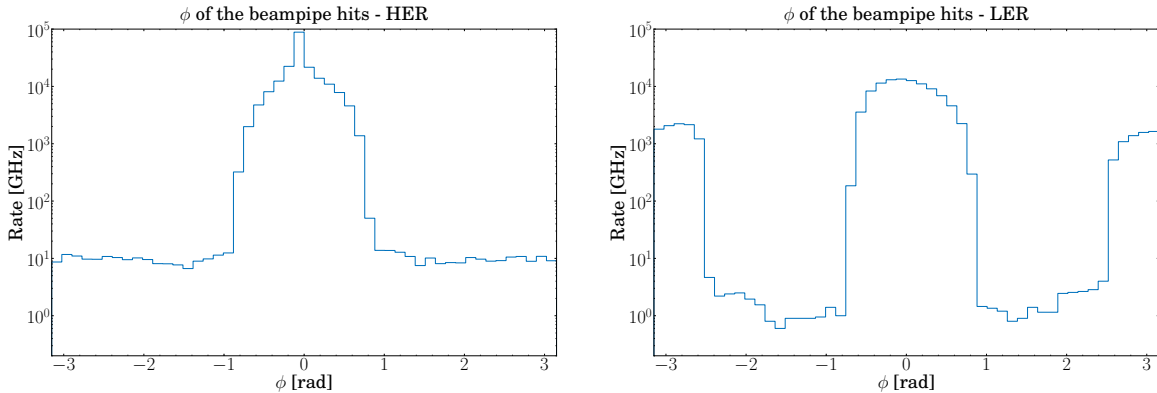


Figure 7.39: The azimuthal angle distributions of the synchrotron photons hitting the beampipe for the HER (left) and LER (right).

The energy of the photons hitting the beampipe is drawn in figure 7.40. The distributions follow an exponential function, with energies ranging from the 5 keV rejection cut up to 200 keV for the HER and 70 keV for the LER. Tracing the photons that caused a hit in the beampipe back to their origin leads to figure 7.41. The synchrotron radiation hitting the beampipe is mostly created by the focusing magnets closest to the IP, QC1LE for the HER and QC1RP for the LER. A significant contribution is also observed from the leak field in the HER, denoted as QC1LPE in the left plot. The plots also indicate that there is no considerable amount of synchrotron radiation created beyond 2.5 m that could hit the PXD which is the main reason to restrict the synchrotron radiation generation to a distance of 3 m from the IP.

The Geant4 synchrotron radiation simulation represents a time span of 20 ns. In order to extrapolate the simulation to the PXD readout time of 20 μ s a toy Monte Carlo production is performed. From the recorded hits in the beampipe distributions for the azimuthal angle ϕ , the z -coordinate and the momentum (p_x, p_y, p_z) are created. Sampling the distributions is per-

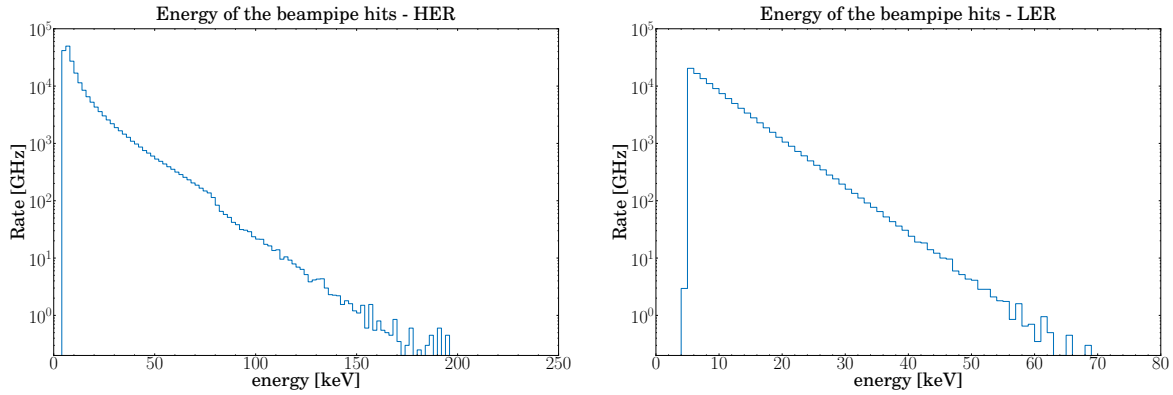


Figure 7.40: Energy of the photons that hit the beampipe for the HER (left) and the LER (right).

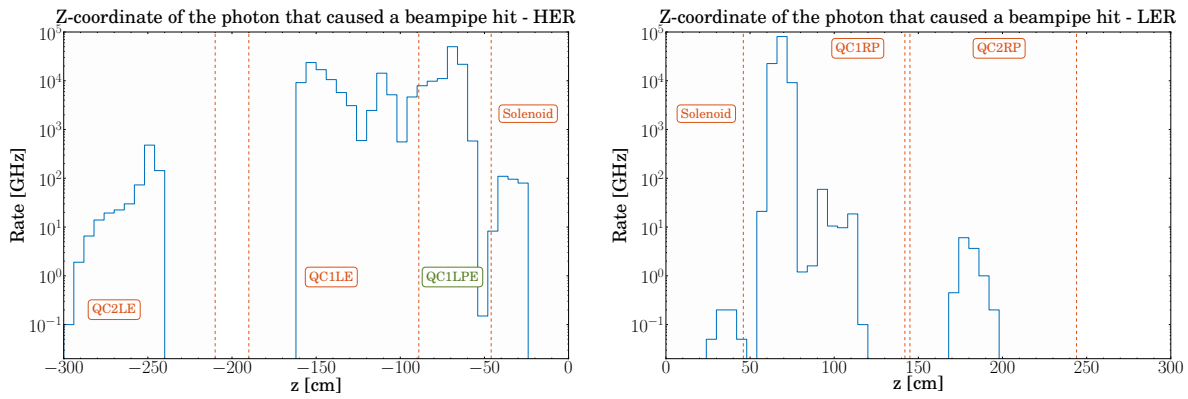


Figure 7.41: Origin of all photons that created a hit in the beampipe. The synchrotron radiation is caused by the innermost focusing magnets (HER and LER) and the leak field in the HER.

formed with the inverse transform sampling method and applies the same algorithm as for the synchrotron radiation energy spectrum. It is found that the 5 variables (ϕ , z , p_x , p_y , p_z) are correlated with each other. Correlations between ϕ and z are removed by binning the hits in the beampipe into bins in z and ϕ and creating separate distributions for each bin. Table 7.4 lists the bins and their ranges. For each bin the correlation matrix of the 5 variables is calculated and it is found that two-dimensional probability distributions are sufficient to model the largest correlations. Figure 7.42 compares the original distribution (left plot) and the toy Monte Carlo generated distribution (right plot) of ϕ and z for bin 7 of the HER. A comparison of the original (ϕ, p_y) 2D distribution with the one obtained from toy Monte Carlo for bin 7 is shown in figure 7.43, illustrating the successful modelling of the correlations. The photons created by the toy Monte Carlo are subject to a full Belle II detector simulation in basf2, using the same setup as for all the other backgrounds.

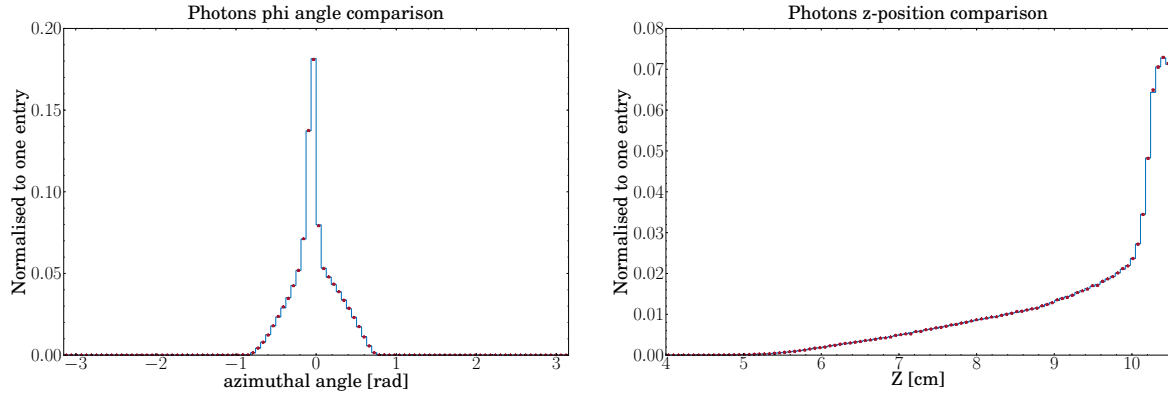


Figure 7.42: Toy Monte Carlo test for the azimuthal angle (left) and the z-position (right). The original data is drawn as a blue histogram and the distribution obtained from toy Monte Carlo is drawn as red stars.

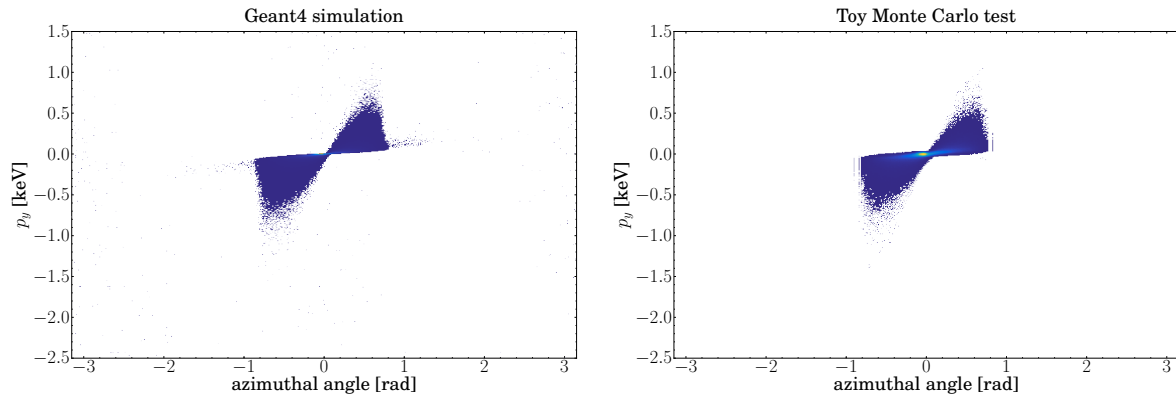


Figure 7.43: 2D Toy Monte Carlo test for the ϕ - p_y distribution. The left plot shows the original distribution, while the right plot shows the result of the toy Monte Carlo.

Bin	HER ϕ range [rad]	HER z range [cm]	LER ϕ range [rad]	LER z range [cm]
1	[-3.15, -1.575]	[-9.5, -6.55]	[-3.15, 3.15]	[-9.5, -6.55]
2	[-1.575, 1.575]	[-9.5, -6.55]	[-3.15, 3.15]	[-6.55, -4.0]
3	[1.575, 3.15]	[-9.5, -6.55]	[-3.15, 3.15]	[-4.0, 10.5]
4	[-3.15, -1.575]	[-6.55, 4.0]	[-3.15, 3.15]	[10.5, 13.8]
5	[-1.575, 1.575]	[-6.55, 4.0]		
6	[1.575, 3.15]	[-6.55, 4.0]		
7	[-3.15, 3.15]	[-4.0, 10.5]		
8	[-3.15, 3.15]	[10.5, 13.8]		

Table 7.4: The bins for the toy Monte Carlo production of the synchrotron radiation. The HER data is binned into 8 bins in ϕ and z , while the LER is binned into 4 bins in ϕ and z .

Particle flux

The synchrotron radiation background seen in the PXD sensors is almost exclusively caused by photons, as figure 7.44 illustrates. Other types of particles do not play a role for the particle flux and will be omitted in the following discussion. Comparing the LER particle flux with the HER particle flux in figure 7.44 shows that the contribution of the LER to the synchrotron radiation background is very small and is therefore neglected.

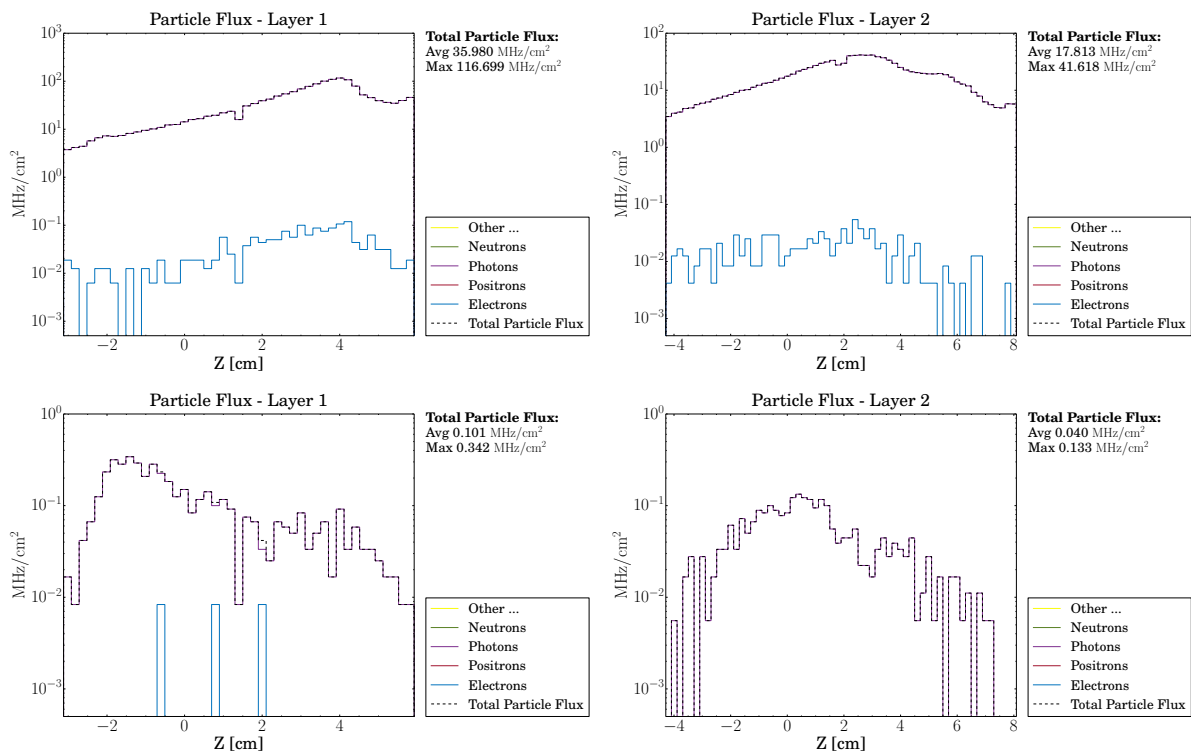


Figure 7.44: The types of particles traversing the PXD layers due to synchrotron radiation. The top row shows the result from the HER, while the bottom row represents the LER. From the plots it is obvious that photons are the dominating type of particle and that the contribution from the LER is negligible compared to the HER.

The polar angle distributions in figure 7.45 show the typical pattern for background particles that enter the interaction region from outside, such as the Touschek and Beam-Gas background. The z - ϕ plots show a peak in the forward part of the sensors at around 180° and peaks in the forward ASICs region at small azimuthal angles. Comparing the distributions of figure 7.45 with those from figure 7.38 it seems odd that the photons traverse the PXD closer to the IP than they traverse the beampipe. The distribution of the azimuthal angle, plotted in figure 7.45, seems even more strange when compared to figure 7.39. The photons hit the beampipe at 0° but are found in the PXD sensors around 180° . The solution to this mystery is revealed in the next section when the origin of the background is investigated.

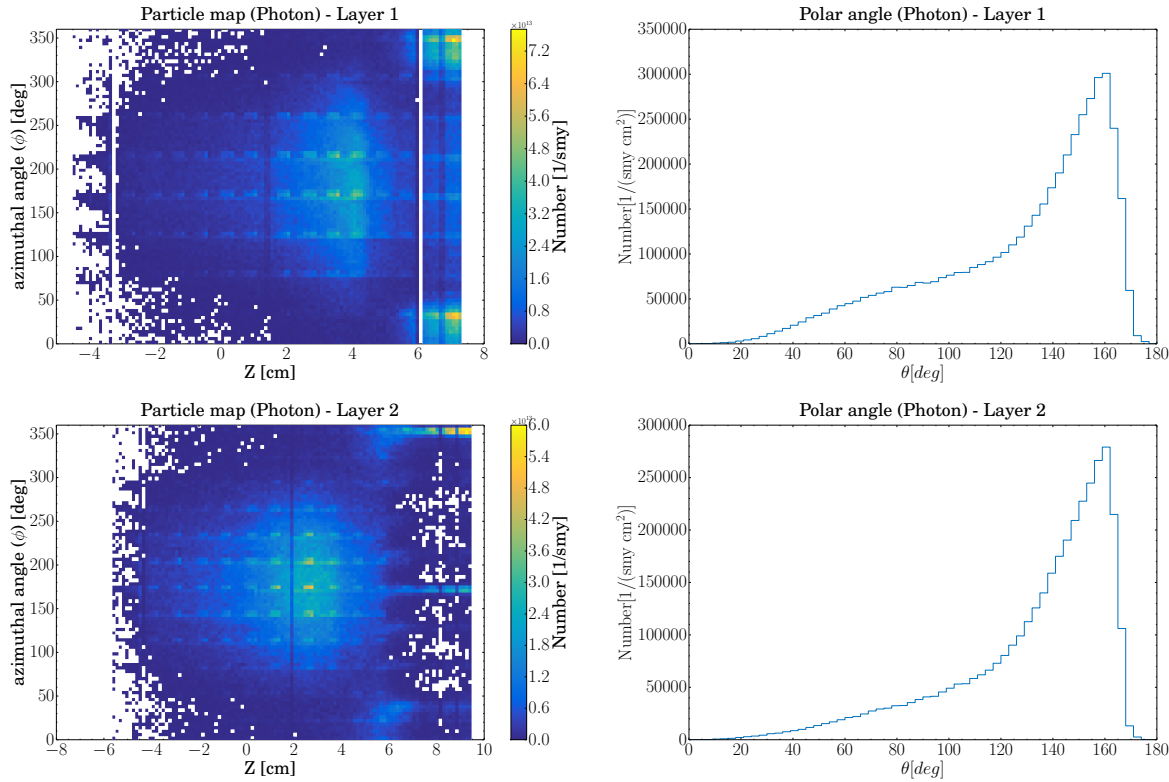


Figure 7.45: Angular and spatial distributions of the photons traversing the PXD from synchrotron radiation per area during one snowmass year. The top row represents the inner layer and the bottom row the outer layer. The left plots show the $z\phi$ distributions of photons traversing the sensor area, the backward ASICs and the forward ASICs.

Origin of particles

As the majority of the contribution from synchrotron radiation originates from the HER, the synchrotron radiation from the LER is neglected in the following discussion. It is mentioned in the particle flux section that the distributions of the particle flux along the global z -axis and the distributions of the azimuthal angle are not as expected. The majority of the photons traverse the PXD in a region closer to the IP than the area where they hit the beampipe in the first place. In addition, almost all photons in the PXD sensors are found at an azimuthal angle of 180° instead of the expected angle of 0° . In order to shed light onto this mystery, each particle that traverses the PXD is traced back to the photon it originated from along with all intermediate Geant4 steps together with the type of interaction that occurred at the step boundaries is plotted. The result is shown in figure 7.46. The trajectory of each photon after it hit the beampipe is drawn as a black line, the Compton scattering effect as green dots and the photo-electric effect as blue dots. In the top and bottom right plot the synchrotron radiation photons enter the interaction area from the left and hit the beampipe at $z = [5, 10]$ cm, $x = 1$ cm. Most photons that are seen in

the PXD do not interact with the beampipe. They traverse the beampipe walls and deposit their energy in the forward ASICs area of the 1.1, 1.2, 1.8 and 2.1, 2.2 ladders, as the hotspots in the top right corner of the left plots in figure 7.45 and figure 7.46 demonstrate. The photons that are recorded in the PXD and do not traverse the beampipe undergo Compton scattering, illustrated by the green dots in figure 7.46. This leads to a “backscattering” effect where the photons travel against the HER direction to the opposite side of the beampipe. In the inner PXD layer, most photons hit, again, the forward ASICs area (as seen by the hotspot in the bottom right corner of the top left plot in figure 7.45) while the outer layer does not see this effect as pronounced. But in contrast to the “non-backscattered” photons, Compton scattered photons make it to the sensor region of the 1.4, 1.5, 1.6, 2.6, 2.7, 2.8 ladders, giving rise to fired pixels and therefore to a contribution to the total background of the PXD.

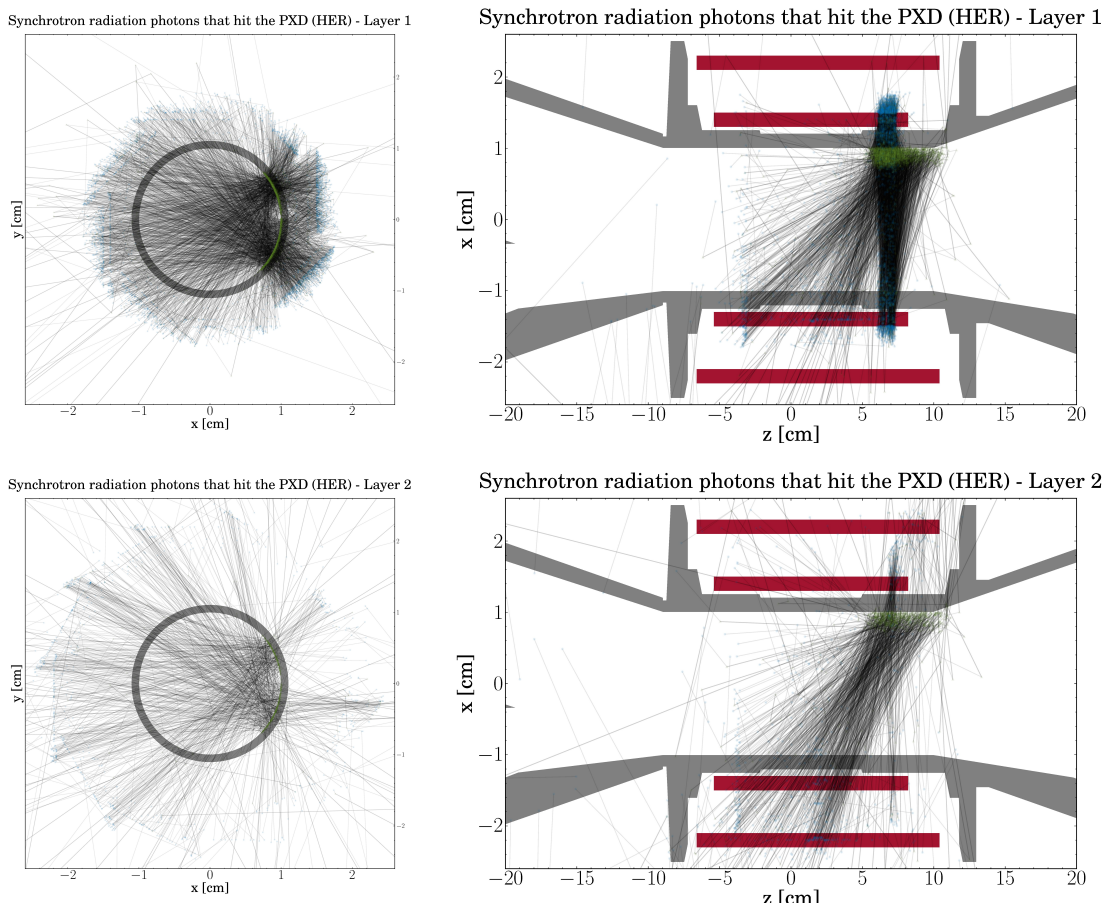


Figure 7.46: The trajectories of the synchrotron radiation photons after they hit the beampipe. Black lines represent the trajectories, green dots Compton scattering and blue dots the photo-electric effect. The top row shows the result for the inner layer, while the bottom row represents the outer layer.

Occupancy

The synchrotron radiation background is somewhat special as its occupancy is the result of photons in contrast to the electrons and positrons of the other backgrounds. For the analysis presented here, 4 ROFs are simulated for the HER and 3 ROFs for the LER. The photons interact with the sensor by the photo-electric effect, depositing their full energy at a single spot in the silicon material (see section 5.5). This leads to very small pixel clusters as the top plot in figure 7.47 demonstrates. The asymmetry illustrated in the xy projection is the result of Compton scattered photons as the previous section explained in detail. The z distribution of the fired pixels has an asymmetry too, with a large peak at 4 cm(2.5 cm) for the ladders of the inner(outer) layer. The HER is the dominating source for the synchrotron radiation occupancy, leading to $0.17 \pm 0.02\%$ for ladder 1.5.1 and $0.09 \pm 0.001\%$ for ladder 2.7.2 as the largest values (see table 7.5).

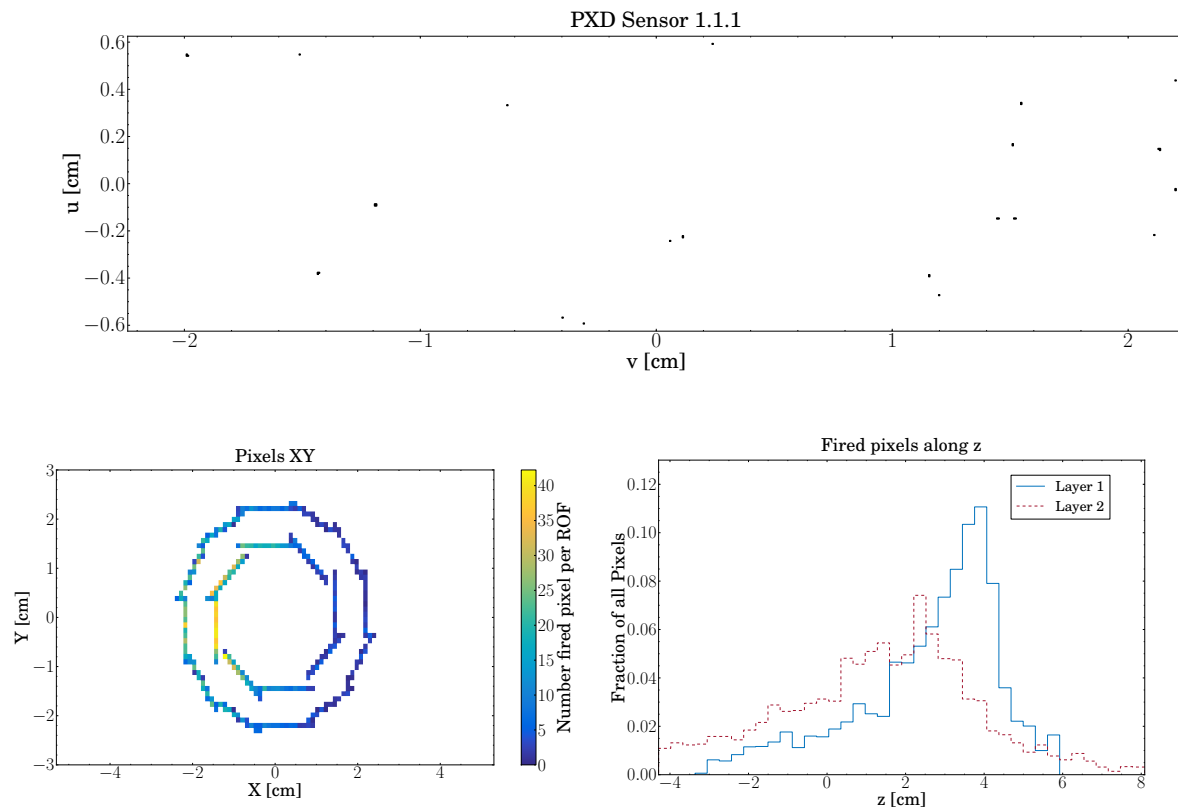


Figure 7.47: The fired pixels from the synchrotron radiation HER background. The top plot presents the content for one ROF of sensor 1.1.1. The bottom left plot shows the xy -projection where the asymmetry is the result of Compton scattered photons. The bottom right plot presents the distribution of the fired pixels along z .

Layer 1 [%] ·10 ⁻³			Layer 2 [%] ·10 ⁻³		
Sensor	LER	HER	Sensor	LER	HER
1.1.1	0.9 ± 0.6	16.3 ± 1.1	2.1.1	0.7 ± 0.3	9.5 ± 1.8
1.1.2	2.2 ± 0.3	3.3 ± 1.6	2.1.2	0.3 ± 0.5	3.5 ± 1.5
1.2.1	1.4 ± 1.2	31.2 ± 0.6	2.2.1	0.5 ± 0.7	11.1 ± 1.3
1.2.2	1.4 ± 0.5	7.9 ± 2.7	2.2.2	0.3 ± 0.5	3.6 ± 0.4
1.3.1	0.9 ± 0.6	93.2 ± 3.7	2.3.1		10.8 ± 1.3
1.3.2	0.7 ± 0.9	20.9 ± 5.2	2.3.2	0.2 ± 0.2	12.2 ± 2.2
1.4.1	0.3 ± 0.2	154.2 ± 14.8	2.4.1		20.4 ± 2.3
1.4.2	2.2 ± 0.9	49.6 ± 3.2	2.4.2	0.3 ± 0.5	31.4 ± 3.6
1.5.1		166.8 ± 16.9	2.5.1		42.2 ± 4.2
1.5.2	1.4 ± 0.2	53.2 ± 5.6	2.5.2		54.4 ± 7.9
1.6.1		129.9 ± 8.8	2.6.1	0.3 ± 0.5	57.9 ± 9.0
1.6.2	1.6 ± 0.7	36.2 ± 4.9	2.6.2		73.8 ± 4.2
1.7.1	1.7 ± 0.2	48.9 ± 7.6	2.7.1	0.5 ± 0.7	60.7 ± 5.9
1.7.2	0.2 ± 0.2	12.1 ± 2.6	2.7.2		88.7 ± 1.4
1.8.1	2.1 ± 0.9	19.1 ± 1.0	2.8.1	0.2 ± 0.2	49.1 ± 2.0
1.8.2	1.4 ± 0.6	5.2 ± 1.1	2.8.2	0.5 ± 0.3	66.5 ± 1.8
			2.9.1		33.6 ± 2.5
			2.9.2	0.9 ± 1.2	42.8 ± 5.8
			2.10.1	0.3 ± 0.5	16.7 ± 1.6
			2.10.2		20.8 ± 1.9
			2.11.1		8.2 ± 2.0
			2.11.2	1.0 ± 0.7	7.9 ± 3.4
			2.12.1		11.7 ± 4.4
			2.12.2	1.9 ± 1.1	3.5 ± 0.9
Max	2.2 ± 0.3	166.8 ± 16.9	Max	1.9 ± 1.1	88.7 ± 1.4

Table 7.5: The detailed occupancy values for the synchrotron radiation background split into their individual contributions for each sensor.

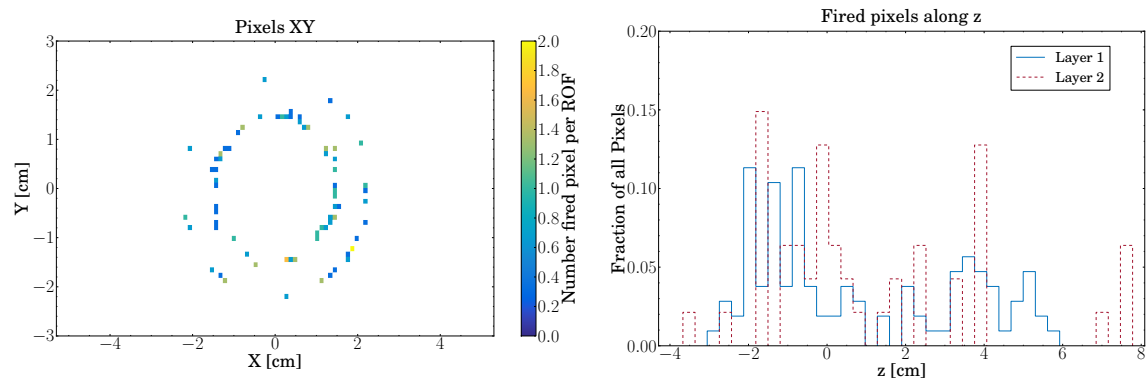


Figure 7.48: The fired pixels from the synchrotron radiation LER background. The left plot shows the xy -projection and the right plot the distribution of the fired pixels along z .

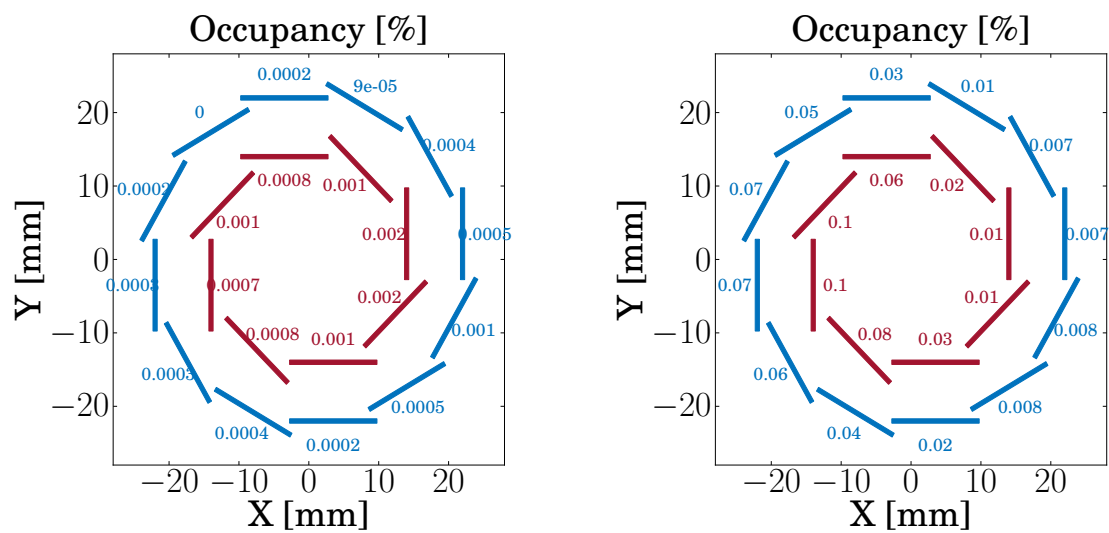


Figure 7.49: Summary of the PXD occupancy values for the synchrotron radiation LER (left) and synchrotron radiation HER (right) background.

7.5 Luminosity-dependent processes

The term “luminosity-dependent processes” groups together all physics processes that are initiated by the collision of the electron and the positron beam. This comprises physics processes as well as processes that contribute to the background of the Belle II detector. Unlike the beam-induced backgrounds, luminosity-dependent backgrounds cannot be reduced by the means of shielding, collimators or lattice tuning. They scale with the luminosity of the accelerator, which makes them 40 times larger at SuperKEKB compared to KEKB. However, the luminosity-dependent background levels measured at Belle cannot be simply scaled to the Belle II luminosity in order to estimate the expected background levels at Belle II. The various Belle II sub-detectors and the interaction region have either seen a re-design or are completely new. In particular, the PXD is a completely new sub-detector and there is no experience with a pixel detector being that close to the IP of such a high luminosity lepton collider.

7.5.1 Radiative Bhabha scattering

Radiative Bhabha scattering is the process in which an electron scatters with a positron[264]

$$e^+ e^- \rightarrow e^+ e^- (\gamma)$$

The process exhibits a large cross-section, especially at small scattering angles. Bhabha scattering is one of the dominant processes at Belle II and due to its simple event topology makes it the primary process for measuring the delivered luminosity at SuperKEKB. On the other hand, Bhabha scattering contributes as a background to several physics analyses, an example being the two-photon analysis from chapter 6. However, for most physics analyses only the wide-angle Bhabha scattering is relevant in which both outgoing leptons enter the detector. If required, those events can be rejected efficiently at the trigger level by cuts on the event topology, cluster distributions in the calorimeter and on particle identification likelihoods. Since the cross-section peaks at small scattering angles, the majority of Bhabha scattered particles travel down the beampipe undetected. If the change in their direction and momentum exceeds the aperture of the magnets and the accelerator, they collide with the beampipe and the magnets downstream from the IP and are lost. The collisions create showers and the particles from the showers can back-scatter into the direction of the IP and hit the PXD. A second and even more severe radiative Bhabha induced background comes from the emitted Bremsstrahlung photon. The photon collides with the material of the beampipe or the magnets and can give rise to a giant dipole resonance (**GDR**) [265, 266]. In this process, photons with an energy in the range of 8 to 30 MeV deposit enough energy into an atomic nucleus in order to separate charges, causing the creation or increase of the nucleus’ dipole moment. This, in turn, leads to a collective excitation

of an atomic nucleus where the protons oscillate against the neutrons. The most probable way of de-exciting an heavy nucleus that has been excited by a photon is the emission of a single neutron [267]. The neutrons created by the GDRs can then hit the PXD and damage its sensors and electronics, if this process is sufficiently frequent.

Theory

Two of the leading-order Feynman diagrams that contribute to the radiative Bhabha scattering process are illustrated in figures 7.50 and 7.51.

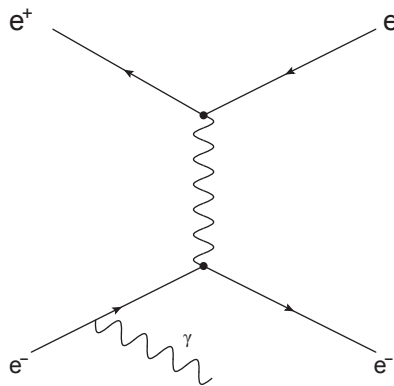


Figure 7.50: One of the four leading annihilation Feynman diagrams for radiative Bhabha scattering.

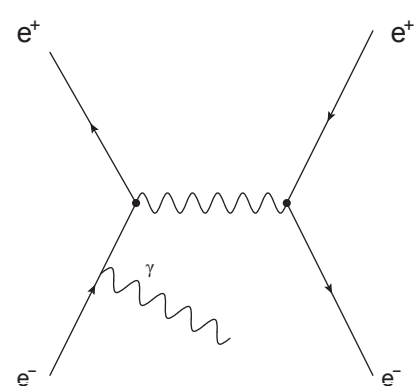


Figure 7.51: One of the four leading scattering Feynman diagrams for radiative Bhabha scattering.

It turns out that the exact theoretical calculation of quantities such as the angular and energy distributions of the photons and the total cross-section of the process is very complicated due to the singular structure of the matrix elements. However, under the assumption of high energetic incoming particles and small angle photon emission, the calculation can be simplified. A full treatment of this calculation, including the equation for the total cross-section, is given in [268]. Performing the calculation of the total cross-section for SuperKEKB and including a correction for the finite beam size (beam size effect) [269] results in

$$\sigma_{tot}^{RBB}(\epsilon) = \frac{16}{3} \alpha r_e^2 \left[\left(\log\left(\frac{1}{\epsilon}\right) - \frac{5}{8} \right) \left(\log\left(\frac{\sqrt{2}m_e c \sigma_y^*}{\hbar}\right) + \frac{\gamma_E}{2} \right) + \frac{1}{4} \left(\frac{13}{3} \log\left(\frac{1}{\epsilon}\right) - \frac{17}{6} \right) \right] \quad (7.55)$$

where α is the fine-structure constant, r_e the classical electron radius, m_e the electron mass and γ_E the Euler-Mascheroni constant.

The total cross-section is given in terms of the energy acceptance ϵ defined as

$$\epsilon = \frac{E_y}{E_{beam}}$$

and σ_y^* , the beam size at the IP in the vertical plane, is given by

$$\sigma_y^* = \frac{a_x \cdot a_y}{a_x + a_y}$$

$$a_x = \sqrt{\sigma_{x,HER}^2 + \sigma_{x,LER}^2 + \left(\left(\frac{\theta_x}{2}\right)^2 (\sigma_{z,HER}^2 + \sigma_{z,LER}^2)\right)}$$

$$a_y = \sqrt{\sigma_{y,HER}^2 + \sigma_{y,LER}^2}$$

Inserting the values for SuperKEKB from table 3.1 and plotting the total cross-section results in the curve shown in figure 7.52.

Simulation

The **BBBrem** generator [177] is used to generate the radiative Bhabha events for the background studies. In order to circumvent the difficulties that would arise during a straightforward integration of the cross-section, BBBrem applies a Monte Carlo method to generate random events in phase space such that their distribution matches as closely as possible the exact distributions. Each event is assigned a weight that represents the discrepancy between the actual and the approximate matrix elements. The average of the weights is then the Monte Carlo estimate of the cross-section. However, the full detector simulation requires unweighted events. The scheme for producing unweighted events in BBBrem follows the one described in section 6.3.2. Figure 7.53 shows the distribution of the weights for a centre-of-mass energy of 10.58 GeV and an energy acceptance of $10^{-4}\%$. It also shows the maximum weight that is used as an input for the production of unweighted events.

Technically, the original FORTRAN based generator code is translated to C++ and implemented into the basf2 software framework. In addition, the code was extended with a treatment of the beam size effect. This effect leads to a reduction of the cross-section due to overlapping electromagnetic fields of the electrons/positrons within a bunch⁸. The result is a finite instead of an infinite interaction range of the leptons, usually in the order of half the average distance between

⁸The beam size effect was discovered for the first time at the MD-1 detector [270].

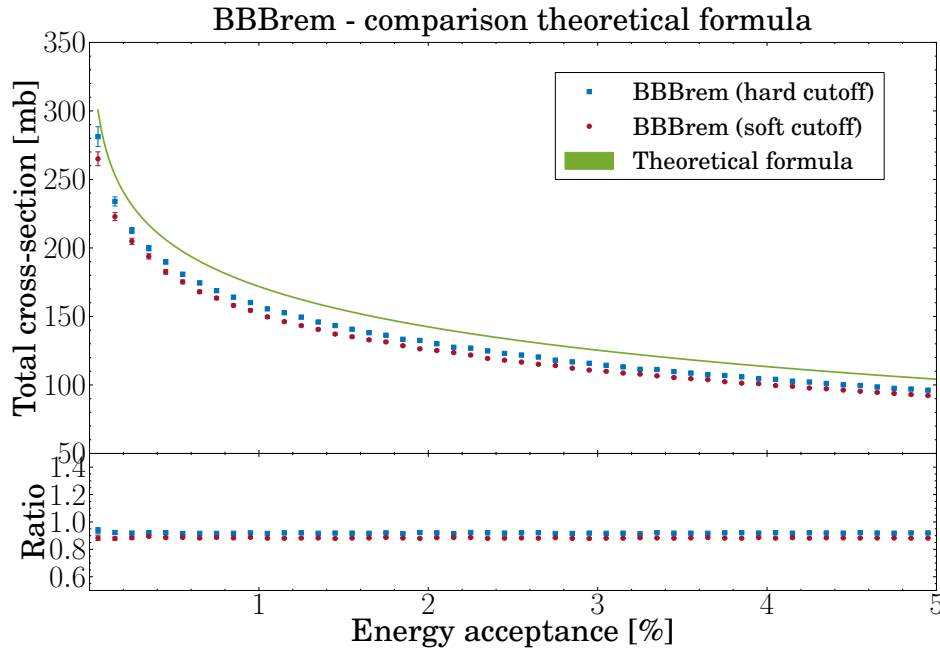


Figure 7.52: Comparison of the total cross-section between BBBrem and equation 7.55. Both methods of dealing with the beam size effect are shown.

two leptons [177]. Transforming the finite interaction range to a measure for the momentum-transfer squared, one can define

$$t_c = \left(\frac{\hbar c}{d} \right)^2$$

where d denotes half the average distance. Using the vertical beam size of the LER, the value for SuperKEKB evaluates to $t_c = 1.68 \times 10^{-17} \text{ GeV}^2$. The beam size effect can be implemented by introducing either a hard cutoff or a soft cutoff. The hard cutoff sets the weight of events that have a momentum transfer squared smaller than t_c to zero. The soft cutoff, on the other hand, suppresses the electromagnetic potential of the electrons by multiplying each event's weight by

$$\frac{t^2}{(t - t_c)^2}$$

A comparison of equation 7.55 with the results from a BBBrem Monte Carlo simulation for varying values of the energy acceptance is shown in figure 7.52. The plot also shows the difference between the two beam size effect implementations. The deviation of the simplified theoretical formula from the Monte Carlo simulation is less than 10 % and constant over the whole range of the energy acceptance levels up to 5 %.

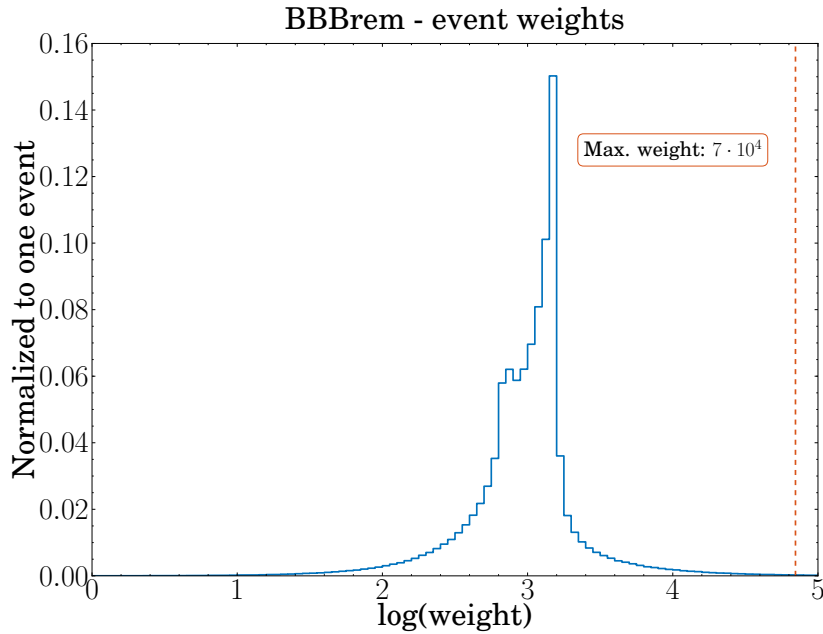


Figure 7.53: The distribution of the event weights for BBBrem at $\sqrt{s} = 10.58$ GeV and $\epsilon = 10^{-4}\%$.

The implementation of BBBrem in basf2 produces 4-vector events containing the two outgoing leptons and the radiated photon. However, since the scattering at very small angles dominate the process, the emission of the Bremsstrahlung photon by the electron and by the positron is essentially independent. Thus BBBrem only uses the Feynman diagrams where the photon is radiated from the electron. In order to produce a complete Monte Carlo sample for the full detector simulation, the BBBrem implementation in basf2 is “symmetrised”. This means, for each event a random number generator decides, with a 50 % probability, whether the electron should be swapped with the positron in order to allow for radiation from both the electron and the positron. By multiplying the final cross-section with a factor two, the swap of the electron with the positron is accounted for.

Due to the large cross-section at small angles, most particles that are lost hit the beampipe a few metres from the IP. Figure 7.54 provides an overview of the locations and the loss rates for those particles.

It is found that an accurate estimation of those locations and rates requires very detailed modelling of the final focus magnets and their fields. This is not provided by the 3D magnetic field implementation of basf2. Therefore, the 4-vector output of BBBrem is given to SAD, which propagates the particles through the magnetic fields and records the position where they are lost. The result is a SAD file that is read and processed by basf2 in order to evaluate the impact of the radiative Bhabha scattering background on the PXD.

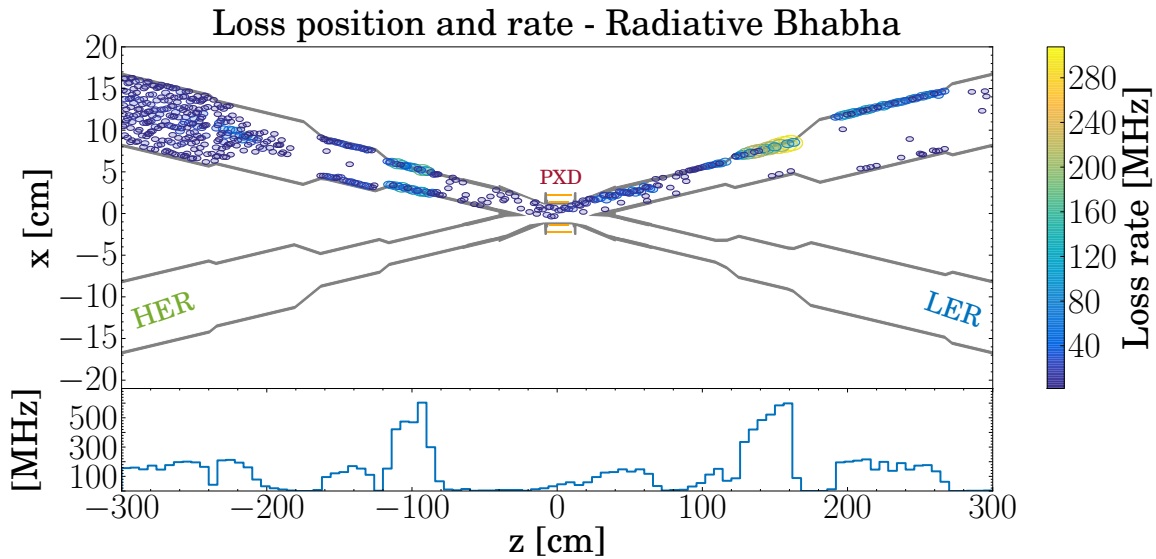


Figure 7.54: The locations and loss rates for the radiative Bhabha particles after the SAD accelerator simulation.

Particle flux

Radiative Bhabha background is the result of scattered particles at the IP, meaning that the background particles emerge from within the IP region, in contrast to the Touschek and Beam-Gas backgrounds. This can be seen in the polar plot distributions of figure 7.55 as they show broad, centralised peaks. Looking at the z - ϕ plots, a few distinct peaks are visible. For the HER those “hotspots” are located in the forward region of the sensors at 120° and 350° for the inner layer and around 140° for the outer layer. The LER does not show such a pronounced structure. Instead, the backward ASICs in the inner layer at 0° are subject to an increased particle flux, while the backward sensors in the outer layer see a moderate peak at 0° .

The particle flux for the HER radiative Bhabha in the forward sensors is dominated by single particle crossings, while the particle flux in the backward sensors originates mostly from particles traversing the sensors multiple time (see figure 7.56). The LER radiative Bhabha shows a mirrored distribution where the backward sensors are dominated by single and double crossings.

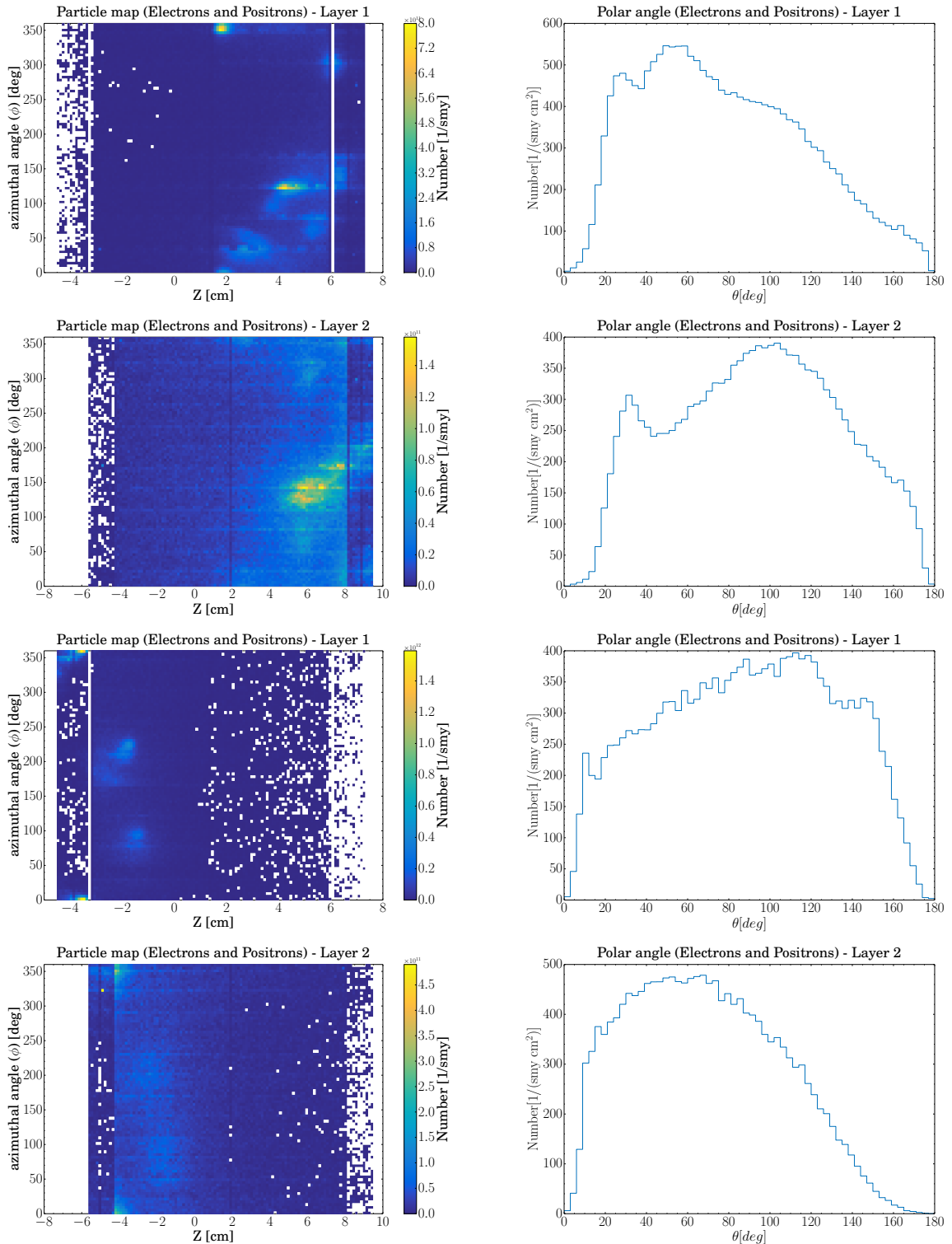


Figure 7.55: Angular and spatial distributions of the electrons and positrons traversing the PXD from radiative Bhabha HER (top two rows) and LER (bottom two rows) per area during one snowmass year.

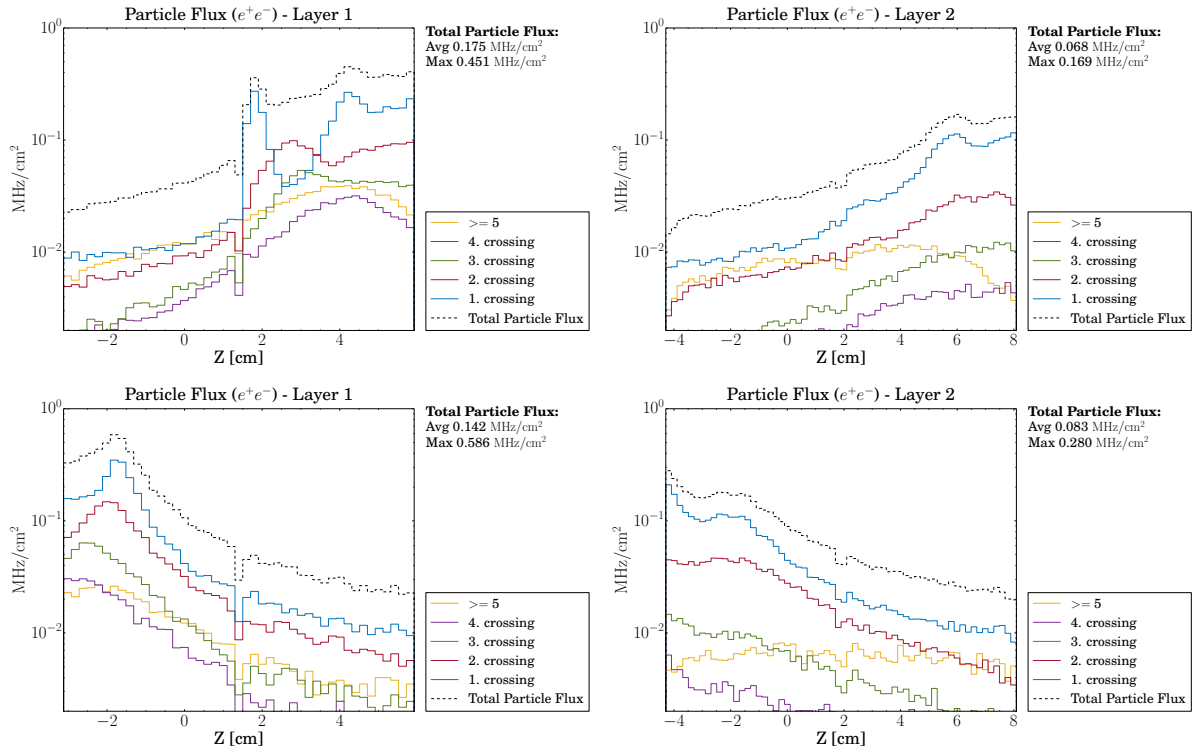


Figure 7.56: Distribution of the number of times a radiative Bhabha generated particle traverses a PXD layer. The top row shows the results from the radiative Bhabha HER, with the inner layer being the left plot and the outer layer the right plot. The bottom row represents the radiative Bhabha LER.

Origin of particles

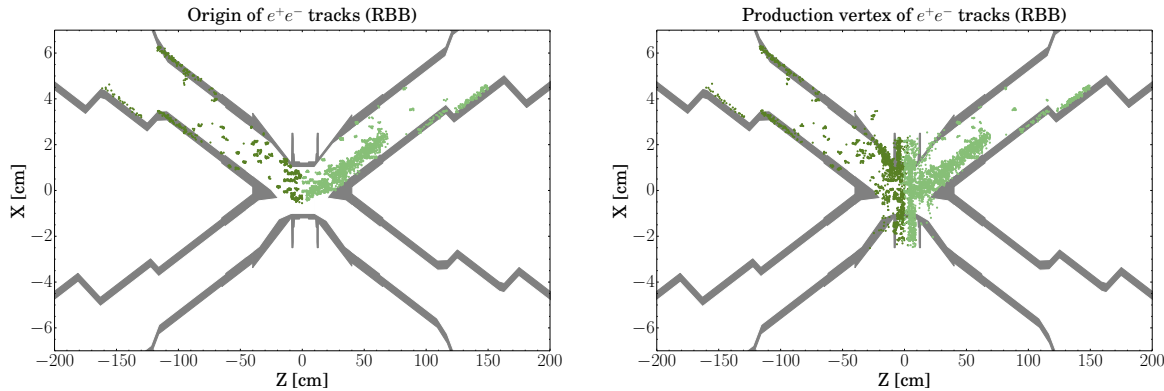


Figure 7.57: The left plot shows the distribution of the origin of all e^+e^- particles that spark the creation of particles that, further down the chain, hit the PXD sensors. The right plot shows primary as well as secondary particles that hit the PXD sensors, thus helping to identify the areas within the interaction region that contribute to the background of the PXD.

The left plot in figure 7.57 shows the positions where the radiative Bhabha particles originate, and reveals that the majority of the particles relevant for the PXD hit the beampipe wall within 150 cm of the IP. Of course, being a QED background, the actual origin of the radiative Bhabha background is the IP. However, as explained in section 7.5.1, the scattered particles are tracked with SAD until they are lost, making the input to the simulation the positions shown in the plot and not the IP. The contribution from secondary particles is much less compared to the Touschek background, as the production vertex plot for radiative Bhabha shows. This is to be expected, as the particles hitting the PXD have to scatter back in to the direction of the IP. This is also the reason why the contribution of the radiative Bhabha background to the PXD background is rather small.

Occupancy

For the occupancy study 908 ROFs are simulated for the HER and 357 ROFs for the LER. The content of sensor 1.1.1 for a single ROF is shown in the top plot of figure 7.58. Most pixel clusters are medium sized clusters with a very interesting looking, long cluster on the right hand side. This cluster is created by a particle traversing the PXD ladder at a very shallow polar angle. The xy plots of figure 7.58 and 7.59 show occupancy hotspots that are also seen in the z distribution. For the HER two peaks are visible in the forward part of the PXD ladders in the inner layer, one at 2 cm and one at 4.5 cm. The outer layer shows only a single peak at 6 cm which is the result of a shifted 4.5 cm peak from the inner layer due to the incident angle of the particles. The location of the peaks in the forward area of the ladder are in agreement with the direction of

the incoming HER beam. In the same way, the radiative Bhabha occupancy for the LER shows a peak in the backward area of the PXD ladders in the inner layer. The peak is located at -2 cm, while the outer layer does not show a peak-like structure. The largest background for the inner layer is found in the 1.1.1 sensor with $(139.5 \pm 15.4) \cdot 10^{-3}\%$ and for the outer layer in the 2.6.1 sensor with $(43.8 \pm 10.7) \cdot 10^{-3}\%$.

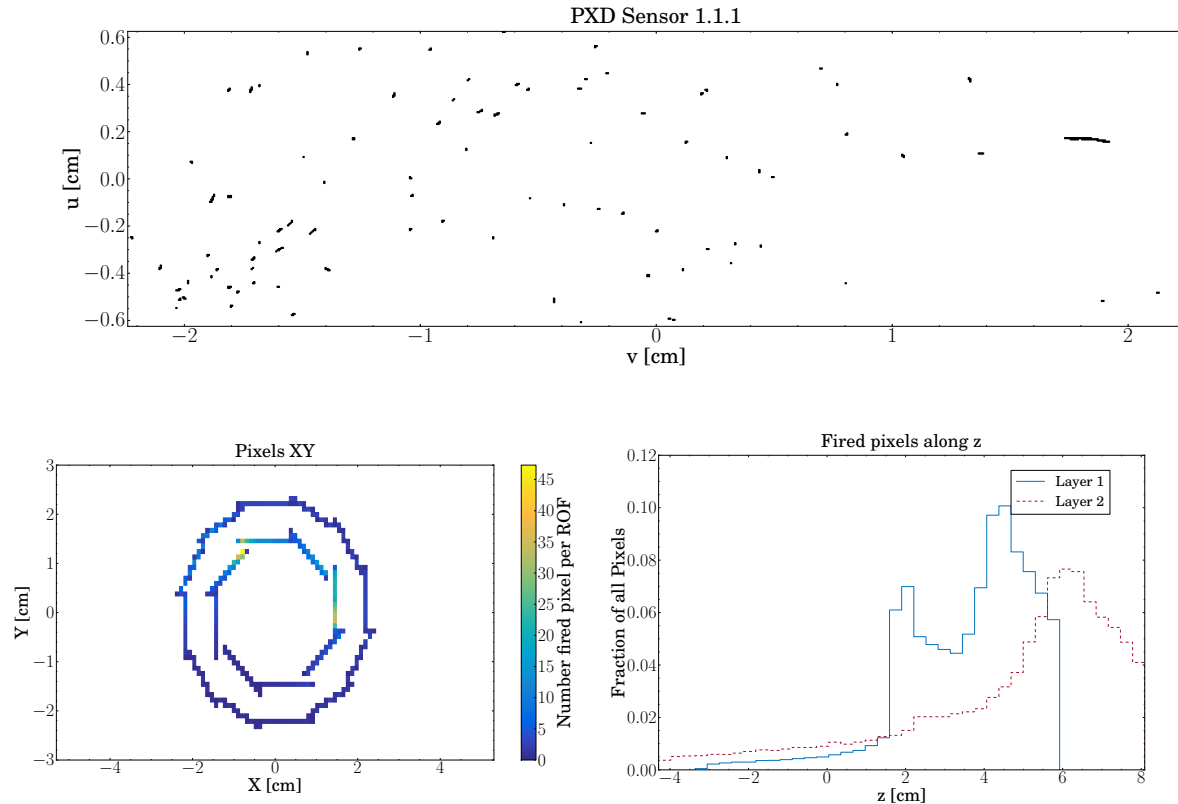


Figure 7.58: The fired pixels from the radiative Bhabha HER background. The top plot presents the content for one ROF of sensor 1.1.1. The bottom left plot shows the xy -projection and the bottom right plot the distribution of the fired pixels along z .

Layer 1 [%] $\cdot 10^{-3}$			Layer 2 [%] $\cdot 10^{-3}$		
Sensor	LER	HER	Sensor	LER	HER
1.1.1	1.9 ± 1.0	139.5 ± 15.4	2.1.1	4.3 ± 2.1	13.2 ± 5.5
1.1.2	4.4 ± 2.3	7.8 ± 4.1	2.1.2	8.8 ± 4.0	4.7 ± 2.4
1.2.1	1.3 ± 0.6	70.3 ± 10.3	2.2.1	3.0 ± 1.5	10.2 ± 4.0
1.2.2	6.1 ± 3.4	6.5 ± 3.1	2.2.2	4.8 ± 2.4	3.8 ± 2.0
1.3.1	1.3 ± 0.5	93.3 ± 13.3	2.3.1	1.7 ± 0.8	13.2 ± 4.9
1.3.2	26.9 ± 7.5	5.4 ± 3.0	2.3.2	3.1 ± 1.5	3.5 ± 1.7
1.4.1	0.9 ± 0.4	116.3 ± 15.5	2.4.1	1.2 ± 0.6	16.3 ± 5.8
1.4.2	6.6 ± 3.0	4.4 ± 2.2	2.4.2	2.2 ± 1.2	3.3 ± 1.7
1.5.1	1.3 ± 0.6	14.4 ± 4.9	2.5.1	0.8 ± 0.2	39.3 ± 8.7
1.5.2	56.6 ± 10.0	2.4 ± 1.2	2.5.2	1.6 ± 0.8	3.2 ± 1.4
1.6.1	1.2 ± 0.6	5.1 ± 2.4	2.6.1	1.2 ± 0.5	43.8 ± 10.7
1.6.2	43.6 ± 7.2	1.6 ± 0.7	2.6.2	1.6 ± 0.7	3.2 ± 1.4
1.7.1	1.5 ± 0.7	8.2 ± 3.2	2.7.1	1.4 ± 0.7	18.6 ± 7.3
1.7.2	3.4 ± 1.8	2.3 ± 1.1	2.7.2	3.3 ± 1.7	2.3 ± 1.1
1.8.1	2.4 ± 1.3	25.9 ± 7.3	2.8.1	1.5 ± 0.7	5.8 ± 3.1
1.8.2	4.5 ± 2.4	4.2 ± 2.2	2.8.2	4.4 ± 2.3	1.7 ± 0.7
			2.9.1	1.6 ± 0.7	3.7 ± 2.0
			2.9.2	2.7 ± 1.3	1.6 ± 0.7
			2.10.1	2.3 ± 1.1	3.9 ± 1.9
			2.10.2	4.3 ± 2.3	1.8 ± 0.8
			2.11.1	3.5 ± 1.6	7.3 ± 3.0
			2.11.2	6.1 ± 3.2	2.9 ± 1.3
			2.12.1	4.7 ± 2.4	9.1 ± 4.1
			2.12.2	9.8 ± 4.2	3.7 ± 1.8
Max	56.6 ± 10.0	139.5 ± 15.4	Max	9.8 ± 4.2	43.8 ± 10.7

Table 7.6: The detailed occupancy values for the radiative Bhabha background split into their individual contributions for each sensor.

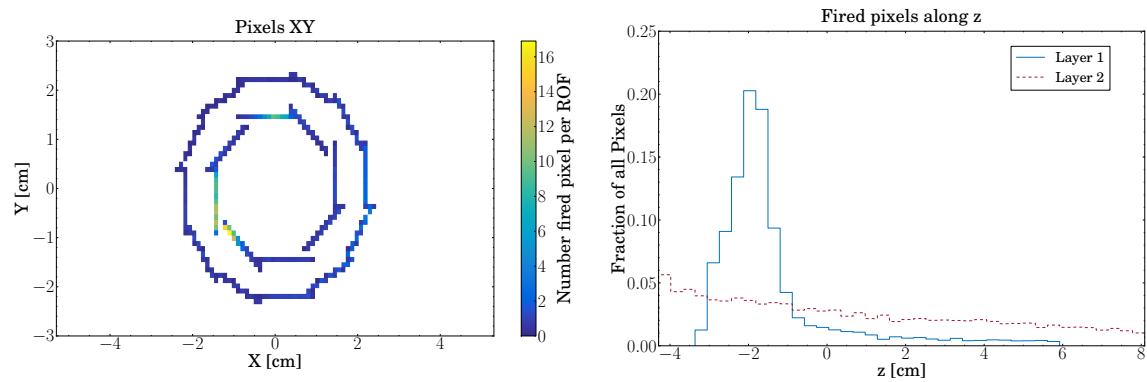


Figure 7.59: The fired pixels from the radiative Bhabha LER background. The left plot shows the xy -projection and the right plot the distribution of the fired pixels along z .

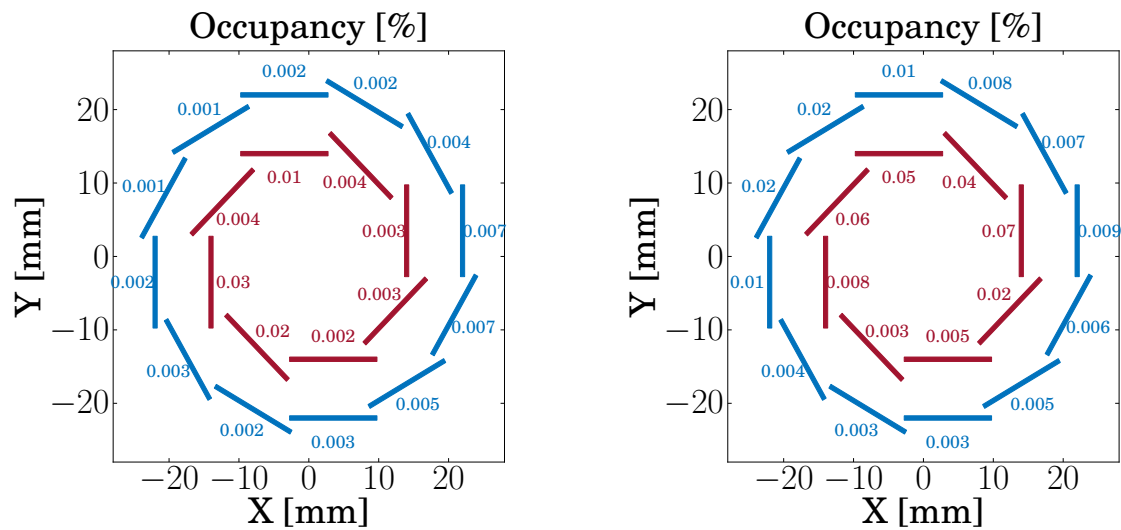


Figure 7.60: Summary of the PXD occupancy values for the radiative Bhabha LER (left) and radiative Bhabha HER (right) background.

Cluster analysis

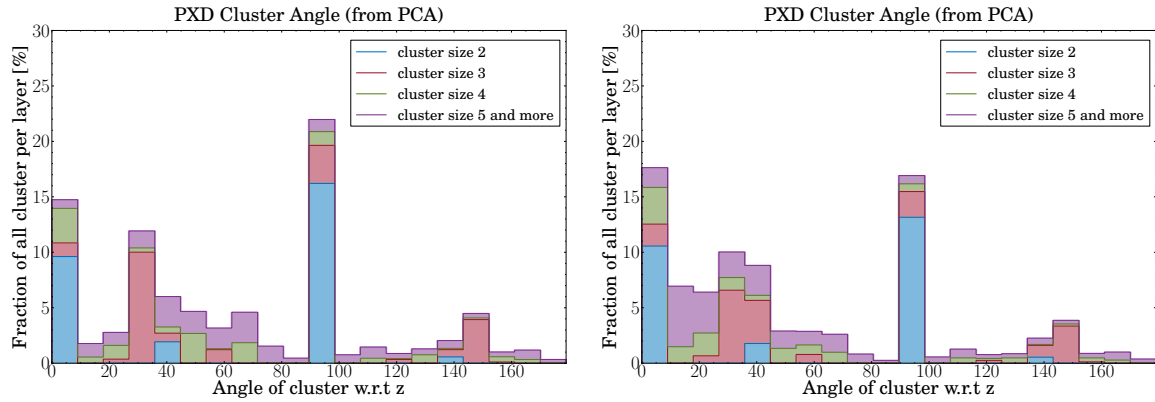


Figure 7.61: Cluster angle distributions for radiative Bhabha LER (left) and radiative Bhabha HER (right). The plots differentiate the different cluster sizes by colours and stack them to provide an overall distribution of the cluster angle. Starting with the cluster size 2 (blue), there are only four possible pixel arrangements with respect to the global z-axis: parallel (0°), perpendicular (90°), diagonal “upward” (45°) and diagonal “downward” (135°).

The radiative Bhabha background is different to the other backgrounds. It exhibits an asymmetry with a trend for smaller angles, especially for the HER. This can be explained by the origin of the radiative Bhabha background. The scattered particles are lost downstream, close to the IP (see figure 7.57) and give rise to showers. Particles from these showers backscatter into the PXD under a shallow angle and, thus, create parallel clusters (see figure 7.61).

7.5.2 Two-photon events

The two-photon process

$$e^+ e^- \rightarrow e^+ e^- \gamma \gamma \rightarrow e^+ e^- e^+ e^-$$

dominates all production processes found at SuperKEKB (see chapter 6). Naively one would, therefore, expect that this process provides the largest contribution to the background in the Belle experiment and will do so for Belle II, too. However, chapter 6 already showed that the cross-section of the two-photon process peaks strongly for very low- p_t values. This explains why the process has not contributed substantially to the background at Belle, as the vertex detector was too far away from the IP and almost all outgoing particles disappeared in the beampipe. This changes at Belle II, as the PXD is extremely close to the IP, exposing it to the large number of low- p_t particles. It is indeed found that the two-photon process is the dominating background

for the PXD and, thus, demands a careful treatment. Chapter 6 introduces the theory behind the process and describes the comparison of data taken at the Belle experiment with two different Monte Carlo generators in order to establish their validity. The comparison shows that the difference between BDK and KoralW in the high cross-section, low p_t (smaller than 20 MeV) and thus most relevant range for the PXD is very small. Therefore both generators qualify to be used for the PXD background studies. For the background study at hand the BDK Monte Carlo generator is used as it is found to generate events faster than the KoralW generator. The Monte Carlo data that was generated for the analysis in chapter 6 is read into basf2 for the full detector simulation. The full Monte Carlo data is given to the detector simulation without any acceptance cuts in order to allow for background contributions originating from particle showers hitting the beampipe up- and downstream from the IP.

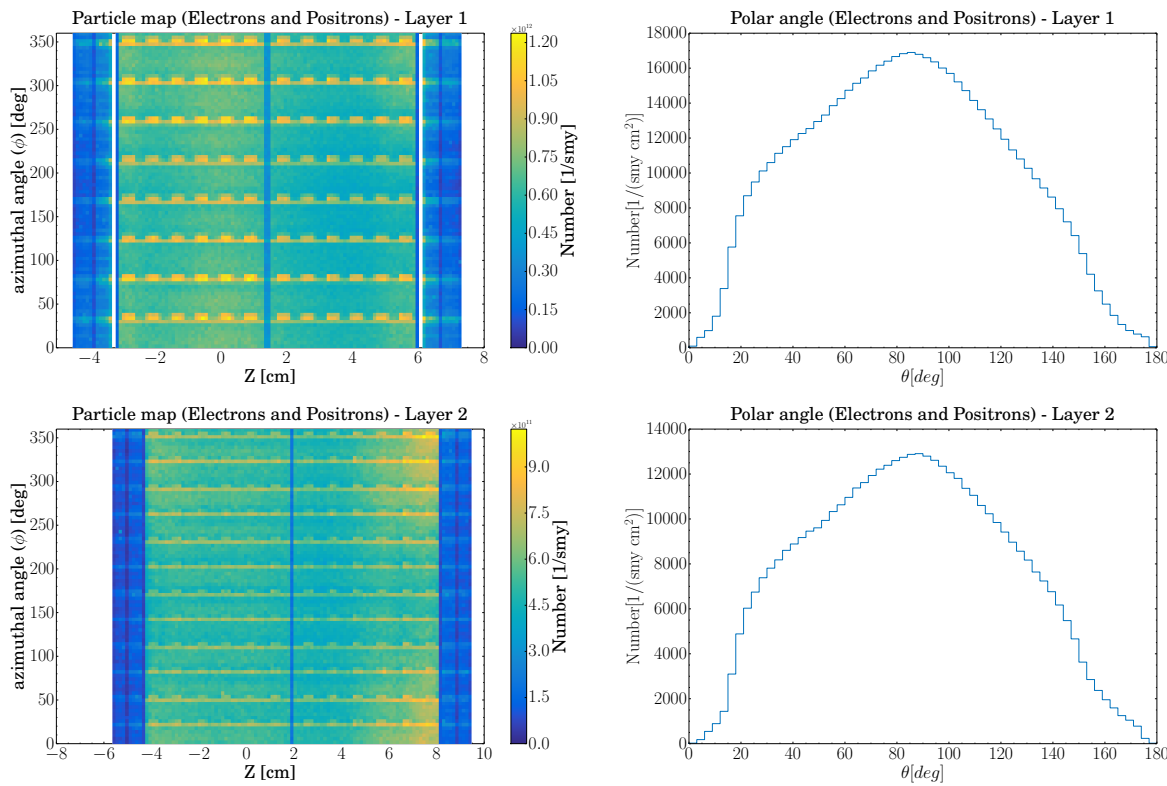


Figure 7.62: Angular and spatial distributions of the electrons and positrons traversing the PXD from the two-photon process per area during one snowmass year. The top row represents the inner layer and the bottom row the outer layer.

Particle flux

The two-photon background is a QED background generated at the IP. As expected the polar angle shows a broad peak at 90° (see right plots of figure 7.62), while the azimuthal angle cover-

age is uniform (see left plots of figure 7.62). The horizontal bands of increased particle flux are caused by the overlap from the windmill structure, as the particles have to traverse two sensors per layer in those areas. The lack of traversing particles in the ASICs is due to the acceptance of Belle II, protecting the ASICs, as intended, from high radiation levels. The vertical band of low particle flux represents the non sensitive area where the two sensors are glued together. The break down of the particle flux into the number of crossings for the two-photon background (see figure 7.63) shows the large amount of curlers contributing to the total particle flux. About 60 % of the particle flux arises from particles that traverse the PXD sensors more than once.

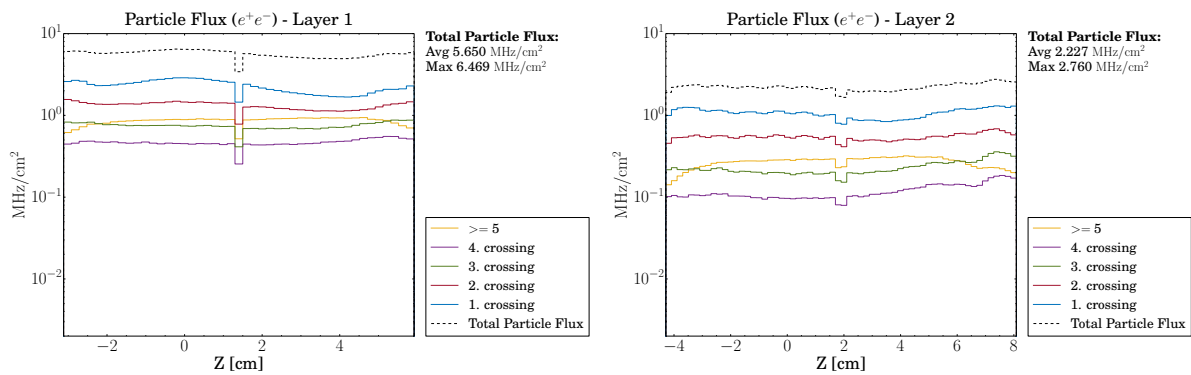


Figure 7.63: Distribution of the number of times a two-photon generated particle traverses a PXD layer. The left plot shows the results from the inner layer of the PXD, the right plot the results from the outer layer. The bump in the forward direction is the result of backscattered particles and is, thus, an effect of the beampipe, while the non-sensitive glue between the two sensors is visible as a gap.

Origin of particles

The distribution of the production vertices (see figure 7.64) shows the expected radial symmetry with the HER upstream region seeing slightly more hits than the other directions due to the boost. The major difference between the two-photon background and all the other backgrounds is the way the particles that traverse the PXD are being created. While the majority of particles for the Touschek, Beam-Gas and radiative Bhabha background originate from interactions of particles with matter and the subsequent creation of showers, the two-photon background in the PXD is the result of direct hits from primary particles rather than hits created by secondary particles. This makes the two-photon background irreducible, as there is no way to increase or add additional shielding material⁹, adjust the radii of apertures, or tune the accelerator magnet lattice¹⁰ in order to protect the PXD from this background. Hence, the two-photon background is the most severe background for the PXD.

⁹as it has been done to reduce the effects of the radiative Bhabha scattering

¹⁰the main handle on reducing the Touschek background

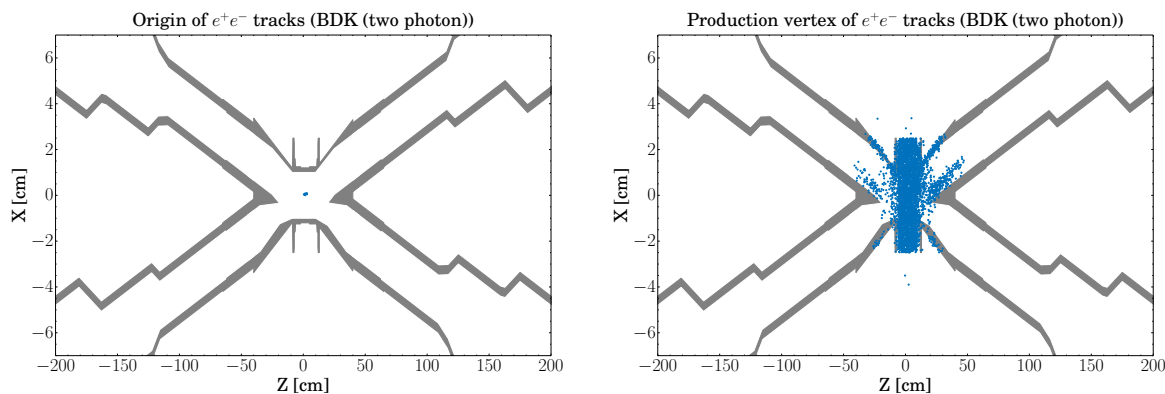


Figure 7.64: The left plot shows the distribution of the origin of all e^+e^- particles that spark the creation of particles that, further down the chain, hit the PXD sensors. The right plot shows primary as well as secondary particles that hit the PXD sensors, thus helping to identify the areas within the interaction region that contribute to the background of the PXD.

Occupancy

In total, 917 ROFs are simulated and analysed. The top plot of figure 7.65 shows a typical PXD ladder for one ROF of the two-photon background. It contains the whole range of pixel cluster sizes. Small clusters are created by high p_t particles traversing the PXD in an almost straight line, while medium to long clusters are the result of low p_t particles curling in the magnetic field. The xy projection shows the typical $1/r^2$ dependence of a spherical symmetric QED process between the inner and the outer layer. All ladders within a layer are exposed to roughly the same occupancy. The distribution in z is flat, with a gap around 1.5 cm (1.8 cm) being the non-sensitive glue between the two sensor of the inner(outer) ladders. Table 7.7 lists the occupancy values for each sensor. Slightly higher values are found for the forward sensors around the azimuthal angle of 0° . This is the result of the boost combined with the crossing-angle of the beams. The largest occupancy value for the inner layer is in the sensor 1.1.1 with $0.89 \pm 0.06\%$ and for the outer layer in the sensors 2.1.1, 2.2.1, 2.11.1, 2.12.1 with $0.29 \pm 0.05\%$.

Cluster analysis

The luminosity dependent two-photon QED background exhibits more perpendicular clusters than parallel clusters as a result of the higher amount of curling tracks (see figure 7.67). This is due to the fact that the cross-section peaks towards low values of p_t .

Sensor	Layer 1 [%]	Sensor	Layer 2 [%]
1.1.1	0.89 ± 0.06	2.1.1	0.29 ± 0.05
1.1.2	0.85 ± 0.07	2.1.2	0.26 ± 0.04
1.2.1	0.87 ± 0.07	2.2.1	0.29 ± 0.05
1.2.2	0.84 ± 0.07	2.2.2	0.25 ± 0.04
1.3.1	0.82 ± 0.07	2.3.1	0.28 ± 0.04
1.3.2	0.80 ± 0.07	2.3.2	0.25 ± 0.04
1.4.1	0.76 ± 0.07	2.4.1	0.27 ± 0.04
1.4.2	0.77 ± 0.07	2.4.2	0.24 ± 0.04
1.5.1	0.74 ± 0.07	2.5.1	0.26 ± 0.04
1.5.2	0.76 ± 0.07	2.5.2	0.24 ± 0.04
1.6.1	0.77 ± 0.07	2.6.1	0.25 ± 0.04
1.6.2	0.78 ± 0.07	2.6.2	0.23 ± 0.04
1.7.1	0.84 ± 0.07	2.7.1	0.24 ± 0.04
1.7.2	0.82 ± 0.07	2.7.2	0.22 ± 0.04
1.8.1	0.88 ± 0.06	2.8.1	0.25 ± 0.04
1.8.2	0.86 ± 0.07	2.8.2	0.23 ± 0.04
		2.9.1	0.26 ± 0.04
		2.9.2	0.23 ± 0.04
		2.10.1	0.27 ± 0.04
		2.10.2	0.24 ± 0.04
		2.11.1	0.29 ± 0.05
		2.11.2	0.25 ± 0.04
		2.12.1	0.29 ± 0.04
		2.12.2	0.25 ± 0.04
Max	0.89 ± 0.06	Max	0.29 ± 0.05

Table 7.7: The detailed occupancy values for the two-photon QED background split into their individual contributions for each sensor.

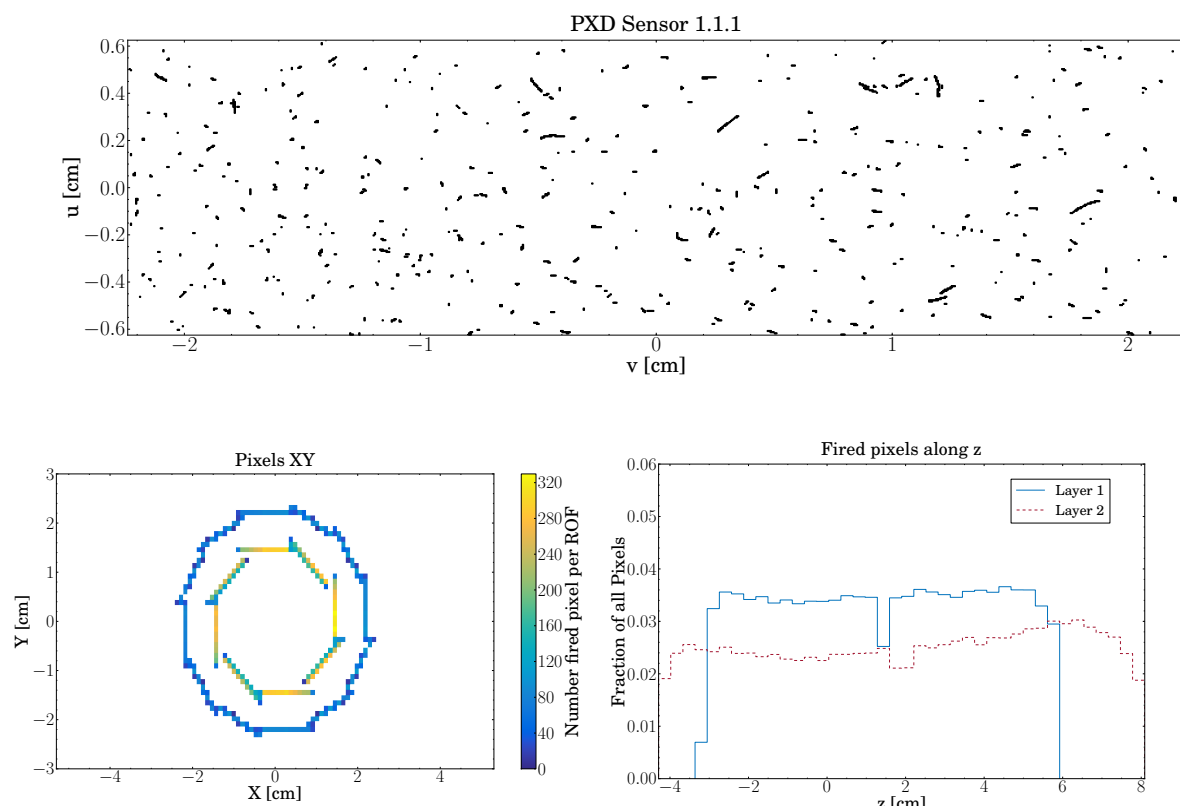


Figure 7.65: The fired pixels from the two-photon QED background. The top plot presents the content for one ROF of sensor 1.1.1. The bottom left plot shows the xy -projection with the typical $1/r^2$ dependence between the inner and the outer layer. The distribution of the fired pixels along z in the bottom right plot is fairly flat. The non-sensitive gaps of the glue are visible.

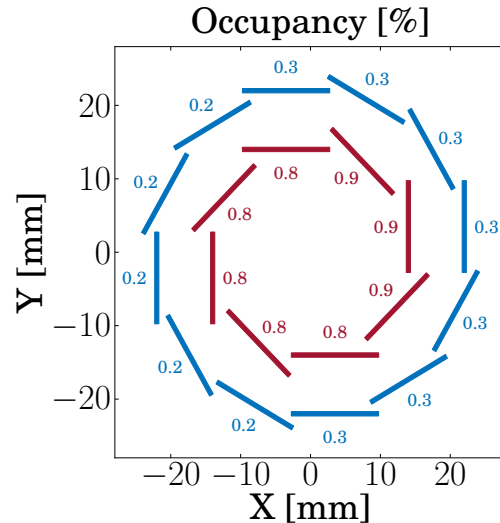


Figure 7.66: Summary of the PXD occupancy values for the two-photon QED background.

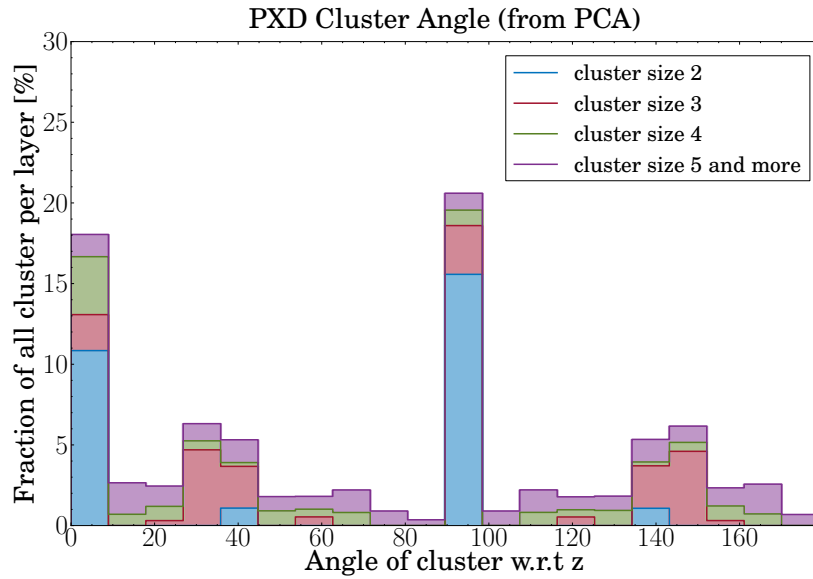


Figure 7.67: Cluster angle distribution for the two-photon process. The plot differentiates the different cluster sizes by colours and stacks them to provide an overall distribution of the cluster angle. Starting with the cluster size 2 (blue), there are only four possible pixel arrangements with respect to the global z -axis: parallel (0°), perpendicular (90°), diagonal “upward” (45°) and diagonal “downward” (135°).

7.6 Summary of all PXD backgrounds

This section summarises the results of all figures of merit for all backgrounds presented in the previous sections.

7.6.1 Particle flux

Figure 7.68 shows the particle flux for electrons and positrons in the first layer of the PXD for each background separately and the total particle flux. The dominating source of particles in the PXD arises from the two-photon BDK background, centring around the IP. The bump in the forward direction is the result of backscattered particles and is thus an effect of the beampipe, while the non-sensitive glue between the two sensors is visible as a gap. Overall, the particle flux is fairly constant along the z -axis with an average of 6.1 MHz cm^{-2} .

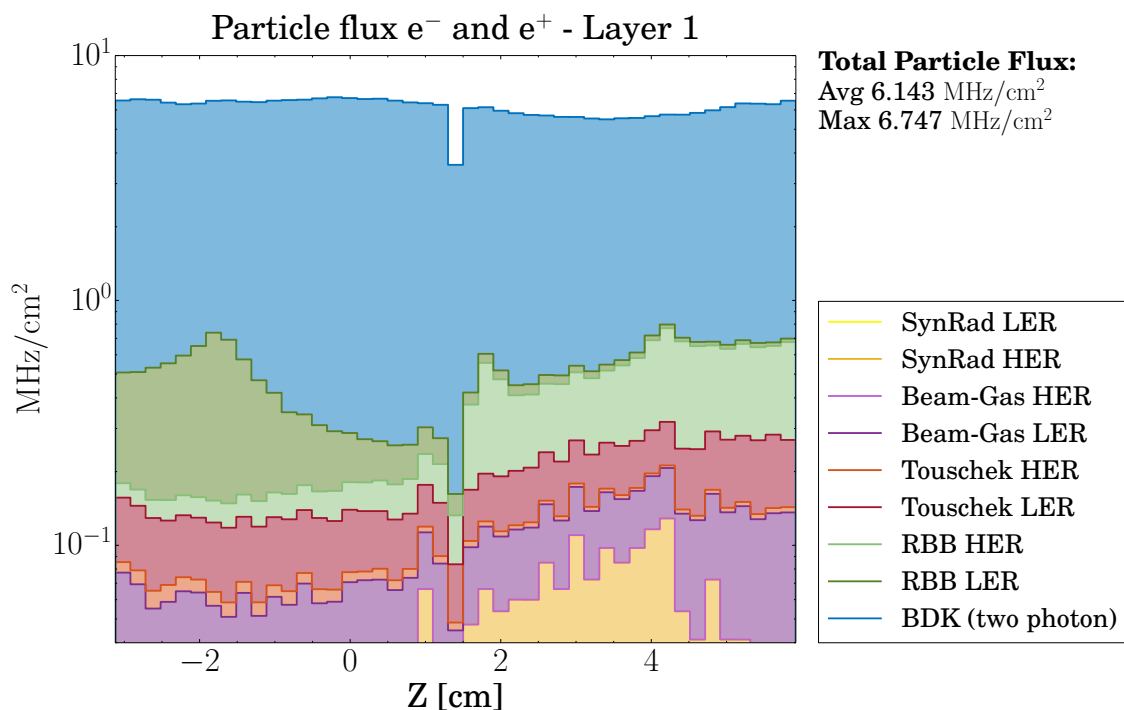


Figure 7.68: Stack plot of the particle flux for electrons and positrons in the inner layer of the PXD, split into the contributions from each background type. The average particle flux is 6.1 MHz cm^{-2} .

The second layer (figure 7.69) shows a similar distribution, with the centre less pronounced. Again, the particle flux is found to be constant along z , exposing the sensors to a flux of 2.5 MHz cm^{-2} on average.

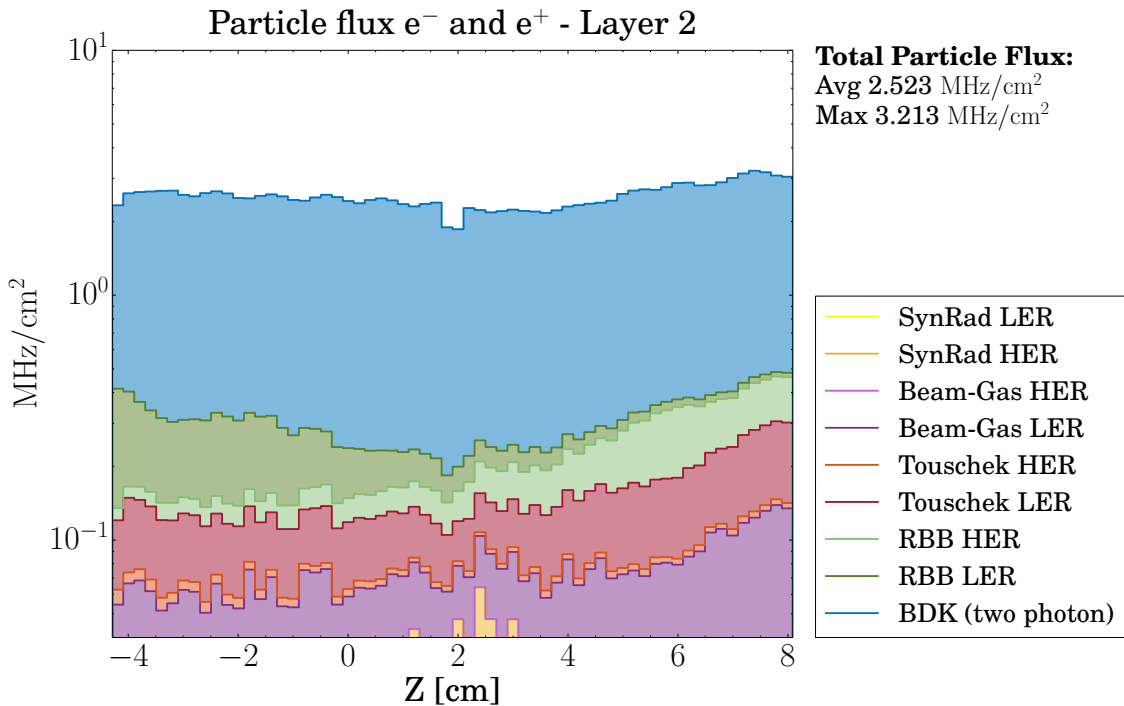


Figure 7.69: Stack plot of the particle flux for electrons and positrons in the outer layer of the PXD, split into the contributions from each background type. The average particle flux is 2.5 MHz cm^{-2} .

In order to evaluate the damage caused by traversing particles to the sensor, the hardware developers are interested in the expected energy distribution of the particles. The typical energy for electrons and positrons is found to be 4 MeV for the inner layer and 6 MeV for the outer layer as figure 7.70 illustrates. The prominent peak at 200 keV originates from delta electrons [271] produced inside the silicon material of the PXD sensor. In total, $6.08 \cdot 10^{13}$ electrons and positrons are expected to traverse the inner layer per cm^2 during one snowmass year¹¹. The outer layer is exposed to about half of the inner layer's particle flux with $2.33 \cdot 10^{13}$ electrons and positrons per cm^2 and snowmass year. While the particle flux for electrons and positrons is dominated by the two-photon background, the majority of the flux for photons emerges, as expected, from synchrotron radiation. The first layer of the PXD shows a photon peak around 4 cm, as shown in figure 7.71, with a maximum particle flux of roughly 117 MHz cm^{-2} . For the second layer (figure 7.71) the peak is broader and located at 2.5 cm, with a maximum particle flux of 42 MHz cm^{-2} .

The energy of the traversing photons is drawn in figure 7.72. The typical energy for photons reaching the PXD sensors is 50 keV. It should be noted that photons above 20 keV do not interact with the PXD sensor. In total, $4.27 \cdot 10^{14}$ photons cross the inner layer and $1.57 \cdot 10^{14}$ the outer layer of the PXD per cm^2 during one snowmass year.

¹¹1 snowmass year = 10^7 s

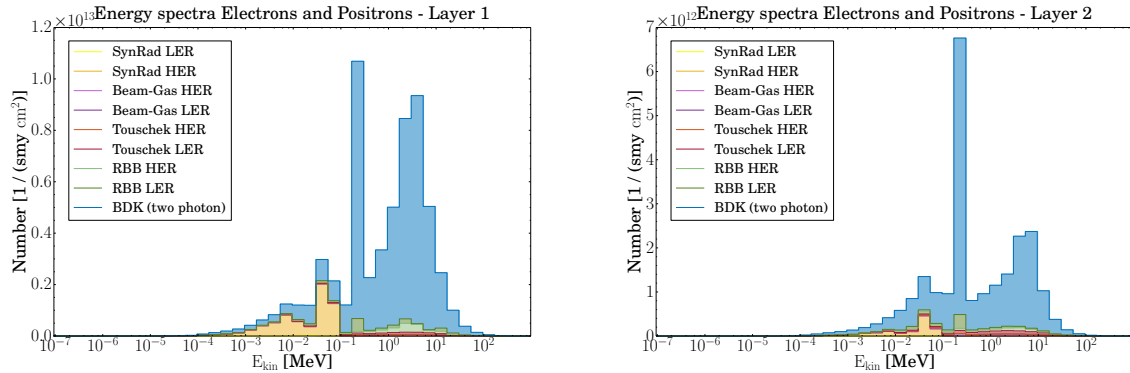


Figure 7.70: Energy spectra of the electrons and positrons traversing the inner (left) and outer (right) layer of the PXD. The typical energy is 4 MeV for the inner layer and 6 MeV for the outer layer. The peak at 200 keV originates from delta electrons. $6.08 \cdot 10^{13}$ electrons and positrons are expected to traverse the inner layer and $2.33 \cdot 10^{13}$ electrons and positrons the outer layer per cm^2 and snowmass year.

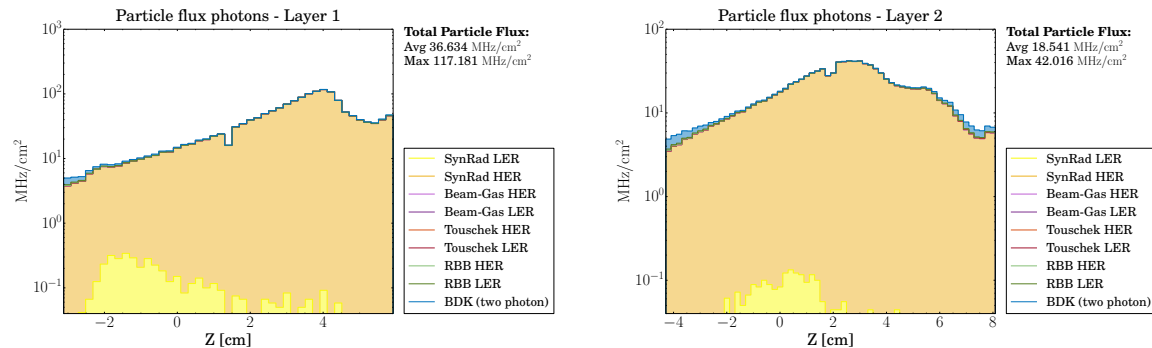


Figure 7.71: Stack plot of the particle flux for photons in the inner (left) and outer (right) layer of the PXD, split into the contributions from each background type.

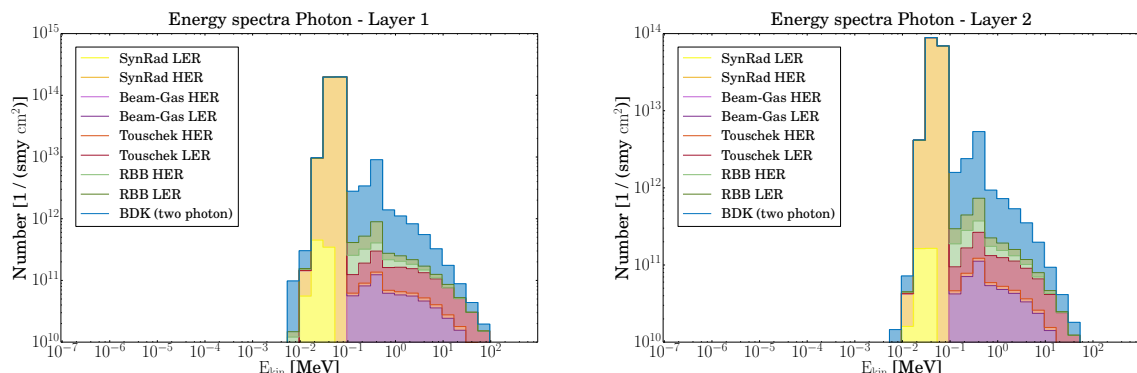


Figure 7.72: Energy spectra of the photons traversing the inner (left) and outer (right) layer of the PXD. The typical energy is 50 keV. $4.27 \cdot 10^{14}$ photons cross the inner layer and $1.57 \cdot 10^{14}$ the outer layer of the PXD per cm^2 during one snowmass year.

7.6.2 Origin of particles

The plot in figure 7.73 shows a z - x scatter plot of the origin for all electrons and positrons traversing the PXD. The different background types are indicated by different colours. As the plot shows, the majority of particles are created within a region of 150 cm in z around the IP, meaning that the PXD is only sensitive to the design of the inner part of the interaction region. This is a result of its small size and its proximity to the IP as the inner quadrupole magnets, heavy metal shields and the Belle II support structure shield the PXD from background created further up- or downstream. From figure 7.73 it can also be seen that the origin for each background type is different and shows a unique pattern. In the following the origin of all particles and the production vertices for the secondary particles is investigated.

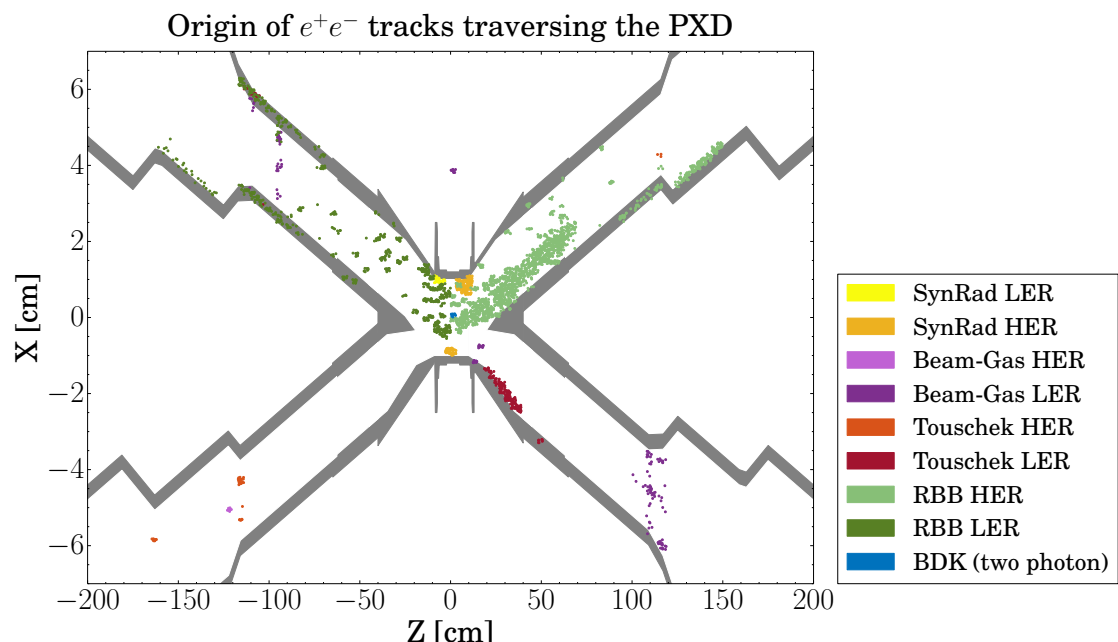


Figure 7.73: Distribution of the origin of all particles that either hit the PXD sensors directly or created a particle that hit the sensors. The HER (LER) beam travels from the bottom left (right) corner to the top right (left) corner.

7.6.3 Occupancy

Plotting the occupancy value in a stacked polar plot, where each arc segment represents the azimuthal angle range a single ladder covers, results in figure 7.74. The left plot shows a summary of the occupancy of the PXD for the inner PXD layer, while the right plot shows the occupancy for the outer layer. Both plots use the radius to indicate the occupancy for values up to 1%.

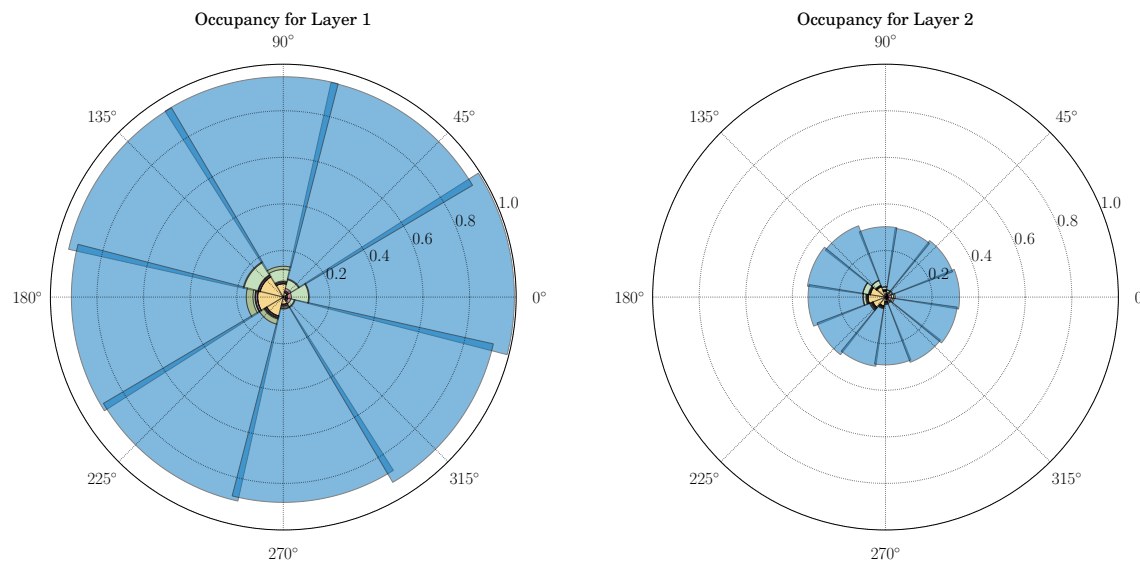


Figure 7.74: Summary of the PXD occupancy values in % for the inner layer (left) and the outer layer (right). The contributions of Touschek (red), two-photon (blue), radiative Bhabha (green) and synchrotron radiation (yellow) can be seen. The radius represents the occupancy while each arc segment represents the azimuthal angle range a single ladder covers.

From the plots it is obvious that the two-photon background is, by far, the dominant background. The second most important background depends on the azimuthal angle. For the region around 0° it is the radiative Bhabha scattering background originating from the HER, while for the region around 180° it is the HER synchrotron radiation. Overall, the occupancy is distributed quite evenly for the whole azimuthal angle range. The occupancy is close to, but still smaller than 1 % for the inner layer of the PXD and smaller than 0.4 % for the outer layer of the PXD. A more pessimistic summary for the expected occupancy of the PXD is given in table 7.8. Instead of using the average of the occupancy values over all ladders, the maximum occupancy value is listed in the table. In summary, the two-photon background is more than 5 times larger than the synchrotron radiation and radiative Bhabha backgrounds. The latter two backgrounds are very similar in size, whereas the Touschek and Beam-Gas backgrounds play only a minor role. The total expected occupancy for the PXD is

$$\text{inner layer : } 1.28 \pm 0.03\% \quad \text{outer layer : } 0.45 \pm 0.01\%$$

Although the expected occupancy value is well below the 3 % limit, the question arises whether this value has to be taken with a grain of salt. Since there is no experience with such a low emittance and high luminosity accelerator, a definite answer will have to wait for the Super-

KEKB commissioning detector¹² [272]. However, it is possible to look into a worst case scenario by assigning safety factors to each background. Those numbers are usually the results of experience and back-of-the-envelope calculations. The two-photon background is a pure QED background and the QED two-photon Monte Carlo generator is very well understood and has been verified in the previous chapter. Thus, a safety factor of 1 is assigned to the two-photon background. The radiative Bhabha background is a pure QED background too. The radiative Bhabha Monte Carlo generator is known to work very well for the energies at Belle II, gaining this background a safety factor of 1 as well. The synchrotron radiation background could be more severe, if the beampipe is misaligned and therefore the apertures cannot block the incoming photons efficiently. For a realistic misalignment of 0.5 mm recent studies[273, 274] show an increase in the number of photons traversing the PXD by a factor of ~ 2.5 . This value is used as the safety factor for the synchrotron radiation background. The amount of the accelerator dependent backgrounds Touschek and Beam-Gas can be larger as in the idealistic simulation due to de-tuned optics. However, even under the extremely pessimistic assumption of a safety factor of 10, both backgrounds are still very small compared to the dominating backgrounds. Applying the safety factors to each background and performing the calculation, the worst case occupancy calculates to 1.7 %. This value is close to the 2 % limit but is still almost a factor of 2 away from the hardware limit of 3 %. Therefore, the conclusion is drawn that the PXD is safe under the expected background at Belle II.

Background	Ring	Layer 1 [%]	Layer 2 [%]
Touschek	HER	$(1.2 \pm 0.4) \cdot 10^{-3}$	$(0.8 \pm 0.2) \cdot 10^{-3}$
	LER	$(17.8 \pm 6.8) \cdot 10^{-3}$	$(14.8 \pm 5.7) \cdot 10^{-3}$
Beam-Gas	HER	$(2.0 \pm 2.0) \cdot 10^{-6}$	$(2.0 \pm 2.0) \cdot 10^{-5}$
	LER	$(9.1 \pm 5.0) \cdot 10^{-3}$	$(5.4 \pm 2.7) \cdot 10^{-3}$
Radiative Bhabha	HER	0.14 ± 0.02	0.04 ± 0.01
	LER	0.06 ± 0.01	0.01 ± 0.01
Two-photon		0.89 ± 0.06	0.29 ± 0.05
Synchrotron radiation	HER	0.17 ± 0.02	0.09 ± 0.01
	LER	$(2.2 \pm 0.3) \cdot 10^{-3}$	$(1.9 \pm 1.1) \cdot 10^{-3}$
Total		1.28 ± 0.03	0.45 ± 0.01

Table 7.8: The maximum occupancy values for each background and PXD layer.

¹²also known as BEAST II in the Belle II collaboration

7.6.4 Cluster analysis

Plotting the distribution of cluster sizes for each background results in figure 7.75. The content is normalised such that the fraction for a specific cluster size can be read from the y -axis. For all backgrounds except synchrotron radiation, the cluster size distribution is very similar. About 30 % of all clusters are made from 2 pixels, followed by 3 pixel clusters (around 20 %) and equal amounts of 4 and 1 pixel clusters (10 %). On the other hand, synchrotron radiation is dominated by 1 pixel clusters, with 64 % of the synchrotron radiation clusters being single pixel clusters in the inner layer and 50 % in the outer layer. Only 27 % of all clusters in the inner layer consist of 2 pixels (31 % in the outer layer). The reason for the domination of single pixel clusters is due to the way in which photons deposit energy in silicon. Unlike charged particles that deposit energy along their travel path through the PXD sensors, photons deposit their full energy via the photo-electric effect at a single spot. This leads to a single pixel being fired, unless of course, the spot happens to be located near a pixel-pixel boundary. Charge sharing between neighbouring pixels can then result in larger clusters. However, this effect is very localised as can be seen in figure 7.75. There are no synchrotron radiation induced clusters beyond 4 pixels.

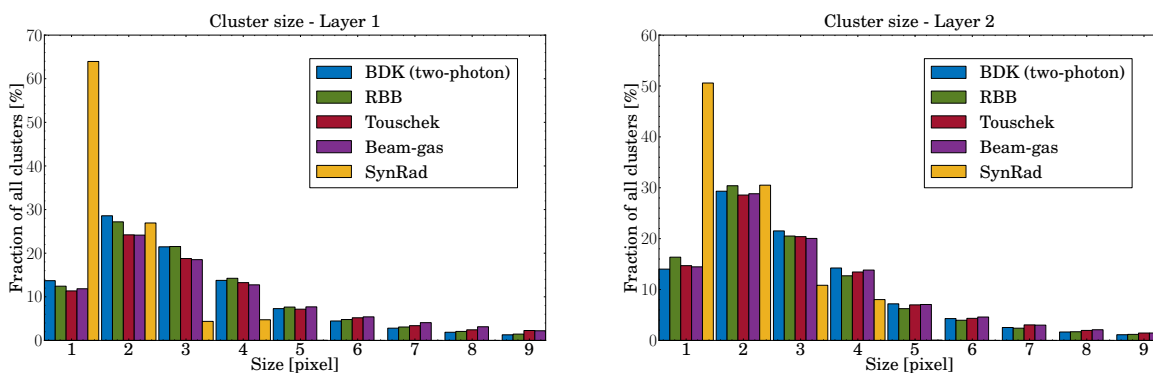


Figure 7.75: The cluster size (number of pixels per cluster) for the various backgrounds. The left plot shows the clusters for the inner layer of the PXD and the right plot for the outer layer.

The distribution of the cluster lengths for all clusters containing 2 or more pixels is shown in figure 7.76. Although it resembles the main features of the cluster size distribution of figure 7.75, it shows additional details that cannot be seen in the cluster size plots. In the left plot, representing the inner layer, two peaks are noticeable. One for two-photon clusters with a length of about 120 μm and one for radiative Bhabha clusters with a length of about 160 μm . This can be explained by the fact that both backgrounds are comprised of a large number of clusters with a low pixel count. Because the radiative Bhabha background is confined to the forward and backward parts of the PXD, it covers mostly the outside areas of a PXD ladder where the large pixel size is present, leading to longer clusters¹³. The two-photon background, on the other

¹³the term “pixel size” as it is used in this section refers to the length of the pixel edge that is parallel to the long edge of a PXD ladder, as the other pixel edge is constant and 50 μm for all pixels.

hand, is evenly spread across the PXD ladder, picking up small as well as larger pixel sizes. On average this results in smaller cluster lengths, compared to the radiative Bhabha background. The Touschek and Beam-Gas backgrounds become more prominent for clusters with a length of 240 μm and above. Having two different pixel sizes per ladder means that for clusters containing 2 or 3 pixels only a small number of possible cluster lengths exists. This “quantisation” effect becomes more prominent in the outer layer of the PXD where the difference between the small and large pixel size is greater compared to the inner layer. This can be seen in the right plot of figure 7.76, where the cluster length of 160 μm is suppressed. For example, there are only two possibilities for 2-pixel clusters to make it into this bin of the histogram: either by consisting of two large pixels ($=170 \mu\text{m}$) or containing a small and a large pixel ($=155 \mu\text{m}$). The latter option is quite unlikely, though.

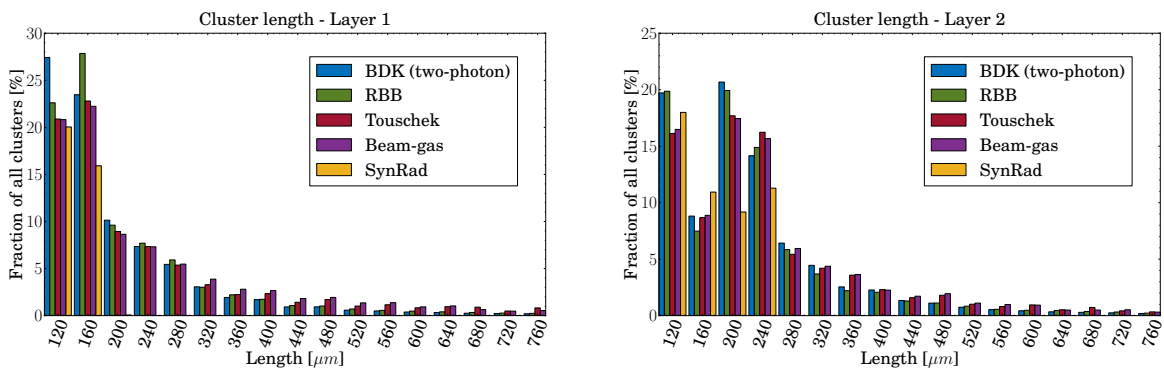


Figure 7.76: The cluster length in μm for clusters with 2 or more pixels. The left plot shows the cluster lengths for the inner layer of the PXD, the right plot for the outer layer.

7.6.5 Radiation dose

The expected radiation dose is drawn in figure 7.77 for the inner and outer layer of the PXD. As expected, the dominating contribution arises from the two-photon background, while the second largest contribution is the radiative Bhabha scattering. The radiation dose along the global z -axis is fairly flat for the inner layer and has only a moderate asymmetry in the outer layer. Reading the average radiation dose from the plots, the inner layer is expected to be exposed to 19.9 kGy/smy and the outer layer to 4.9 kGy/smy. Irradiation tests of DEPFET sensors, similar to those being used in the PXD, were conducted with 10 MeV electrons for a dose up to 100.0 kGy [275]. The sensors were found to work properly after the irradiation and it is believed that they can cope with up to 200.0 kGy. Using the numbers obtained from the simulation, this translates to a lifetime of roughly 10 years for the PXD sensors, the typical operation time of a high energy physics detector.

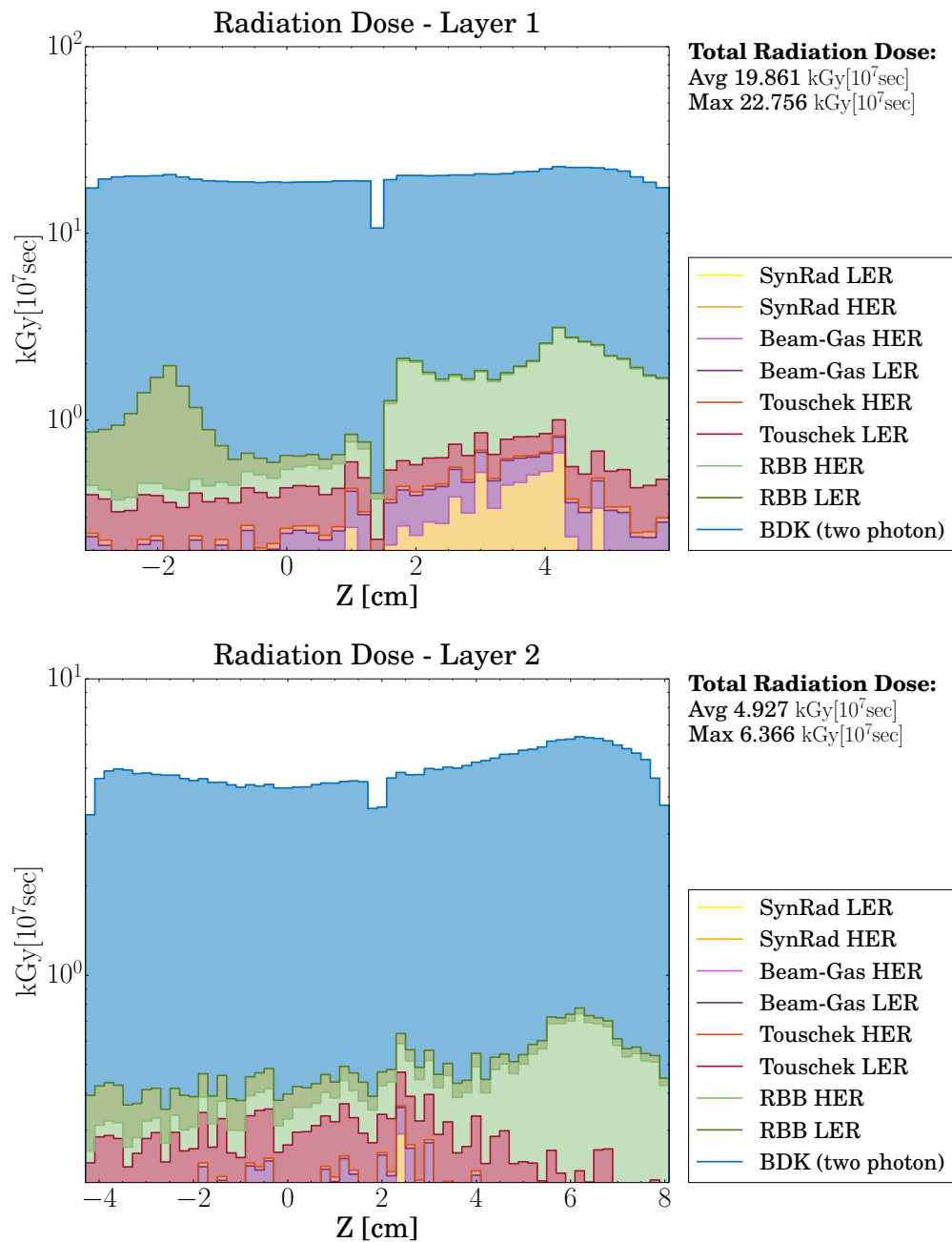


Figure 7.77: Stack plot of the expected radiation dose for the inner layer (top) and outer layer (bottom) of the PXD with respect to the global z -axis. The dominating background is the two-photon process with the average dose 19.9 kGy/smy (layer 1) and 4.9 kGy/smy (layer 2).

7.6.6 Neutron flux

Plotting the energy spectra of the neutrons traversing the inner and outer layer of the PXD results in figure 7.78. The distributions peak at around 100 keV for both layers, with a long tail towards lower energies, covering the intermediate to low temperature range of neutrons. The y -axis shows the number of neutrons normalised to one snowmass year, with a total number of $5.98 \cdot 10^{10}$ neutrons passing through 1 cm^2 of the inner layer and $6.08 \cdot 10^{10}$ of the outer layer of the PXD. The majority of neutrons originate from the radiative Bhabha background through the creation of giant dipole resonances (see section 7.5.1). The two-photon background, usually being the dominating background, is only the second largest source for neutrons.

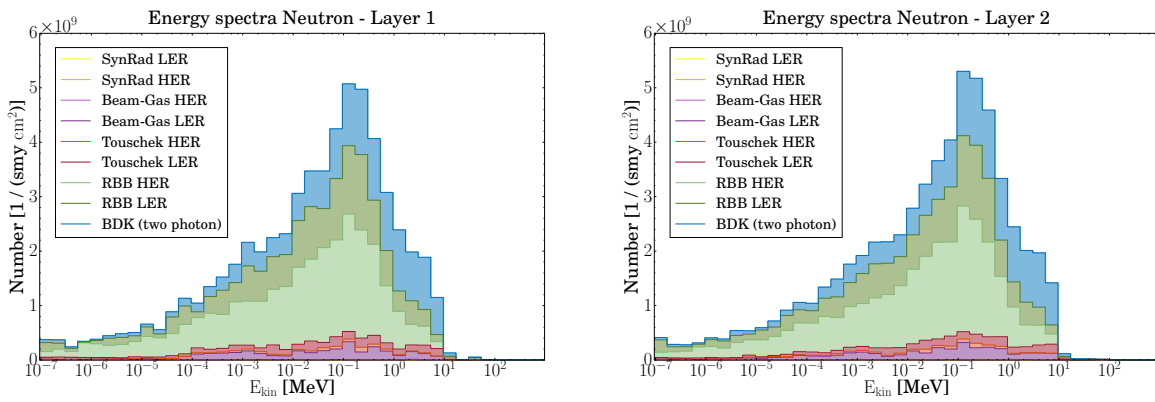


Figure 7.78: Energy distribution of the neutrons traversing the inner layer (left plot) and outer layer (right plot) of the PXD. The dominating source for neutrons is the radiative Bhabha background, followed by the two-photon background.

Multiplying each bin of the energy spectrum with the associated D value, the NIEL folded energy spectra is obtained (figure 7.79). The D value is estimated using spline interpolation and a look up table taken from [236].

Plotting the fluence rate for the PXD sensors with respect to the global z -axis (figure 7.80) reveals an increased rate by about a factor of 3 for the very forward and very backward regions of the sensor compared to its centre area. Those increased rates are the result of the shielding materials in front and behind the PXD. The fluence rate is constant across the centre of the sensors, with a slight rise for the forward areas in the outer layer. Overall, the neutron rate is very small and its damage to the PXD can be neglected [276].

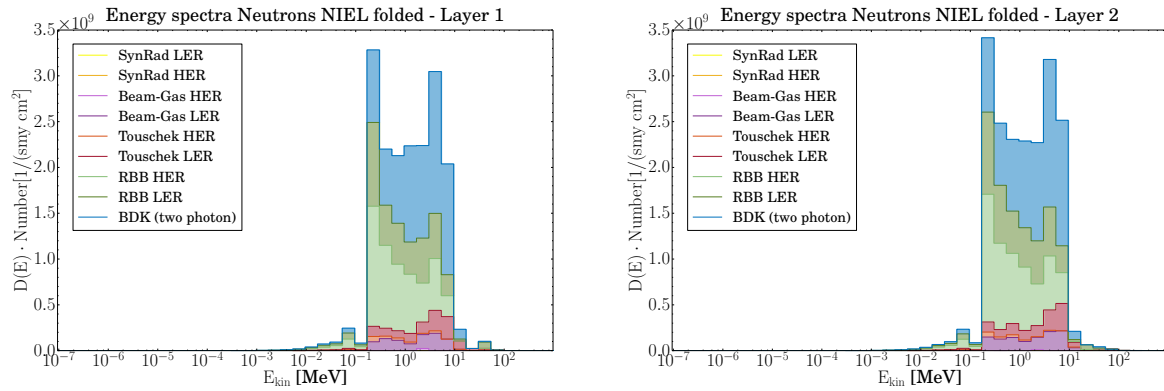


Figure 7.79: NIEL folded energy distribution of the neutrons traversing the inner layer (left plot) and outer layer (right plot) of the PXD.

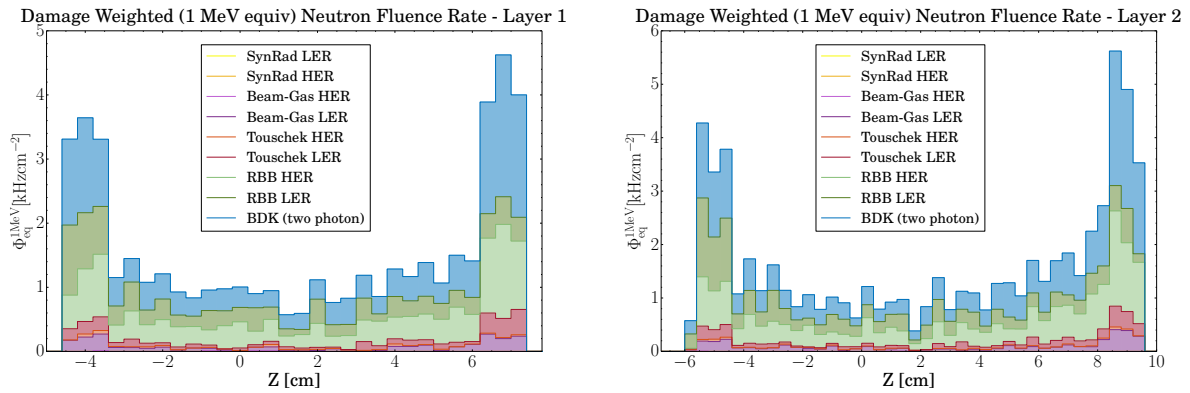


Figure 7.80: NIEL folded fluence rate. The distribution is the result of weighting each particle with the D value using the particle's kinetic energy.

7.7 Background merging for physics events

Having established the tools to generate and simulate the various background components, the question arises how the simulated background data can be fed back into the simulation of processes relevant for physics analyses. This is an important step as it ensures that the Monte Carlo simulation resembles the data recorded at the Belle II detector as closely as possible. At the predecessor experiment of Belle II, Belle, special random-trigger background runs were taken and for each run all hits in the sub-detectors were recorded. During the Monte Carlo simulation of a physics process, those hits were added after the Geant3 simulation and before the track, photon etc. reconstruction. For Belle II a similar approach is employed. As there is no measured background data available for Belle II yet, the background mixing scheme relies solely on Monte Carlo data. Figure 7.81 illustrates an overview of the background mixing scheme.

It starts with the production of the background. Each background component is generated and

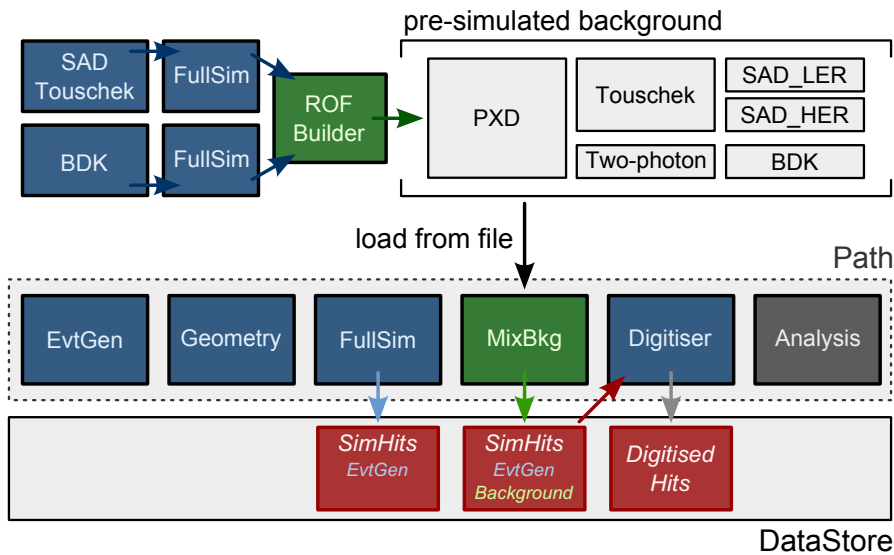


Figure 7.81: The background mixing scheme for basf2. The background is generated and simulated for each detector and component separately. The result is merged into sub-detector ROFs and stored into files, using the hierarchy sub-detector → component → generator. The background is then mixed with the physics process using the MixBkg module. In this example the physics process is generated using EvtGen [179].

simulated separately, following the procedures described in this chapter. In order to account for different readout times of the sub-detectors and the readout-time aware SAD background generators, the background simulation is performed for each sub-detector individually. The result is a dataset of SimHits for a specific sub-detector and background component. This implies to store the SimHits according to the following hierarchy:

sub-detector → component → generator

For the PXD this results in:

PXD → Touschek → SAD_LER
 PXD → Touschek → SAD_HER
 PXD → TwoPhoton → BDK
 PXD → ...

A special process called **ROF building** takes the SimHits of a specified sub-detector and generator and merges them into readout frames (**ROF**), where one ROF represents one readout cycle of the sub-detector. The ROFs are stored in a ROOT file together with information indicating for which sub-detector the specific background component was produced and which generator delivered the data. This results in self-describing background files, respecting the hierarchy above.

They can easily be shared and accessed in the next step, the **background mixing**. The mixing of the background with a physics process is implemented in a single basf2 module, which has to be placed between the Geant4 FullSim module and the digitisation modules. This makes sure the digitisation is applied to both the hits from the physics process and the background hits at the same time. Although this background mixing approach cannot be used for background data taken at the Belle II experiment later, it delivers, for the moment, the most correct results for Monte Carlo-based backgrounds. It incorporates, for example, the effect of pixels in the PXD that are hit by both the physics process and the background, where each contribution separately would be below the digitisation threshold. Together, however, they are above the threshold and, thus, represent a fired pixel. The input for the background mixing module are the background files produced in the ROF building stage. Since they follow the hierarchy above and are self describing, specifying the requested input files in the basf2 mixing module is enough to load their content. Inside the mixing module the content is managed in the same hierarchy scheme as above, allowing one to turn on and off specific sub-detectors and background components in order to study their effect. It should be noted that the background mixing scheme described here is optimised for the PXD. It does not incorporate features such as timing and randomisation yet, which are important for other sub-detectors, particularly the SVD and CDC. However, an implementation of those features is under development.

7.8 Concluding remarks on the PXD backgrounds

This chapter was devoted to a detailed study of the expected background types at Belle II and their contribution to the PXD background. There are two types of background present at SuperKEKB: beam-induced backgrounds and luminosity-dependent backgrounds. While the first background originates from the accelerator itself and can be tuned to some degree, the latter is irreducible. The beam-induced backgrounds presented in this chapter are the Touschek effect, Beam-Gas scattering and synchrotron radiation. Due to the new concept of a high-luminosity nano-beam lepton collider, the amount of background produced by SuperKEKB is not yet measured and has to be simulated using Monte Carlo techniques at the time being. For the Touschek and Beam-Gas background the SAD simulation tool is used, while the synchrotron radiation is simulated using software that has been developed specifically for the studies presented in this chapter. The luminosity-dependent backgrounds are comprised of radiative Bhabha scattering and the two-photon background. The simulation of the radiative Bhabha scattering is a combination of the BBBREM Monte Carlo generator and SAD. For the two-photon background the BDK generator is used. All backgrounds are then fed into the full Belle II detector simulation, followed by a detailed simulation of the PXD response. It is found that the dominant background is the two-photon QED process accounting for almost 70 % of the total PXD background. The second largest background is synchrotron radiation, closely followed by radiative Bhabha scattering.

By counting the number of electrons and positrons that traverse the PXD sensors the particle fluxes are estimated. On average the inner layer experiences a particle flux of 6.1 MHz cm^{-2} and the outer layer of 2.5 MHz cm^{-2} . The distribution of the particle flux along the global z -axis is fairly flat, meaning that the radiation damage is evenly distributed along the PXD ladders, a scenario favoured by the hardware developers. Of similar interest is the expected radiation dose. The simulation shows that the inner layer of the PXD is exposed to 19.9 kGy/smy and the outer layer to 4.9 kGy/smy . Irradiation tests of DEPFET sensors with 10 MeV electrons showed that the sensors work reliably for a dose of at least 100 kGy. It is believed that they can even cope with up to 200 kGy. Using the radiation dose values obtained from the simulation, the numbers translate to a lifetime of roughly 10 years for the PXD sensors, the typical operation time of a high energy physics detector.

The most important figure of merit, though, is the occupancy. It is defined as the number of pixels fired within one read out frame divided by the total number of pixels of the PXD. The occupancy values obtained from the simulation are

$$\text{inner layer : } 1.28 \pm 0.03\% \quad \text{outer layer : } 0.45 \pm 0.01\%$$

The upper limit for the PXD, imposed by the data acquisition and the track reconstruction is 3 %. The estimated values are below the limit and, thus, the PXD will withstand the harsh background conditions that are expected at Belle II.

8 Conclusion and Outlook

This thesis revolves around the Belle II experiment, the successor of the highly successful Belle experiment at the KEKB electron-positron collider in Tsukuba, Japan. The KEKB collider sees major upgrades in order to increase the luminosity by a factor 40, leading to an unprecedented luminosity of $8 \times 10^{35} \text{ cm}^{-2} \text{ s}^{-1}$. During the upgrade, scheduled to be finished by 2017, the KEKB accelerator will become the SuperKEKB accelerator, with the asymmetric beam energies of 7 GeV (e^-) and 4 GeV (e^+). The rich physics program offered by the collider focuses on the measurement of CP -violation and will search for Physics beyond the Standard Model. SuperKEKB is going to produce particle beams with a vertical size of only 48 nm, a size that has never been reached at any particle collider before. This leads to a largely increased background rate, making the upgrade from the Belle detector to the Belle II detector necessary. Additionally the upgrade aims to increase the physics performance of the detector, making it more sensitive to the effects of New Physics. Belle II will see improvements and redesigns of almost all sub-detectors as well as the inclusion of a whole new sub-detector, the Pixel Vertex Detector (PXD). The introduction of the PXD will make sure that decay vertices are reconstructed with an extremely high precision in the harsh background conditions at Belle II. The PXD is a semi-conductor based particle tracking detector and the innermost detector of Belle II. It offers excellent track and vertex reconstruction capabilities, while having a sensor thickness of only 75 μm in order to minimise multiple scattering effects.

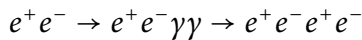
Due to the innovative concept of a high-luminosity nano-beam accelerator, the scale of background being produced at the future SuperKEKB cannot be derived from a traditional electron-positron collider, and has therefore to be simulated using first-principle Monte Carlo techniques. This thesis focused on a detailed study of the expected background for the pixel vertex detector at the upcoming Belle II experiment. For the Belle II experiment a new software framework, basf2, has been developed. The development of basf2 was initiated by the author of this thesis. It is a crucial element of the Belle II experiment as it will be used for the whole of the data processing. The data taken by the various sub-detectors is sent to a computing farm where it is decided whether the data contains interesting physics and should therefore be stored on disk. This decision process requires an analysis of the data in real-time and is performed using the Belle II software framework. The same software framework is then used to read the stored data, reconstruct the collision and is employed by the user to perform the final physics analysis. In order to be able to handle the vast amount of data in real-time, the software framework basf2 makes use of multi-core systems by having an advanced parallel processing mechanism built-

in. On the other hand, basf2 is also designed to be user-friendly in order to allow physicists to concentrate on their analysis rather than on the software. As an example for the application of a full event generation, simulation, reconstruction and analysis chain the intrinsic detector resolution of the PXD was estimated from an impact parameter resolution study using basf2. The result for *muons* with a p_t in the range of 2.5 GeV to 3 GeV is

$$\begin{aligned}\sigma_{int}(d_0) &= (10.3 \pm 0.1) \mu\text{m} \\ \sigma_{int}(z_0) &= (12.9 \pm 0.1) \mu\text{m}\end{aligned}$$

The impact parameter resolution of Belle II improves by roughly a factor of two compared to Belle. Without the PXD, the resolution is comparable to the one at Belle (d_0) or even worse (z_0). This proves that the PXD is crucial for achieving an excellent impact parameter resolution and that the PXD is essential for the precise reconstruction of vertices and, in turn, the precise measurement of the time-dependent asymmetry of the B-meson decay rate.

The dominating background for the PXD is the two-photon QED process



as this process has a very large cross-section (especially at low values of p_t) and dominates all other production processes found at SuperKEKB. Almost all outgoing particles carry a very low transverse momentum which confines them to the innermost region around the IP. Hence this process is almost exclusively observed as a background by the PXD and does not play a role for the other sub-detectors. Being the dominant background, the Monte Carlo generators used to produce two-photon events require a thorough investigation of their reliability. This is particularly true for Belle II as the Monte Carlo generators at hand have been developed for and tested at $e^+ e^-$ colliders running at a much higher centre-of-mass energy, such as LEP. It is found that the difference between the two-photon Monte Carlo generators BDK and KoralW in the high cross-section, low p_t (smaller than 20 MeV) for the produced electron and positron, and thus most relevant range for the PXD is very small. Both Monte Carlo generators agree with the experiment in this important low momentum regime. Therefore they qualify to be used for the PXD background studies. However, the question arises as to whether the delivered cross-section of the Monte Carlo generators is correct over an intermediate phase space. This calls for a comparison between recorded detector data and Monte Carlo data, an analysis that has never been done for centre-of-mass energies of the order of those of the Belle and Belle II experiments. For this purpose an experiment was conducted at Belle specifically for this thesis in 2010, shortly before the KEKB accelerator and the Belle detector were shut down. The author of this thesis was involved in the planning and preparation (e.g. DAQ histograms, triggers) of the experiments and took the data during his detector shifts. A random trigger setup has been used to record events that would otherwise have been missed with the standard Belle trigger

configuration. By analysing the number of hits in the SVD for different luminosity settings, the contribution of two-photon QED events to the total number of SVD hits were estimated and compared to the Monte Carlo prediction. It was found that the Monte Carlo generators agree with the recorded data. While this analysis focused on the dominating low p_t region of the two-photon process, the second analysis dealt with the high p_t region. It aimed at fully reconstructing two-photon events and on producing a “clean” data sample from the recorded data. The normalisation between Monte Carlo and measured data was accomplished with the help of Bhabha events. A two-photon event reconstruction chain was developed and applied to the recorded data as well as the Monte Carlo data produced by BDK and KoralW. In order to be able to reconstruct “clean” events, the analysis focused on no-tag events with transverse particle momenta larger than 320 MeV. From the recorded data

$$N_{exp} (\text{Exp73}) = 24$$

events are reconstructed as two-photon events. The predicted number of events from the BDK and KoralW generator are

$$N_{exp} (\text{BDK}) = 33.8 \pm 3.2$$

$$N_{exp} (\text{KoralW}) = 793.4 \pm 99.9$$

This results in a 3.1σ agreement between BDK and the data, while KoralW is consistent within 7.7σ with the data. The conclusion is drawn that both Monte Carlo generators agree very nicely for low values of p_t but differ significantly for larger values. The recorded data proved that for larger p_t the behaviour of BDK is correct. Since the cross-section peaks strongly for low values of p_t both generators can be used for further background studies. Due to performance advantages of BDK and possible contributions from back-scattered particles originating from high p_t tracks, KoralW was not used for the generation of the two-photon background.

There are two types of background present at SuperKEKB: beam-induced backgrounds and luminosity-dependent backgrounds. The beam-induced processes originate from the accelerator due to residual gas in the beampipe, bending magnets or interactions of particles within a single bunch, whereas luminosity-dependent processes comprise normal QED processes, such as Bhabha scattering or two-photon processes. The expected amount of background produced by SuperKEKB has not yet been measured and Monte Carlo techniques had again to be employed to simulate the various background contributions. Among the tools that were used are the SAD accelerator simulation, BBBREM radiative Bhabha generator, BDK and a synchrotron radiation simulation that has been developed by the author of this thesis. All backgrounds are subject to a full Belle II detector simulation, followed by a detailed simulation of the PXD response. It is found that the dominant background is the two-photon QED process accounting

for almost 70 % of the total PXD background. The second largest background is synchrotron radiation, closely followed by radiative Bhabha scattering. In contrast to the other background types the two-photon background is irreducible, though, as there is no way to increase or add additional shielding material, adjust the radii of apertures or tune the accelerator magnet lattice in order to protect the PXD from this background. Hence, the two-photon background is the most severe background for the PXD.

The thesis finished with a detailed study of various figures of merit, such as particle flux, radiation dose and occupancy. On average the inner layer experiences a particle flux of 6.1 MHz cm^{-2} and the outer layer of 2.5 MHz cm^{-2} . The distribution of the particle flux along the global z -axis is fairly flat meaning that the radiation damage is evenly distributed along the PXD ladders, a scenario favoured by the hardware developers. The simulation showed that the inner layer of the PXD is exposed to a radiation dose of 19.9 kGy/smy^1 and the outer layer to a dose of 4.9 kGy/smy . Irradiation tests of DEPFET sensors with 10 MeV electrons showed that the sensors work reliably for a dose of at least 100 kGy. It is believed that they can even cope with up to 200 kGy. Using the radiation dose values obtained from the simulation, the numbers translate to a lifetime of roughly 10 years for the PXD sensors, the typical operation time of a high energy physics detector. The study revealed that the expected PXD occupancy from background events is

inner layer : $1.28 \pm 0.03\%$

outer layer : $0.45 \pm 0.01\%$

The upper limit for the PXD, imposed by the data acquisition and the track reconstruction is 3 %. The estimated values are below the limit and, thus, the PXD will withstand the harsh background conditions that are expected at Belle II.

This thesis is dedicated to the estimation of the expected background for the PXD at the SuperKEKB collider running at its nominal luminosity and under ideal conditions, such as vacuum levels, beam orbit and detector alignment. However, especially in the first phase of the experiment, the conditions will be less than ideal. The work presented in this thesis can be extended to cover those non-idealistic cases. Possible studies include de-tuned beam optics resulting in higher Touschek and synchrotron radiation background, lower vacuum levels giving rise to a higher contribution of Beam-Gas events or misaligned detector parts and beam-masks exposing the PXD sensors to a largely increased flux of photons from synchrotron radiation. In general the first operation phase of SuperKEKB will see a larger contribution from beam-induced backgrounds as the luminosity will be low and, in turn, the two-photon background might not be as severe. A first reference will be provided by the BEAST experiment², a detector being developed to measure the background levels during the first commissioning phase of SuperKEKB.

¹1 smy = 1 snowmass year = 10^7 s

²Beam Exorcism for A STable experiment

This offers another opportunity to continue the work done in this thesis. The expected background for the sensors of the BEAST experiment can be estimated using the tools and workflows developed in this thesis. As soon as measured beam-induced background data is available, it can be used in order to improve the Monte Carlo simulation of those background components. From a technical point of view, the basf2 software has seen major advances during the time this thesis was under completion. Recent background studies with the latest version of basf2 are in nice agreement with the results obtained in this thesis but it might be worthwhile to apply the latest improvements on pattern recognition, tracking, simulation and background mixing to the various studies presented in this work.

Appendix A

Tables and figures for the two-photon process measurement

A.1 Tables

No	θ (Lab frame)	θ (CMS frame)	$\sigma \cdot 10^9 [pb]$	$\sigma_{vis} \cdot 10^9 [pb]$	t per event [s]
1	(0.0°, 180.0°)	(0.0°, 180.0°)	7.22 ± 0.94	2.68 ± 0.35	147
2	(2.0°, 180.0°)	(3.02°, 180.0°)	7.22 ± 0.94	2.67 ± 0.35	146
3	(4.0°, 176.0°)	(6.04°, 177.35°)	4.49 ± 0.25	2.52 ± 0.14	116
4	(6.0°, 172.0°)	(9.06°, 174.7°)	3.89 ± 0.19	2.5 ± 0.12	109
4	(8.0°, 168.0°)	(12.07°, 172.04°)	3.48 ± 0.16	2.49 ± 0.12	104
5	(10.0°, 164.0°)	(15.07°, 169.38°)	3.21 ± 0.15	2.48 ± 0.12	100
6	(12.0°, 160.0°)	(18.06°, 166.69°)	2.98 ± 0.14	2.5 ± 0.12	96
7	(14.0°, 156.0°)	(21.04°, 163.99°)	2.75 ± 0.13	2.46 ± 0.11	94
8	(15.0°, 154.0°)	(22.52°, 162.63°)	2.66 ± 0.13	2.44 ± 0.12	93
9	(16.0°, 152.0°)	(23.99°, 161.27°)	2.62 ± 0.14	2.46 ± 0.13	92
10	(17.0°, 150.0°)	(25.47°, 159.89°)	2.55 ± 0.14	2.43 ± 0.13	92
11	(18.0°, 148.0°)	(26.94°, 158.52°)	2.50 ± 0.16	2.42 ± 0.15	90
12	(19.0°, 146.0°)	(28.4°, 157.13°)	2.42 ± 0.15	2.36 ± 0.14	90
13	(20.0°, 144.0°)	(29.86°, 155.74°)	2.3 ± 0.13	2.27 ± 0.12	91
14	(22.0°, 140.0°)	(32.76°, 152.93°)	2.22 ± 0.14	2.21 ± 0.14	93
15	(24.0°, 136.0°)	(35.64°, 150.07°)	2.09 ± 0.13	2.09 ± 0.13	96
16	(26.0°, 134.0°)	(38.49°, 148.63°)	1.97 ± 0.12	1.97 ± 0.12	98
17	(27.0°, 133.0°)	(39.9°, 147.91°)	1.93 ± 0.12	1.92 ± 0.12	99
18	(28.0°, 132.0°)	(41.31°, 147.18°)	1.88 ± 0.12	1.88 ± 0.12	100
19	(29.0°, 131.0°)	(42.71°, 146.45°)	1.84 ± 0.11	1.83 ± 0.11	101
20	(30.0°, 130.0°)	(44.11°, 145.72°)	1.79 ± 0.11	1.79 ± 0.11	103
21	(31.0°, 129.0°)	(45.5°, 144.98°)	1.75 ± 0.1	1.75 ± 0.1	103
22	(32.0°, 128.0°)	(46.88°, 144.24°)	1.71 ± 0.1	1.71 ± 0.1	104
23	(33.0°, 127.0°)	(48.26°, 143.49°)	1.67 ± 0.1	1.67 ± 0.1	105
24	(34.0°, 126.0°)	(49.62°, 142.75°)	1.63 ± 0.09	1.62 ± 0.09	106
25	(36.0°, 124.0°)	(52.33°, 141.25°)	1.53 ± 0.08	1.53 ± 0.08	109
26	(38.0°, 122.0°)	(55.01°, 139.73°)	1.46 ± 0.08	1.45 ± 0.08	111
27	(40.0°, 120.0°)	(57.65°, 138.19°)	1.38 ± 0.08	1.33 ± 0.08	115

Table A.1: *KoralW* polar angle configurations used for the σ_{vis} (*KoralW*) stability test. Listed are the polar angle cuts in the laboratory and the centre-of-mass system, the generator cross-section, the visible cross-section in the detector acceptance and the time it took to generate a single event within the detector acceptance.

Name	Fortran variable	Value
CMS total Energy [GeV]	CmsEne	10.58
Photon spectrum parameter	vvmin	10^{-6}
Max weight for reject	wtmax	$1.2 \cdot 10^9$
Min vis p_t^2 (GeV^2)	arbitr	0.0
Inv_{mass}^2 cut for $e^+ e^- \rightarrow \text{xx}$ [GeV^2]	arbitr1	0.0
Min theta with beam (0=no cut) [rad]	themin	0.0
Max p_t^2 of photons in $e^+ e^- \rightarrow \text{xx}$ [GeV^2]	arbitr2	0.0
Angle of $e^+ e^-$ with respect to the beam below which t-channel like bremsstrahlung is emulated	tAngMax	180.0 deg
Initial state radiation	KeyISR	on (=1)
Alpha/pi in yfs formfactor is kept	KeyNLL	on (=1)
Coulomb correction	KeyCul	on (=1)
IBA from the CKM matrix (PDG '96)	KeyBra	on (=2)
Weighted events	KeyWgt	off (=0)
RANMAR random number generator	KeyRnd	on (=1)
Second presampler for all 4fermion final states	KeySmp	on (=2)
EXTERNAL matrix element	Key4f	on (=1)
ZZ type final states	KeyZon	on (=1)
WW type final states	KeyWon	off (=0)
Decay mode τ^+	JAK1	off (=1)
Decay mode τ^-	JAK2	off (=1)
Bremsstrahlung in Tauola	ITDKRC	off (=0)
PHOTOS switch	IFPHOT	off (=0)
Hadronisation W^-	IFHADM	off (=0)
Hadronisation W^+	IFHADP	off (=0)

Table A.2: The settings for the KoralW Monte Carlo production

Description	Value	Unit
Beam energy in the centre-of-mass system	5.29	GeV
Momentum vector for e^- as a fraction of the beam energy	(0, 0, 1)	
Momentum vector for e^+ as a fraction of the beam energy	(0, 0, -1)	
Minimum invariant mass for a fermion pair	0.001	GeV
Minimum theta angle for the produced particles	0.0	degree
Maximum theta angle for the produced particles	180.0	degree

Table A.3: The settings for the BDK Monte Carlo production

Run	Start time	Run time [s]	Events	Barrel Bhabha	HadronC	Tau-Pair	Lumi deliv [pb ⁻¹]	Lumi accum [pb ⁻¹]	Avg Lumi (*10 ³)	fill
401	11:21:58	990.-9	502384	55660	96	5237	11.235	10.270	1133-789	19170
403	11:48:48	1029.-3	509040	45192	79	4184	9.089	8.280	883-045	19170
408	12:20:44	1036.-9	502680	35756	55	3267	7.192	6.670	693-569	19170
409	13:17:27	939.-9	443944	20840	51	1941	4.191	3.800	445-939	19170
411	16:32:32	512914	36752	62	3395	7.392	6.750	699-226	19171	
414	18:21:18	958.-1	485416	53314	75	5095	10.723	9.860	1119-222	19173
416	19:26:43	1026.-8	509021	46602	71	4524	9.373	8.500	912-814	19174
417	19:50:38	1041.-0	502004	34136	53	3284	6.866	6.270	659-526	19174
418	20:44:38	1077.7	510625	26608	50	2653	5.352	4.910	496-588	19174
419	21:49:32	667.-8	300234	0	0	0	0	0	0	19174
420	22:06:31	223.-5	100314	0	0	0	0	0	0	19174
421	23:16:04	838.-3	424769	46830	87	4297	9.419	8.570	1123-620	19175
422	23:32:21	879.-7	440175	46402	77	4372	9.333	8.450	1060-946	19175
424	23:51:06	880.-5	433893	40030	62	3786	8.051	7.280	914-413	19175
425	00:07:21	882.-0	422069	35146	60	3282	7.069	6.340	801-464	19175
426	00:24:18	882.-5	424003	29752	29	2955	5.984	5.410	678-044	19175
427	00:40:36	422.-4	200160	11458	20	1125	2.305	2.070	545-547	19175
Total				5.65 · 10 ³	927	53397	113.57	103.43	12167.75	

Table A.4: Official run info - Experiment 73 (luminosity run, 05/28/2010, b20090127_0910). For each run the following information is shown: run number, local start time (JST), time the detector measured (total run time - detector dead time), collected number of events, different event classifications (Barrel Bhabha, HadronC, Tau-Pair), accelerator delivered luminosity, detector accumulated luminosity, average luminosity calculated from online and offline luminosity values, the ID of the bunch fill.

No	θ (Lab frame)	θ (CMS frame)	$\sigma[nb]$	$\sigma_{vis}[nb]$
1	(12.0°, 155.0°)	(18.06°, 163.31°)	78.06 ± 0.2	6.89 ± 0.02
2	(17.0°, 150.0°)	(25.47°, 159.89°)	35.02 ± 0.08	6.81 ± 0.02
3	(20.0°, 145.0°)	(29.86°, 156.44°)	23.91 ± 0.05	6.93 ± 0.02
4	(23.0°, 142.0°)	(34.20°, 154.34°)	17.09 ± 0.04	6.94 ± 0.01
5	(25.0°, 140.0°)	(37.06°, 152.93°)	13.93 ± 0.03	6.94 ± 0.01
6	(25.0°, 138.0°)	(37.06°, 151.50°)	13.92 ± 0.03	6.95 ± 0.01
7	(25.0°, 135.0°)	(37.06°, 149.35°)	13.91 ± 0.03	6.97 ± 0.01
8	(28.0°, 132.0°)	(41.31°, 147.18°)	10.49 ± 0.02	6.95 ± 0.01
9	(30.0°, 130.0°)	(44.11°, 145.72°)	8.82 ± 0.02	6.89 ± 0.01
10	(32.0°, 128.0°)	(46.88°, 144.24°)	7.49 ± 0.02	6.74 ± 0.01
11	(35.0°, 125.0°)	(50.98°, 141.99°)	5.97 ± 0.01	5.38 ± 0.01
12	(37.0°, 123.0°)	(53.67°, 140.49°)	5.18 ± 0.01	4.69 ± 0.01
13	(40.0°, 120.0°)	(57.65°, 138.19°)	4.22 ± 0.01	3.83 ± 0.01
14	(42.0°, 118.0°)	(60.26°, 136.65°)	3.72 ± 0.01	3.38 ± 0.01
15	(45.0°, 115.0°)	(64.12°, 134.29°)	3.09 ± 0.01	2.83 ± 0.01

Table A.5: *BHWide* polar angle configurations used for the σ_{vis} (BHWide) stability test

Name	Value
CMS total Energy [GeV]	10.58
Detector range θ_{Min} [deg] for positrons	41.31
Detector range θ_{Max} [deg] for positrons	147.18
Detector range θ_{Min} [deg] for electrons	41.31
Detector range θ_{Max} [deg] for electrons	147.18
Energy minimum [GeV] for detected positrons	0.2
Energy minimum [GeV] for detected electrons	0.2
Maximum acollinearity [deg] of final e^+e^-	10.0
Infrared cut on photon energy [GeV]	10^{-5}
Maximum Weight for rejection	3.0
Z mass [GeV]	91.1882
Z width [GeV]	2.4952
$\sin^2(\theta_W)$	0.22225
Top quark mass [GeV]	174.3
Higgs mass [GeV]	115.0
Weighted events	off (=0)
Random number generator	RANMAR (=1)
Channel choice	s-channel and t-channel (=0)
Z-contribution	on (=0)
Total electroweak correlations included	on (=1)
Electroweak corrections library	ALIBABA
Hard bremsstrahlung matrix element library	CALKUL
Photon vacuum polarisation library	BURKHARDT

Table A.6: *BHWide generator settings used for the final production.*

Selection criterion	Events passed
Input	10^7
Confidence level track fit	9928381
Impact parameter	9911476
p_t	9902915
Barrel region	7151360
Momentum (hard radiation photon rejection)	6608109
Event topology (acollinearity angle)	6604734
Event energy (ECL cluster)	6558207
Reconstruction efficiency ϵ_{rec} (BHWide)	0.656

Table A.7: *Result of the reconstruction procedure on the BHWide Monte Carlo data*

Run	Input	Tracking	d_0, z_0	p_t	Barrel	γ rej	Topology	ECL	Efficiency
401	54119	46958	46711	46636	41695	37120	35225	35219	0.651
403	43867	38019	37820	37774	33733	29984	28467	28463	0.649
408	35034	30259	30088	30038	26915	23927	22707	22703	0.648
409	20147	17406	17298	17274	15510	13809	13119	13119	0.651
411	35623	30913	30729	30690	27361	24339	23188	23186	0.651
414	51771	44943	44704	44640	39937	35454	33619	33615	0.649
416	45118	39057	38875	38819	34687	30911	29357	29351	0.651
417	32898	28583	28423	28389	25430	22542	21425	21418	0.651
418	25930	22394	22278	22253	19836	17612	16673	16664	0.643
419	235	32	0	0	0	0	0	0	0.000
420	75	12	0	0	0	0	0	0	0.000
421	45176	39162	38969	38918	34856	31014	29384	29382	0.650
422	44723	38791	38595	38543	34454	30666	29158	29151	0.652
424	38783	33564	33402	33350	29734	26475	25210	25206	0.650
425	33822	29203	29061	29028	25996	23153	22038	22030	0.651
426	28818	24924	24778	24734	22119	19710	18713	18711	0.649
427	11097	9499	9445	9436	8453	7532	7167	7165	0.646
Total	547236	473719	471176	470522	420716	374248	355450	355383	0.649

Table A.8: Radiative Bhabha reconstruction results - Experiment 73, Trigger 42 (brl_bhabha). The efficiency is given under the assumption that the trigger is ideal.

Run	Input	Tracking	d_0, z_0	p_t	Barrel	γ rej	Topology	ECL
401	433721	1407	290	275	93	56	52	49
403	450420	1257	241	232	77	35	33	30
408	453377	1124	202	195	63	33	29	24
409	411137	840	116	110	44	19	17	15
411	462426	1189	228	224	82	37	35	34
414	419097	1272	275	263	79	42	36	35
416	449210	1089	263	249	91	47	43	41
417	455144	892	177	173	63	41	37	35
418	470788	801	144	140	48	28	23	22
419	291674	1003	10	9	4	0	0	0
420	97592	126	0	0	0	0	0	0
421	366934	1150	249	238	93	46	42	41
422	385012	1035	246	231	88	48	44	42
424	385190	941	238	230	79	31	29	28
425	385446	830	201	196	66	27	24	23
426	385654	705	156	147	41	22	20	19
427	184635	271	53	51	21	8	6	6
Total	6487457	15932	3089	2963	1032	520	470	444

Table A.9: Radiative Bhabha reconstruction results - Experiment 73, Trigger 77 (random_ev)

p_t cut	Exp73	BDK	KoralW
210	46	88.8 ± 5.2	1624.6 ± 143.1
220	45	81.8 ± 5.0	1586.8 ± 141.4
230	43	75.0 ± 4.8	1549.0 ± 139.7
240	42	71.0 ± 4.7	1397.9 ± 132.7
250	41	66.1 ± 4.5	1347.5 ± 130.3
260	39	60.9 ± 4.3	1271.9 ± 126.6
270	35	56.9 ± 4.2	1183.8 ± 122.1
280	33	51.6 ± 3.9	1146.0 ± 120.1
290	30	47.0 ± 3.8	1045.3 ± 114.7
300	27	43.0 ± 3.6	1007.5 ± 112.7
310	27	40.9 ± 3.6	931.9 ± 108.3
320	26	38.4 ± 3.4	856.4 ± 103.9
330	26	35.7 ± 3.3	818.6 ± 101.5
340	24	33.8 ± 3.2	793.4 ± 99.9
350	22	33.5 ± 3.2	780.8 ± 99.2
360	22	31.9 ± 3.1	755.6 ± 97.6
370	22	30.4 ± 3.1	730.4 ± 95.9
380	20	29.2 ± 3.0	692.6 ± 93.4
390	20	27.4 ± 2.9	642.3 ± 89.9
400	19	26.4 ± 2.9	591.9 ± 86.3
410	18	26.4 ± 2.9	554.1 ± 83.5
420	18	25.2 ± 2.8	503.7 ± 79.7
430	18	24.9 ± 2.8	491.2 ± 78.7
440	18	23.1 ± 2.7	465.9 ± 76.6
450	15	22.8 ± 2.6	465.9 ± 76.6

Table A.10: The number of expected events for each p_t cut.

Recon.	events	Generator	Input	Tracking	d_0, z_0	p_t	Barrel	Pair	Bhabha rej	Topology	Inv. mass	Electron ID	Efficiency	
KoralW		12249896	15441	10859	3672	2193	1431	1160	1159	64	5.14	10^{-4}	%	
BDK		50376689	26344	6414	300	149	146	138	131	119	110	2.19	10^{-5}	%

Table A.11: The result of the final Monte Carlo signal reconstruction. Listed are the event numbers for the KoralW and BDK two-photon Monte Carlo events after each reconstruction step and the reconstruction efficiency.

Run	Input	Tracking	d_0, z_0	p_t	Barrel	Pair	Bhabha rej	Topology	Inv. mass	Electron ID
401	433721	1407	226	81	68	8	8	8	8	1
403	450420	1257	241	68	56	16	15	15	15	1
408	453377	1124	202	163	48	41	6	5	5	1
409	411137	840	116	92	35	30	9	8	8	1
411	463426	1189	228	175	64	54	14	12	12	5
414	419097	1272	275	217	63	55	8	8	8	0
416	449210	1089	263	209	79	64	7	4	4	1
417	455144	892	177	147	51	46	3	2	2	0
418	470788	801	144	116	38	33	3	3	3	1
419	291674	1003	10	2	2	1	1	1	1	0
420	97592	126	0	0	0	0	0	0	0	0
421	366934	1150	249	200	80	69	16	14	14	5
422	385012	1035	246	177	67	58	6	4	4	1
424	385190	941	238	181	57	45	10	9	9	3
425	385446	830	201	144	48	40	8	8	8	2
426	388654	705	156	121	32	25	3	3	3	0
427	184635	271	53	44	17	15	3	3	3	2
Total	6487457	15932	3089	2411	830	701	121	107	107	24

Table A.12: The result of the reconstruction of the random trigger data from experiment 73. Listed are the event numbers after each reconstruction step for all runs separately.

Generator	Input	Tracking	d_0, z_0	p_t	Barrel	Pair	Bhabha rej	Topology	Inv. mass	Electron ID	Efficiency
Recon. events	Bhabha	10000000 841275	9928381 430874	9814476 335066	9840948 198517	7067054 108609	10407 108281	464 97822	140 97821	131 133	99.9987 % 99.9842 %
	$\pi^+ \pi^-$										
	$\mu^+ \mu^-$										
Expected events	Bhabha	59033004	20620512	11537358	1908121	8903333	883059	868388	771942 771331	232	99.9996 %
	$\pi^+ \pi^-$	662.84	658.10	656.98	652.30	471.72	468.44	0.69	0.03 18.87	0.01 17.04	0.01 0.02
	$\mu^+ \mu^-$	145.58	75.08	58.38	34.59	18.92	18.88				
		2706.37	945.62	528.93	87.48	40.82	40.48	39.81	35.39	35.36	0.01

Table A.13: The result of the background Monte Carlo reconstruction. Listed are the number of events after each reconstruction step for the three backgrounds: $\pi^+ \pi^-$, $\mu^+ \mu^-$ and Bhabha scattering. The overall rejection efficiency is given in the last column.

A.2 Figures

A.2.1 Momentum distribution of the recorded data, simulated background and the simulated BDK signal after each reconstruction step

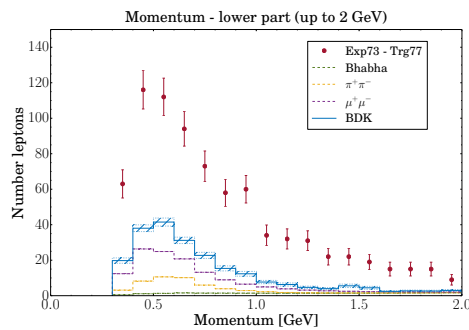


Figure A.1: $46.7^\circ < \theta(\text{CMS}) < 145.7^\circ$

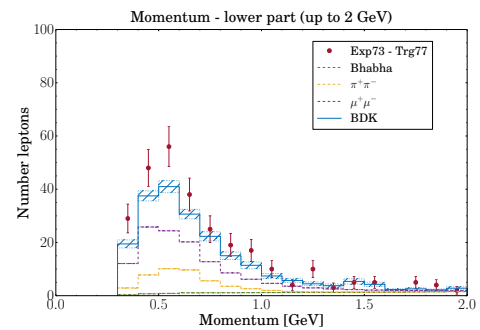


Figure A.2: Exactly one e^+ and one e^- particle

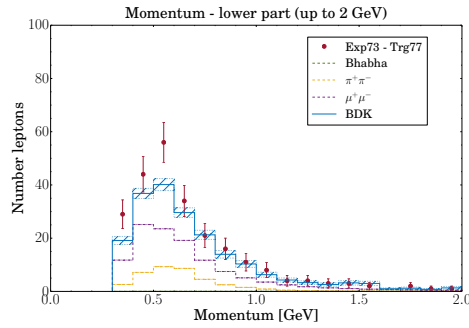


Figure A.3: e^+e^- momentum is < 2.645 GeV

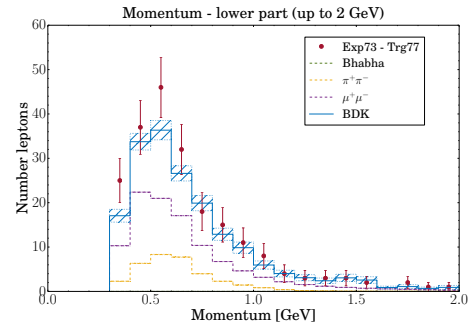


Figure A.4: Accollinearity angle is $> 10^\circ$

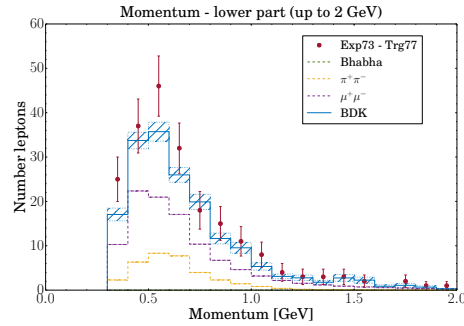


Figure A.5: Invariant mass > 100 MeV

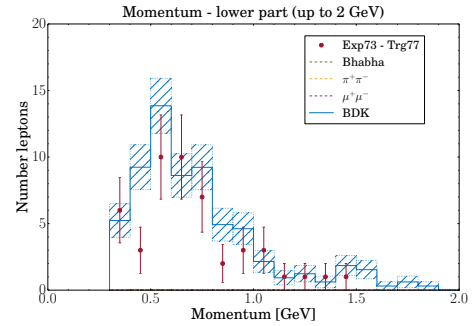


Figure A.6: Electron ID likelihood

A.2.2 Momentum distribution of the recorded data, simulated background and the simulated KoralW signal after each reconstruction step

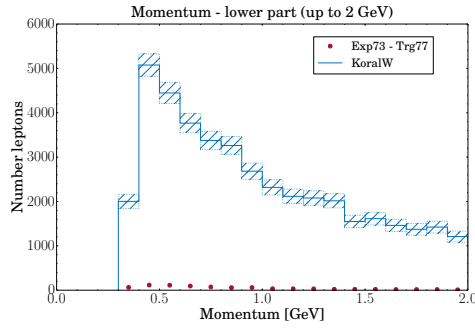


Figure A.7: $46.7^\circ < \theta(\text{CMS}) < 145.7^\circ$

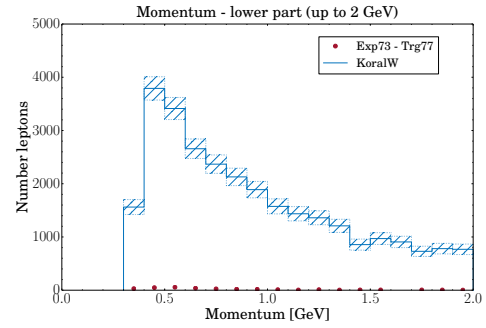


Figure A.8: Exactly one e^+ and one e^- particle

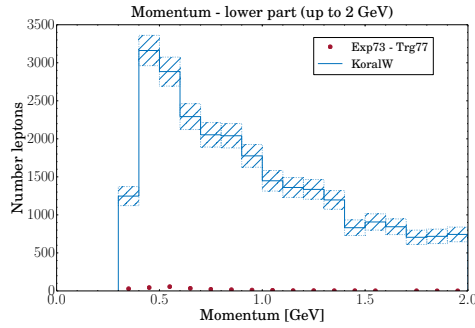


Figure A.9: e^+e^- momentum is < 2.645 GeV

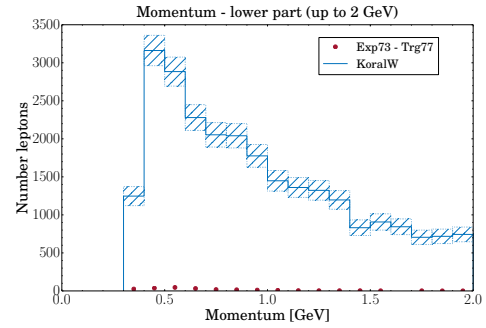


Figure A.10: Accollinearity angle is $> 10^\circ$

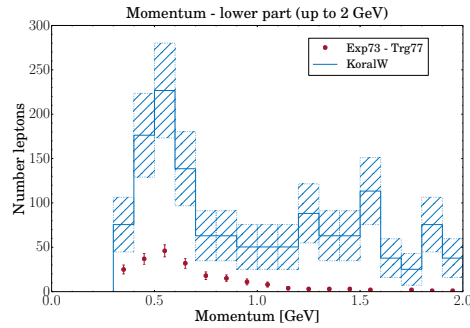


Figure A.11: Invariant mass > 100 MeV

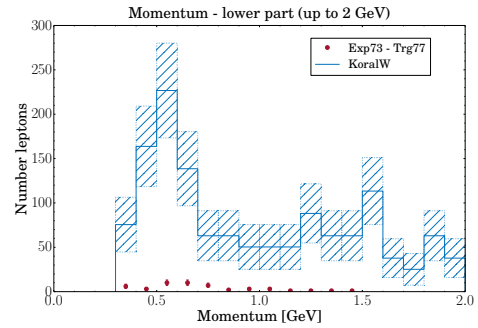


Figure A.12: Electron ID likelihood

A.2.3 Opening angle distribution of the recorded data, simulated background and the simulated BDK signal after each reconstruction step

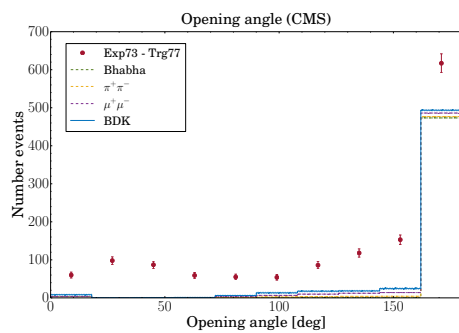


Figure A.13: $46.7^\circ < \theta(\text{CMS}) < 145.7^\circ$

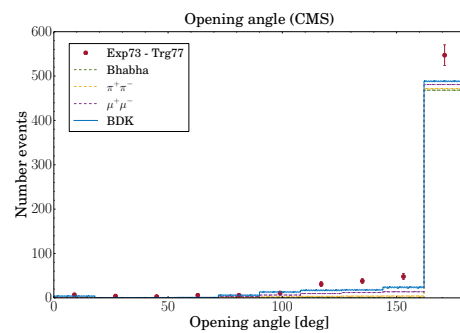


Figure A.14: Exactly one e^+ and one e^- particle

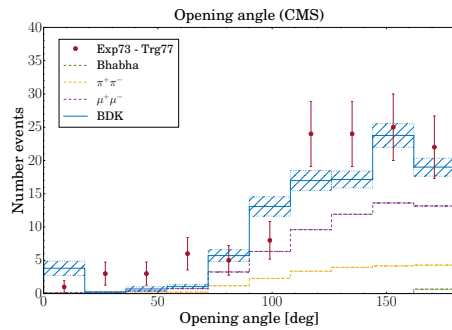


Figure A.15: e^+e^- momentum is $< 2.645 \text{ GeV}$

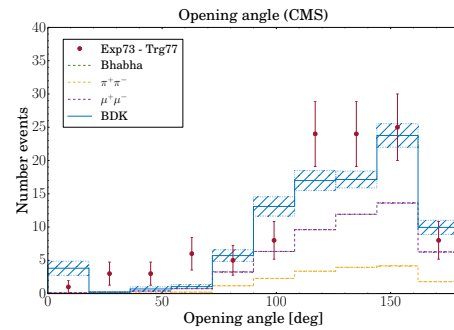


Figure A.16: Accollinearity angle is $> 10^\circ$

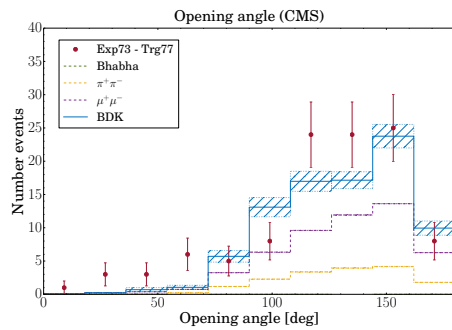


Figure A.17: Invariant mass $> 100 \text{ MeV}$

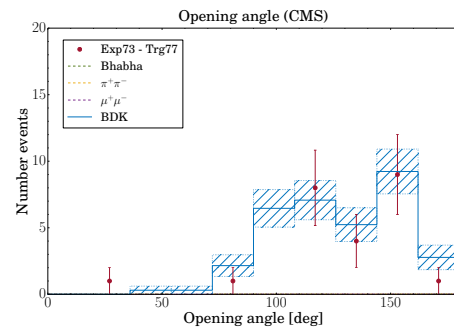


Figure A.18: Electron ID likelihood

A.3 The Belle and Belle II boost

Almost all Monte Carlo generators used in this thesis produce events in the centre-of-mass frame (**CMS**). In order to perform a full detector simulation, they have to be boosted into the laboratory frame (**Lab**) of the Belle/Belle II detector. In the following, the boost method used in this thesis and in basf2 is presented. The momentum of the HER and LER beam in the lab system is given by

$$\vec{P}_{HER} = \begin{pmatrix} \sqrt{E_{HER}^2 - m_e^2} \cdot \sin(\phi - \psi) \\ 0 \\ \sqrt{E_{HER}^2 - m_e^2} \cdot \cos(\phi - \psi) \end{pmatrix} \quad \vec{P}_{LER} = \begin{pmatrix} \sqrt{E_{LER}^2 - m_e^2} \cdot \sin(\pi - \psi) \\ 0 \\ \sqrt{E_{LER}^2 - m_e^2} \cdot \cos(\pi - \psi) \end{pmatrix}$$

Since all data is assumed to have been taken or simulated at the $\Upsilon(4S)$ resonance, the following four-momentum describes the $\Upsilon(4S)$ in the lab system

$$\vec{P}_{\Upsilon(4S)} = \begin{pmatrix} \vec{P}_{HER} \\ E_{HER} \end{pmatrix} + \begin{pmatrix} \vec{P}_{LER} \\ E_{LER} \end{pmatrix}$$

With $E = E_{HER} + E_{LER}$, the velocity $\vec{\beta}$ is then

$$\vec{\beta} = \left(\frac{\vec{P}_{\Upsilon(4S),x}}{E}, \frac{\vec{P}_{\Upsilon(4S),y}}{E}, \frac{\vec{P}_{\Upsilon(4S),z}}{E} \right)$$

The numerical values for β and $\beta\gamma$ for Belle and Belle II are shown in table 6.2. In order to transform a particle's four-momentum \vec{P} from the CMS frame to the lab frame, the general Lorentz transformation, applied to the four-momentum $\vec{P} \equiv (\vec{p}, E)$ with $c = 1$ and $\gamma^* = \frac{\gamma-1}{\beta^2}$, is used [277]

$$\vec{P}_{Lab} = \underbrace{\begin{pmatrix} 1 + \gamma^* \beta_x^2 & \gamma^* \beta_x \beta_y & \gamma^* \beta_x \beta_z & \gamma \beta_x \\ \gamma^* \beta_y \beta_x & 1 + \gamma^* \beta_y^2 & \gamma^* \beta_y \beta_z & \gamma \beta_y \\ \gamma^* \beta_z \beta_x & \gamma^* \beta_z \beta_y & 1 + \gamma^* \beta_z^2 & \gamma \beta_z \\ \gamma \beta_x & \gamma \beta_y & \gamma \beta_z & \gamma \end{pmatrix}}_L \cdot \vec{P}_{CMS} \quad (A.1)$$

The inverse transformation from lab frame to CMS frame can easily be computed by changing $\vec{\beta}$ to $-\vec{\beta}$. However, to be precise, equation (A.1) with $-\vec{\beta}$ transforms a particle from the lab frame into the $\Upsilon(4S)$ rest frame and all Monte Carlo generators used in this thesis assume that the z -axis is parallel to the electron flight direction. This means that the transformation in (A.1) has to be corrected for the asymmetry of the beams. This is accomplished by rotating the CMS of the HER in such a way that it is parallel to the Monte Carlo generator's z -axis. The rotation

angle and axis is calculated by transforming the four-momentum of the HER from the lab to the CMS frame

$$\vec{Q}_{HER} = L^{-1} \cdot \begin{pmatrix} \vec{P}_{HER} \\ E_{HER} \end{pmatrix}$$

Normalising $\vec{Q}_{HER} \rightarrow \hat{Q}_{HER}$ and calculating the vector product with the generator's assumed z-axis

$$\vec{R} = \begin{pmatrix} 0 \\ 0 \\ 1 \end{pmatrix} \times \begin{pmatrix} \hat{Q}_{HER,x} \\ \hat{Q}_{HER,y} \\ \hat{Q}_{HER,z} \end{pmatrix}$$

gives the rotation axis \vec{R} and the rotation angle

$$\alpha = \sin^{-1}(|\vec{R}|)$$

Multiplying a rotation matrix with the rotation axis \vec{R} and angle α on the transformation matrix L in (A.1) yields the desired matrix for the lab frame to generator CMS frame Lorentz transformation. This Lorentz transformation has been implemented into the basf2 software as a central and common tool and is used upon user request in the several Monte Carlo generators.

Appendix B

Theory of additional background components

B.1 Beam-Gas Bremsstrahlung

The total Beam-Gas loss rate is dominated by the elastic Coulomb scattering, described in section 7.4.2. The most important second order process, with respect to the Beam-Gas loss rate, is Bremsstrahlung. In this process, a beam particle interacts with the field of the residual gas nucleus and emits photons. The original differential cross-section for the Bremsstrahlung process is given by Bethe-Heitler [278, 279] and has been corrected and extended for various effects in the meantime. A nice overview, especially for the use in practical calculations, is given in [280]. Because of the high energies and velocities that the beam particles reach at SuperKEKB, a high energy limit of the Bremsstrahlung process should be applied. According to the criteria given in [280], a Born approximation for extremely relativistic particles with complete screening is appropriate for the description of the Beam-Gas Bremsstrahlung process. The Born approximation considers free particle wave functions that are perturbed to the first order in Z . Given the low Z values for the residual gas atoms ($Z(H_2) = 1$, $Z(CO) = 7$)¹ and $\beta \approx 1$, the Born approximation condition $(2\pi\alpha Z/\beta) \ll 1$ is fulfilled at SuperKEKB. For high energetic beam particles, the screening of the Coulomb field of a nucleus by the atomic electrons has to be taken into account. The formula for the cross-section that is differential with respect to the photon energy k , taking into account the approximations given above and a Coulomb correction term, is [281]

$$\frac{d\sigma}{dk} = \frac{4\alpha r_e^2}{3k} \left[(4 - 4y + 3y^2) [Z^2 (F_{el} - f) + ZF_{inel}] + (1 - y) \frac{Z^2 + Z}{3} \right] \quad (B.1)$$

where $y = k/E_{e^\pm}$ is the fraction of energy taken by the photon from the initial beam particle. As usual, α is the fine structure constant and r_e the classical radius of the electron. F_{el} and F_{inel} are

¹For CO the average value $Z = 7$ is used

the **elastic** and the **inelastic** form factors, respectively. F_{el} describes the scattering of the beam particle on the nucleus and F_{inel} the scattering on the shell electrons. This can also be seen from the factor Z^2 for F_{el} , which comes from the Coulomb field of the nucleus, carrying the charge Ze . On the other hand, the shell electrons contribute individually with Z times the charge e , leading to the factor Z (instead of Z^2) for F_{inel} .

For values of $Z > 4$, F_{el} and F_{inel} can be approximated by [42]

$$F_{el} = \ln\left(\frac{184.15}{Z^{\frac{1}{3}}}\right) \quad F_{inel} = \ln\left(\frac{1194}{Z^{\frac{2}{3}}}\right)$$

The Coulomb correction in equation B.1 is given by [42]

$$f = \alpha^2 Z^2 \sum_{n=1}^{\infty} \frac{1}{n(n^2 + \alpha^2 Z^2)}$$

With $a = \alpha Z$ and n the number of atoms per unit volume, the explicit calculation of f for elements up to uranium yields

$$f = a^2 \left[\frac{1}{1 + a^2} + 0.20206 - 0.0369a^2 + 0.0083a^4 - 0.002a^6 \right]$$

The **total cross-section** for the particles lost due to Beam-Gas Bremsstrahlung is calculate by the integral

$$\sigma_{Loss}^{Brem} = \int_{E_c}^E \frac{d\sigma}{dk} dk$$

with E_c being the lowest energy loss, which results in a particle loss. Using a lower energy bound in the integral above has the additional benefit of avoiding the divergence of the total cross-section. Performing the integration gives

$$\begin{aligned} \sigma_{Loss}^{Brem} = \frac{4\alpha r_e^2}{3} & \left[\left(4 \ln \frac{E}{E_c} - 4 \frac{E - E_c}{E} + \frac{3}{2} \left(1 - \frac{E_c^2}{E^2} \right) \right) \left[Z^2 (F_{el} - f) + Z F_{inel} \right] \right. \\ & \left. + \left(\ln \frac{E}{E_c} - \frac{E - E_c}{E} \right) \frac{Z^2 + Z}{3} \right] \end{aligned} \quad (\text{B.2})$$

Using the assumption that $E_c \ll E$, equation B.2 simplifies to the final cross-section

$$\sigma_{Loss}^{Brem} = \frac{4\alpha r_e^2}{3} \left[\left(4 \ln \frac{E}{E_c} - \frac{5}{2} \right) \left[Z^2 (F_{el} - f) + Z F_{inel} \right] + \left(\ln \frac{E}{E_c} - 1 \right) \frac{Z^2 + Z}{3} \right] \quad (\text{B.3})$$

List of Figures

2.1	Plaque outside the Cavendish laboratory in Cambridge commemorating Sir Joseph Thomson's discovery of the electron.	5
2.2	The Standard Model of particle physics consists of elementary particles divided into three generations of leptons, quarks and gauge bosons as force carriers and the Higgs boson [26].	9
2.3	The normalised unitary triangle in the B -meson system.	14
2.4	Summary of the measurements for the unitary triangle as of 2013. Compiled by the CKMfitter group [49]. The yellow area around the top tip of the triangle depicts the one sigma range of the average of all individual measurements. . . .	15
2.5	The leading order box diagrams involved in flavour mixing.	16
2.6	Semi-leptonic B decays, where the charge of the lepton is used in order to tag the event. If an e^+ is found it must have originated from a B^0 , if an e^- is found it must have originated from a \bar{B}^0	18
2.7	Production of two entangled B -mesons from the Υ (4S) resonance.	19
2.8	The left diagram shows the lowest order Feynman diagram for the transition $b \rightarrow s$ in the Standard Model. The right drawing shows possible physics beyond the Standard Model, which changes the prediction for observables such as the branching ratios or the angles in the unitary triangle.	21
2.9	The three coupling constants within the Standard Model a) and the MSSM b). .	22
2.10	Unification of all four forces in a Grand Unification Theory [61].	23
3.1	The SuperKEKB double-ring structure. Shown are the HER and LER for the electrons and positrons, respectively. The particles collide at the IP, which is surrounded by the Belle II detector. The wigglers in the straight sections are drawn as brown rectangles, the ARES cavities as red rectangles and the SCC cavities as green rectangles (see sections 3.3 and 3.8).	25
3.2	Total hadronic cross-section in nb for $e^+ e^-$ collisions as a function of the $e^+ e^-$ centre-of-mass energy [75].	27

3.3	The coordinate system used to describe the motion of particles in the accelerator. The left drawing shows the definition for the LER (positrons), with the s vector being parallel to the particle's flight direction. The right drawing shows the definition for the HER (electrons), with the s vector being anti-parallel to the particle's flight direction.	28
3.4	A schematic drawing of the SuperKEKB dipole magnet.	29
3.5	Weak focusing magnetic field of a bending magnet [81]. The beam particle enters the plane.	30
3.6	Left: Magnetic field of a quadrupole magnet [85]; Right: The technical realisation of a quadrupole magnet [81]. The strength of the magnetic field scales linearly with the deviation from the axis: $B_x \propto y, B_y \propto x$. The shown magnet is horizontally focusing and vertically defocusing.	32
3.7	The beam phase space ellipse [85]. Shown is the (x, x') slice through the six-dimensional phase space.	34
3.8	Before entering the quadrupole magnet focusing in the x -direction, the ellipse represents a diverging beam. After the magnet, the ellipse is rotated and the beam is converging. The drift section leads to a distortion of the beam such that it becomes divergent again. The beam waist is the location of the beam at which it reaches its minimum size in the drift section. In order to prevent the diverging beam from growing beyond the vacuum chamber aperture and being lost as a result another focusing magnet follows each drift section.	35
3.9	Influence of the bending and focusing magnets on the ellipse. A point on the ellipse moves around the ellipse as it travels along the accelerator ring.	36
3.10	A FODO lattice of focusing and defocusing magnets where each peak originates from a F and each valley from a D. Shown is a single particle with a non-integer betatron tune making multiple turns around the ring. Each turn has a different colour. The dashed line represents the beam envelope.	36
3.11	The J-shaped linear accelerator delivers the electrons and positrons for SuperKEKB. Its total length is 600 m and the circumference of the damping ring is 136 m.	40
3.12	The SuperKEKB movable mask. The collimator is cooled with water and has an adjustable aperture.	43
4.1	An artistic rendering of the Belle II detector [114].	45
4.2	The Belle II coordinate system.	48
4.3	The IR of Belle II. Shown are the incoming and outgoing beampipes and the final focusing magnets [117].	50
4.4	The beampipe surrounding the IP, including the support structure for the PXD [118].	50
4.5	The layout of the Belle II Pixel Vertex Detector [122].	51

4.6	Schematic drawing of the operating mode of a DEPFET [121]. An internal gate modulates the channel current that flows from the Source to the Drain. The external gate is used to switch the DEPFET on and off. In order to remove the collected charges in the internal gate, the Clear contact is used.	52
4.7	The layout and number of pixels for the two sensors. The red rectangles represent the 6 switchers.	53
4.8	The windmill-like arrangement of the PXD ladders, with the inner layer being flipped [122].	55
4.9	(a) Implant the p+ contact onto the backside of the top wafer. (b) Bond the handle wafer from the bottom onto the top wafer. The handle wafer allows to thin the top wafer down to the required 75 μm by standard wafer grinding and polishing techniques, without taking any special precautions for the protection of the p+ backside contact. (c) Implant the DEPFET structures on the top wafer (d) Etch the handle wafer partially back, leaving a support frame that is large enough to provide mechanical stability.	56
4.10	Mechanical layout of the PXD ladder for the inner and outer layer. The sizes of the chips are: DCD 3240 $\mu\text{m} \times$ 4969 μm , DHP 3280 $\mu\text{m} \times$ 4200 μm , Switcher 2030 $\mu\text{m} \times$ 3600 μm	57
4.11	PXD support and cooling structure [122]. Fabricated with a 3D laser sintering technology. The blue channels contain the CO ₂ , while the green and yellow channels blow nitrogen between the two PXD layers.	58
4.12	The ladder numbering for the PXD	59
4.13	The sensor numbering for the PXD	59
4.14	An artistic rendering of the SVD [138]. The picture shows the outermost layer of the SVD and the support structure.	60
4.15	The mechanical design for the SVD layers [140]. The forward direction is on the left hand side of the picture. Following the naming convention (section 4.3.8), the innermost layer of the SVD is given the ID 3, as it follows layers 1 and 2 of the PXD.	61
4.16	The measuring principle of a DSSD. A charged particle creates electron-hole pairs that drift to the appropriate strips: electrons to the strips on the n-side and holes to the strips on the p-side.	62
4.17	Left: True hits and ghost hits in a double sided strip detector in case of two particles traversing the detector. Right: Measured hits in a pixel detector in case of two particles traversing the detector.	62
4.18	The sense wire configuration of the CDC. Axial superlayers are drawn in blue, stereo superlayers in red.	64
4.19	A single TOP module [80]. The module is made from two synthetic fused silica blocks which are glued together (0.5 mm glue thickness). The radius of the spherical mirror is 700 cm. All values in the drawing are given in [mm].	66

4.20	The K^\pm/π^\pm separation principle of the TOP [80].	66
4.21	The π^\pm/K^\pm separation principle of the ARICH detector [152]. The red solid line represents a pion, the blue dashed line a kaon.	68
4.22	The resolution is improved by splitting the aerogel radiator [80]. The dashed, blue line represents a Cherenkov cone starting in the first layer. The solid, red line second a cone starting in the second layer.	69
4.23	Schematic drawing of the CDC. Shown are the Forward, Barrel and Backward regions, together with their angles.	70
4.24	The constituents of a RPC superlayer of the BKLM [80].	73
4.25	The operation mode of the BKLM scintillator. The polystyrene is covered with TiO_2 reflective coating and delivers blue light to an embedded WLS fibre (Kuraray Y11 MC, 1.2 mm diameter).	74
4.26	Schematic overview of the Belle II DAQ. About 300 COPPER boards take the data and transfer it to ~ 30 R/O PCs. The data is then merged in the Event Builder and the events are reconstructed in the HLT, which consists of $\mathcal{O}(10)$ units with ~ 400 cores per unit. The reconstructed data is merged with the PXD data and stored in ~ 10 storage units.	77
4.27	A charged track that has been identified and fitted with SVD and CDC information, is propagated back to the PXD. All pixels within an area (ROI) around the intersection point between the propagated track and a PXD sensor are kept. The size of the area depends mainly on the uncertainty of the track fit.	78
5.1	The typical data processing chains for a physics analysis. a) The Monte Carlo simulation chain, b) The detector data processing chain	80
5.2	The core architecture of the Belle II software framework. Modules, encapsulating a particular functionality, are arranged in a linear order. The event data enters the chain on the left and progresses to the right, using the DataStore to feed data from one module to another.	81
5.3	Conditional linking of paths in basf2: Three paths are connected by conditions. Both possible condition types are shown: An integer value and a simple boolean value.	82
5.4	Modules and libraries are separated in basf2, allowing to share a library among multiple modules. Modules are loaded on-demand from shared object files by a user request.	83
5.5	The parallel processing architecture of basf2. The module chain is divided into a single processing input and output group and a parallel processing group. The groups are connected by ring buffers (RB), taking care of the event distribution and collection.	84
5.6	The architecture of the geometry handling system in basf2. If needed, the Geant4 geometry can be converted to a ROOT TGeo [168] geometry.	86

5.7	The Geant4 PXD detector geometry. Shown is the outer layer and the support.	87
5.8	Cut through the Geant4 PXD geometry to reveal the inner layer.	87
5.9	Cut through the Geant4 geometry of the silicon tracking detectors (PXD, SVD), their support structures and the Beampipe.	87
5.10	Stack plot of a spherical material budget scan of the PXD. The x -axis is the polar angle, with the forward direction being on the left and the backward direction on the right. The y -axis measures the radiation length X in units of X_0	88
5.11	Stack plot of a spherical material budget scan of the full Belle II detector. The forward direction of the detector is on the left and the backward direction on the right.	89
5.12	The 3D magnetic field map of the Belle II detector in the zx -plane.	90
5.13	The 3D magnetic field map in the inner region of the Belle II detector in the zx -plane.	90
5.14	A particle enters the sensor at one side and leaves it on the other. The PXDTrueHit is then the position at which the particle crossed the zero plane.	90
5.15	A particle enters and leaves the sensor on the same side. In this case the positions of the two crossing points are averaged.	90
5.16	The PXD digitisation procedure. Electron clouds drift from the position where they have been generated to the drift field minimum. There, they perform a random walk to the internal gates. The local coordinate system of the PXD sensors is a right-handed Cartesian coordinate system (u, v, w) , where v is parallel to the global z axis of the Belle II detector and w is the normal vector of the sensor surface.	91
5.17	The PXD clustering method. Clusters 1, 2, 3 and 4 have already been found. The current pixel under investigation is added to cluster 3. The next pixel to the right will fill the gap between cluster 3 and 4. This will lead to clusters 3 and 4 being merged to a large cluster.	95
5.18	The PXD Event model. Relations connect collections with each other. A 1:n relation connects one object of the first collection with n objects of the second collection, while n:m Relations connect n objects of the first collection with m objects of the second collection.	97
5.19	The solid green line represents the particle trajectory, while the dashed green line the projection of the trajectory onto the xy plane. The definition of the impact parameter of a track is as follows: d_0 is the signed distance between the origin and the point of closest approach of the projected track to the origin; z_0 is the z coordinate of the track at the point of closest approach.	98
5.20	Impact parameter resolution for d_0 . The lower curve represents the Belle II detector, the dashed, green curve the Belle detector and the upper curve the Belle II detector without the PXD.	101

5.21	Impact parameter resolution for z_0 . The lower curve represents the Belle II detector, the dashed, green curve the Belle detector and the upper curve the Belle II detector without the PXD.	102
6.1	The Feynman diagrams for $\gamma\gamma$ scattering in QED: a) elastic $\gamma\gamma$ scattering, b) inelastic $\gamma\gamma$ scattering.	104
6.2	The kinematics of the two-photon process $e^+e^- \rightarrow e^+e^-\gamma\gamma \rightarrow e^+e^-X$ in the centre-of-mass system.	105
6.3	The production of a final state X in e^+e^- collisions at SuperKEKB: a) production via the annihilation process, b) production via the two-photon process.	107
6.4	The production cross-sections for colliding e^+e^- particles [206]: $e^+e^- \rightarrow e^+e^-\pi^+\pi^-$, $e^+e^- \rightarrow e^+e^-\mu^+\mu^-$, $e^+e^- \rightarrow e^+e^-\pi^0$ (two-photon production) and $e^+e^- \rightarrow \pi^+\pi^-$, $e^+e^- \rightarrow \mu^+\mu^-$ (annihilation)	108
6.5	The lowest order Feynman diagrams for the process $e^+e^- \rightarrow e^+e^-e^+e^-$: a) multiperipheral, b) bremsstrahlung, c) conversion and d) annihilation. a) and b) are t -channel diagrams, c) and d) involve s -channel diagrams.	109
6.6	The KoralW event weights. The dashed line indicates the maximum weight.	112
6.7	Stability of σ_{vis} (KoralW) for different polar angle configurations.	113
6.8	The transverse momentum of KoralW (solid line) and BDK (dashed line) in the centre-of-mass system after the acceptance cut. The left plot shows the momentum up to 6 GeV and the right plot up to 100 MeV.	116
6.9	The concept behind the low p_t analysis: measure the SVD hits per event for different values of the luminosity. Then extrapolate to zero luminosity in order to retrieve the beam background contribution. The difference is then the rate of the luminosity dependent processes for full luminosity.	120
6.10	The CDC current (left) and CDC hit multiplicity as a function of the instantaneous luminosity.	124
6.11	The hit multiplicities in the first SVD layer (rz -plane) for experiment B. Left: before the CDC correction; Right: after the CDC correction.	125
6.12	Stack plot for the three experiments of the number of hits extrapolated to zero luminosity.	127
6.13	Stability of σ_{vis} (BHWide) for different BHWide angle configurations. See table A.5 in the appendix for a detailed listing of the configurations.	133
6.14	Momentum spectrum of the generator BHWide events before and after the boost. The left figure shows the momentum spectrum in the centre-of-mass frame. The right figure the momentum spectrum after applying the boost to the lab frame. Electrons are drawn in blue, positrons in red and their sum in black.	134

6.15	Impact of the p_t cut on the number of expected events. The dashed lines in the upper plot illustrate the boundaries of the ACC, TOF and ECL. The dashed line in the lower plot is the average of the values within the grey area.	144
6.16	Momentum of the two outgoing leptons after the last reconstruction step. The left plot shows the result for BDK, the right plot for KoralW. The measured data is drawn as red dots, while the histogram represents the Monte Carlo data.	145
6.17	$\text{Cos}(\theta)$ of the two outgoing leptons after the last reconstruction step, with the BDK data on the left and the KoralW data on the right.	146
6.18	Opening angle in the centre-of-mass system of the two outgoing leptons after the last reconstruction step. The BDK result is shown in the left plot, the KoralW result in the right plot.	146
6.19	Transverse momentum spectrum before (left) and after (right) the acollinearity cut.	147
6.20	Momentum distribution of the background and the BDK signal after the invariant mass cut and before the electron ID cut.	148
7.1	Result of the clustering algorithm applied to one ROF of the two-photon background on sensor 1.1.1.	155
7.2	The angle of a cluster is defined as the angle between the major axis of a cluster and the global z -axis of Belle II (which is also the global z -axis of the PXD).	155
7.3	The result of the PCA after applying it to the data of figure 7.1. For each cluster the major axis (red), the minor axis (blue) and the number of pixels contained in the cluster is shown.	156
7.4	Definition of the length of a cluster. The left drawing illustrates the smallest enclosing ellipse fitted around a pixel cluster. The major axis of the ellipse is then defined as the length of the cluster. The right drawing shows the definition of the centre of the ellipse (c_u, c_v) and the semi-major axis a and the semi-minor axis b . The major axis is then $2 \cdot a$ and the minor axis is $2 \cdot b$	157
7.5	The result of the ellipse fitting algorithm applied to the two-photon data of figure 7.1. For each cluster the fitted ellipse is drawn.	158
7.6	Normalised NIEL damage cross-section $D(E)$ for neutrons in silicon [236].	159
7.7	The $\{j, k, l\}$ laboratory coordinate system in which the colliding particles lie in the plane spanned by the k -axis and the l -axis.	162
7.8	The coulomb scattering in the center-of-mass system of the bunch. Blue are the incoming particles and red the scattered particles.	162
7.9	The locations and loss rates for the Touschek particles after the SAD accelerator simulation. The bottom plot shows the loss rate in [MHz].	166

7.10	Angular and spatial distributions of the electrons and positrons traversing the PXD from Touschek LER per area during one snowmass year. The top row represents the inner layer and the bottom row the outer layer. The left plots show the $z\text{-}\phi$ distributions of electrons and positrons traversing the sensor area, the backward ASICs and the forward ASICs. The plots on the right hand side show the polar angle distribution.	167
7.11	Angular and spatial distributions of the electrons and positrons traversing the PXD from Touschek HER per area during one snowmass year. The top row represents the inner layer and the bottom row the outer layer. The left plots show the $z\text{-}\phi$ distributions of electrons and positrons traversing the sensor area, the backward ASICs and the forward ASICs. The plots on the right hand side show the polar angle distribution.	168
7.12	Distribution of the number of times a particle traverses a layer. The left plot shows the result for the inner layer and the right plot for the outer layer. Due to the low statistics of the Touschek HER, the plots only show the result for the LER.	169
7.13	The left plot shows the distribution of the origin of all e^+e^- particles that spark the creation of particles that, further down the chain, hit the PXD sensors. The right plot shows primary as well as secondary particles that hit the PXD sensors, thus helping to identify the areas within the interaction region that contribute to the background of the PXD.	169
7.14	The fired pixels from the Touschek LER background. The top plot presents the content for one ROF of sensor 1.1.1. The bottom left plot shows the xy -projection where the asymmetry is caused by the beam-crossing angle. The distribution of the fired pixels along z in the bottom right plot is fairly flat.	170
7.15	The fired pixels from the Touschek HER background. The left plot shows the xy -projection where the asymmetry is caused by the beam-crossing angle. The distribution of the fired pixels along z in the right plot is fairly flat with a slight rise in the forward direction.	171
7.16	Summary of the PXD occupancy values for the Touschek LER (left) and Touschek HER (right) background.	171
7.17	Cluster angle distributions for Touschek LER (left) and Touschek HER (right). The plots differentiate the different cluster sizes by colours and stack them to provide an overall distribution of the cluster angle. Starting with the cluster size 2 (blue), there are only four possible pixel arrangements with respect to the global z -axis: parallel (0°), perpendicular (90°), diagonal “upward” (45°) and diagonal “downward” (135°).	173
7.18	Feynman diagram for Beam-Gas Coulomb scattering.	174
7.19	Feynman diagram for Beam-Gas Bremsstrahlung scattering.	174
7.20	Definition of the quantities for the Beam-Gas rate calculation.	176

7.21	The locations and loss rates for the Beam-Gas particles after the SAD accelerator simulation.	178
7.22	Angular and spatial distributions of the electrons and positrons traversing the PXD from Beam-Gas LER per area during one snowmass year. The top row represents the inner layer and the bottom row the outer layer. The left plots show the z - ϕ distributions of electrons and positrons traversing the sensor area, the backward ASICs and the forward ASICs. The plots on the right hand side show the polar angle distribution.	179
7.23	Distribution of the number of times a Beam-Gas generated particle traverses a PXD layer. The left plot shows the result for the inner layer and the right plot for the outer layer.	181
7.24	The left plot shows the distribution of the origin of all e^+e^- particles that spark the creation of particles that, further down the chain, hit the PXD sensors. The right plot shows primary as well as secondary particles that hit the PXD sensors, thus helping to identify the areas within the interaction region that contribute to the background of the PXD.	181
7.25	The fired pixels from the Beam-Gas LER background. The left plot shows the xy -projection where an asymmetry in x is visible. The distribution of the fired pixels along z in the right plot is fairly flat.	181
7.26	The fired pixels from the Beam-Gas HER background. The left plot shows the xy -projection and the right plot the distribution of the fired pixels along z	182
7.27	Summary of the PXD occupancy values for the Beam-Gas LER (left) and Beam-Gas HER (right) background.	182
7.28	Cluster angle stack plot for Beam-Gas LER.	182
7.29	The left figure illustrates the deformation of the electric field of a point charge due to a parallel (longitudinal) acceleration of the charge. The right figure shows the deformation for a perpendicular (transversal) acceleration. Figure adapted from [85].	185
7.30	The left figure shows the emission of synchrotron radiation due to a transversal accelerated charge in the rest frame of the charge. The right figure illustrates the narrow cone with a half-opening angle of γ^{-1} for the synchrotron radiation in the laboratory frame. Figure adapted from [253]	186
7.31	A particle travelling from P_0 to P_1 emits synchrotron radiation. The radiation is collected by a detector as a radiation pulse with duration Δt . Figure adapted from [85].	187
7.32	The power spectrum function S and the number spectrum function F of synchrotron radiation.	190
7.33	Deviation of the beam position from the ideal orbit for the LER (left) and the HER (right). The result from PySynRad is compared with the values obtained from SAD.	193

7.34	The horizontal and vertical β Twiss parameters for the LER (left) and the HER (right). Shown is a comparison between the results from PySynRad and SAD.	193
7.35	The size of the beam along s for the LER (left) and the HER (right). Both results, from PySynRad and from SAD are drawn.	194
7.36	Sampling the synchrotron radiation energy spectrum. The left plot shows the CDF gained from the synchrotron power spectrum of figure 7.32, the middle plot the inverted CDF and the right plot compares samples drawn from the inverted CDF with the original synchrotron power spectrum.	195
7.37	The energy spectrum of the emitted photons from synchrotron radiation in the LER. The rejection cut of 5 keV is clearly visible on the left hand side.	196
7.38	The distributions illustrate the regions that are hit by the synchrotron radiation inside the beampipe. The coverage along z of the inner PXD layer is drawn in red.	197
7.39	The azimuthal angle distributions of the synchrotron photons hitting the beampipe for the HER (left) and LER (right).	197
7.40	Energy of the photons that hit the beampipe for the HER (left) and the LER (right).	198
7.41	Origin of all photons that created a hit in the beampipe. The synchrotron radiation is caused by the innermost focusing magnets (HER and LER) and the leak field in the HER.	198
7.42	Toy Monte Carlo test for the azimuthal angle (left) and the z -position (right). The original data is drawn as a blue histogram and the distribution obtained from toy Monte Carlo is drawn as red stars.	199
7.43	2D Toy Monte Carlo test for the ϕ - p_y distribution. The left plot shows the original distribution, while the right plot shows the result of the toy Monte Carlo. .	199
7.44	The types of particles traversing the PXD layers due to synchrotron radiation. The top row shows the result from the HER, while the bottom row represents the LER. From the plots it is obvious that photons are the dominating type of particle and that the contribution from the LER is negligible compared to the HER.	200
7.45	Angular and spatial distributions of the photons traversing the PXD from synchrotron radiation per area during one snowmass year. The top row represents the inner layer and the bottom row the outer layer. The left plots show the z - ϕ distributions of photons traversing the sensor area, the backward ASICs and the forward ASICs.	201
7.46	The trajectories of the synchrotron radiation photons after they hit the beampipe. Black lines represent the trajectories, green dots Compton scattering and blue dots the photo-electric effect. The top row shows the result for the inner layer, while the bottom row represents the outer layer.	202

7.47	The fired pixels from the synchrotron radiation HER background. The top plot presents the content for one ROF of sensor 1.1.1. The bottom left plot shows the xy -projection where the asymmetry is the result of Compton scattered photons. The bottom right plot presents the distribution of the fired pixels along z	203
7.48	The fired pixels from the synchrotron radiation LER background. The left plot shows the xy -projection and the right plot the distribution of the fired pixels along z	205
7.49	Summary of the PXD occupancy values for the synchrotron radiation LER (left) and synchrotron radiation HER (right) background.	205
7.50	One of the four leading annihilation Feynman diagrams for radiative Bhabha scattering.	207
7.51	One of the four leading scattering Feynman diagrams for radiative Bhabha scattering.	207
7.52	Comparison of the total cross-section between BBBrem and equation 7.55. Both methods of dealing with the beam size effect are shown.	209
7.53	The distribution of the event weights for BBBrem at $\sqrt{s} = 10.58$ GeV and $\epsilon = 10^{-4}\%$	210
7.54	The locations and loss rates for the radiative Bhabha particles after the SAD accelerator simulation.	211
7.55	Angular and spatial distributions of the electrons and positrons traversing the PXD from radiative Bhabha HER (top two rows) and LER (bottom two rows) per area during one snowmass year.	212
7.56	Distribution of the number of times a radiative Bhabha generated particle traverses a PXD layer. The top row shows the results from the radiative Bhabha HER, with the inner layer being the left plot and the outer layer the right plot. The bottom row represents the radiative Bhabha LER.	213
7.57	The left plot shows the distribution of the origin of all e^+e^- particles that spark the creation of particles that, further down the chain, hit the PXD sensors. The right plot shows primary as well as secondary particles that hit the PXD sensors, thus helping to identify the areas within the interaction region that contribute to the background of the PXD.	214
7.58	The fired pixels from the radiative Bhabha HER background. The top plot presents the content for one ROF of sensor 1.1.1. The bottom left plot shows the xy -projection and the bottom right plot the distribution of the fired pixels along z	215
7.59	The fired pixels from the radiative Bhabha LER background. The left plot shows the xy -projection and the right plot the distribution of the fired pixels along z	217
7.60	Summary of the PXD occupancy values for the radiative Bhabha LER (left) and radiative Bhabha HER (right) background.	217

7.61	Cluster angle distributions for radiative Bhabha LER (left) and radiative Bhabha HER (right). The plots differentiate the different cluster sizes by colours and stack them to provide an overall distribution of the cluster angle. Starting with the cluster size 2 (blue), there are only four possible pixel arrangements with respect to the global z -axis: parallel (0°), perpendicular (90°), diagonal “upward” (45°) and diagonal “downward” (135°)	218
7.62	Angular and spatial distributions of the electrons and positrons traversing the PXD from the two-photon process per area during one snowmass year. The top row represents the inner layer and the bottom row the outer layer.	219
7.63	Distribution of the number of times a two-photon generated particle traverses a PXD layer. The left plot shows the results from the inner layer of the PXD, the right plot the results from the outer layer. The bump in the forward direction is the result of backscattered particles and is, thus, an effect of the beampipe, while the non-sensitive glue between the two sensors is visible as a gap.	220
7.64	The left plot shows the distribution of the origin of all e^+e^- particles that spark the creation of particles that, further down the chain, hit the PXD sensors. The right plot shows primary as well as secondary particles that hit the PXD sensors, thus helping to identify the areas within the interaction region that contribute to the background of the PXD.	221
7.65	The fired pixels from the two-photon QED background. The top plot presents the content for one ROF of sensor 1.1.1. The bottom left plot shows the xy -projection with the typical $1/r^2$ dependence between the inner and the outer layer. The distribution of the fired pixels along z in the bottom right plot is fairly flat. The non-sensitive gaps of the glue are visible.	223
7.66	Summary of the PXD occupancy values for the two-photon QED background.	224
7.67	Cluster angle distribution for the two-photon process. The plot differentiates the different cluster sizes by colours and stacks them to provide an overall distribution of the cluster angle. Starting with the cluster size 2 (blue), there are only four possible pixel arrangements with respect to the global z -axis: parallel (0°), perpendicular (90°), diagonal “upward” (45°) and diagonal “downward” (135°)	224
7.68	Stack plot of the particle flux for electrons and positrons in the inner layer of the PXD, split into the contributions from each background type. The average particle flux is 6.1 MHz cm^{-2}	225
7.69	Stack plot of the particle flux for electrons and positrons in the outer layer of the PXD, split into the contributions from each background type. The average particle flux is 2.5 MHz cm^{-2}	226

7.70 Energy spectra of the electrons and positrons traversing the inner (left) and outer (right) layer of the PXD. The typical energy is 4 MeV for the inner layer and 6 MeV for the outer layer. The peak at 200 keV originates from delta electrons. $6.08 \cdot 10^{13}$ electrons and positrons are expected to traverse the inner layer and $2.33 \cdot 10^{13}$ electrons and positrons the outer layer per cm^2 and snowmass year. 227

7.71 Stack plot of the particle flux for photons in the inner (left) and outer (right) layer of the PXD, split into the contributions from each background type. 227

7.72 Energy spectra of the photons traversing the inner (left) and outer (right) layer of the PXD. The typical energy is 50 keV. $4.27 \cdot 10^{14}$ photons cross the inner layer and $1.57 \cdot 10^{14}$ the outer layer of the PXD per cm^2 during one snowmass year. 227

7.73 Distribution of the origin of all particles that either hit the PXD sensors directly or created a particle that hit the sensors. The HER (LER) beam travels from the bottom left (right) corner to the top right (left) corner. 228

7.74 Summary of the PXD occupancy values in % for the inner layer (left) and the outer layer (right). The contributions of Touschek (red), two-photon (blue), radiative Bhabha (green) and synchrotron radiation (yellow) can be seen. The radius represents the occupancy while each arc segment represents the azimuthal angle range a single ladder covers. 229

7.75 The cluster size (number of pixels per cluster) for the various backgrounds. The left plot shows the clusters for the inner layer of the PXD and the right plot for the outer layer. 231

7.76 The cluster length in μm for clusters with 2 or more pixels. The left plot shows the cluster lengths for the inner layer of the PXD, the right plot for the outer layer. 232

7.77 Stack plot of the expected radiation dose for the inner layer (top) and outer layer (bottom) of the PXD with respect to the global z -axis. The dominating background is the two-photon process with the average dose 19.9 kGy/smy (layer 1) and 4.9 kGy/smy (layer 2). 233

7.78 Energy distribution of the neutrons traversing the inner layer (left plot) and outer layer (right plot) of the PXD. The dominating source for neutrons is the radiative Bhabha background, followed by the two-photon background. 234

7.79 NIEL folded energy distribution of the neutrons traversing the inner layer (left plot) and outer layer (right plot) of the PXD. 235

7.80 NIEL folded fluence rate. The distribution is the result of weighting each particle with the D value using the particle's kinetic energy. 235

7.81 The background mixing scheme for basf2. The background is generated and simulated for each detector and component separately. The result is merged into sub-detector ROFs and stored into files, using the hierarchy sub-detector → component → generator. The background is then mixed with the physics process using the MixBkg module. In this example the physics process is generated using EvtGen [179]. 236

A.1	$46.7^\circ < \theta(\text{CMS}) < 145.7^\circ$	255
A.2	Exactly one e^+ and one e^- particle	255
A.3	e^+e^- momentum is $< 2.645 \text{ GeV}$	255
A.4	Accollinearity angle is $> 10^\circ$	255
A.5	Invariant mass $> 100 \text{ MeV}$	255
A.6	Electron ID likelihood	255
A.7	$46.7^\circ < \theta(\text{CMS}) < 145.7^\circ$	256
A.8	Exactly one e^+ and one e^- particle	256
A.9	e^+e^- momentum is $< 2.645 \text{ GeV}$	256
A.10	Accollinearity angle is $> 10^\circ$	256
A.11	Invariant mass $> 100 \text{ MeV}$	256
A.12	Electron ID likelihood	256
A.13	$46.7^\circ < \theta(\text{CMS}) < 145.7^\circ$	257
A.14	Exactly one e^+ and one e^- particle	257
A.15	e^+e^- momentum is $< 2.645 \text{ GeV}$	257
A.16	Accollinearity angle is $> 10^\circ$	257
A.17	Invariant mass $> 100 \text{ MeV}$	257
A.18	Electron ID likelihood	257

List of Tables

2.1	The fundamental forces [10]. They are ordered in ascending order of their strength. The strength values are normalised to the strength of the strong force.	6
3.1	The SuperKEKB storage ring parameters.	39
3.2	The expected beam-lifetime at SuperKEKB. All values are given in seconds.	42
4.1	Required minimal transverse momentum in order to reach a specific sub-detector. The values are calculated using the well-known formula for relativistic electrons: $p_t[\text{GeV}] = 0.3 \cdot B[\text{Tesla}] \cdot R[m]$	47
4.2	The final focusing magnets of Belle II as illustrated in figure 4.3. The position of each magnet is measured from the IP.	49
4.3	The pixel size and the active area for the PXD sensors. The pixel size is given as width \times length.	53
4.4	Summary of the numerical values for the PXD mechanical layout. In the case that the tolerances add up unfavourably, the overlap can become as small as 3-5 pixels. The overlap is measured for a single edge and not the full sensor.	56
4.5	Listing of the layer radii, number of ladders and the windmill angles for the SVD.	61
4.6	The pitch sizes for the rectangular and trapezoidal sensors.	63
4.7	The numerical values for the CDC wire configuration. The innermost super-layer has two additional layers with active guard wires.	65
4.8	The Belle II trigger channels [160]. The rates of Bhabha and $\gamma\gamma$ are pre-scaled by factor 100. The maximum average trigger rate for Belle II is 30 kHz.	76
5.1	The standard units of the Belle II software. All other units in basf2 are based on those. In general, units are implemented in the framework such that multiplying a unit to a value automatically converts the value from the specified unit to the standard unit.	85
5.2	The default input values for the PXD Digitiser.	94
5.3	The default input values for the PXD Clusteriser.	96
6.1	The table summarises the number of events after each cut and the calculated values for the visible cross-section.	115

6.2	Comparison of the beam parameters of KEKB and SuperKEKB and their respective boosts.	117
6.3	Run summary - Experiment 73. For each run the following information is shown: the total number of events, the number of events from the random trigger (Trg77), the number of Bhabha-like events (Trg42), the time the detector measured (<i>total run time - detector dead time</i>), the luminosity delivered from the accelerator, the accumulated luminosity by the detector. The runs are grouped according to the type of the sub-experiment, explained in detail in the text.	119
6.4	The increase of the beam size per run. Due to the squeezing of the beams, the change in height has a much larger influence on the luminosity than the change of the width of the beam.	121
6.5	The beam currents for sub-experiment C in [mA]. The values for both, the start and the stop time of the run are given for HER and LER.	121
6.6	Hit multiplicity in the $r - z$ plane for all runs and all layers of the SVD2.	123
6.7	Hit multiplicity in the $r - \phi$ plane for all runs and all layers of the SVD2.	123
6.8	Hit multiplicity and current in the CDC for all runs.	126
6.9	Estimated QED background contribution in each SVD layer.	126
6.10	Systematic study of the QED contribution for correction factors derived from different subsets of CDC layers.	128
6.11	Systematic study of the QED contribution for correction factors derived from different group sizes of CDC layers.	128
6.12	Comparison between the measured SVD hit multiplicity and the KoralW Monte Carlo simulation.	129
6.13	Beamspot position and width values for the MonteCarlo simulation of experiment 73.	133
6.14	Luminosity in pb^{-1} calculated from radiative Bhabha events from experiment 73, trigger 42.	137
6.15	Memory time of the detector in μs , calculated from experiment 73, trigger 77	138
6.16	The Monte Carlo to data scaling factors for the signal and background Monte Carlo samples.	143
7.1	Summary of the number of datasets that represent one ROF event	153
7.2	The detailed occupancy values for the Touschek background split into their individual contributions for each sensor.	172
7.3	The detailed occupancy values for the Beam-Gas background split into their individual contributions for each sensor.	180
7.4	The bins for the toy Monte Carlo production of the synchrotron radiation. The HER data is binned into 8 bins in ϕ and z , while the LER is binned into 4 bins in ϕ and z	199

7.5	The detailed occupancy values for the synchrotron radiation background split into their individual contributions for each sensor.	204
7.6	The detailed occupancy values for the radiative Bhabha background split into their individual contributions for each sensor.	216
7.7	The detailed occupancy values for the two-photon QED background split into their individual contributions for each sensor.	222
7.8	The maximum occupancy values for each background and PXD layer.	230
A.1	KoralW polar angle configurations used for the σ_{vis} (KoralW) stability test. Listed are the polar angle cuts in the laboratory and the centre-of-mass system, the generator cross-section, the visible cross-section in the detector acceptance and the time it took to generate a single event within the detector acceptance. .	246
A.2	The settings for the KoralW Monte Carlo production	247
A.3	The settings for the BDK Monte Carlo production	247
A.4	Official run info - Experiment 73 (luminosity run, 05/28/2010, b20090127_0910). For each run the following information is shown: run number, local start time (JST), time the detector measured (<i>total run time - detector dead time</i>), collected number of events, different event classifications (<i>Barrel Bhabha, HadronC, Tau-Pair</i>), accelerator delivered luminosity, detector accumulated luminosity, average luminosity calculated from online and offline luminosity values, the ID of the bunch fill.	248
A.5	BHWide polar angle configurations used for the σ_{vis} (BHWide) stability test . .	249
A.6	BHWide generator settings used for the final production.	250
A.7	Result of the reconstruction procedure on the BHWide Monte Carlo data	250
A.8	Radiative Bhabha reconstruction results - Experiment 73, Trigger 42 (brl_bhabha). The efficiency is given under the assumption that the trigger is ideal.	251
A.9	Radiative Bhabha reconstruction results - Experiment 73, Trigger 77 (random_ev)	251
A.10	The number of expected events for each p_t cut.	252
A.11	The result of the final Monte Carlo signal reconstruction. Listed are the event numbers for the KoralW and BDK two-photon Monte Carlo events after each reconstruction step and the reconstruction efficiency.	253
A.12	The result of the reconstruction of the random trigger data from experiment 73. Listed are the event numbers after each reconstruction step for all runs separately.	253
A.13	The result of the background Monte Carlo reconstruction. Listed are the number of events after each reconstruction step for the three backgrounds: $\pi^+\pi^-$, $\mu^+\mu^-$ and Bhabha scattering. The overall rejection efficiency is given in the last column.	254

Bibliography

- [1] Planck Collaboration: P. A. R. Ade et al. Planck 2013 results. I. Overview of products and scientific results. *pre-print*, 2013. arXiv: astro-ph/1303.5062v1.
- [2] C. L. Bennett et al. Nine-Year Wilkinson Microwave Anisotropy Probe (WMAP) Observations: Final Maps and Results. *pre-print*, 2013. arXiv: astro-ph/1212.5225v3.
- [3] A. Sakharov. Violation of CP Invariance, C Asymmetry, and Baryon Asymmetry of the Universe. *JETP Lett*, 5:24–26, 1967.
- [4] P. Harrison. Nature’s flawed mirror. *Physics World*, 7:27–31, 2003.
- [5] M. Peskin. The matter with antimatter. *Nature*, 419:24–26, 2002.
- [6] Sir Isaac Newton. *The Mathematical Principles of Natural Philosophy*. (translated into English by Andrew Motte), 1729.
- [7] D. J. Griffiths. *Introduction to Electrodynamics*. Prentice-Hall International Inc., 1998.
- [8] J.J. Thomson. Cathode rays. *Philosophical Magazine*, 44:293, 1897.
- [9] J. Chadwick Sir E. Rutherford and C.D. Ellis. *Radiations from Radioactive Substances*. Cambridge University Press, 1930.
- [10] W.S.C. Williams. *Nuclear and Particle Physics*. Oxford University Press, 2003.
- [11] M. Planck. Über das Gesetz der Energieverteilung im Normalspectrum. *Annalen der Physik*, 309(3):553–563, 1901.
- [12] A. Einstein. Über einen die Erzeugung und Verwandlung des Lichtes betreffenden heuristischen Gesichtspunkt. *Annalen der Physik*, 322(6):132–148, 1905.
- [13] A.H. Compton. A Quantum Theory of the Scattering of X-rays by Light Elements. *Phys. Rev.*, 21(5):483–502, 1923.
- [14] P.A.M. Dirac. The Quantum Theory of the Electron. *Proc. R. Soc. Lond.*, A 117:610–624, 1928.
- [15] C.D. Anderson. The Positive Electron. *Phys. Rev.*, 43:491–494, 1933.

- [16] R.P. Feynman. Space-Time Approach to Quantum Electrodynamics. *Phys. Rev.*, 76(6):769–789, 1949.
- [17] J. Schwinger. On Quantum-Electrodynamics and the Magnetic Moment of the Electron. *Phys. Rev.*, 73(4):416–417, 1948.
- [18] S. Tomonaga. On a Relativistic Invariant Formulation of the Quantum Theory of Wave Fields. *Proc. Theor. Phys.*, 1(2):27–42, 1946.
- [19] E. Reya. Perturbative quantum chromodynamics. *Phys. Rept.*, 69(3):195–333, 1981.
- [20] S.L. Glashow. Partial-symmetries of weak interactions. *Nucl. Phys.*, 22(4):579–588, 1961.
- [21] S. Weinberg. A Model of Leptons. *Phys. Rev. Lett.*, 19(21):1264–1266, 1967.
- [22] A. Salam. *Elementary Particle Theory*. Almqvist and Wiksells, Stockholm, 1968.
- [23] J. Iliopoulos S.L. Glashow and L. Maiani. Weak Interactions with Lepton-Hadron Symmetry. *Phys. Rev.*, D 2(7):1285–1292, 1970.
- [24] ALEPH, DELPHI, L3, OPAL, SLD, LEP Electroweak Working Group, SLD Electroweak, and Heavy Flavour Groups: S. Schael et al. Precision electroweak measurements on the Z resonance. *eprint hep-ex/0509008*, 2007.
- [25] P.W. Higgs. Broken Symmetries and the Masses of Gauge Bosons. *Phys. Rev. Lett.*, 13:508–509, 1964.
- [26] Wikipedia. Standard Model — Wikipedia, The Free Encyclopedia, 2013. [Online; accessed 26-January-2014].
- [27] D.H. Saxon. The lepton-hadron interaction. *Proc. R. Soc. Lond.*, A 404:233–251, 1986.
- [28] C.D. Anderson and S.H. Neddermeyer. Cloud Chamber Observations of Cosmic Rays at 4300 Meters Elevation and Near Sea-Level. *Phys. Rev.*, 50:263–271, 1936.
- [29] C.D. Anderson and S.H. Neddermeyer. Note on the Nature of Cosmic-Ray Particles. *Phys. Rev.*, 51:884–886, 1937.
- [30] R. Brandelik et al. Measurement of tau decay modes and a precise determination of the mass. *Phys. Lett.*, B 73:109–114, 1978.
- [31] K. Goulian L.M. Lederman N. Mistry M. Schwartz G. Danby, J.M. Gaillard and J. Steinberger. Observation of High-Energy Neutrino Reactions and the Existence of Two Kinds of Neutrinos. *Phys. Rev. Lett.*, 9:36–44, 1962.
- [32] K. Kodama et al. Observation of tau neutrino interactions. *Phys. Lett.*, B 504:218–224, 2001.

- [33] G. Aad et al. Observation of a new particle in the search for the Standard Model Higgs boson with the ATLAS detector at the LHC. *Phys. Lett. B*, 716(1):1–29, 2012.
- [34] S. Chatrchyan et al. Observation of a new boson at a mass of 125 GeV with the CMS experiment at the LHC. *Phys. Lett. B*, 716(1):30–61, 2012.
- [35] E. Noether. Invariante Variationsprobleme. *Nachr. D. König. Gesellsch. D. Wiss. Zu Göttingen, Math-phys. Klasse*, pages 235–257, 1918.
- [36] T.D. Lee and C.N. Yang. Question of Parity Conservation in Weak Interactions. *Phys. Rev.*, 104(1):254–258, 1956.
- [37] R.W. Hayward D.D. Hoppes C.S. Wu, E. Ambler and R.P. Hudson. Experimental Test of Parity Conservation in Beta Decay. *Phys. Rev.*, 105(4):1413–1415, 1957.
- [38] V.L. Fitch J.H. Christenson, J.W. Cronin and R. Turlay. Evidence for the 2π Decay of the K_2^0 Meson. *Phys. Rev. Lett.*, 13(4):138–140, 1964.
- [39] D. Dorfan et al. Charge Asymmetry in the Muonic Decay of the K_2^0 . *Phys. Rev. Lett.*, 19(17):987–993, 1967.
- [40] S. Bennett et al. Measurement of the Charge Asymmetry in the Decay $K_L^0 \rightarrow \pi^\pm + e^\mp + \nu$. *Phys. Rev. Lett.*, 19(17):993–997, 1967.
- [41] I. Bigi and A. Sanda. *CP Violation*. Cambridge University Press, 2009.
- [42] K.A. Olive et al. Review of Particle Physics. *Chin.Phys.*, C38:090001, 2014.
- [43] M. Kobayashi and T. Maskawa. CP-Violation in the Renormalizable Theory of Weak Interaction. *Progress of Theoretical Physics*, 49(2):652–657, 1972.
- [44] L. Wolfenstein. Parametrization of the Kobayashi-Maskawa Matrix. *Phys. Rev. Lett.*, 51(21):1945–1947, 1983.
- [45] A. B. Carter and A. I. Sanda. CP violation in B-meson decays. *Phys. Rev. D*, 23(7):1567–1579, 1981.
- [46] K. Abe et al. (Belle Collaboration). Observation of Large CP Violation in the Neutral B Meson System. *Phys. Rev. Lett.*, 87(9):091802, 2001.
- [47] B. Aubert et al. (BABAR Collaboration). Observation of CP Violation in the B^0 Meson System. *Phys. Rev. Lett.*, 87(9):091801, 2001.
- [48] L.L. Chau and W.Y. Keung. Comments on the Parametrization of the Kobayashi-Maskawa Matrix. *Phys. Rev. Lett.*, 53(19):1802–1805, 1984.
- [49] J. Charles et al. (CKMfitter Group). CP Violation and the CKM Matrix: Assessing the Impact of the Asymmetric B Factories. *Eur. Phys. J.*, C 41:1–131, 2005. updated results and plots at <http://ckmfitter.in2p3.fr>.

- [50] B. Podolsky A. Einstein and N. Rosen. Can Quantum-Mechanical Description of Physical Reality Be Considered Complete? *Phys. Rev.*, 47(10):777–780, 1935.
- [51] R. N. Cahn. The eighteen arbitrary parameters of the standard model in your everyday life. *Rev. Mod. Phys.*, 68(3):951–959, 1996.
- [52] The Belle Collaboration: K. Abe et al. Measurement of CP Violation Parameters in $B^0 \rightarrow K_S^0 \pi^0 \pi^0$ and $B^0 \rightarrow K_S^0 K_S^0$ Decays. *pre-print*, 2007. arXiv: hep-ex/0708.1845.
- [53] The Belle Collaboration: Y. Chao et al. Measurements of time-dependent CP violation in $B^0 \rightarrow \omega K_S^0$, $f_0(980)K_S^0$, $K_S^0 \pi^0$ and $K^+ K^- K_S^0$ decays. *Phys. Rev. D*, 76(9):091103(R), 2007.
- [54] The Belle Collaboration: I. Adachi et al. Measurement of the Differential Branching Fraction and Forward-Backward Asymmetry for $B \rightarrow K^* l^+ l^-$. *pre-print*, 2008. arXiv: hep-ex/0810.0335.
- [55] The Belle Collaboration: S. W. Lin et al. Difference in direct charge-parity violation between charged and neutral B meson decays. *Nature*, 452:332–335, 2008.
- [56] T. E. Browder et al. New Physics at a Super Flavor Factory. *pre-print*, 2008. arXiv: hep-ph/0802.3201v2.
- [57] H. P. Nilles. Supersymmetry, Supergravity and Particle Physics. *Phys. Rep.*, 110(1-2):1–162, 1984.
- [58] H. E. Haber and G. L. Kane. The search for supersymmetry: Probing physics beyond the standard model. *Phys. Rep.*, 117(2-4):75–263, 1985.
- [59] B. Farmer et al. Should we still believe in constrained supersymmetry? *Eur. Phys. J.*, 73(2563):1–38, October 2013.
- [60] M. Shifman. Reflections and Impressionistic Portrait at the Conference Frontiers Beyond the Standard Model, FTPI, Oct. 2012. 2012. arXiv: pop-ph/1211.0004v1.
- [61] Y. Okada J. Brau and N. Walker. International Linearcollider Reference Design Report, Volume 1. Technical report, ILC Global Design Effort and World Wide Study, August 2007.
- [62] F. Zwicky. Die Rotverschiebung von extragalaktischen Nebeln. *Helvetica Physica Acta*, 6(2):110–127, 1933.
- [63] W. K. Jr. Ford V. Rubin and N. Thonnard. Rotational Properties of 21 Sc Galaxies with a Large Range of Luminosities and Radii from NGC 4605 (R = 4kpc) to UGC 2885 (R = 122kpc). *The Astrophysical Journal*, 238(1):471–487, 1980.
- [64] S. M. Faber and R. E. Jackson. Velocity dispersions and mass-to-light ratios for elliptical galaxies. *The Astrophysical Journal*, 204:668–683, 1976.

- [65] R. Massey et al. Dark matter maps reveal cosmic scaffolding. *Nature*, 445(7129):286–290, 2007.
- [66] D. Clowe et al. A direct empirical proof of the existence of dark matter. *The Astrophysical Journal*, 648(2):109–113, 2006.
- [67] E. Komatsu et al. Five-Year Wilkinson Microwave Anisotropy Probe Observations: Cosmological Interpretation. *The Astrophysical Journal Supplement*, 180(2):330–376, 2009.
- [68] S. Weinberg. A New Light Boson? *Phys. Rev. Lett.*, 40(4):223–226, 1978.
- [69] F. Wilczek. Problem of Strong P and T Invariance in the Presence of Instantons. *Phys. Rev. Lett.*, 40(5):279–282, 1978.
- [70] R. D. Peccei and H. R. Quinn. CP conservation in the presence of pseudoparticles. *Phys. Rev. Lett.*, 38:1440–1443, 1977.
- [71] The CDMS II Collaboration. Dark Matter Search Results from the CDMS II Experiment. *Science*, 327(5973):1619–1621, 2010.
- [72] G. Angloher et al. Results from 730kg days of the CRESST-II Dark Matter Search. *preprint*, 2011. arXiv: astro-ph/1109.0702v1.
- [73] R. Bernabei et al. First results from DAMA/LIBRA and the combined results with DAMA/NaI. *Eur. Phys. J.*, C 56(3):333–355, 2008.
- [74] S. Kurokawa and E. Kikutani. KEK-B: The KEK B-factory. *Nucl. Instrum. Meth.*, A 499(1), 2003.
- [75] T.E. Browder and K. Honscheid. B mesons. *Prog. Part. Nucl. Phys.*, 35:81–219, 1995.
- [76] J. Schwinger. On the Classical Radiation of Accelerated Electrons. *Phys. Rev.*, 75(12):1912–1925, 1949.
- [77] Y. Yamazaki and T. Kageyama. A Three-Cavity System which Suppresses the Coupled-Bunch Instability Associated with the Accelerating Mode. *Particle Accelerators*, 44:107 – 127, 1994.
- [78] T. Furuya et al. High Power Input Coupler for KEKB SC Cavity. *Proc. 9th Workshop on RF Superconductivity*, LA-13782-C:31, 1999.
- [79] J.W. Flanagan and Y. Ohnishi. Letter of Intent for KEK Super B Factory. *KEK-REPORT-2004-4*, pages 337 – 542, 2004.
- [80] T. Abe et al. Belle II Technical Design Report. *pre-print*, 2010. arXiv:1011.0352v1.
- [81] J. Rossbach and P. Schmüser. *Basic course on accelerator optics*. DESY-M-93-02, 1993.

- [82] D. W. Kerst and R. Serber. Electronic Orbits in the Induction Accelerator. *Phys. Rev.*, 60(1):53–58, 1941.
- [83] M. Steenbeck. Device for producing electron rays of high energy. *U.S. Patent*, (2,103,303), 1937.
- [84] E. Wilson. *An Introduction to Particle Accelerators*. Oxford University Press, 2001.
- [85] H. Wiedemann. *Particle Accelerator Physics I*. Springer, 2003.
- [86] N. Christofilos. Focussing System for Ions and Electrons. *U.S. Patent*, (2,736,799), 1950.
- [87] M. S. Livingston E. D. Courant and H. S. Snyder. The Strong-Focusing Synchrotron - A New High Energy Accelerator. *Phys. Rev.*, 88(5):1190–1196, 1941.
- [88] S. Earnshaw. On the Nature of the Molecular Forces which Regulate the Constitution of the Luminiferous Ether. *Trans. Camb. Phil. Soc.*, 7:97–112, 1842.
- [89] W. Demtröder. *Experimentalphysik 2 - Elektrizität und Optik*. Springer Verlag Berlin Heidelberg New York, 2002.
- [90] R. Q. Twiss and N. H. Frank. Orbital Stability in a Proton Synchrotron. *Rev. Sci. Instrum.*, 20(1), 1949.
- [91] A. Chao and M. Tigner. *Handbook of Accelerator Physics and Engineering*. World Scientific, 1999.
- [92] K. Yokoya and H. Koiso. Tune shift of coherent beam-beam oscillations. *Particle Accelerators*, 27:181 – 186, 1990.
- [93] P. Raimondi. Status of the SuperB Effort, 2006. Presentation at the 2nd Workshop on SuperB Factory, LNF-INFN, Frascati, <http://www.lnf.infn.it/conference/superb06/talks/raimondi1.ppt>.
- [94] W. H. Preece. On Peculiar Behavior of Glow-Lamps When Raised to High Incandescence. *Proc. Roy. Soc. (London)*, Ser. A, 38:219, 1885.
- [95] Y. Kamiya et al. Development of an S-Band Cs_2Te - Cathode RF Gun with New RF Tuners. *Proceedings of PAC07, Albuquerque, New Mexico, USA*, THPMN040, 2007.
- [96] H.M. Marcos J.E. Geusic and L. Van Uitert. Laser oscillations in nd-doped yttrium aluminum, yttrium gallium and gadolinium garnets. *Appl. Phys. Let.*, 4(10):182–185, 1964.
- [97] G. I. Kuznetsov. Cathodes for Electron Guns. *Physica Scripta*, T71:39–45, 1997.
- [98] H. Hertz. Über den Einfluss des ultravioletten Lichtes auf die electrische Entladung. *Annalen der Physik*, 267(8):983–1000, 1887.

- [99] M. Trenary. Surface science studies of metal hexaborides. *Sci. Technol. Adv. Mater.*, 13(2):023002, 2012.
- [100] Z. Huang and R.D. Ruth. Radiative cooling of relativistic electron beams. *Particle Accelerator Conference 1999, Accelerator Science and Technology, Proceedings of the 1999 IEEE*, 1:262 – 266, 1999.
- [101] J. Liouville. Note sur la Théorie de la Variation des constantes arbitraires. *Journal de Mathématiques Pures et Appliquées*, Série 1, Tome 3:342 – 349, 1838.
- [102] B. Goddard M.J. Barnes, J. Borburgh and M. Hourican. Injection and extraction magnets: septa. *CERN Accelerator School CAS 2009*, 2011. arXiv: abs/1103.1062.
- [103] D. Mohl and A.M. Sessler. Beam cooling: principles and achievements. *Nucl. Instr. and Meth.*, A 532(1):1 – 10, 2004.
- [104] J.H. Booske et al. Periodic magnetic focusing of sheet electron beams. *Physics of Plasmas*, 1(5):1714 – 1720, 1994.
- [105] S. Humphries et al. Focusing of High-Perveance Planar Electron Beams in a Miniature Wiggler Magnet Array. *IEEE Transactions on plasma science*, 33(2):882 – 891, 2005.
- [106] P. Thompson et al. RHIC beam loss monitor system commissioning in RHIC year 0 Run. *AIP Conf. Proc.*, 546:313 – 321, 2000.
- [107] F. Zimmermann et al. Trapped macroparticles in electron storage rings. *Proceedings of the 1995 Particle Accelerator Conference*, 1:517 – 519, 1995.
- [108] S. Myers. Performance Related Measurements on LEP. *CERN-SL-99-002 DI*, 1999.
- [109] T. Sanami T. Kageyama Y. Suetsugu, K. Shibata and Y. Takeuchi. Development of movable mask system to cope with high beam current. *Rev. Sci. Instrum.*, 74(7):3297 – 3305, 2003.
- [110] E. D. Courant and H. S. Snyder. Theory of the alternating-gradient synchrotron. *Annals of Physics*, 3(1):1–48, 1958.
- [111] D.C. Carey. Turtle, Trace Unlimited Rays Through Lumped Elements. *Fermilab report*, NAL-64, 1971.
- [112] K. Hirata. An introduction to SAD. *Second Advanced ICFA Beam Dynamics Workshop*, CERN 88-04, 1988.
- [113] C. Grupen and B. Shwartz. *Particle Detectors*. Cambridge University Press, 2008.
- [114] Official Belle II collaboration website. <http://belle2.kek.jp>.
- [115] Martin Ritter. Private communication, 2015. See basf2 code: generators/examples/ParticleGunPlots.py.

- [116] S. Henderson. A method for gold coating experimental detector beampipes. *Proceedings of the 1999 Particle Accelerator Conference*, 2:1351–1353, 1999.
- [117] Hiroyuki Nakayama. Private communication, 2012.
- [118] K. Kanazawa. IR Beam Pipe. Talk at the Belle II Focused Review, October 2012.
- [119] J. Kemmer and G. Lutz. New detector concepts. *Nucl. Instrum. Meth.*, A 253(3):365–377, 1987.
- [120] G. Lutz et al. J. Kemmer. Experimental confirmation of a new semiconductor detector principle. *Nucl. Instrum. Meth. in Phys. Res.*, A 288(1):92–98, 1990.
- [121] R. Richter et al. Design and technology of DEPFET pixel sensors for linear collider applications. *Nucl. Instrum. Meth.*, A 511(1):250–256, 2003.
- [122] Karlheinz Ackermann. Private communication, 2012.
- [123] V. H. Grinich and H. G. Jackson. *Introduction to Integrated Circuits*. McGraw-Hill Series on the Fundamentals of Electronic Science, 1975.
- [124] O. Kilgenstein. *Formeln und Diagramme der Elektronik - Diskrete Halbleiterbauelemente*. Vogel-Verlag, 1981.
- [125] E. Gatti and P. Rehak. Semiconductor drift chamber - An application of a novel charge transport scheme. *Nucl. Instrum. Meth. in Phys. Res.*, 225(3):608–614, 1984.
- [126] K. Gärtner and R. Richter. DEPFET sensor design using an experimental 3D device simulator. *Nucl. Instrum. Meth.*, A 568(1):12–17, 2006.
- [127] K. Prothmann A. Moll and Z. Drasal. Optimization Studies with Single Tracks. Talk at the 4th International Workshop on DEPFET Detectors and Applications, Prague, January 2010.
- [128] J. Knopf I. Peric, P. Fischer and Thi Hong Hanh Nguyen. DCDB and SWITCHERB, the readout ASICS for belle II DEPFET pixel detector. *Nuclear Science Symposium and Medical Imaging Conference (NSS/MIC)*, pages 1536–1539, 2011.
- [129] T. Hemperek T. Kishishita H. Krüger M. Lemarenko, M. Havranek and N. Wermes. The Data Handling Processor for the Belle II Pixel Vertex Detector: efficiency optimization. *Topical Workshop On Electronics For Particle Physics 2011*, 2012.
- [130] P. Kodys. The DEPFET pixel detector for the Belle II experiment at SuperKEKB. *arXiv:1406.3864v1 [physics.ins-det]*, 10(02):C02037, 2015.
- [131] D. Greenwald S. Paul D. Levit, I. Konorov. FPGA Based Data Read-Out System of the Belle 2 Pixel Detector. *arXiv:1406.3864v1 [physics.ins-det]*, 2014.

- [132] G. Lindström. Radiation damage in silicon detectors. *Nucl. Instrum. Meth.*, A 512(1):30–43, 2003.
- [133] G. Kramberger G. Lindström, E. Fretwurst and I. Pintilie. Toward Super Radiation Tolerant Semiconductor Detectors For Future Elementary Particle Research. *Journal of Optoelectronics and Advanced Materials*, 6(1):23–38, 2004.
- [134] H. Jakubaschk. *Das große Elektronikbastelbuch*. Deutscher Militärverlag, 1967.
- [135] J. R. Black. Electromigration - A brief survey and some recent results. *IEEE Transactions on Electron Devices*, 16(4):338–347, 1969.
- [136] B. Essick. Pad for Evaporative Coolers. *U.S. Patent*, (2,391,558), 1945.
- [137] J.J. Senkevich and S.B. Desu. Compositional studies of near-room-temperature thermal CVD poly(chloro-p-xylylene)/SiO₂ nanocomposites. *Appl. Phys.*, A 70(5):541–546, 2000.
- [138] M. Friedl et al. Status of SVD. Talk at the Belle II Focused Review by BPAC, KEK, November 2011.
- [139] G. Lutz. *Semiconductor Radiation Detectors*. Springer, Device Physics, 1999.
- [140] M. Friedl. SVD Status. Talk at the Joint DEPFET/PXD and SVD Workshop, Göttingen, September 2012.
- [141] M. J. French et al. Design and results from the APV25, a deep sub-micron CMOS front-end chip for the CMS tracker. *Nucl. Instrum. Meth.*, A 466(2):359–365, 2001.
- [142] K. Emi et al. Study of a dE/dx measurement and the gas-gain saturation by a prototype drift chamber for the BELLE-CDC. *Nucl. Instrum. Meth.*, A 379(2):225–231, 1996.
- [143] S. Uno et al. Study of a drift chamber filled with a helium-ethane mixture. *Nucl. Instrum. Meth.*, A 330(1):55–63, 1993.
- [144] H.A. Bethe. Theorie des Durchgangs schneller Korpuskularstrahlen durch Materie. *Ann. d. Phys.*, 5:325–400, 1930.
- [145] F. Bloch. Bremsvermögen von Atomen mit mehreren Elektronen. *Z. Phys.*, 81:363–376, 1933.
- [146] K. Inami. Development of a TOP counter for the Super B factory. *Nucl. Instrum. Meth.*, A 595(1):96–99, 2008.
- [147] P. A. Cherenkov. Visible Emission of Clean Liquids by Action of γ Radiation. *Doklady Akad. Nauk SSSR*, 2:451, 1934.
- [148] K. Inami et al. Cross-talk suppressed multi-anode MCP-PMT. *Nucl. Instrum. Meth.*, A 592(3):247–253, 2008.

- [149] B. N. Ratcliff. Imaging rings in Ring Imaging Cherenkov counters. *Nucl. Instrum. Meth.*, A 502(1):211–221, 2003.
- [150] T. Matsumoto et al. Studies of proximity focusing RICH with an aerogel radiator using flat-panel multi-anode PMTs (Hamamatsu H8500). *Nucl. Instrum. Meth.*, A 521(2-3):367–377, 2004.
- [151] S. S. Kistler. Coherent Expanded Aerogels and Jellies. *Nature*, 127:741, 1931.
- [152] I. Adachi et al. E-PID: ARICH other Issues. Talk at the Belle II Focused Review by BPAC, KEK, November 2011.
- [153] T. Iijima et al. A novel type of proximity focusing RICH counter with multiple refractive index aerogel radiator. *Nucl. Instrum. Meth.*, A 548(3):383–390, 2005.
- [154] P. Križan et al. Study of a nonhomogeneous aerogel radiator in a proximity focusing RICH detector. *Nucl. Instrum. Meth.*, A 565(2):457–462, 2006.
- [155] S. Shiizuka et al. Study of 144-channel hybrid avalanche photo-detector for Belle II RICH counter. *Nuclear Instruments and Methods in Physics Research Section A*, 628(1):315–318, 2011.
- [156] A. Abashian et al. The Belle-detector. *Nucl. Instrum. Meth.*, A 479(1):117–232, 2002.
- [157] H. Ikeda et al. A detailed test of the CsI(Tl) calorimeter for BELLE with photon beams of energy between 20 MeV and 5.4 GeV. *Nucl. Instrum. Meth.*, A 441(3):401–426, 2000.
- [158] A. Abashian et al. Muon identification in the Belle experiment at KEKB. *Nucl. Instrum. Meth.*, A 491(1):69–82, 2002.
- [159] R. Santonico and R. Cardarelli. Development of resistive plate counters. *Nucl. Instrum. Meth.*, 187(2):377–380, 1981.
- [160] Y. Iwasaki et al. Level 1 Trigger System for the Belle II Experiment. *IEEE Transactions on Nuclear Science*, 58(4):1807–1815, 2011.
- [161] A. Moll. The Software Framework of the Belle II Experiment. *J. Phys.*, Conf. Ser. 331:032024, 2011.
- [162] PCI Industrial Computer Manufacturers Group. PICMG 3.0 Revision 2.0 AdvancedTCA Base Specification. *specification ECN-002*, 2006.
- [163] R. Itoh. BASF - Belle AnalysiS Framework. Talk at the Computing in High-energy Physics (CHEP 97), Berlin, Germany, April 1997.
- [164] F. Gaede. Marlin and LCCD - Software tools for the ILC. *Nucl. Instrum. Meth.*, A 559(1):177–180, 2006.

- [165] P. Mato. GAUDI-Architecture design document. Technical Report LHCb-98-064, CERN, 1998.
- [166] E. Sexton-Kennedy. A User's Guide to the AC++ Framework. Technical Report CDF Internal Note 4178, 1997.
- [167] A. Gheata. ALICE Analysis Framework. *Proceedings of Science, Advanced Computing and Analysis Techniques in Physics Research*, 2008.
- [168] R. Brun and F. Rademakers. ROOT - An object oriented data analysis framework. *Nucl. Instrum. Meth.*, A 389(1):81–86, 1997.
- [169] <http://www.boost.org>.
- [170] <http://proj-clhep.web.cern.ch/proj-clhep>.
- [171] <http://www.xmlsoft.org>.
- [172] B. D. Ward D. M. Beazley and I. R. Cooke. The inside story on shared libraries and dynamic loading. *Computing in Science and Engineering*, 3(5):90–97, 2001.
- [173] <http://www.python.org>.
- [174] R. Love. *Linux System Programming*. O'Reilly, 2007.
- [175] T. Sjöstrand et al. Z physics at LEP 1. *CERN 89-08*, page 143, 1989.
- [176] M. Melles B.F.L. Ward W. Placzek, S. Jadach and S.A. Yost. Precision calculation of Bhabha scattering at LEP. *CERN-TH-99-07*, 1999.
- [177] R. Kleiss and H. Burkhardt. BBBREM - Monte Carlo simulation of radiative Bhabha scattering in the very forward direction. *Comput. Phys. Commun.*, 81(3):372–380, 1994. arXiv:hep-ph/9401333.
- [178] M. Skrzypek B.F.L. Ward S. Jadach, W. Placzek and Z. Was. Monte Carlo program KoralW 1.42 for all four-fermion final states in e+ e- collisions. *Comput. Phys. Commun.*, 119:272–311, 1999. arXiv:hep-ph/9906277.
- [179] D. J. Lange. The EvtGen particle decay simulation package. *Nucl. Instrum. Meth.*, A 462(1):152–155, 2001.
- [180] B. Aubert et al. The BABAR detector. *Nucl. Instrum. Meth.*, A 479(1):1–116, 2002.
- [181] S. Mrenna T. Sjöstrand and P. Skands. A brief introduction to PYTHIA 8.1. *Comput. Phys. Commun.*, 178(11):852–867, 2008. arXiv:0710.3820.
- [182] D. Hunter et al. *Beginning XML, 4th Edition*. Wiley Publishing, Inc., 2007.
- [183] <http://www.w3.org/standards/xml>.

- [184] J. Allison et al. Geant4 developments and applications. *IEEE Trans. Nucl. Sci.*, 53:270, 2006.
- [185] S.K. Feiner J.D. Foley, A van Dam and J.F. Hughes. *Computer Graphics - Principles and Practice*. Addison-Wesley, 1997.
- [186] G.B. Benedek and F.M.H. Villars. *Physics With Illustrative Examples From Medicine and Biology - Statistical Physics*. Springer-Verlag, 2000.
- [187] T. Rohe L. Rossi, P. Fischer and N. Wermes. *Pixel Detectors: From Fundamentals to Applications*. Springer, 2006.
- [188] R.K. Bock and A. Vasilescu. *The Particle Detector BriefBook*. Springer, 1998.
- [189] W.T. Vetterling W.H. Press, S.A. Teukolsky and B.P. Flannery. *Numerical Recipes: The Art of Scientific Computing*. Cambridge University Press, 2007.
- [190] D. Green. *The Physics of Particle Detectors*. Cambridge University Press, 2000.
- [191] P.A. Tipler. *Physics for Scientists and Engineers*. W. H. Freeman, 2007.
- [192] K. Prothmann Z. Drasal and B. Schwenker. Silicon simulation code for Belle II and ILC. *Proceedings of Science*, Vertex 2011:27–38, 2011.
- [193] R. Turchetta. Spatial resolution of silicon microstrip detectors. *Nucl. Instrum. Meth.*, A 335(1):44–58, 1993.
- [194] E. F. Codd. A relational model of data for large shared data banks. *Commun. ACM*, 13(6):377–387, 1970.
- [195] H.A. Bethe. Molière’s Theory of Multiple Scattering. *Phys. Rev.*, 89(6):1256–1266, 1953.
- [196] C. Höppner et al. A novel generic framework for track fitting in complex detector systems. *Nucl. Instrum. Meth.*, A 620(2):518–525, 2010.
- [197] R. E. Kalman. A new approach to linear filtering and prediction problems. *Transactions of the ASME-Journal of Basic Engineering*, D 82:35–45, 1960.
- [198] R. Früwirth. Application of Kalman filtering to track and vertex fitting. *Nucl. Instrum. Meth.*, A 262(2):444–450, 1987.
- [199] A. Kibayashi H. Ishino and K. Takahashi. Alignment Method for the SVD2 and its Performance. *Comput. Phys. Commun.*, 119:272–311, 1999. arXiv:hep-ph/9906277.
- [200] M. Lamont S. Myers D. Brandt, H. Burkhardt and J. Wenninger. Accelerator physics at LEP. *Reports on Progress in Physics*, 63(6):939, 2000.
- [201] S.N. White W.J. Marciano and A. Zichichi. *Electromagnetic Probes of Fundamental Physics: Erice, Italy, 16-21 October 2001*. World Scientific, 2003.

- [202] V.N. Baier and V.S. Fadin. Description of Electroproduction Processes by using the Approximation of Quasi-Real Photons. *Soviet Physics JETP*, 36(3):399–403, 1973.
- [203] E.V. Pakhtusova V.A. Sidorov V.E. Balakin, A.D. Bokin and A.G. Khabakhpashev. Evidence for Electron-Positron Pair Electroproduction. *Phys. Lett. B*, 34(7):663–664, 1971.
- [204] H. Terazawa M.S. Chen, I.J. Muzinich and T.P. Cheng. Lepton Pair Production from Two-Photon Processes. *Phys. Rev. D*, 7(11):3485–3502, 1973.
- [205] L.D. Landau and E.M. Lifshitz. On creation of electrons and positrons in collision of two particles. *Phys. Zs. Sowjet*, 6:244, 1934.
- [206] G.V. Meledin V.M. Budnev, I.F. Ginzburg and V.G. Serbo. The Two-Photon Particle Production Mechanism. Physical Problems. Applications. Equivalent Photon Approximation. *Phys. Lett. C*, 15(4):181–282, 1974.
- [207] V.N. Baier and V.S. Fadin. Electroproduction of Pairs of Particles at High Energies. *Soviet Physics JETP*, 34(2):253–259, 1972.
- [208] J. Fujimoto et al. GRACE User's manual, version 2.0. Technical Report MINAMITATEYA collaboration, 1994.
- [209] M. Skrzypek and Z. Was. How to generate four-fermion phase space. *Comput. Phys. Commun.*, 125(1):8–20, 2000.
- [210] S. Frautschi D.R. Yennie and H. Suura. The infrared divergence phenomena and high-energy processes. *Ann. Phys.*, 13(3):379–452, 1961.
- [211] S. Jadach and B.F.L. Ward. YFS2 - The second-order Monte Carlo program for fermion pair production at LEP/SLC, with the initial state radiation of two hard and multiple soft photons. *Comput. Phys. Commun.*, 56(3):351–384, 1990.
- [212] A.D. Martin V.S. Fadin, V.A. Khoze and W.J. Stirling. Higher-order Coulomb corrections to the threshold $e^+e^- \rightarrow W^+W^-$ cross section. *Phys. Lett. B*, 363(2):112–117, 1995.
- [213] A.P. Chapovsky and V.A. Khoze. Screened-Coulomb ansatz for the nonfactorizable radiative corrections to off-shell W^+W^- production. *Eur. Phys. J.*, C9(3):449–457, 1999.
- [214] M. Skrzypek B.F.L. Ward S. Jadach, W. Placzek and Z. Was. Electric charge screening effect in single- W production with the KoralW Monte Carlo. *Eur. Phys. J.*, 27(1):19–32, 2003.
- [215] P.H. Daverfeldt F.A. Berends and R. Kleiss. Monte Carlo simulation of two-photon processes. *Comput. Phys. Commun.*, 40(2):285–307, 1986.
- [216] B.F.L. Ward S. Jadach, E. Richter-Was and Z. Was. Monte Carlo program BHLUMI 2.01 for Bhabha scattering at low angles with Yennie-Frautschi-Suura exponentiation. *Comput. Phys. Commun.*, 70(2):305–344, 1992.

- [217] D. Bardin et al. Event Generators for WW Physics. *pre-print*, 1997. arXiv:hep-ph/9709270v1.
- [218] Z. Natkaniec et al. Status of the Belle silicon vertex detector. *Nucl. Instrum. Meth.*, A 560(1):1–4, 2006.
- [219] T. Iijima et al. Aerogel Cherenkov counter for the BELLE detector. *Nucl. Instrum. Meth.*, A 453(1):321–325, 2000.
- [220] H. Kichimi et al. The BELLE TOF system. *Nucl. Instrum. Meth.*, A 453(1):315–320, 2000.
- [221] K. Miyabayashi. Belle electromagnetic calorimeter. *Nucl. Instrum. Meth.*, A 494(1):298–302, 2002.
- [222] A. Abashian. The K_L/μ detector subsystem for the BELLE experiment at the KEK B-factory. *Nucl. Instrum. Meth.*, A 449(1):112–124, 2000.
- [223] S. Koblitz E. Nedelkovska, C. Kiesling. Estimation of the two-photon QED background in Belle II. *Belle II Note*, 12, 2012.
- [224] M. Friedl et al. The Silicon Vertex Detector of Belle II. *Proceedings of Science*, Vertex 2011, 2011.
- [225] A. Kuzmin H. Sagawa V. Zhilich, A. Bondar and B. Shwartz. Offline luminosity measurements from the Belle detector. *BELLE Note*, 453, 2001.
- [226] Official Belle runinfo. http://belle.kek.jp/secured/runinfo/command/fig/data_per_run.dat.
- [227] S. Uehara. TREPS: A Monte-Carlo Event Generator for Two-photon Processes at e^+e^- Colliders using an Equivalent Photon Approximation. *KEK Report*, 96-11, 1996.
- [228] Sadaharu Uehara. Private communication, 2012.
- [229] H. Ikeda T. Iijima T. Tsukamoto M. Yamauchi K. Hanagaki, H. Kakuno. Status of Electron Identification. *BELLE-Note 312*, 312, 2000.
- [230] K. Pearson. On Lines and Planes of Closest Fit to Systems of Points in Space. *Philosophical Magazine*, 2(11):559–572, 1901.
- [231] H. Abdi and L. J. Williams. Principal component analysis. *Wiley Interdisciplinary Reviews: Computational Statistics*, 2(4):433–459, 2010.
- [232] B. Gärtner and S. Schönherr. Exact Primitives for Smallest Enclosing Ellipses. *Information Processing Letters*, 68:33–38, 1998.
- [233] Computational Geometry Algorithms Library. <http://www.cgal.org>.

[234] A. McNair. ICRU Report 33 - Radiation Quantities and Units Pub: International Commission on Radiation Units and Measurements. *Journal of Labelled Compounds and Radiopharmaceuticals*, 18(9):1398, 1981.

[235] ASTM Standard. Standard Practice for Characterizing Neutron Fluence Spectra in Terms of an Equivalent Monoenergetic Neutron Fluence for Radiation-Hardness Testing of Electronics. *ASTM International, West Conshohocken, PA*, E722-93:1-27, 1993.

[236] G. Lindström. NIEL folding data for neutrons. <http://sesam.desy.de/members/gunnar/Si-dfuncs.html>.

[237] G. Di Giugno G. Ghigo J. Haassisnski P. Marin R. Querzoli C. Bernardini, G.F. Corazza and B. Touschek. Lifetime and Beam Size in a Storage Ring. *Phys. Rev. Lett.*, 10(9):407, 1963.

[238] G. Pancheri L. Bonolis. Bruno Touschek: particle physicist and father of the electron-positron collider. *arXiv:1103.2727v1 [physics.hist-ph]*, 2011.

[239] J. Haissinski. Single and Multiple Touschek Effects. *Rapport technique interne, LAL Orsay*, (41-63), 1963.

[240] D. M. Ritson B. Gittelmann. *HEPL-291, Stanford University*, (41-63), 1963.

[241] U. Völkel. Particle Loss by Touschek Effect in a Storage Ring. *DESY*, (67/5), 1965.

[242] Y. Miyahara. A New Formula for the Lifetime of a Round Beam Caused by the Touschek Effect in an Electron Storage Ring. *Jap. Journal of Appl. Phys.*, 24(9):L742, 1985.

[243] A. Piwinski. The Touschek Effect in Strong Focusing Storage Rings. *DESY*, (98-179), 1998.

[244] H. Nakano. A simulation study of beam backgrounds at the KEKB and Super KEKB colliders. *Master Thesis*, 2011.

[245] H. Brück. Circular Particle Accelerators. *PUF, Paris*, 1966.

[246] H. Nakayama. Beam-gas background. Talk at the Joint Belle II and SuperB Background Meeting, Vienna, February 2012.

[247] E. Clapeyron. Mémoire sur la puissance motrice de la chaleur. *Journal de l'École Polytechnique*, XIV:153–90, 1834.

[248] S. K. Sahu. A Generator for Study of Background due to Beam-gas Interaction at KEK B-factory. *BELLE Note*, 97-172, 1997.

[249] A. Liénard. Champ électrique et magnétique produit par une charge concentrée en un point et animée d'un mouvement quelconque. *L'éclairage électrique*, 16:5, 53, 106, 1898.

[250] E. Wiechert. Elektrodynamische Elementargesetze. *Archives Néerlandaises*, 5:549, 1898.

[251] I. Ya. Pomeranchouk D. Ivanenko. On the Maximal Energy Attainable in a Betatron. *Phys. Rev.*, 65(11-12):343, 1944.

[252] R. Langmuir F. Elder, A. Gurewitsch and H. Pollock. Radiation from Electrons in a Synchrotron. *Phys. Rev.*, 71(11):829–830, 1947.

[253] P.L. Hartman D.H. Tomboulian. Synchrotron Radiation Sources. *Phys. Rev.*, 102:1423–1447, 1956.

[254] H. Fukuma J.W. Flanagan, M. Arinaga and H. Ikeda. Diamond Mirrors For The Super-kekbo Synchrotron Radiation Monitor. *Proceedings of IBIC2012, Tsukuba, Japan*, TUPB74, 2012.

[255] M. Sands. The Physics of Electron Storage Rings An Introduction. *SLAC-121*, UC-28:190, 1970.

[256] G. J. Roy. A new method for the simulation of synchrotron radiation in particle tracking codes. *Nucl. Inst. Meth.*, A298:128–133, 1990.

[257] S. D. Henderson. Synchrotron Radiation Background Simulation with SRGEN/SRSIM, 1995. Private communication with Tom Browder.

[258] S. K. Swain T. Browder, S.Olsen and H. Yamamoto. Synchrotron Radiation Background Simulation Study for Belle. *BELLE Note*, 361, 2001.

[259] S. D. Henderson. Beam Backgrounds at CLEO: Design and Performance of the CESR High Luminosity Interaction Region. *CLNS 97*, 1528:36, 1997.

[260] A. Moll. PySynRad - Synchrotron radiation generator for Belle II. <https://github.com/portrain/PySynRad>.

[261] J. von Neumann. Various techniques used in connection with random digits. Monte Carlo methods. *Nat. Bureau Standards*, 12:36–38, 1951.

[262] L. Devroye. *Non-Uniform Random Variate Generation*. Springer-Verlag, New York, 1986. Web edition at: <http://luc.devroye.org/rnbookindex.html>.

[263] H. Burkhardt. Monte Carlo Generation of the Energy Spectrum of Synchrotron Radiation. *EUROTEV-Report*, 018:11, 2007. CLIC-Note-709.

[264] H. J. Bhabha. The Scattering of Positrons by Electrons with Exchange on Dirac's Theory of the Positron. *Proc. R. Soc. Lond. A.*, 154:195–206, 1936.

[265] G. C. Baldwin and G. S. Klaiber. Photo-Fission in Heavy Elements. *Phys. Rev.*, 71(1):3–10, 1947.

[266] B. L. Berman and S. C. Fultz. Measurements of the giant dipole resonance with monoenergetic photons. *Rev. Mod. Phys.*, 47(3):713–761, 1975.

- [267] P. S. Rudenko A. V. Varlamov, V. V. Varlamov and M. E. Stepanov. Atlas of Giant Resonances. *International Nuclear Data Committee*, INDC(NDS)-394:1–328, 1999.
- [268] G. Altarelli and F. Buccella. Single photon emission in high-energy e+-e- collisions. *Il Nuovo Cimento*, 34(5):1337–1346, 1964.
- [269] Y. Ohnishi et al. Accelerator design at SuperKEKB. *Prog. Theor. Exp. Phys.*, 03A011:1–17, 2013.
- [270] A.E. Blinov et al. Large impact parameter cut-off in the process $e^+e^- \rightarrow \gamma$. *Phys. Lett. B*, 113(5):423–426, 1982.
- [271] H. Bichsel. Straggling in thin silicon detectors. *Reviews of Modern Physics*, 60(3):663–699, 1988.
- [272] D. M. Asner et al. US Belle II Project Technical Design Report. *pre-print*, 2013. <http://belleweb.pnnl.gov/forTDRreview/TDR-SLAC-13Dec8.pdf>.
- [273] Y. Soloviev. Synchrotron Radiation Background Simulation. Talk at the 16th International Workshop on DEPFET Detectors and Applications, Kloster Seeon, May 2014.
- [274] Y. Soloviev. Synchrotron Radiation Background Simulation. Talk at the 18th Open Meeting of the Belle II Collaboration, KEK Japan, June 2014.
- [275] A. Ritter et al. Investigations on radiation hardness of DEPFET sensors for the Belle II detector. *Nucl. Instrum. Meth.*, A 730(1):79–83, 2013.
- [276] A. Ritter. Radiation Hardness Studies for DEPFETs in Belle II. *PhD Thesis*, 2013.
- [277] R. Hagedorn. *Relativistic Kinematics*. W. A. Benjamin, 1964.
- [278] H. Bethe and W. Heitler. On the Stopping of Fast Particles and on the Creation of Positive Electrons. *Proc. Roy. Soc.*, A146:83, 1934.
- [279] W. Heitler. *The Quantum Theory of Radiation*. Clarendon Press, Oxford, 1954.
- [280] H. W. Koch and J. W. Motz. Bremsstrahlung Cross-Section Formulas and Related Data. *Rev. Mod. Phys.*, 31:920, 1959.
- [281] Yung-Su Tsai. Pair production and bremsstrahlung of charged leptons. *Rev. Mod. Phys.*, 46:815–851, Oct 1974.

Acknowledgements

The past six years have been an extraordinary journey and, without any doubt, the best period of my life so far. I have had the privilege of travelling around the world, seeing places, staying and spending time in foreign countries, and presenting my work at various meetings, workshops and conferences. I had met heaps of nice people with many of them eventually becoming colleagues and then friends. This section is dedicated to them and their support during these past years.

Without any doubt, this amazing time wouldn't have been possible without the support, guidance and supervision of **Christian Kiesling**. He believed in me and supported me from the start of my Diploma thesis to the end of my PhD thesis. I had the luck of working for and with him over the course of the past seven years. His door has always been open and his skills as a group leader and supervisor are among the best one can find. Nobody could escape his mesmerising "magic" powered by "enthusiasm" and "optimism". They are the driving forces behind the PXD project. I hope that you, Christian, will never run out of them.

Whenever I needed advice on Geant4, algorithms and Miles&More cards **Frank Simon** was there to help me. He has been a fantastic second supervisor and has been forced to listen to my complaints about the world of particle physics far too often. Frank, thank you so much for that. He also funded me during my time as a PhD student and I'm more than grateful for this support. Frank also deserves special thanks for proofreading this thesis and giving me valuable feedback and suggestions.

If there was a way to apply the `git clone` command to real life, I would make myself a copy of **Martin Ritter**. His coding skills, git knowledge, graphic design capabilities and aptitude at everything that happens between a human and a computer made him the most precious work colleague. And he is a great friend too! He introduced me to Python, matplotlib and numpy, the evil that is `catch{...}` and showed me the beauty of Firefly, cider and Guinness stew. I was very lucky to have him as a work colleague for most of my time at MPI, as he was almost sold to a fitting club in Hamburg. Thank you so much for being such a great colleague and friend.

From my first day at MPI **Kolja Prothmann** accompanied me as a great and fun work colleague. We performed the early Belle II tracking studies and survived nerve-wracking meeting deadlines and near-death plane accidents together. The stories of his ability to get seriously sick in Japan each time we went there are legendary and should be told to future generations of Belle II students as cautionary tales.

Zbynek Drasal was the first colleague from outside of MPI that I worked with and he has been a close working colleague ever since. From the first Belle II tracking studies in the ILC framework to the PXD simulation and optimisation, continuing to early background estimations and Belle II software development, we collaborated on countless projects during my time at MPI. Thank you so much for your tour through Prague (pickled cheese!), great dorm parties and all the PXD/SVD software work you have done for Belle II.

Peter & Peter from Prague, also known as **Peter Kodys** and **Peter Kvasnicka**, are among the most fun, entertaining and relaxed people I have had the pleasure of meeting and working with during my time as part of Belle II. I will never forget the fermented stingray dinner in Seoul with Peter Kodys and the many occasions I enjoyed a beer (or two) with Peter Kvasnicka at Castle Ringberg. Thank you, Peter & Peter, for an inspirational, entertaining five years.

My stay in Japan wouldn't have been as enjoyable as it was without the support and guidance of **Takanori Hara-San**. He introduced me to the culture of the hammer-helmet birthday game, Japanese food and the importance of the Bourne trilogy. Thank you so much for organising the most delicious meeting dinners and being the most friendly, supportive and optimistic KEK employee I worked with during my PhD.

Hiro Nakayama-San has done a fantastic job of mediating between the Belle II software group and the SuperKEKB accelerator group. I very much enjoyed the time we worked together on developing the background simulation tools. I'm quite proud of what we have achieved and hope that our results will be confirmed in 2016.

There are heaps more people I would like to thank. Among them are: **Jeremy Dalseno**, **Pit Vanhoefer** and **Veronika Chobanova** for those great dorm gatherings where vending machine food and Japanese beer made the place a little bit more enjoyable. Those nights completely changed my view on the performance advantages of shaved legs and why the KEK ring road should be fitted with racing curbs; The CLIC crew, **Katja Seidel**, **Lars Weuste** and **Chris Soldner**, for sharing yummy barbies, cakes, beer, various ROOT bugs, and compiler quirks; **Tscharlie Ackermann** for not only being a fantastic engineer, but also a very supportive colleague and great travel companion; **Silke Zollinger** for all her hard and often not appreciated enough work on the organisation of ScienceSlams and open days; **Dieter Fischer** for patiently booking flights at the last minute and working his way through confusing Reiseanträge; My colleagues from Karlsruhe, **Thomas Kuhr** and **Martin Heck**, for lively discussions about build systems, shared pointers and default units. Thank you very much for the great support during the development of the framework and your trust in me. Please, Martin, never change the way you present talks; **Ryosuke Itoh-San** and **Nobu Katayama-San** for agreeing to the development of a new framework and their support throughout that process. Your "Aufheben solution" slide will always remind me of the legendary meeting in 2010; **Rudolf Frühwirth** for autographing a copy of his book (now part of the MPI library), the great meetings in Vienna and the "Sturm"; **HEPHY** for giving the most interesting people in particle physics a home.

I wouldn't have been able to take this thesis to the level it is at now without the support of the computing team at the Australian Synchrotron: **Ulrich Felzmann, Gary Ruben, Lenneke Jong, Rosemary Waghorn and Lauren Baird**. In particular, Ulrich Felzmann has provided me with computing resources, a flexible work schedule and entertaining stories from the self-acclaimed world centres of particle physics. Gary Ruben kept me up-to-date with the latest news from the Python and micro 4/3 communities and helped me with Latex fonts and colour palettes. I would like to thank the **MASSIVE** team at Monash University for their computing resources and support. They may not be aware of it, but they've got a Belle II project now.

Last but not least I would like to thank those people "behind the scenes" who helped, supported and encouraged me. My parents, **Peter** and **Mariele** have always provided me with everything they had and everything I needed. I can't say how grateful and thankful I am for their never-ending support and encouragement for more than 34 years. They taught me to never restrict myself and to be open to the unknown. Without them I wouldn't be what and where I am today. Thank you so much from the bottom of my heart. Now, get out and see the world! You deserve it!

My brothers **Richard** and **Maximilian** are the best mates I could ever wish for. Whenever we are together, it is always an extremely entertaining time. I had an incredible time sharing an apartment with Richard, when soccer and Roooobert ruled the evenings and I managed to double the electricity bill. Maximilian has always been an inspiration and as the youngest brother he is something special for me. Rock the world Maxi!

The most precious "discovery" I made in Japan is, without any doubt, my girlfriend **T'Mir**. Since 2010 I've been learning that there is a connection between Germany and Australia that reaches further than the two neighbouring offices in San-Go-Kan. You have shown me that a long-distance relationship can work. But living together with you is the best thing that ever happened to me. Thank you so much for all the fun we had in the past five years and for your support and encouragement. I love you!